Mohammad Ali Muhsin Awabdeh

Active tectonics of the Amman-Hallabat and Shueib structures (NW of Jordan) and their implication in the Quaternary evolution of the Dead Sea Transform Fault System

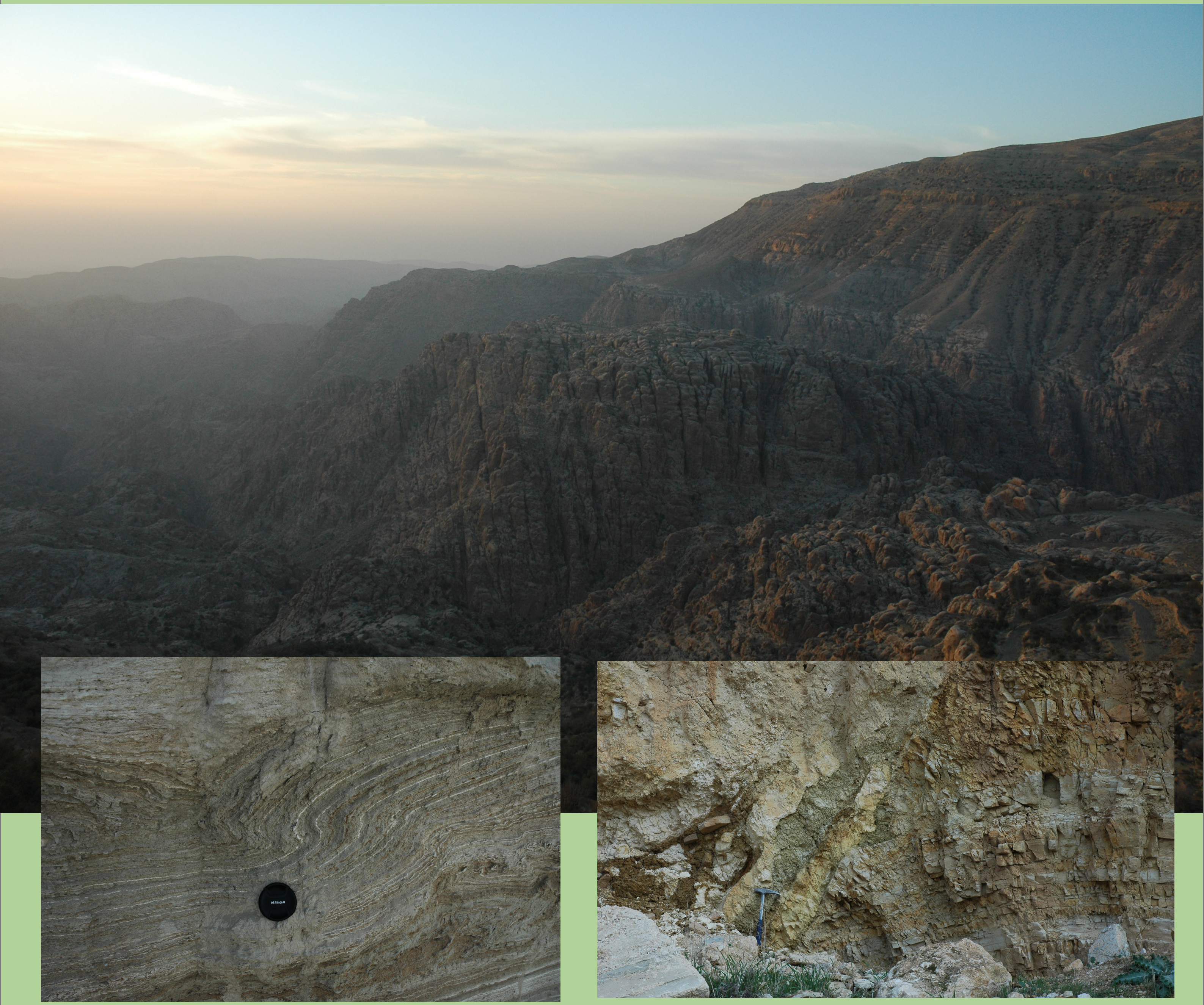

Tesis Doctoral 2015
Universidad de Granada
Departamento de Geodinámica

Editor: Universidad de Granada. Tesis Doctorales
Autor: Mohammad Ali Muhsin
ISBN: 978-84-9125-379-2
URI: http://hdl.handle.net/10481/41356

PHD THESIS

University of Granada
Department of Geodynamics

Quaternary tectonic activity of the Amman-Hallabat structure and the Shueib structure and their relations with the Dead Sea Transform Fault (NW Jordan)

Mohammad Ali Muhsin Awabdeh

University of Granada 2015

El doctorando D. Mohammad Ali Muhsin Awabdeh y los directores de la tesis doctoral D. José Miguel Azañón Hernández y José Vicente Pérez Peña garantizamos al firmar esta tesis doctoral, que el trabajo ha sido realizado por el doctorado bajo la dirección de los directores y hasta donde nuestro conocimiento alcanza, en la realización del trabajo, se han respetado los derechos de otros autores a ser citados, cuando se han utilizado sus resultados o publicaciones

Granada a 06 de Octubre de 2015

Los directores

Fdo. José Miguel Azañón Hernández

Fdo. José Vicente Pérez Peña

El doctorando

Fdo. Mohammad Ali Muhsin Awabdeh

Agradecimientos

Quiero expresar mis profundos y sinceros agradecimientos a muchas personas que hayan sido el apoyo constante y que formaron parte de mi vida diaria durante mi estancia en Granada.

En primer lugar, a mis directores de esta tesis doctoral, ***Jose Miguel Azañón Hernandez y Jose Vicente Pérez-Peña***, por la motivacion y la confianza que han depositado en mí en varios momentos cruciales, por la enseñaza y la orientacion constante que he recibido a lo largo de estos años. La cual, esta tesis doctoral jamas pudiera existir sin vuestra supervision, muchisimas gracias.

Tambien quiero agradecer a Guillermo Booth-Rea, Jesus Galindo, Fernando Semanca, David Poyato por sus ideas y discusiones de la interpretaciones de los datos de esta tesis doctoral. A Antonio Garcia Casco por los consejos y la oportunidad de participar y asistir las conferncias y los seminares del programa de doctorado en la UGR. Agradezco al tribunal de examinacion asignado para evaluar esta version de tesis.

El apoyo familiar, de parte de mi mujer (***Mimonte***) y mi preciosa hija (***Salma Estrella***), no lo agradeceria todas las palabras que quisiera decir. La vida es imposible sin vosotras y me enfrento a cualquier desafio solo si estais a mi vera. A mis padres (***Ali y Fatima***) que preocuparon por esta tesis mas que yo mismo y por la paciencia, el carino y la comprension que me han dado constantemente. Sin ellos no habria podido llegar a esta altura. A mis hermanos y hermanas por sus permenente preocupacion y carino .Os quiero una JARTA.

Agradezco a mis mejores amigos de Granada por estar siempre a mi lado y quererme sin condiciones: A Marcos (y su cachimba), Yasmina (y los paseos), Zaid (y su familia), Ahmad, Bachir. Gracias por los mejores momentos que vivia con vosotros y que ya son inolvidables. Gracias a Fadi (y Sana), Othman, Sami, Shahm, Anas.

A mis companer@s del despacho, Eduardo, Idaira, Enric, Julia, Juan Antonio, Juan Cardenas, Angel, Lara, Fran, Juampe, Irene, Manuel, Rafa. A los viejos companer@s del departmento: Pedrera, Patricia, Ana Ruiz, Duque, Pedro, Farida, Silvia, John, Chema, (*Vicente el becario*), Ana luque, Ana Arizzi, Veronica, Vanesa, Rute, Julia, Juan, Zoltan, Erwin, Pilar. Espero que no haya olvidado alguien.

Por último, quiero expresar mis agradecimientos a todas aquellas personas que no he llegado a recordar al escribir estas lineas y que formaron parte de mi vida en Granada durante la elaboracion de esta tesis.

"I acknowledge funding from the Erasmus mundus external cooperation window 3 for the PhD grant awarded through 2009-2011 and the one year research grant from the Tafila Technical University in Jordan".

Abstract

The Dead Sea Transform Fault (DSTF) constitutes the transform plate boundary between Africa and Arabia plates and it is one of the biggest strike-slip faults in the world (ca. 1000 km long). This fault formed by mid-Cenozoic breakup of a region that had been stable until that moment; and, therefore this breakup has not been complicated by a previous history. There are still some open questions regarding this strike-slip fault. The links between its two southern segments (Wadi Araba Fault and Jordan Valley Fault), the deformation along the Lebanon and Syrian in its northern part, or the differences in offset between its southern and northern parts remain poorly known. Moreover, active tectonic studies are scarce in some areas as in the Jordanian part of the Dead Sea Transform, which has been considered tectonically inactive in Pleistocene Times.

The southern part of this fault is divided in two main segments, the Wadi Araba Fault (WAF) and the Jordan Valley Fault (JVF) connected through the Dead Sea continental pull-apart basin. Active tectonic studies in NW Jordan have traditionally focused on these DSTF structures and have discarded other prominent structures in the region like the Amman Hallabat (AHS) and the Shueib (SHS) faults system, as they have been considered inactive from the Cretaceous. However some recent studies have suggested a possible local reactivation of the northern parts of these structures. In this Thesis I carried out a detailed geological study in the NW Jordan in order to analyze the Quaternary activity of the AHS and SHS based on landscape anlysis trhought geomorphic indexes, field observations, structural analyses and archaeological evidences of recent earthquakes.

From a methodological point of view I present in this Thesis two ArcGIS Add-Ins to automatically delineate swath and normalized river profiles. Both tools are programmed in Visual Basic .NET and use ArcObjects library-architecture to access directly to vector and raster data. The SwathProfiler Add-In allows analyzing the topography within a swath or band by representing maximum-minimum-mean elevations, first and

third quartile, local relief and hypsometry. I have defined a new transverse hypsometric integral index (THi) that analyzes hypsometry along the swath and works better in this kind of representation. The NProfiler Add-In allows representing longitudinal normalized river profiles and their related morphometric indexes as normalized concavity (C_T), maximum concavity (C_{max}) and length of maximum concavity (L_{max}). Both tools facilitate the spatial analysis of topography and drainage networks directly in a GIS environment as ArcMap and provide graphical outputs in image (jpg) and vectorial (wmf) formats.

The landscape analysis presented in this Thesis focused in the eastern margin of the Dead Sea, with the intention of analyzing the effects that the Quaternary activity of the Dead Sea Transform Fault (DSTF) produces in the landscape and in the drainage network. This landscape analysis has two well-differentiated parts. First I analyzed the general landscape pattern through the application of spatial-based geomorphic indices as the slope, surface roughness, hypsometry and topographic swath profiles. With this analysis I aimed to describe and evaluate the general stage of landscape evolution in the study area, and examine the links between the tectonic structures and the general topographic patterns. These results of these geomorphic parameters show a good correlation with the active structures of the study area that act as boundaries for erosion processes. They also highlight a clear erosion wave advancing eastwards from the Dead Sea into the TransJordanian Plateau (TJP). Moreover, these analysis lacks clear evidences of a northern structure closing the Dead Sea apart of the NW-SE normal faults related to the AHS and SHS. Secondly, I analyzed several geomorphic indexes in order detect different pattern and highlight differences that could be due to dissimilar tectonic activity along the study area. The geomorphic indexes suggest that the study area is very young and it is in a transient state of landscape development. Normalized profiles have characteristics convex or linear-convex shapes, as well as the hypsometric curves. Area-slope plots have high Ksn values and lacks clear linear correlation, especially in their middles and lower parts (near mouths), due to the transient state of the analyzed rivers.

The field campaigns made in this Thesis have revealed that AHS and SHS structures present clear Quaternary activity and accommodate a small part of the deformation of the southern DSTF. The southwestern part of the AHS acts in the Quaternary as the northernmost continuation of the WAF, whereas the SHS works as a transfer of NW-SE normal faults with low to moderate throws that connects this structure with the JVF.

The stress analysis based on fault-slip data for two of the Amman Hallabat (AHF) and Shueib (SHF) structures suggests that most of the structures are coherent with the present-day stress pattern associated to the Dead Sea fault system. In most of the field stations there is a clear overprint of new striations over the older ones. Present-day stress in the region has horizontal to sub-horizontal maximum and minimum compressive axes ($\sigma 1$ and $\sigma 3$), striking NNW-SSE and ENE-SWS respectively, and a vertical intermediate stress axis ($\sigma 2$). These new findings suggest a rejuvenation of the AHF and the SHF in the Quaternary in the context of the Dead Sea Transform Fault (DSTF) tectonic activity.

A seismogenic character of the AHS can be claimed from the damage found in the archaeological site of Tall el-Hamman, which has been recently interpreted as the ancient city of Sodom. The destruction of this city is attributed to bid earthquake, that may be also related with this structure.

The NW-SE normal faults bounding the AHS and SHS could merge into a single fault plane that will act as the northern closure of the Dead Sea. Future geophysical research in the area should pay attention to these active structures as research in southern areas has prove fruitless.

Chapter 1

Introduction

Preface

In this first chapter I will introduce a general view of my PhD Thesis. I will discuss very briefly the general approach of this Thesis and highlight the interes of the geological research in the area of the Dead Sea Transform Fault (DSTF). Despite the numerous research studies that have been carried out in this area, there are still some open questions that deserve a scientific study. Some of them imply the stress transference between the Wadi Araba Fault and the Jordan Valley fault in the northern termination of the Dead Sea and how this can have reactivated some Jordanian structures thought inactive since Cretaceous. Moreover, in this Thesis I have performed a detailed geomorphic study in order to decipher the landscape evolution of the DSTF and their related structures.

I will present the main objective of this thesis and the study areas where the landscape analysis and the field campaigns have been carried out.

This chapter includes the following subtitles:

1.1 General approach

1.2 Objectives of this PhD Thesis

1.1 General approach

The Dead Sea Transform Fault is one of the biggest strike-slip faults in the world (ca. 1000 km long) and has been studied from many diverse perspectives. It constitutes an excellent natural laboratory to study a variety of geological topics, as it can be viewed in the high number of papers dealing with different topics about this plate-boundary structure. This fault formed by mid-Cenozoic breakup of a region that had been stable until that moment; and, therefore this breakup as not complicated by a previous history. Large pull-apart basins (some of the largest on earth) and transpressional structures associated with this fault constitute excellent examples to study the relations between transpression and transtension structures related to strike slips faults. The area has been populated since prehistory and it played a significant role in the human migration out of Africa as well as in the history of our ancient civilization. Therefore, the Dead Sea Transform Fault offers an opportunity to study how seismic shaking affects not only sediments but also historical buildings, thus constituting a high-resolution paleoseismic and archaeoseismic archive.

The detailed movement along the Dead Sea Transform is now better constrained thanks to new high-resolution GPS motion data. In the last 10 years several studies have characterized the horizontal movement along the Dead Sea Fault, in particular in its southern part. However, these studies does not provide reliable vertical resolution, needed to understand the evolution of pull-apart basins as the Dead Sea.

There are still some open questions regarding this strike-slip fault. The links between its two southern segments (Wadi Araba Fault and Jordan Valley Fault), the deformation along the Lebanon and Syrian in its northern part, or the differences in offset between its southern and northern parts remain poorly known. Moreover, active tectonic studies are scarce in some areas as in the Jordanian part of the Dead Sea Transform, which has been considered tectonically inactive in Pleistocene Times.

Between the different tectonic studies carried out along this fault, none of them has quantitatively characterized the drainage network and landscape evolution related to the tectonic history through the application of morphometric indexes. The Dead Sea formed as a pull-apart basin between the two main segments of the southern Dead Sea Transform and it constitutes an outstanding natural laboratory to explore some concepts about steady- and transient-state conditions. It is the only place in the world where rivers flow beneath the present-day sea level and has experienced a continuous base-level lowering since its formation.

This thesis have two well-differentiated part; in the first part I have investigated the landscape evolution of the southern Dead Sea fault, specifically the eastern margin of the Dead Sea pull-apart basin (**Fig. 1.1**). This study improves the knowledge about the northern termination of the Wadi Araba fault and the closure of the Dead Sea basin and their implications, in terms of tectonic activity, in some important Jordanian structures (Amman-Hallabat and Shueib structures) thought inactive since Cretaceous. There were no such studies in this structure until present. In order to calculate some of the gemorphic indexes used in this Thesis, I developed some ArcGIS Add-Ins to extract Normalize and Swath Profiles. These tools improve the calculation by using built-in ESRI arcobjects and facilitate the calculation process. I the third chapter of this Thesis I will describe them in detail.

In a second part, I focus in the tectonic activity of two of the main Jordanian Structures thought inactive since Cretaceous (the Amman Hallabat Structure and Shueib Structure). To accomplish that I have carried out some field campaigns to analyze the tectonic activity of these Jordanian structures and their relations with the Dead Sea transform. These filed studies focus between Amman city and the NE corner of the Dead Sea lake (**Fig. 1.2**). In this Thesis I will present new field evidences of the Quaternary activity of and structural data and measurements that prove the links between the kinematic of these structures respect to the Dead Sea stress field. Finally I analyzed a recent discovered archaeological site located between the two Jordanian structures. In a first field campaign I analyzed some damages that could indicate historical evidences of past earthquakes. This site has been further excavated and it is thought to be the ruins of the ancient kingdom of Sodom, whose destruction is referred in biblical and koranic texts. The archaeoseismological evidences found in the first excavation of this site could point to the activity of the structures studied in this Thesis as well as provide an alternative to the destruction of this ancient realm.

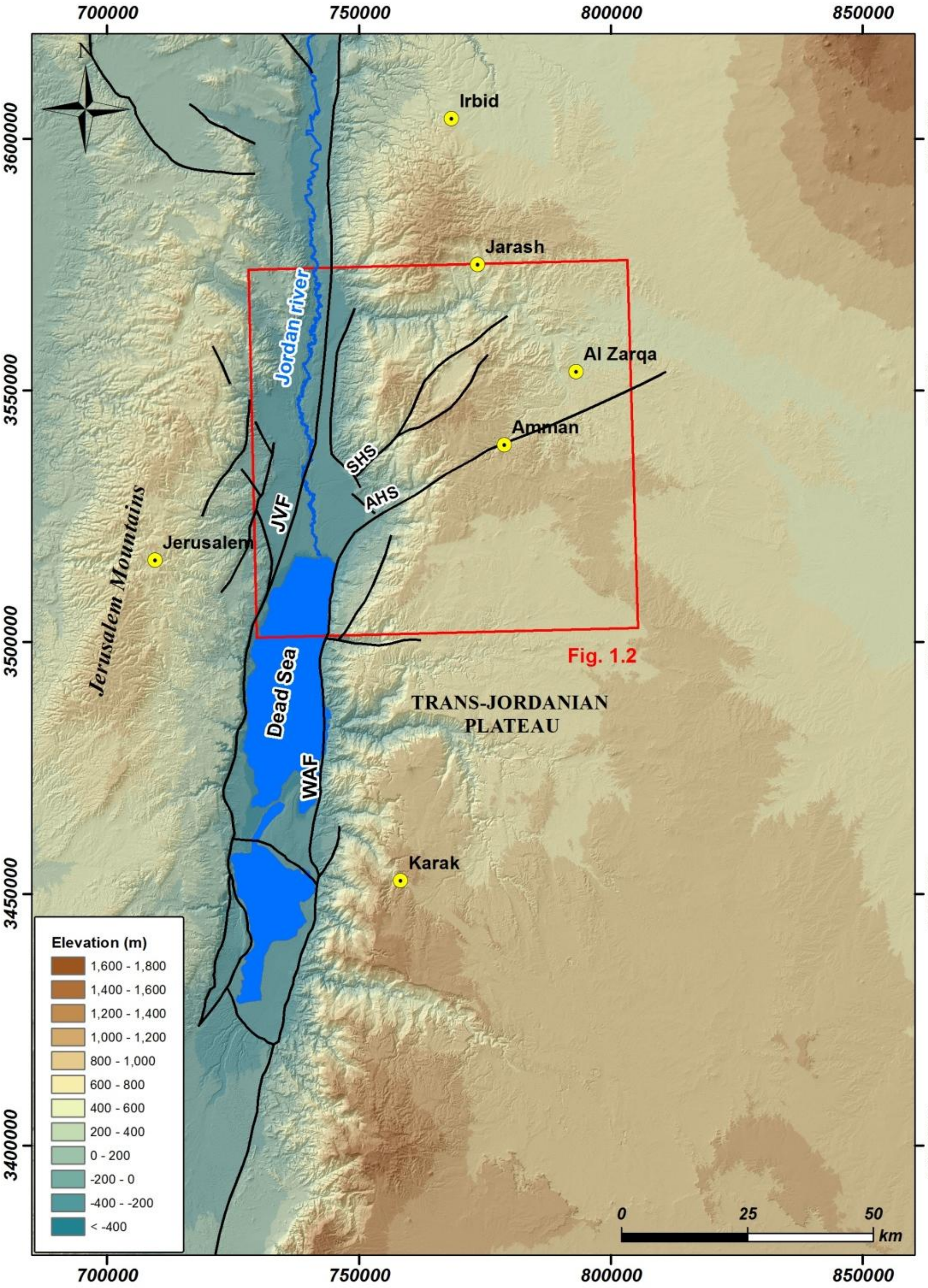

Figure 1.1. Study area where geomorphic analysis have been carried out.

The social-economic consequences of this study would better enhance the perception of the natural risk along the northern coast of the Dead Sea. This area is the focus of important touristic investments with hundreds of millions Jordanian Dinars constructions projects executed yearly. This study will serve as a preliminary work for identifying the required active tectonic framework for future natural risk assessment related to the studied geological structures.

This PhD Thesis has been financed by two research grants: the Erasmus Mundus External Cooperation Window Lot3 and a one year research grant from The Tafila Technical University in Jordan.

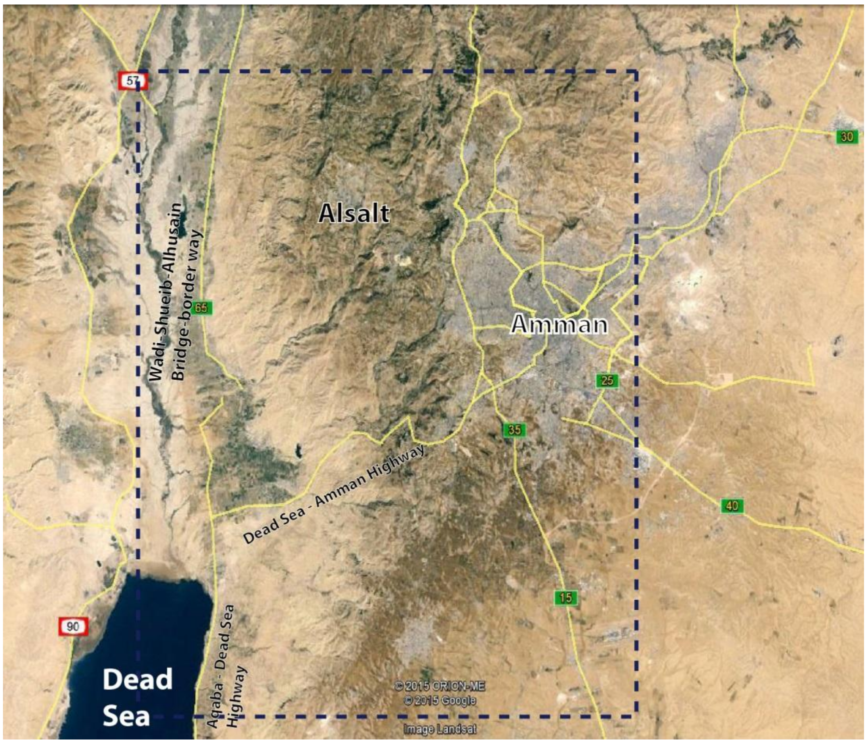

Figure 2.2. NE corner of the study area where field campaigns have been focused and structural measures have been taken

1.2 Objectives of this PhD Thesis

A first objective of this Thesis is to perform a landscape analysis in the southern DSTF, focusing in the Jordanian part of the Dead Sea. Such analysis have not been carried out until present. This geomorphic analysis will help to understand the recent landscape evolution conditioned by the tectonic activity of the DSTF and related structures. In the area have been carried out several studies to evaluate the horizontal displacement with detailed GPS measures, but vertical movements still remain poorly known. Through geomorphic indexes it is possible to evaluate the landscape signature of vertical movements in terms of tectonic-uplift and erosion. Moreover, the study area represents a excellent laboratory not only to explore the tectonic activity of the DSTF structures but also to explore the concepts of steady- and transient-state landscape. This area has been subjected to a continuous base level lowering in the Pleistocene and its base level is located more than 400 bellow present-day sea level.

A second objective of this Thesis will be presenting new tools for analyzing the landscape. I present in this Thesis two ArcGIS Add-Ins to extract normalized and swath profiles. I will discuss the methodological aspects of the calculation of such geormophic indexes in ArcGIS and the advantages that these two new tools offer in landscape analysis.

A third objective is focused in analyzing the field evidences of the tectonic activity of two of the most important Jordanian structures, the Amman Hallabat Structure (AHS) and the Shueib Structure (SHS). These two structures have been thought to remain inactive since Cretaceous, but some recent studies have pointed to a possible Quaternary reactivation of them (Diabat et al., 2009). In this Thesis I performed several field campaigns to analyze their possible tectonic activity and kinematics with the aim to relate them to the present-day stress field of the DSTF. The findings presenting in this Thesis not only prove the Quaternary activity of both structures but also include some interesting implications for the northern closure of the Dead Sea.

A fourth objective of this Thesis is the structural analysis of microstructures measured in the AHS and SHS with the aim of evaluating their relation with the present-day stress field of the DSTF. We have more than 300 fault-slip data from 14 field station that have been analyzed with the aid of T-TECTO 3.0 structural software. These new findings suggest a rejuvenation of the AHF and the SHF in the Quaternary in the context of the DSTF tectonic activity.

Finally, a last objective of this Thesis is to evaluate the seismicity in the area. The instrumental seismicity related to the DSTF is high, but the other structures studied in this Thesis do not present much instrumental seismicity. However a recent archaelogical excavation has discovered a Bronce-Age ruins that present clear evidences of seismic damages. These ruins are located between AHS and SHS, and could suggests a possible seismic potential of both structures. In this Thesis I analyzed some damages in the first stages of the excavation. This site has been further excavated and it is thought to be the ruins of the ancient kingdom of Sodom, whose destruction is referred in biblical and koranic texts. The archaeoseismic evidences found in this site could prove a clear seismogenic character of the AHS and SHS, but a more detailed research in the new unburied sites is required.

Chapter 2

Geological and tectonic setting

Preface

This chapter is divided into three main parts that focus in the DSTF regional context and the PhD study area in particular. I have make an intensive review of the scientific literature of the regional as well as the local geological and tectonic setting. In this chapter I highlight the regional tectonic and geologic context of the Arabia Plate and the evolution of the movement and stress released along the DSTF. I will emphasize some of the problematic conclusions and results on the nature and slip rates of different DSTF parts as well as the remaining question of *"where is the northern closure of the Dead Sea pull-apart basin?"*. Moreover, I will a present general review of the studies suggesting possible stress accommodation of regional tectonic structures apart of the DSTF.

This chapter includes the following subtitles:

2.1 Regional tectonic context

2.1.1 General plate tectonics and Red Sea opening

2.1.2 Nature and evolution of the DSTF

2.1.3 Slip rates of the DSTF

2.1.4 The Syrian Arc System

2.2 Main tectonic structures in the PhD study-area

2.2.1 Northern Wadi Araba and southern Jordan Valley faults.

2.2.2 The Dead Sea pull-apart basin.

2.2.3 The Amman Hallabat and Shueib Structures.

2.2.4 Seismicity in the study area

2.3 Stratigraphy of the study area

2.3.1 Mesozoic sequence

2.3.2 Quaternary sediments

2.1 Regional tectonic context

2.1.1 General plate tectonics and Red Sea opening

The study area of this PhD Thesis forms part of the NW Arabian Plate. The Arabian plate consists of two main parts; the Arabian Platform in the east and the Arabian Shield in the west. The latter part is also part of the Arabian- Nubian shield (Stern and Johnsn, 2010; Krienitz and haase 2011; **Fig. 2.1**). This area remained as stable platform through most of the Phanerozoic (Stern et al. 2006).

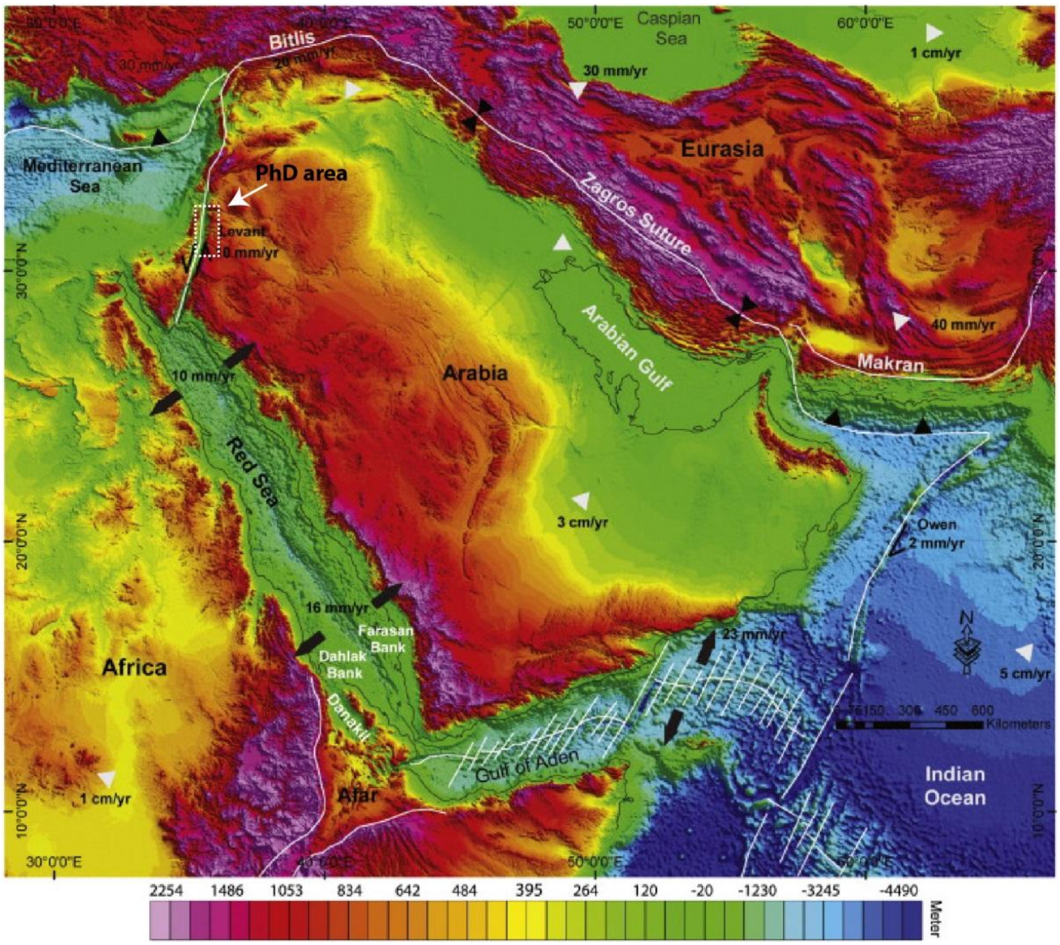

Figure 2.1. Present-day regional map of plate tectonic setting over a hill-shaded relief map of the Middle East and African-Arabia Plates (After Almalki et al., 2015).

The Rifting occurred in Permian, Triassic and Early Jurassic times. in the context of the Neo-Tethys evolution in the eastern Mediterranean and shaped its passive continental margin (Stern and Johnson, 2010). In the Late Cretaceous the closure of the neighboring part of the Neo-Tethys was accompanied by moderate NW-SE compressional stress that produced the Syrian Arc System (SAS).

The continental breakup phase of the Arabia Plate that formed the African Plate began in the Oligocene at 30-25 Ma with widespread basaltic volcanism (Garfunkel 1981, Weinstein and Garfunkel, 2014). Major rifting and faulting followed in the Miocene and led to the detachment of Arabia from Africa (**Fig. 2.2**).

The Arabian-African plates separation created the Red Sea spreading center which opened as propagating rift with incipient seafloor spreading in its southern and some deep extensional basins in its northern part (Almalki et al., 2015). This divergence counterclockwise rotated the Arabian plate around a pole at about 33± N, 24± E and favored a northward movement toward the Eurasia plate (Girdler, 1990). The convergence between Arabia and Eurasia causes the orogenic processes leading to form the Zagros-Biltis mountain ranges in Turkey (Stern and Johnson, 2010),

The present-day tectonism of the Red Sea is influenced by the DSTF system and East Anatolian Fault. On the other hand, the Pre-collision of the western parts of Africa Plate with the Eurasia Plate (about 40 Ma) reduced the northward motion of the entire plate by at least (20 mm /yr). According to this theory, the pre-collision might have accelerated the detachment of Africa Plate from the Arabian plate. Conversely, the Arabian Plate is sutured with Asia in Turkey for the same time-span (Almalki et al., 2015).

Several geophysical studies have revealed the deeper structure of the NW Arabia Plate and the Arabian-Nubian shield (Ginzburg et al., 1979; Makris and Rihm, 1991; Rybakov et al., 1997; Ben-Avraham et al., 2002, Weber et al. 2009). However, the structural patterns in the NW Arabian Plate are complex due to the reorganization of lithospheric plates and plate collision with the Eurasia Plate (Zeyen et al., 1997). This collision points to an escape tectonics within Eurasia to accommodate convergence between Arabia and Eurasia (Westaway, 1994).

Across the NW Arabia plate, the deeper structures are congruent with inherited structures of the pre-rift. The NW-SE regional structures “Najd rift structure” is reactivated in the Pliocene-Pleistocene that evidenced by the lava flows on their fault planes. The DSTF is the connection plate boundary between the Arabian, African and

Eurasia and is transmitted the divergence rate of the northern Red Sea (10 mm/yr) in a left lateral transform boundary (Almalki et al., 2015).

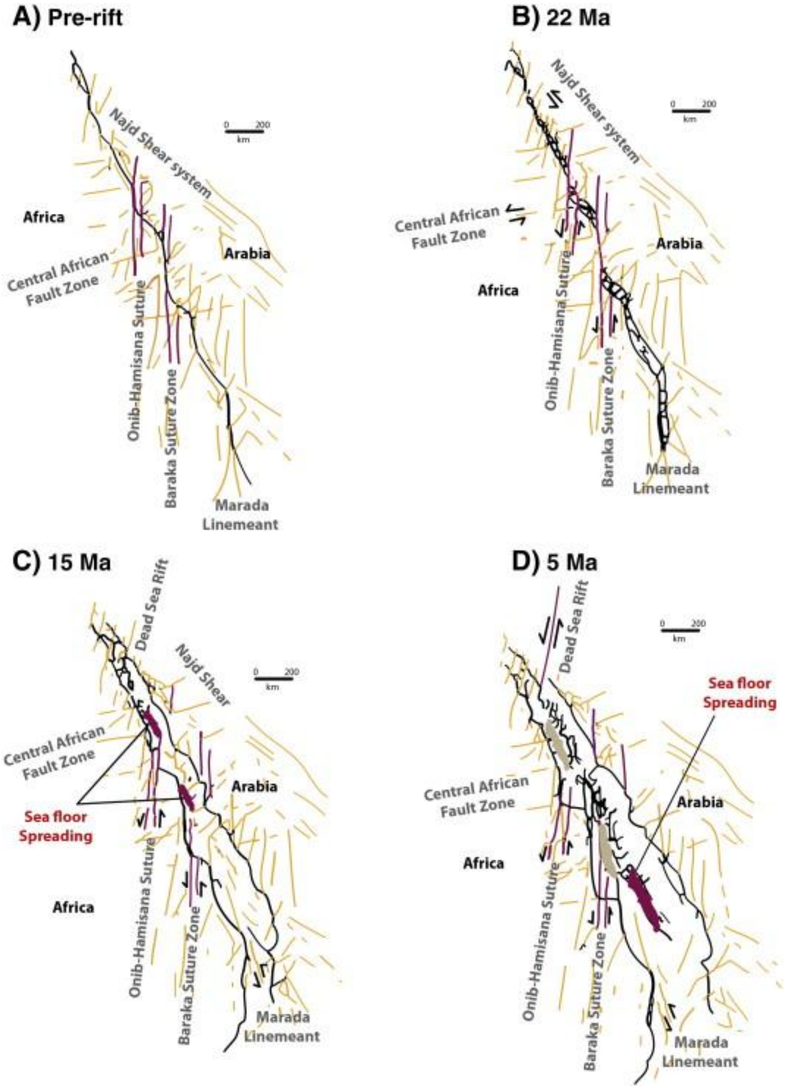

Figure 2.2. The evolution of the breakup of Arabia-Africa and the spreading of the Red Sea floor (Taken from Almalki et al., 2015).

2.1.2 Nature and evolution of the DSTF

The most tectonically active structure in the Levant is the DSTF (Quenelle, 1959; and Garfunkel, 1981). It forms the plate boundary between the Arabian and African plates that extends approximately 1100 km northward linking the Red Sea, along Wadi Araba, the Dead Sea, the Jordan Valley, Lake Tiberias, and Lebanon and northward to the Taurus-Biltis Mountains in Turkey (**Fig. 2.3**).

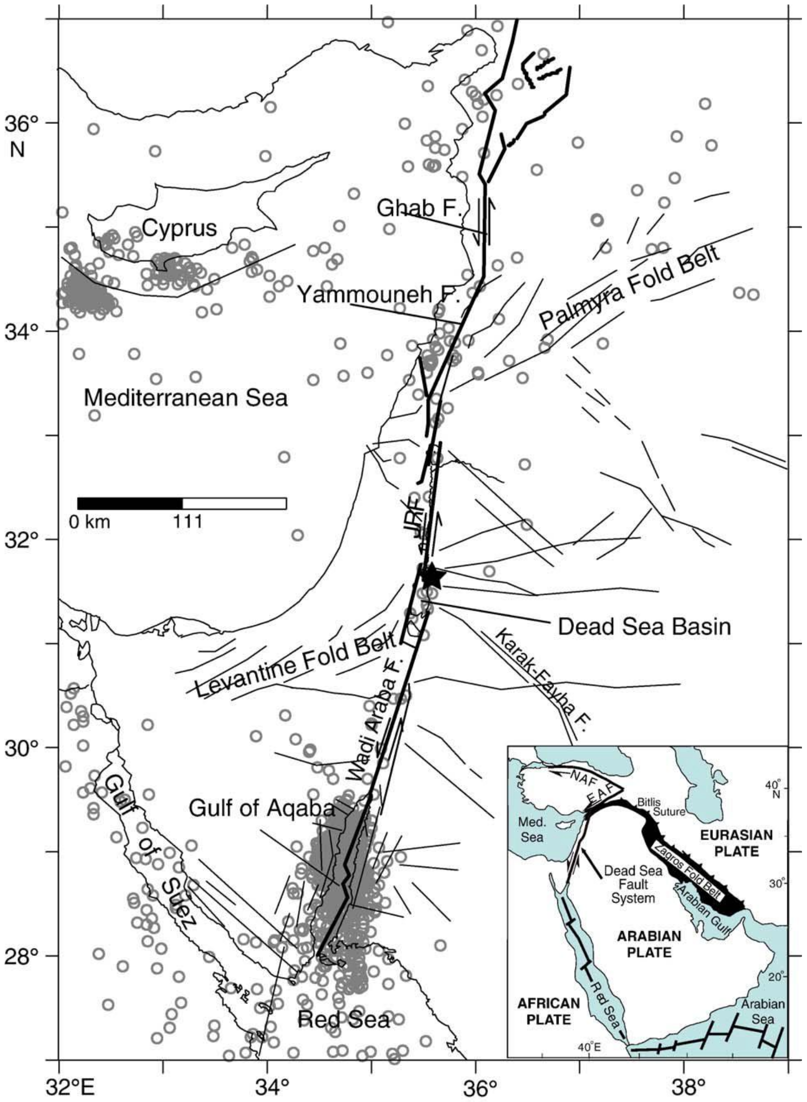

Figure 2.3 DSTF segments (After AlTarazi et al., 2006). The black star in the Dead Sea basin points to the 11th of February of the 2004 earthquake.

The DSTF is part of the lithospheric boundary between the African Plate and the Arabian Plate which probably started formation during the Pliocene-Late Miocene because of interactions between several stresses. These stresses may be linked to the post-opening of the Red Sea during the Oligocene (Almalki et al., 2015). Tectonic movement along the DSTF began between 20 and 14 Ma (Garfunkel, 1981; Bayer et al., 1988; Makris and Rihm, 1991). The DSTF comprises several fault segments and associated transpressional and transtensional structures, such pull-apart basins, fault escarpments and pressure ridges (Garfunkel, 1981; Atallah, 1992; Butler et al., 1998; Ben-Avraham et al., 2008; Abou Romeih et al., 2009).

The DSTF is a sinsitral transform fault and consists of three main sectors; the northern, the central and the southern sectors. The evidence for left-lateral shear along the Dead Sea Fault (DSF) since the early-middle Miocene is based on observations from four independent sources: I) Regional plate tectonics. II) Local geology. III) Seismology. IV) Geodesy. The illustration of the plate tectonics indicate that the opening of the Red Sea is transferred to the collision with Eurasia via sinisterly shear along the DSF (Quennell 1959; Freund 1965 ; Garfunkel 1981 ; Atallah, 1992; Garfunkel et al., 2014; Almalki et al., 2015). The pre-Miocene geologic features explains the sinistral motion the systematic offset in the southern sector, especially the lithological comparison in the east and west flanks of the southern DSFT (Quennell 1956). Using seismological data in the southern DSTF, Hofestter et al. (2007) and Palano et al., (2013) highlighted that most of the focal mechanisms earthquakes show sinistral motion along the DSF. The GPS velocities based researches support the left lateral motion along the DSTF by indicating the velocities of the plates in either sides of the transform (LeBeon et al, 2008; Al-Tarazi et al., 2011; Palano et al., 2013; Masson et al., 2015).

The southern sector extends from the Gulf of Aqaba in the Red Sea to the Sea of Galilee. It runs in NNE direction (between N12ºE and N20ºE; **Fig. 2.2**). The calculated offset along this sector is about 105 km of a left lateral motion. (Marco and Klinger, 2014). This 105 km offset in the southern took place in two main phases; 60 km of displacement was developed during the Miocene, whilst about 45 km evidenced for the time-span (Pliocene – present) (Garfunkel, 1981).

The southern sector includes two main fault segments; the Wadi Araba Fault (WAF) and Jordan Valley Fault (JVF) (Attallah, 1992, Al-Taj, 2000; Garfunkel, 2014; **Fig. 2.2**). Both segments are connected through the Dead Sea, the largest pull-apart basin in the DSTF system and one of the topographic lowest points in the world (430 m below sea level, in the 2014). Considered the longest segment of the southern DSTF sector, the WAF is about 160 km long segmented fault and encompasses a prominent 5–20 km wide valley (transform valley), mostly with uplifted flanks, in which all or most of the lateral motion takes place (Palano et al., 2013). The valley floor, especially in the Dead Sea and the Jordan valley area, is thickly filled with young sediments; thus the deeper structures were studied upon deep boreholes and geophysical data. Buffered from the WAF and the JVF, the most conspicuous structures are longitudinal faults of two types

(Garfunkel 1981; Garfunkel and Ben-Avraham 2001): (a) normal faults that extend along most of the faults margins, and (b) left stepping strike slip or oblique slip faults within the valley that delimit a string of pull-apart basins (Garfunkel, 1981, Atallah, 1992).

In general, both WAF and JVF might divided into at least six major overlapping, sinistral strike-slip faults with deep rhomb-shaped depressions (sag ponds) and/or pressure ridges between each fault pair (Garfunkel, 1981, Girdler, 1990; Garfunkel and Ben-Avraham, 1996; Attallah et al., 2005; Ten Brink and flores, 2012). The largest depression of the DSTF system is the Dead Sea basin that is best-known as the lowest topographic land on the earth (Hall et al., 1996, Alzoubi et al., 2007). Among the other depressions, three deep depressions are recognized in the Gulf of Aqaba (on the Red Sea). The Sea of Galilee is also interpreted to be a depression of the interaction between the JVF and the Yamouneh fault (Garfunkel and Ben-Avraham, 1996). All these depressions are interpreted as pull-apart basins due to transtension at transform offsets and related to the lateral movement along the forming fault segments. These basins are partly filled with sediments, which reach a maximum thickness of about 10 km under the Lisan diapir in the Dead Sea basin (ten Brink et al., 1990; Hassouneh, 2003).

The central sector of the DSFT is more complicated than the southern sector (Gomez et al., 2007; Abou Romieh et al., 2009). Bifurcating in NNE-SSW, NE-SW and NW-SE directions, the central DSTF is partitioned in the region (**Fig. 2.3**). The major branch of these faults is the Yammouneh fault that connects the southern and northern sectors of the DSTF and runs through the Syrian western plains (Gomez et al., 2003, 2006). The simple structure of the DST in this sector changes between latitude 33± N and 35± N, where the transform bends to the right, leading to transpressional structures. Within this restraining bend, the transform system comprises several distinct fault branches, which trend roughly parallel and immersed to the Palmyrides fold range (Garfunkel, 1981; Girdler, 1990; Gomez et al., 2003).

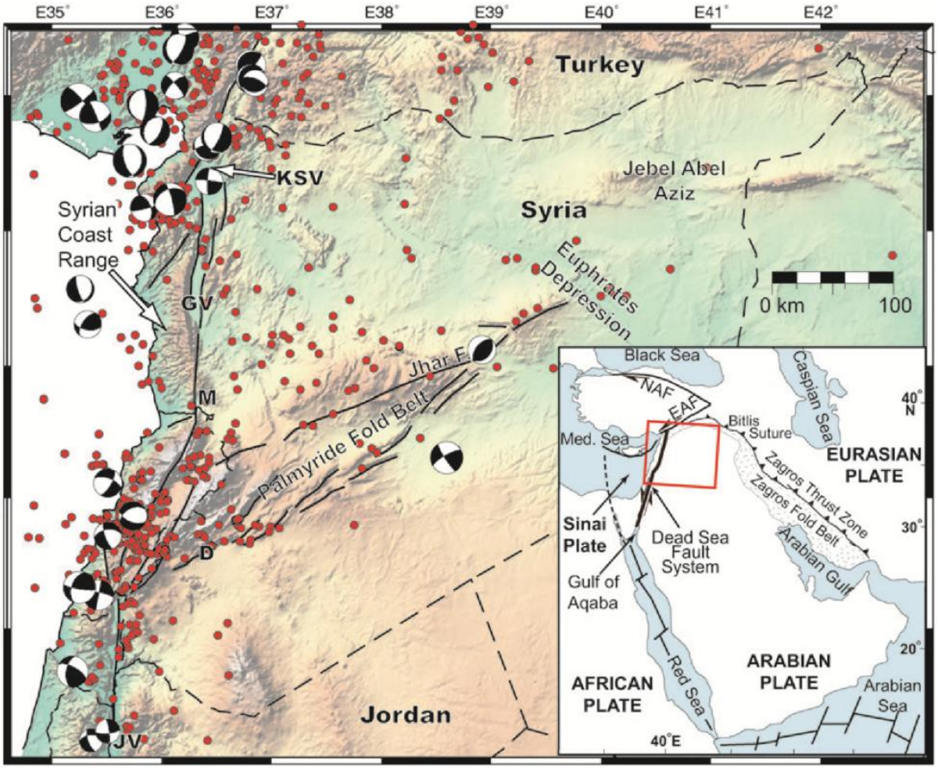

Figure 2.3. central and northern sectors of the DSTF (After, Alchalabi et al., 2010).

The Northern sector consists of two distinguishable faults striking N-S through the Ghab Valley (GV, **Fig. 2.3**) in Western Syria and intersecting with the East Anatolian Fault in Bitlis mountain ranges in Turkey. This intersection exhibits the triple junction point of the three plates; the Arabian, the African and the Eurasia. In the central and northern sectors, the displacement is considerably less than the other sectors at least to the second phase of the DSTF movement. The total movement in these sectors for the last 3.7 Ma is about 5.3-16.8. These differences were suggested to be accommodated in shortening by the SAS.

Seismicity of the DSTF

The earthquake catalogues for most of the major and moderate earthquakes in the region occur in the last 1000 year is documented in the historical record (Ambraseys and Jackson, 1998; Klinger et al., 2000b) (Fig. 2.4). Among these record, eight large earthquakes in the northern sector, three in the central and five in the southern sectors are well studied (Ambraseys and Jackson, 1998; Klinger et al., 2000; Sbeinti et al., 2005; Akyuz et al., 2006; Marco, 2008; Salamon, 2010).

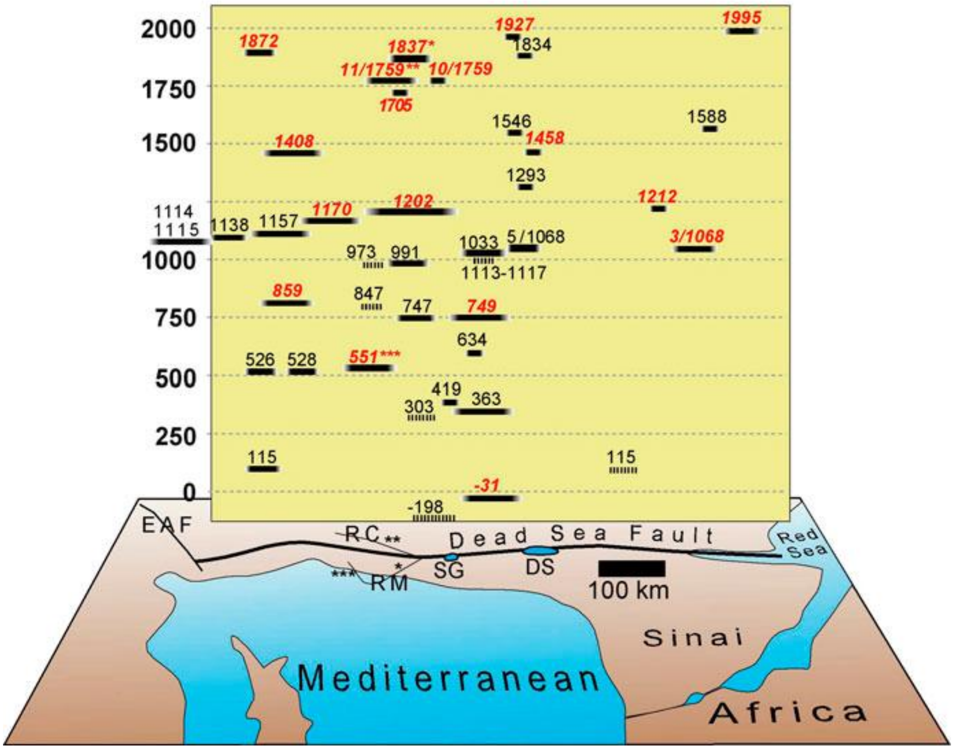

Figure 2.4. Historical approximation of the earthquakes distribution in space and time for the entire DSTF (After Marco and Klinger et al., 2014).

However, the magnitudes of these earthquakes remained questionable and mainly were estimated due to the lack of adequate documentation, anthropologic influences and/or political conflicts (Palano et al., 2013). These estimated events could have a larger magnitude than similar instrumentally recorded earthquakes. The only large earthquake (M > 7.0) is instrumentally documented and occurred in the Gulf of Aqaba on November 1995 (Klinger et al., 2000). Another weaker earthquake of (M=5.2) occurred in the Dead Sea Basin on February 2004 but slight damage was reported in the regional countries (Al-Tarazi et al., 2006). An analysis of seismicity in the 20th Century and geomorphological studies lead to potential recurrence intervals of 385 a and about 200 a, respectively, for earthquakes with a moment magnitude MW = 7 along the DST (Klinger et al., 2000b; Salamon, 2010).

In the southern DSTF, four strong historic earthquakes hit the segment of the DST south of the Dead Sea in the years 1068, 1212, 1293, and 1458 A. D. (Klinger et al., 2000b; Garfunkel and Klinger, 2014). These earthquakes were inferred by opened trenches and preserved in sedimentary records. During the 20th century most of the seismic moment at the DST was released by a few large earthquakes (Salamon et al., 2003), which record the predominant strike-slip motion of the transform: September

1918 in the northern segment, July 1927 in the northern Dead Sea basin (both with ML = 6.2), and November 1995 in the Gulf of Aqaba (MW = 7.2). Nevertheless, the current seismicity of the southern DST section is rather small (Salamon, 2010), although recent activity there is indicated by Offset gullies and alluvial fans (Klinger et al., 2000a).

Based on 40000 seismic events of magnitude greater than 1.5 and depths ranging between 0 and 40 km, Palano et al. (2013) proposed detailed seismic map (**Fig. 2.5**) for the DSTF system. They applied a filter for the data to take in account all the earthquake that have magnitude equal or greater than 2.6 to compute the cumulative frequency plot of the depth-distribution seismicity. This plot shows that 90% of the seismic events of the upper crust of the DSTF region hit at depth, generally, less than 22 km. The seismicity along and around the DSTF is not homogeneously distributed and structures that been thought inactive exhibit considerable seismicity (Shamir, 2006; Hofestter et al., 2007; Palano et al., 2013). The different sectors of the DSTF present different patterns of the seismicity´s depth and magnitude.

The central and northern sectors of the DSTF have a widespread seismicity (**Fig. 2.5**). This trend decreases in NE direction to the east of the PFB (Palano et al., 2013) which point to the decreasing in the tectonic reactivation of the northeastern sector of the SAS. The southern sector shows seismic clustering in or near tensional structures at fault offsets and pull-apart basins, e.g. at the Gulf of Aqaba and the Dead Sea basin, and conjugated regional structures (i.g. NW-SE faults of Sirhan, Karak Faiha and Al-Attar) in Jordan. Four main clusters are concentrated in the ruptures of the main fault segments. In the Gulf of Aqaba the seismicity is moderate and eight M>5.0 earthquakes occurred in this region (Palano et al., 2013). In the Dead Sea and the Sea of Galilee clusters are minor but with deeper earthquakes. The last cluster is visible in in the southern tip point of the Karak-faiha fault with the deepest earthquakes (about 40 km) (Palano et al., 2013).

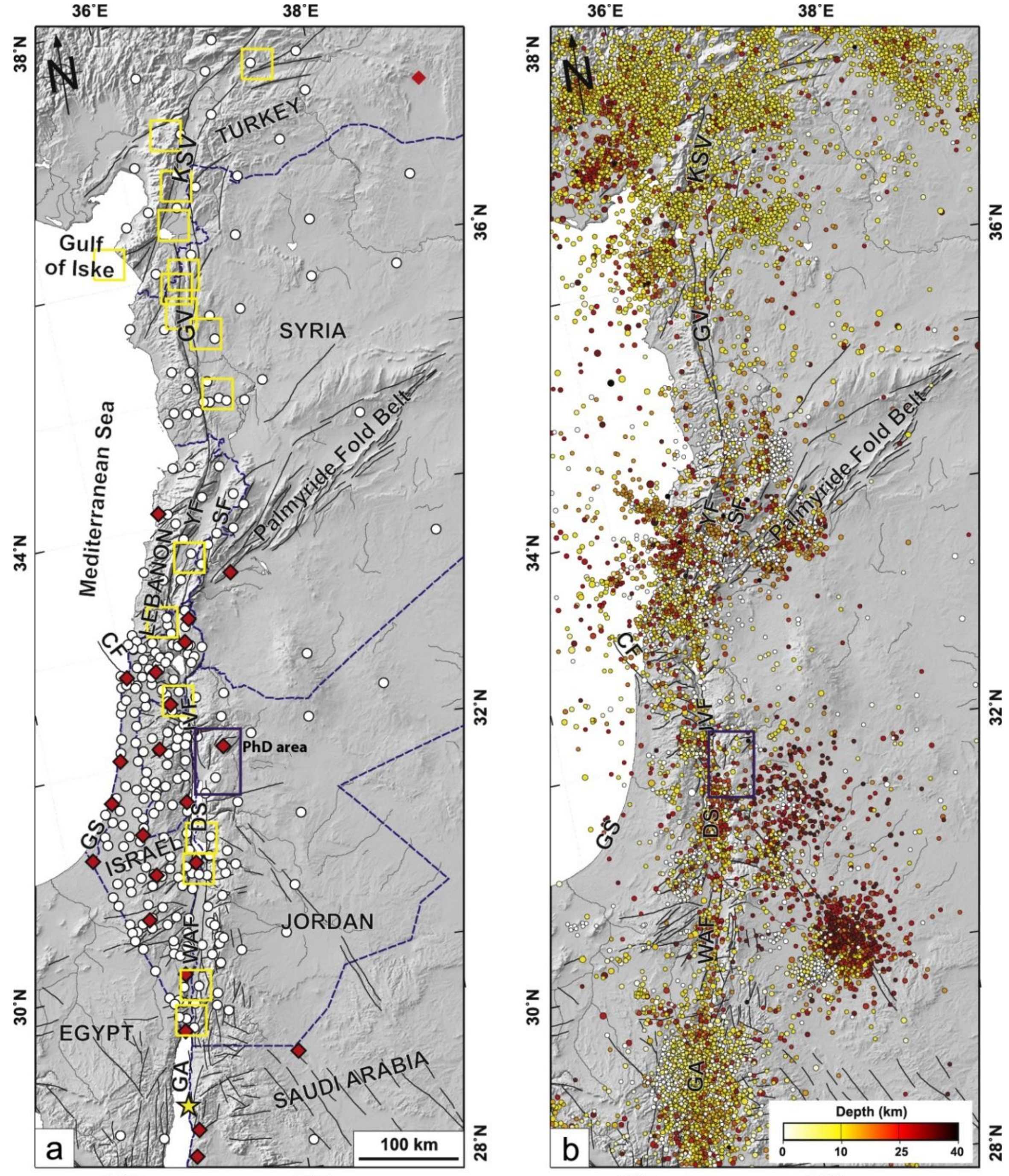

Figure 2.5. Map of tectonic map of the DSTF with GPS points and Seismicity over a hill-shaded relief base-map (after Palano et al., 2013)

Stress field of the DSTF

The Stress-strain fields in the region suggest that the of the DSTF and related structures formed/is forming in a combination of mainly strike slip and dip-slip movements and new phase of NE-SW oblique thrusting (Eyal et al., 1996; Zain Eldeen, et al., 2002; Diabat, 2009; Palano et al., 2013).

The paleostress data published for the DSTF evidence a general clockwise rotation for the maximum compressive stress axis (from E-W trend in the Cretaceous to a NNW-SSE in the Pleistocene. Two main stages can be indicated for this axis rotation (Zain Eldeen et al., 2002). The older stage took place in the Miocene and caused a 50º toration from E-W to NW-SE. This stage is related to the post-breakup of Arabia plate and the northward motion of the plate with important rotational forces (Almalki et al., 2015). The younger one, which is still active, started in the Pleistocene and caused a 38º from NW-SE to almost N-S direction (Zain Eldeen et al., 2002; Diabat et al., 2004; Diabat, 2009).

Most of the studies of the stress-strain analysis were based on fault-slip data (Zain Eldeen et al., 2002; Diabat et al., 2004; Diabat, 2009; Hardy et al., 2010). However, other studies were based on geodetic and seismological data (Hofstetter et al., 2007; Palano et al., 2013). The maximum compressive stress axis near the fault zone is horizontal with a NNW-SSE direction, whilst the minimum compressive stress is also horizontal, favoring NE-SW-directed extension in a general strike-slip stress regime (**Fig. 2.6**). The DSTF accommodates most of the crustal stress in the region (McClusky et al., 2003; Gomez et al., 2007; Al Tarazi et al., 2011). However, other regional structures as the Syrian Arc System have been suggested to accommodate part of this stress (Chaimov et al., 1990; Badawy and Horvath, 1999; Abou Romieh et al., 2009;, Alchalbi et al., 2010). The central part of the latter arc system, in Jordan, is partially composed of two main structures: the Amman Hallabat Structure (AHS) and the Shueib Structure (SHS) (Mikbel and Zacher, 1981; Diabat 2009). Both structures are dextral fold-thrust belts formed in the Cretaceous under E-W to ESE-WNW maximum compressive stresses (Quennell, 1959; Mikbel and Zacher, 1981). They were considered inactive during the Neogene but recent studies have proposed a Quaternary tectonic activity of these structures (Diabat 2009).

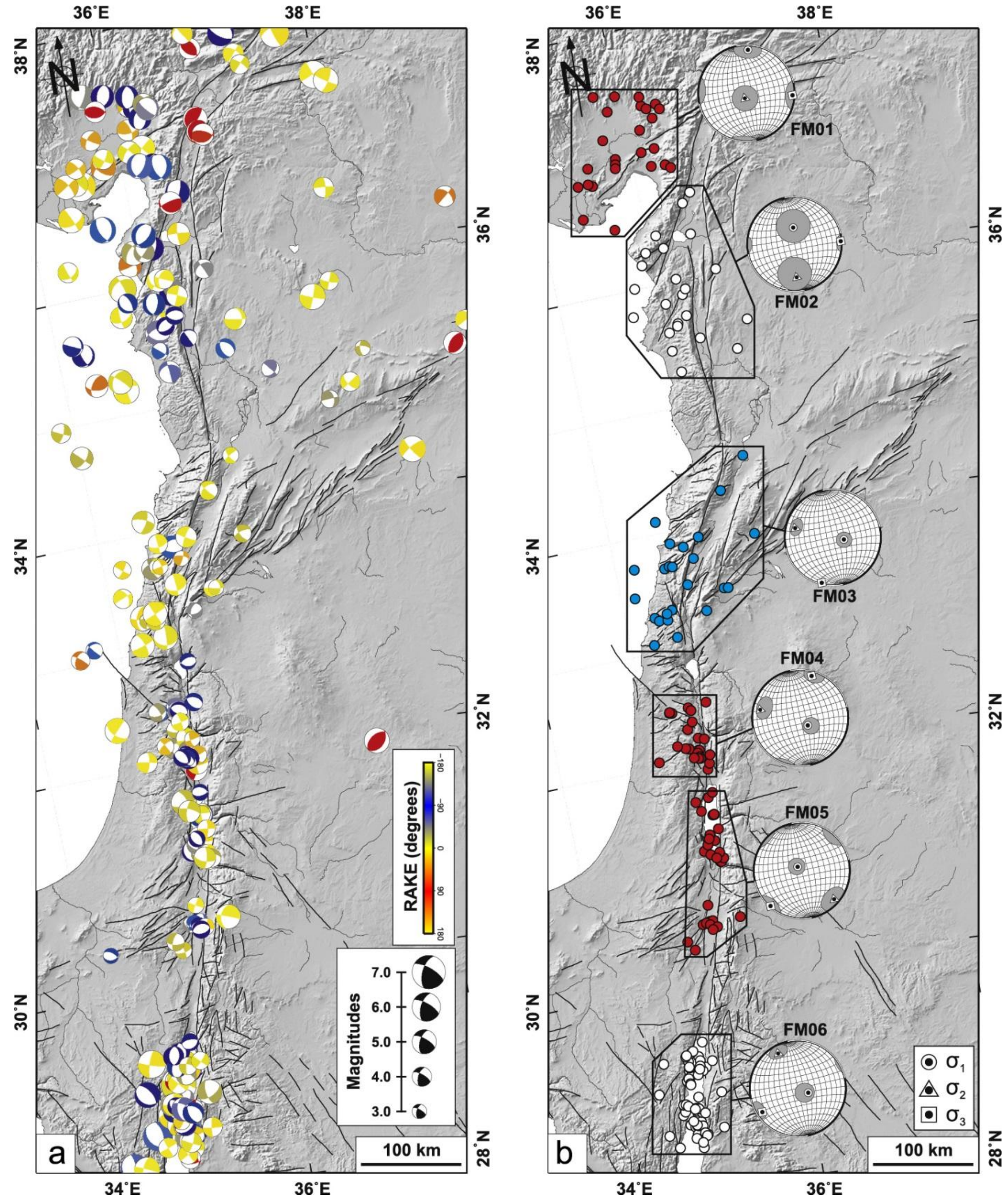

Figure 2.6. Left) Beach-ball Focal mechanism solutions of seismic events associated with the activity of the DSFT. Right) Stress tensor derived from the focal mechanisms. (After Palano et al., 2013)

Indicating the σ1 is vertical, geodetic studies suggest that the stress fields of the DSTF exhibit more influence for the extensional forces in E-W direction in the stress tensors calculated for the seismic cluster near the Dead Sea (Hofstetter et al., 2007; Palano et al., 2013; **Fig. 2.6**). This lead to consider the activity of NW-SE conjugated fault system to the DSTF where normal faults are the main structures of these systems.

2.1.3 Slip rates of the DSTF

The slip rate of the DSTF have been the topic of many research studies in the DSTF region, and different methodologies and time-span have been chosen to derive rates; offset of geological markers, GPS, satellite images, historical seismic events, offsets in drainage systems, etc. (Eyal et al., 1996; Klinger et al., 2000a; Wdowinski et al., 2004; Marco and Agnon., 2005; Ferry et al., 2007; LeBeon et al., 2008; Alchalbi et al., 2010; Palano et al., 2013; Masson et al., 2015).

The most recent GPS data presented by Palano et al. (2013) suggest that the slip rate in the southern sector of the DSTF is higher than in the other sectors with slip rate ranging from 2.9 to 5.0 mm/yr. The central sector depicts velocities of about 3.5 mm/yr in the main fault of this sector; the Yammouneh fault; whereas the northern sector has a SSW-directed velocity field with motion ranging from 7.5 to 1.8 mm/yr .

Two geological markers offsets were used to infer the slip rate; one marker is pre-Miocene, which determines the total offset and thus the long-term slip rate. The other marker uses features that formed/is forming while the DSF was active, which determine short-term rates of individual sections of the fault (Marco and klinger, 2014). Paleoseismic studies based on historical/archaeological deformation target the Pleistocene-Recent time-span activity. The long term slip rate do not explain the deficit of the slip rate in the different DSTF sectors, whilst the short term present good assumption to the total slip. Along the southern section of the DSF, geological marker offset rate is determined by dividing the 105 km total slip by the 20-25 Ma that present the pre-DSF geologic features visible both in the Sinai and in Jordan. This rough calculation provides minimum long slip rate of about 5.35 mm/year.

Recently and more accurate present-day geodetic measurements for the very short-term deformation are consistent with overall geologic observations of a sinistral slip-rate of 4–5 mm/year (Le Beon et al. 2008; Palano et al., 2013; Mahmoud et al., 2013; Masson et al., 2015; **Fig. 2.7**). As there are many estimation of the offset along the DSTF by most of In a review of the slip and seismicity of the DSF, Garfunkel (2011) concludes that the slip rate is slowing from an average rate of 6–7 mm/year over the last 5 Ma to 4–5.5 mm/year in the Pleistocene together with a slight eastward shift of the Euler pole of rotation between Sinai and Arabia.

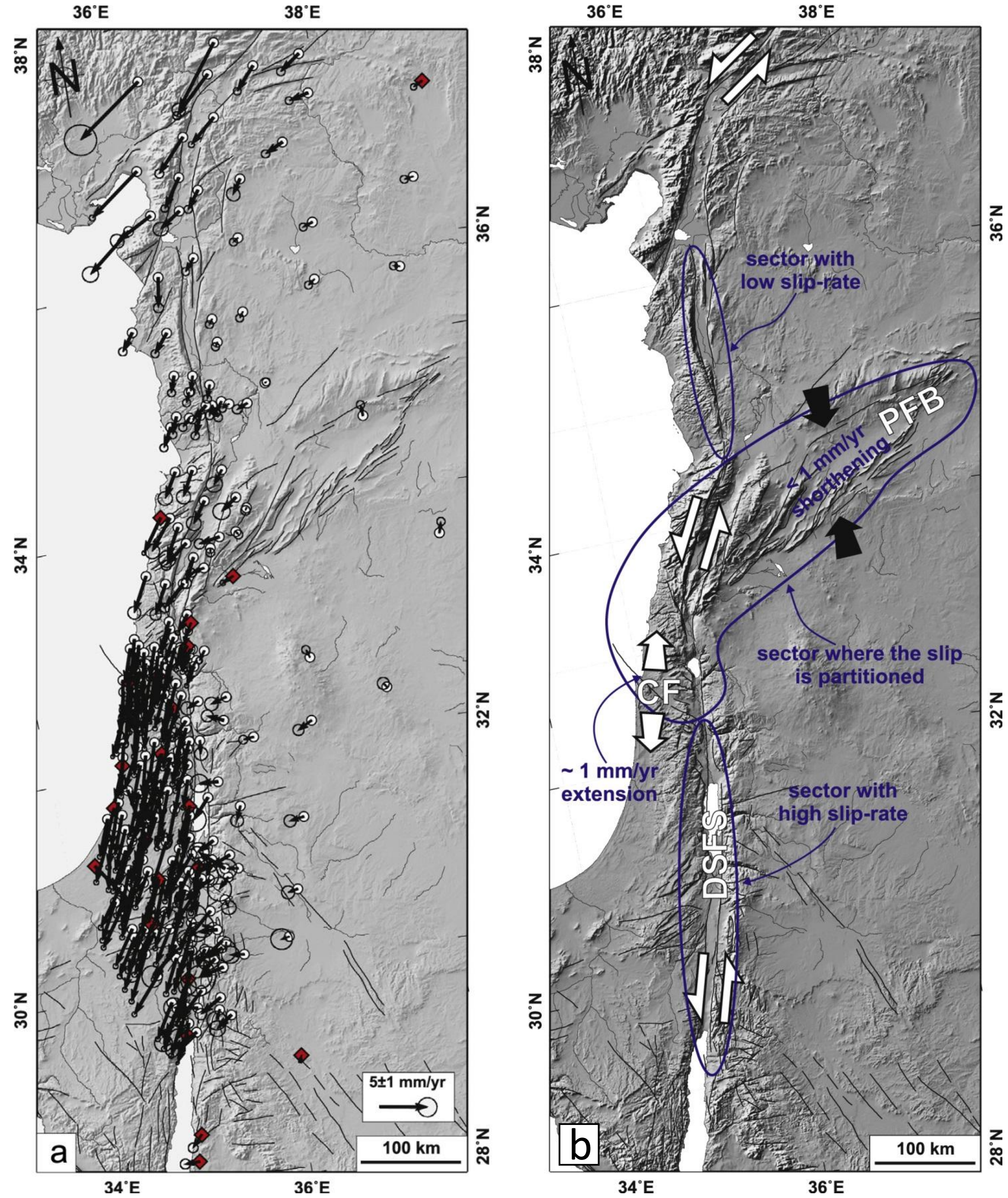

Fig 2.7.a) GPS velocities of the fixed points in the Arabian and African Paltes pointing to a left lateral movement of this transform boundary. Length of the arrows in this map indicate the velocities of each point as a rate of slipping. b) Different slip rates of the different sectors of the DSTF based on geodetic data analysis (After Palano et al., 2013).

Slip rates obtained for the fault segments WAF and JVF are 4.9 +/- 0.4 mm/yr and 4.7 +/- 0.4 mm/yr respectively; agree with the general slip rate of the DSTF (Al-Tarazi et al., 2011). There is certain consistency of the slip rates inferred by GPS data (Le Beon et al. 2008; Palano et al., 2013; Masson et al., 2015; **Fig. 2.7**), Quaternary rates (Klinger et al. 2000a; Niemi et al. 2001; Le Beon et al. 2010; 2012) and several millions-years-long slip rates (Bartov et al. 1980). The paleoseismological studies might give irrelevant rates. This may be explained either by distributed deformation unaccounted for by on-fault palaeoseismic studies or by too short time-span of observation along some fault segments. As a real example, the offset of a Roman period aqueduct suggested that slip rate is of 7 mm/a (Meghraoui et al. 2003) whereas relics offset are displaced only 2.1 m (Ellenblum et al. 1998).

2.1.4 The Syrian Arc System

The SAS is a regional system of en-echelon arranged, NNE and NNE oriented fold-thrust structures extends in S- shaped belt runs from east Syria (Palmyra Fold Belt), through Jordan and Palestine to the Sinain Fold Belt, forming a series of anticlines and synclines, most asymmetrical and faulted locally by normal and strike-slip faults (Mikbel and zacher, 1986; Abed et al., 1989; Chaimove et al., 1992; Shaher et al. 1994; Badawy and Horvath, 1999; El motaal et al., 2003; Diabat, 2009; **Fig. 2.8**). This system formed by the tectonic inversion after an extensional stage occurred in the Late Triassic (El Motaal et al., 2003). The main pattern of the extensional tectonic style is half grabens rotating in a clockwise direction along NE (in Farafra-Sinai and Palmyra) and NNE (in Levant) (Hardy et al., 2010). The half grabens are transversely broken by NW oriented right-lateral wrench transfer fault zones. The compressional tectonic style coincided with the Late Cretaceous closing of the Neo-Tethys and the convergence of The African-Arabian plate with the Eurasian plate (Shaher, 1994; Badawy and Horvath, 1999; Hardy et al., 2010). The new NNW oriented compressive stress of the DSTF region led to a reverse rotation of the pre-existing fault blocks along the NE oriented listric faults and to a tectonic inversion of the rift basin (Tarawneh, 2011). This rotation caused flexuring of the strata forming a number of anticlines with their southeastern limbs much steeper than the northwestern ones (El motaal et al., 2003). Reverse and/or thrust faults are often associated with the steep limbs of the anticlines in NE orientation and perpendicular to the maximum compressive stress axes (Diabat, 2009).

The separation of the Arabian plate from Africa that initiated in Oligo- Miocene time through the Red Sea rift enhanced the intensity of folding and thrusting of the study belt. More shortening and left-lateral offset along the almost N-S oriented Dead Sea transform fault began in the Miocene and is still active at present (El Motaal et al., 2003).

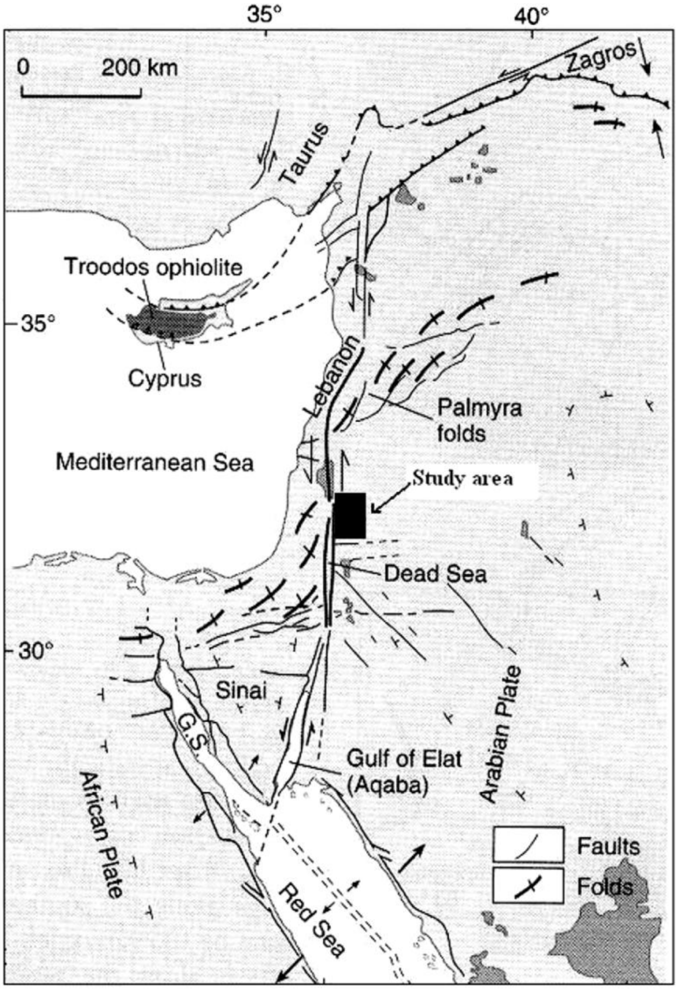

Figure 2.8. The S-Shaped form of the Syrian Arc System and its structures related to the DSTF (After Diabat, 2009).

Palmyraide Fold Belt

The PFB was been thought the only structure representing the SAS in the region, however several studies indicated that this structure only present the NE part of the greater SAS in Western Arabia plate (Hardy et al. 2010, Wood, 2011; **Fig. 2.9**).

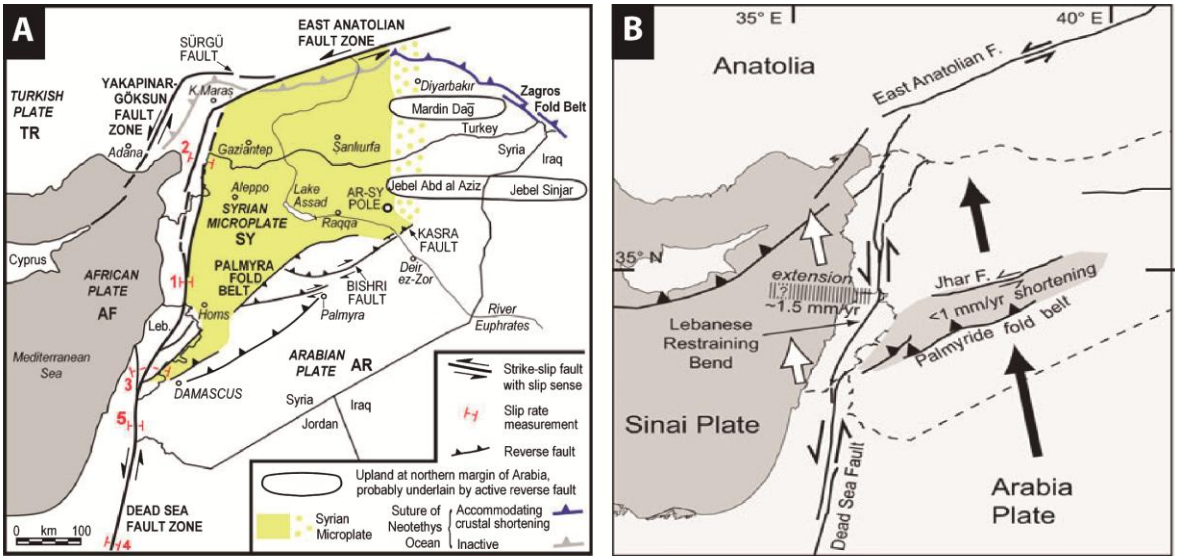

Figure 2.9. A) General map of the Palmyride fold belt (After Abou Romieh et al., 2009). B) The active shortening rate of the PFB (After Alchalbi et al., 2010).

The PFB extends 450 km from the southwestern corner of Syria in NE direction with a 100 km width (Al-Saad et al., 1992; **Fig. 2.9**). Structures and folded sediments of this belt belong to Late Cretaceous to Oligocene. The tectonic inversion in Palmyra was the change of stress regime from rifting and thick sedimentation to compression and uplift (Lovelock, 1984; Chaimov et al., 1992). The reactivation of the PFB started in the Miocene by new phase of uplift and tilting to the east of Palmyra (Shaher, 1994). In the Recent (Neogene – Quaternary) time, the tectonic movement became orogenic leading to the block faulted zone (Shaher, 1994).

The PFB accommodates part of the stress released in the NW of the Arabian Plate and exhibits clockwise rotation of microplate to the NW (Abou Romieh et al., 2009). The kinematics of the central DSTF is consistent with the Quaternary activity of the PFB and major slipping along the southwestern PFB is causing significant earthquake hazard, uncounted before, to the city of Damascus (Alchalbi et al., 2010).

The Central Segment of the SAS and the SAS in Sinai

Since the Cretaceous times, either sides of the Dead Sea have experienced the three major tectonic events; the Levant basin rifting, the tectonic inversion and SAS formation and the shear stresses presented in the southern DSTF sector movements (Hardy et al., 2010). The SAS in NW Egypt is limited to the Sinai tectonics that forms part of the structural evolution of the region. The Sinai triple point was

The central N-S segment of the SAS includes structures between the Sinai structure and PFB on both sides of the DSTF, like the Hebron, Jerusalem, Rammallah and Fariah anticlines in Palestine and AHS and SHS to the east of the Jordan River (Mikbl and Zacher, 1986; Abed, 1989; Shaher, 1994). There is no clear evidence as to the northeast continuation of structural axis under the Golan basalts (Shaher, 1994). The SAS in NW western Jordan was evidenced by the Late Cretaceous sediment syn-deformation accompanied with the NW-SE regional compression (Abed, 1989; Hardy et al., 2010; **Fig. 2.10**).

The first phase of folding occurred during the Late Cretaceous ,similar to the PFB, in the Turonian, as evidenced by stratigraphic relatioships (Mikbel and Zacher, 1986; Abed, 1989; Hardy et al., 2010). In this region, the sub-horizontal Eocene formations that unconformably overly the steeply dipping older sequences mark the termination of the regional folding in this area (Picard, 1959). Normal faults trending E–W and NE–SW that were active during this period have been also described (Bartov et al., 1976; Bruner, 1990). In the Quaternary times, these normal fault are associated with the DSTF stress field (Zain Eldeen, 2002; Diabat, 2009). The second phase was in the Oligocene and characterized by new compressional stresses applied in NW-SE as resulted in the rotational of the maximum compressive stress axis from WNW-SES (Shaher, 1994; Zain Eldeen, et al., 2002; Diabat, 2009)

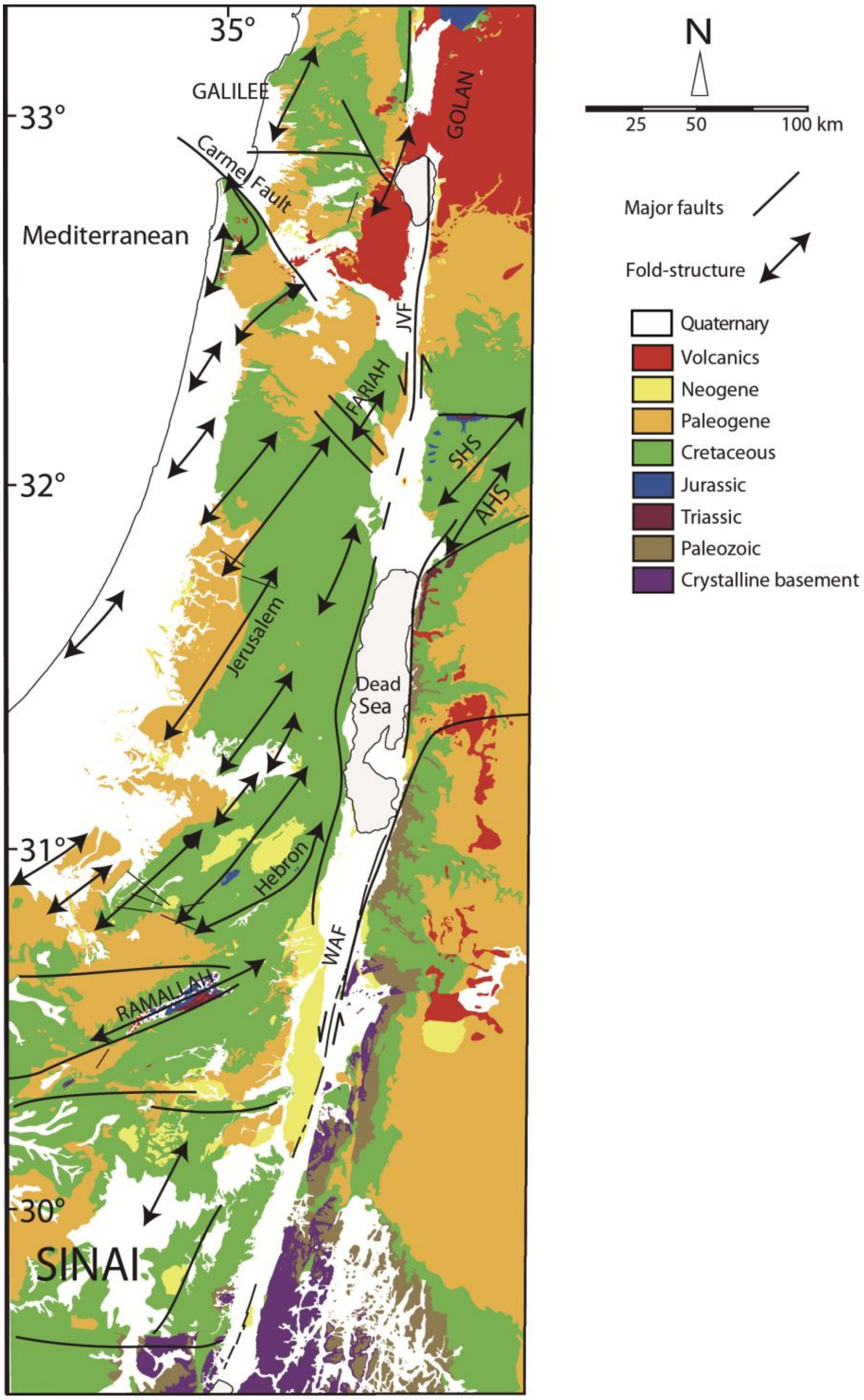

Figure 2.10. Central SAS in the either sides of the southern DSTF sector (After Hardy et al., 2010).

2.2 Main tectonic structures in the PhD study-area

2.2.1 Northern Wadi Araba and southern Jordan Valley faults.

The WAF is a morphotectonic depression and one of the main strike-slip faults between the Gulf of Aqaba and the northern corner of the Dead Sea (Abed, 2000; Attallah et al., 2005; **Fig. 2.11**). However, several authors have suggested that the WAF do not spatially excess the E-W trending Khunayzira (Amatzayahu) fault that bounds the southern end of the Dead Sea (Attallah, 1992; Neimi et al., 2001, LeBeon et al., 2008; 2010) and the fault northward is a different one that called the eastern boundry fault (Alzoubi et al., 2006, 2007).

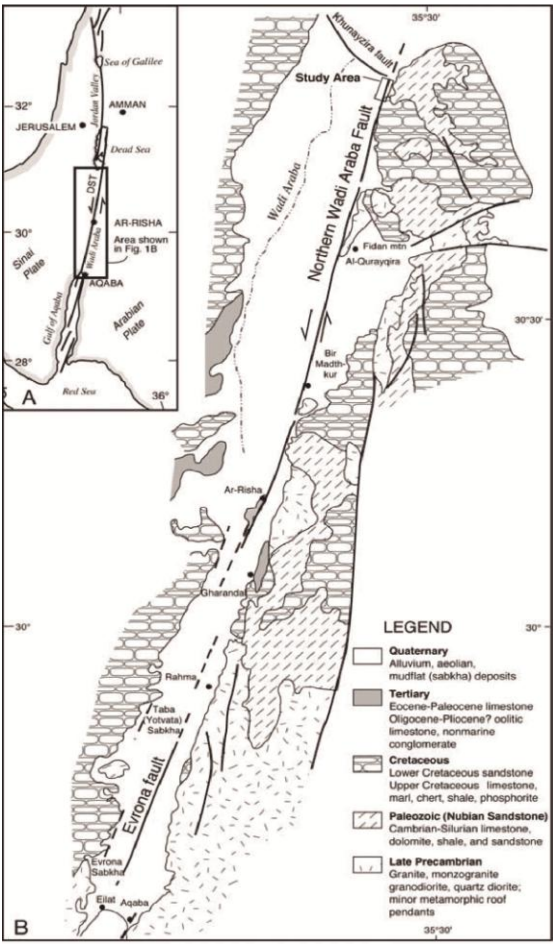

Figure 2.11. Simplified map of the WAF (After Neimi et al., 2001)

The WAF was mapped as part of the Jordanian Natural Resources Authority 1:50,000-scale mapping. Due to the activity of the fault and the active deposition from tens of vallyes in the JWM, tracing the WAF is mostly inferred or is based on aerial-photos lineaments. However, seveal field studies have mapped certain parts of this structure using open trenches, archaeological deformation and deformation of Neogene-Quaternary age sediments (Garfunkel, 1981; Atallah, 1992; Klinger, 2000a; Neimi et al., 2001; Haynes et al., 2006; LeBeon et al., 2008; 2010; 2012). In the areas to south of the Dead Sea, the WAF cuts across several generations of alluvial fans that formed on tributaries to the Wadi Dahal after the regression of Late Pleistocene Lake Lisan ca. 15 ka (Neimi et al., 2001).

The WAF between the southern and northern Dead Sea is almost running underneath the Dead Sea and authors of several researches suggested that it has a major normal fault rather than a pure-sinistral movement (Bender, 1968, Fruend, 1970; Alzoubi et al., 2005; 2006; 2007). The eastern boundary fault extends up to the NE corner of the Dead Sea and then, according to, 1974); Fig. 1(B)), bends to the east, where, however, only normal throw is evident (Bender, 1968; Alzoubi et al., 2006, 2007). Recent seismic activity was encountered in the region early in 2004 with the strongest shock at 11th February, 2004 and many aftershocks. The epicenter of the strongest event having been located just eastern flank of the Dead Sea area close to the Eastern Boundary Fault Zone with dominantly normal slip first motions (Al-Zoubi, 2005; 2006).

The northeast corner of the Dead Sea present new strike of the WAF to become NE-SW and previous works terminate the WAF/Eastern boundary fault few kilometers to the NE of the Dead Sea corner. This part of the fault was considered to show normal throws (Alzoubi et al., 2006; 2007). However, the NW-SE extension resulted from this normal displacements is incompatible with the regional maximum compressive stresses and instead reverse motion is more coherent to conform to the NW-SE shortening (Marco and Klinger, 2014).

The JVF is the main structure in the Jordan Valley that present a tectonic depression formed as a rift and has accumulated about 5 km of Quaternary sediments (Garfunkel et al., 1981; **Fig. 2.12**). The extension of the JVF in this depression is bounded by the Sea of Galilee and Dead Sea with a total 110-km-long fault segments (**Fig. 2.12**). The JVF consists of linear strands that show left-lateral offsets of drainage systems, right-stepping ruptures with pressure and shutter ridges, and small pull-apart basins along strike (Al-Taj, 2000; Ferry et al., 2007; 2011). The deformation in the lower Jordan Valley is almost constant throught the last 70 ka with observed buried major and minor faults. A record of syn-depositional and post-depositional deformation is preserved in the soft sediment of the Great Dead Sea Lake through the Mid-Pleistocene to present-day (El-Isa and Mustafa, 1986). Most of this deformation is presented in form of seismites (Reches and Hoexter (1981); El-Isa and Mustafa (1986); Malkawi and Alawneh (2000) and Marco et al. (2005) in the Lisan and Damya.

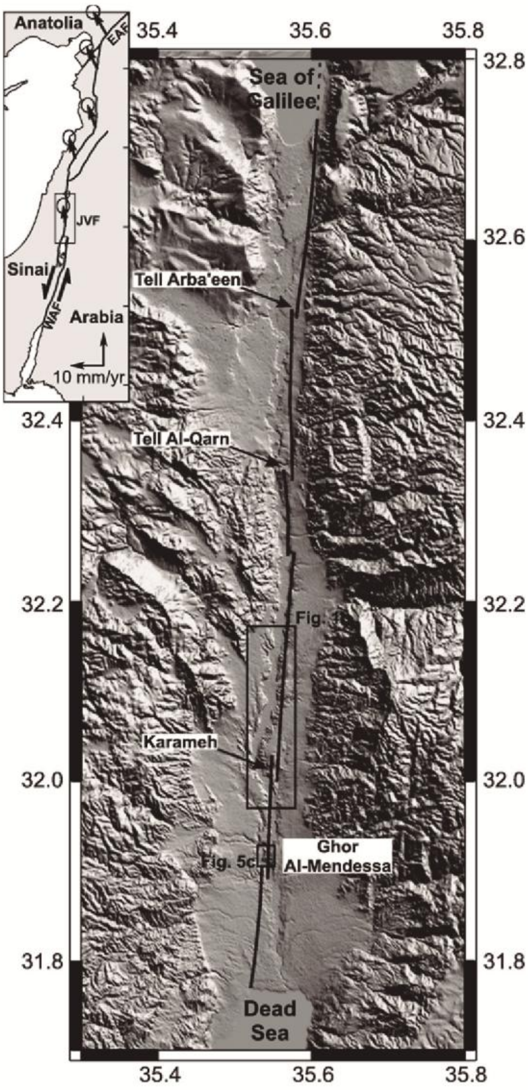

Figure 2.12. Tectonic map of the JVF (After Ferry et al., 2007)

The structural studies in the area between the northern WAF and the southern JVF to the north of the Dead Sea are few and different interpretations were adopted based on geophysical prospecting. Most of these studies were planned to reconstruct the northern closure of the Dead Sea pull-apart basin (Alzoubi et al., 2006; 2007; Ten Brink and flores, 2012). Suggesting that the WAF dies in the NE corener of the Dead Sea, the deformation is transferred from the WAF (Eastern boundary fault) to the JVF through NW-SE transverse faults.

2.2.2 The Dead Sea pull-apart basin.

The DSB is an excellent example of pull-apart basin developed along strike-slip faults (Lazar et al. 2006) (**Fig. 2.13**). The structure of the Dead Sea basin is dominated by the relative motion between the WAF in the east and the JVF (Jericho fault) in the west (Garfunkel and Ben-Avraham, 1996). Several sub-basins are indicated within the DSB as there is several block down-faulted by a few kilometers (Garfunkel and Ben-Avraham, 1996; Lazar, 2006; Al-Zoubi, 2007; Ten Brink and Flores, 2012).

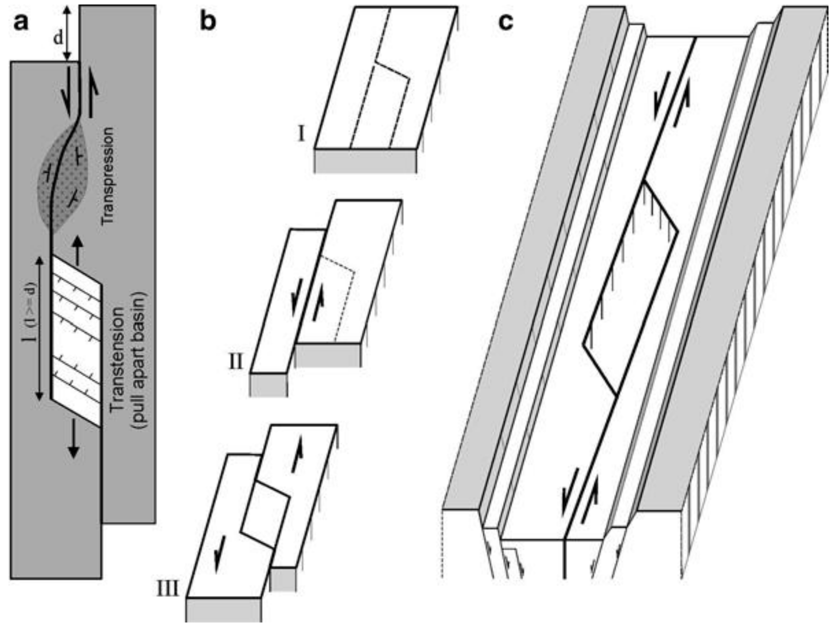

Figure 2.13. Secondary structures along the DST (After Garfunkel, 2014).a) Transpressions and transtension possibilities with controls on either mechanism. B) Evolution of the pull-apart basin with the ongoing movement of the two faults. c) Structural relationship and type of the possible northern and southern closures of the basin.

Three main sub-basins are inferred by tomographic and seismic profiles for which NW-SE transverse fault are will imaged (Lazalr et al. 2006; Garfunkel, 2011). In a recent work, Wetzler et al. (2014) have used a micro-earthquake clustering to map these faults, but the northern closure couldn’t be well determined.

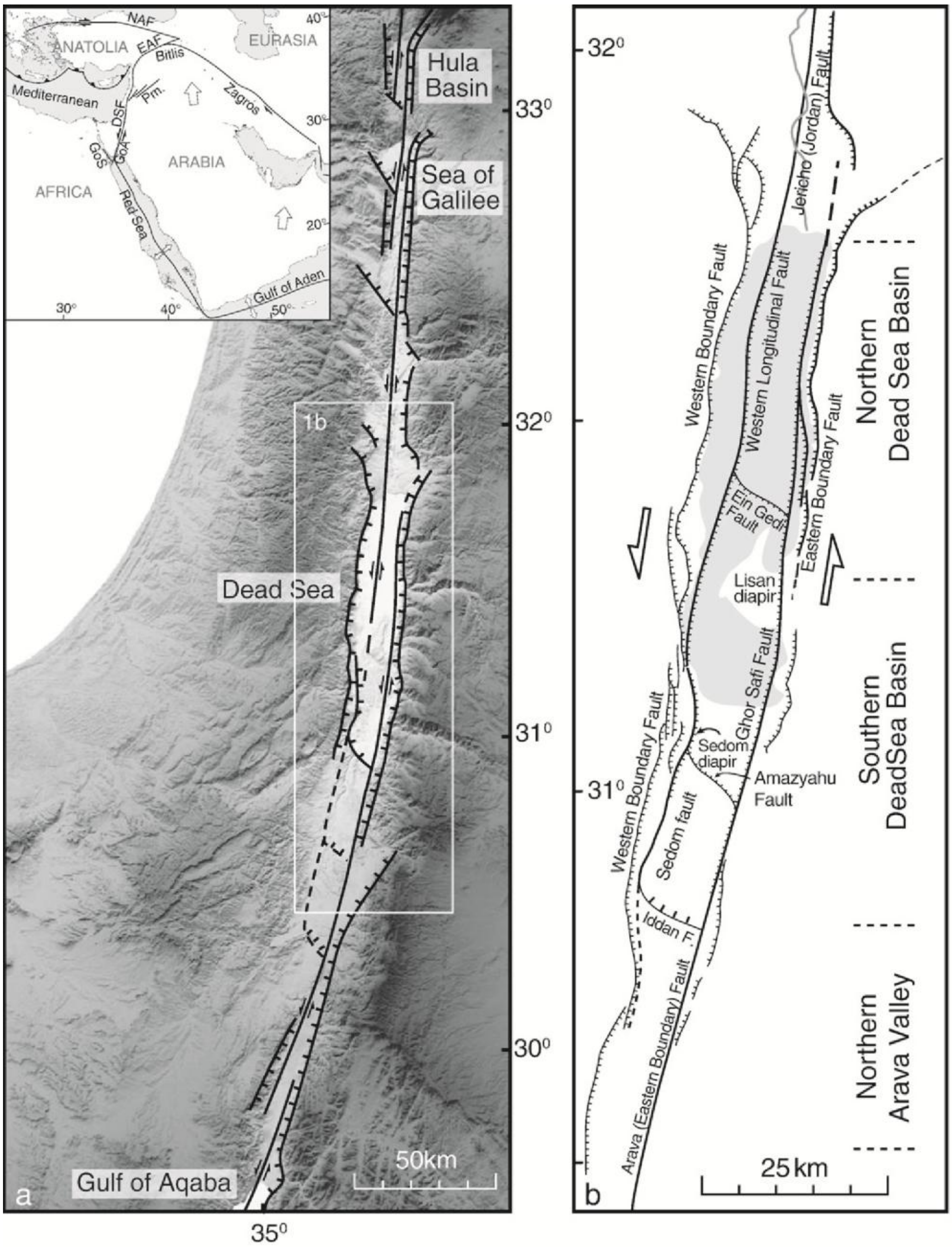

Figure 2.14. Different sub-basins of the Dead Sea pull-apart basin. The southern closure is well defined, but the northern one lacks well-known faults connecting WAF and JVF(After Smit et al., 2008)

The identification and detailed mapping of the eastern border fault (WAF) present problems in determining the shape and the northern closure structure of this basin (Alzoubi et al. 2007; Smit et al., 2008: Ten Brink and Flores 2012; **Fig. 2.14**). Several models had been suggested for this basin and most of them point that there is no clear transverse fault structures in the northern end of the basin (Lazar et al. 2006; ten Brink and Flores 2012). All these models assume that the eastern boundary fault (WAF) dies few kilometers NE from the Dead Sea Lake and geophysical data are scarce within the Jordanian side of the DSTF (Al-Zoubi et al., 2007).

2.2.3 The Amman Hallabat and Shueib Structures.

The AHS and the SHS are two fold-thrust structures striking NE-SW from the easternmost corner to the Dead Sea toward the Zarqa city and Baqa basin (in north of the Amman area), respectively, and are part of the central Syrian Arc System in the NW Jordan (Mikbel and Zacher, 1981; Attalla and Mikbel, 1992; Sahawneh and Attalla, 2002; Diabat, 2009).

The first authors who addressed the AHS and the SHS were Burden (1959) and Quennell (1959) and their interpretations were to consider both structures as monoclines that might be reltated to the DSTF. Since that time, the SHS as well as the AHS had received little attention in the active tectonic studies and they were considered inactive in the Miocene-Recent times (Al-Zoubi, 2006).The tectonic inversion that formed the fold-thrust belts, the AHS and the SHS, in NW Jordan had been aged to occur through two main phases: The Late Cretaceous and Oligocene (Abed, 1989).

The AHS extends about 80 km from the northeastern corner of the Dead Sea in the west to Qaser Al Hallabat in the east out of the study area boundaries. This structure is mainly represented by a dextral strike-slip fault accompanied by smaller antithetic and synthetic faults and subparallel folds (anticlines and synclines). It strikes generally NE-SW in the study area and in Amman sheet as a whole, and curves ENE-WSW where it disappears underneath the basaltic flows. The geometry of the AHS in detail is rather complex, and is formed by a set of dextral reverse faults with synthetic and antithetic faults and sub-parallel related-folds (Diabat, 2009). This fault-fold system has been traditionally interpreted as inactive since the late Cretaceous. However, in a recent study Diabat (2009) proposed a Neogene reactivation of local faults related to this structure close to the town of Amman. Since there is a lack of Neotectonic studies for these structures, their structural relationships with the DSTF remain unclear.

2.2.4. Seismicity in the study area

Instrumental seismicity recorded in the region indicates that most events have focal depths of less than 30 km, mean magnitudes ranging 2.0-3.5 and spread in a wide area around the southern DSTF. In the WAF (southern segment) there is a close relation between earthquakes and surface active faulting (**Fig. 2.15**); whereas in the JVF the seismicity is more dispersed.

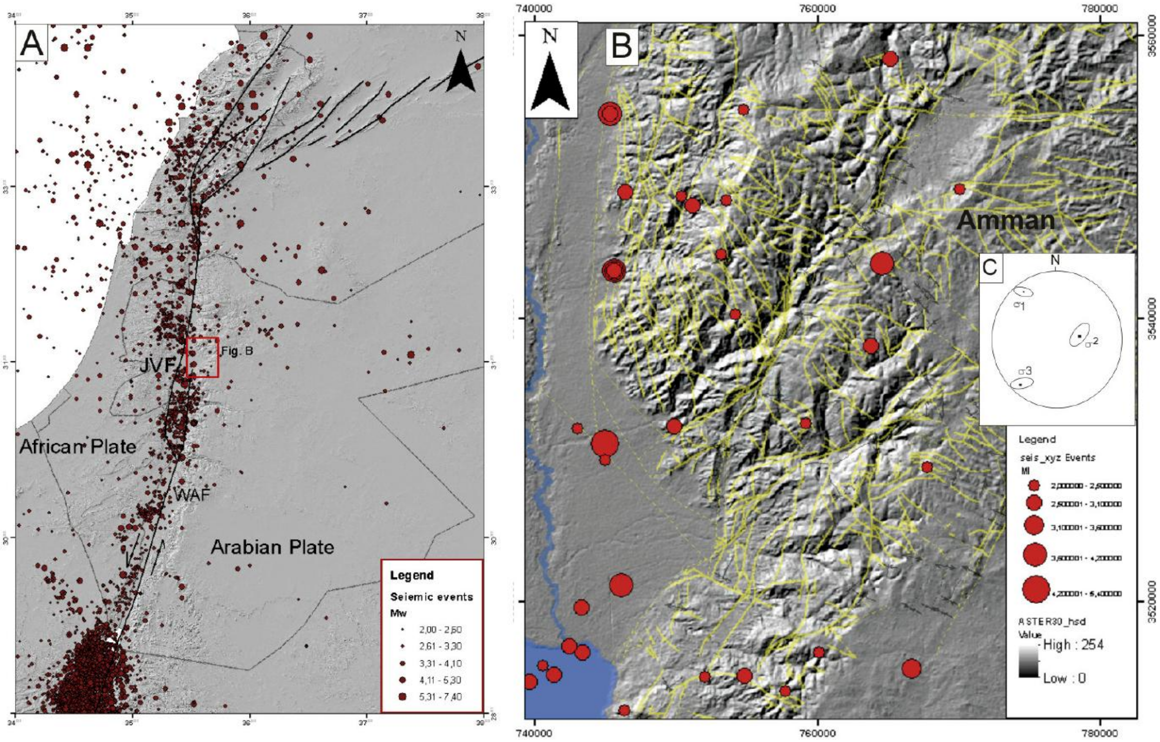

Figure 2.15. (A) Projection of seismic events for the last 35 years in the area of the DSTF and related structures collected from earthquake catalogues from the Jordan Seismological Observatory in Amman (JSO) and the Geophysical Institute of Israel (GII, 2005). The Digital Elevation Model has been obtained from the ASTER GTOPO30. (B) Instrumental seismicity for the study area taken from the same earthquake catalogs. (C)NW-SE horizontal maximum compressive stress revealed by seismic data (Hofstteter et al., 2007).

Spite the moderate magnitude of instrumental seismic events, there are evidences of historical large earthquakes on the southern DSTF (Ambraseys and Jackson, 1998; Al-Tarazi, 1999; Galli and Galadini, 2001; Ambrasyes, 2006; Marco, 2008; Leroy et al., 2010; Salamon, 2010; Ferry et al., 2011; Braeuer et al., 2014; Hofstetter et al., 2014). Moreover, the northeastern area of the Dead Sea contains several ruins and archaeological sites (i.g.Tall Alsaaydah; Tall el-Kafrain; Tall al-hammam) that are affected by historical earthquake deformation (Ferry et al., 2011, this study).

Recent earthquake catalogs for the past 80 years in our study area indicate that present-day seismic activity is scarce with low-to-moderate magnitudes ranging from 2.0 to 5.5 Mw and focal depth of less than 30 km (Nusier and Alawaneh, 2006) (**Fig. 2.15**). This seismicity concentrates preferably at the northern termination of the WAF and at the Dead Sea area (Haynes et al., 2006). The last felt earthquake in our study area was on the 12th of September 2013 with a magnitude of 3.4 and a depth of 20 km to the northeast corner of the Dead Sea.

2.3 Stratigraphy of the study area

The geology in the area comprises a sediment sequence from the Triassic to the Cretaceous that is unconformably overlain by Quaternary to Holocene sediments. However, the formations belong to the Mesozoic and cover large area of the study area are belong to the Triassic and Cretaceous. Most of the formations between the Mesozoic and younger formations were eroded and two formation belong to the Late Pleistocene are Holocene are preserved namely, Lisan and Damya formation; respectively.

2.3.1 Mesozoic sequence

Triassic formations

Two formations belonging to the Triassic are well exposed in the study area; Hisban and Mukheries formations (**Fig. 2.16**). The Hisban Formation consists of bedded limestones/dolomite with marly limestone intercalations. This formation is made of four distinctive members; Dolomitic member, Fossiliferous limestone member, Massive limestone and Sandy member. It is well exposed in many valleys of the study area; Wadi El Muhtariqa and Wadi El Hijar El Twall. The formation's top and base limits are very clear consequently that this is the only formation in the area of the eastern Dead Sea where is almost completely formed by carbonate layers (Abed, 2000). The age of this formation was been assigned to be of Anisian (Lower Triassic) (Makhlouf et. al 1996, Abed 2000).

The Mukheiris formation consists of a lower tidal unit and an upper fluvial unit (Makhlouf, 1996). The tidal unit was deposited in a shallow marine environment during a gradual retreat of the Tethyan strandline. The fluvial unit was deposited within a low sinuosity braided plain fluvial environment. Stacked channels and fining-upward cycles developed as a result of fluctuations in hydrodynamic energy and regime as a result of local tectonism and uplift.

During the Lower-Middle Triassic, transgression of the Tethys advanced from the west and northwest to Jordan east of the Dead Sea, where Triassic siliclastics and carbonates disconformably overlie Lower Paleozoic sediments.

Figure 2.16. Best outcrop of the Triassic rocks in study area. The lower layers of dolomitic limestone cliffs belong to Hisban formation with overlying layers are the Mukhieries formation.

Jurassic formations

After a period of regression associated with tectonic activity, a major unconformity and absence of lower Jurassic, the Jurassic ocean invaded the Jordan. Renewed uplift and erosion, epeirogenic movements and local volcanism during the upper Jurassic preceded the deposition of Lower Cretaceous sandstones (Bender, 1968). The eastern borders of the marine depositional environment and the thickness of the deposited sediments were remarkably influenced by a structural weakness zone.

The Jurassic sequence is represented by seven formations that are, from bottom to top; Hihi Claystone, Nimr Limestone, Silal Sandstone, Dhahab Limestone, Ramla Sandstone, Hamam Sandstone, Mughanniyya Limestone (Muneizel and Khalil, 1993).The Jurassic formations in study area are mostly eroded and few oucrops are preserved in area. The best outcrop of the Jurassic formation is to the west of the Zarqa Rive, however, few scattered sockets of these rocks outcops to the west of Amman and in the Baqa´a basin.

Cretaceous formations

Early Cretaceous siliclastics rocks unconformably overlie the Triassic and Jurassic rocks in northwestern Jordan. This unconformity is angular due to the late Jurassic epeirogenic movements. A gradual transgression occurred throughout the Lower Cretaceous and spread clastic continental sediments across the Jordan Valley to the east, while a marine platform environment dominated northwest Jordan (Bender, 1968). During the early Cretaceous, the Middle East was characterized by broad regional Paleo-highs, basement controlled north- northeast to south-southeast trending horst, and tilted blocks and salt domes (Abed, 1989).

A regional transgression and regression movements are localized to a great extent in the beginning of the Late Cretaceous (Cenomanian), as well as the Post-Cenomanian age (Abed, 1989; Almalki et al., 2015). Significant tectonic movements took place during the Late Cretaceous which led to folding, uplift, erosion and tilting of fault blocks which also accompanied several volcanic activities (Bender, 1974; Abed, 1989; 2000).

Lower Cretaceous in the Jordan's rock sequence refers to Kurnub Group. This group is cropping out everywhere in Jordan, especially in deep wadis. The base of the Kurnub Group marks an erosional unconformity. For this reason, this group can be found overlying different formations across Jordan (Amireh, 1998).

This group divides into two distinguishable units; the lower one is massive white sandstone, while the upper is varicolored sandstone unit. The Massive White Unit represents the lower part of which contains plant fossils in muddy intercalations and it is extensively cross bedded. Its thickness reaches about 180 m. (Bender, 1968, 1974 , Sahawneh and Attallah, 2002).

The Varicolored Sandstones Unit is composed of light, violet and multi-colored sandstones with sandy shale and shale intercalations, with a total thickness of about 150 m. (Bender, 1968). However, more precise classification presented by (Amireh 1998), where, he indicated that the Early Cretaceous Kurnub Group of Jordan consists of three regressive-transgressive (fluvial-marine) depositional sequences in northern Jordan, whereas, continental clastics dominated central and southern Jordan. Deposition of the Kurnub Group started in the late Neocomian above a regional angular unconformity by basal conglomerate and sandstone facies association of an alluvial braid plain origin and overlies different rock formations (**Fig. 2.17**).

Fig 2.17. The unconformity between the Early Cretaceous Kurnub formation and the Late Triassic Mukheriris formation in Al-Muhtariqa valley 3 Km east of the Al-Rama village.

This group, in the study area, is found in very restricted site in the northern most eastern parts and in one site southern western part of the study areas, and always above the Triassic formations, especially, Mukheiris formation. The age of this formation is of lower Cretaceous, as concluded form the studies carried by (Bender, 1968 and Amireh 1998).

Upper cretaceous sedimentary rocks are considered to be of marine origin (Quennell 1959). The typical upper cretaceous columnar section in Jordan is subdivided into five formations, Nodular limestone unit, Echinoidal limestone unit, Massive limestone Unit, Silicified limestone unit and Phosphorite limestone unit (Sahawneh and Attallah, 2002). This formation s are equal to Na'ur Formation, F/H/S undefined Formation, Wadi As Sir Formation, Amman Formation and Hasa Formation respevtively (Abed 2000). The age of this group is Cenomanian – Turonian - Maastrichtian (Bender 1974, Basha 1978, Dilley 1985, Shahrrour 1996 , Abed, 2000).

Upper Cretaceous Orogenic activity aided the formation of a fore deep along the Tethys margin, which contributed to the accumulation of deep marine bituminous limestone and Cherts under anoxic conditions (Bender, 1974).

2.3.2 Quaternary sediments

The Quaternary, uppermost Pleistocene, in the Jordan Valley is represented by two closed lakes: the Lisan Lake (63 to 16–15 ka; **Fig. 2.18**) and the Damya Lake (16–15 to 12 ka; **Fig. 2.19**) (Abed and Yaghan, 2000). These two lakes were responsible of the sedimentation of the two main formation; the Lisan and Damya formations, respectively (Hass-Schramm, 2004). The Lake Lisan occupied part of the DSTF extending for 220 km from Lake of Tiberias to 20 km south of the southern nowadays Dead Sea with E-W width vary between 7 and 15 km (Abou Ghazalah, 2009).

The Lisan Formation in the central Jordan Valley consists mainly of varied sediments, is capped by a conspicuous white cliff containing abundant gypsum lamina and is overlaid by the evaporite-free Damya Formation (**Fig. 2.19**). The white cliff sediments represent the driest period of the Lidan–Damya times (63–12 ka). This cold, dry period extended from 23–22 to 16– 15 ka BP, which corresponds to the Last Glacial Maximum (LGM) world-wide and ended by the demise of Lake Lisan. In its best outcrop in the Jordan valley (in the site of Al karamah Dam, Jordan) the Lisan Formation is divided into three main units (**Fig. 2.18**). The lower and the upper units comprise laminate calcareous silt interlaminated with Aragonite (Abed and Yaghan, 2000; Bartov et al. 2002).

Figure 2.18. Best outcrop of the Lisan formation in the study area. The location of this outcrop is about 7 km NE the Dead Sea.

Figure 2.19. The Damya formation overlaying the Lisan formation. The colluvium sediments of the Damya vary in the study area depending on the mother rock-formation of the sediments.

Chapter 3

Methodology

Preface

This chapter describes the general methodology that I followed to achieve the objectives of this Thesis. The main work developed throughout this research includes several field surveys followed by desk work and computer analysis. The methodology has been divided into three main parts that constitute the sections of this chapter: landscape analysis through geomorphic indexes, field geology and structural interpretation, and paleostress study. The presented methods have been widely used in the fields of tectonics all over the world.

The landscape analysis made in this work is completed with the next chapter (chapter 4), where I describe two news Add-Ins tools to extract normalized and swath profiles. The methodological description of these two index will be further explained in the next chapter.

This chapter includes the following subtitles:

3.1 Landscape analysis

3.1.1 Drainage network and watershed extraction

3.1.2 Spatial analysis of the landscape pattern

Topographic roughness.

Topographic swath profiles

Hypsometry

3.1.3 Analysis of the drainage network through geomorphic indexes

Normalized profiles

Ridgeline profiles and bulk erosion estimation

Area-slope plots and Ksn index

3.2 Field geology and structural interpretation

3.3 Paleostress analysis

3.1 Landscape analysis

3.1.1. Drainage network and watershed extraction

The first step for the calculation of geomorphic indexes is the extraction of the drainage network and the delineation of watersheds. This first step was carry out with the aid of a Digital Elevation Model (DEM) of 30 meters of pixel resolution and the aid of ArcGIS software. The DEM used in this work was built by radar from the Shuttle Radar Topography Mission (SRTM) in February 2000. This project was a joint endeavor of NASA, The National Geoespatial-Intelligence Agency, and the German and Italian Space Agencies and produced the most complete, highest-resolution DEM for the whole earth (Farr et al., 2007). The US Government progressively released this DEM since September 2014.

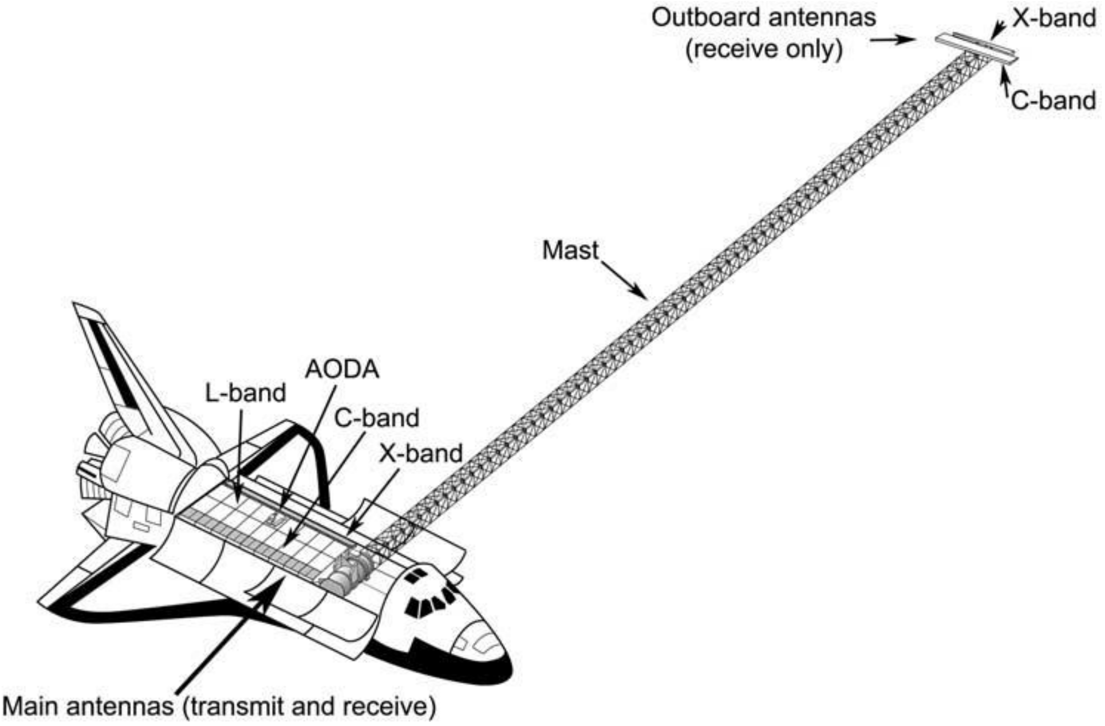

Figure 3.1. Major components of SRTM (Taken from Farr et al., 2007). In the shuttle payload bay are the main antennas (L band was not used) and the attitude and orbit determination avionics (AODA). At the end of the 60-m-long mast are the secondary antennas.

SRTM employed two synthetic aperture radars, a C band system (5.6 cm, C Radar) and an X band system (3.1 cm, X Radar) (**Fig. 3.1**). SRTM data were validated on continental scales through comparisons with reserved ground control. SRTM-DEMs have an absolute high error of 5-6 meters because SRTM did not always map the true ground surface (Farr et al., 2007). Instead, it measured an effective height determined by the phase of the complex vector sum of all the returned signals from within the pixel being imaged. If the pixel contained bare ground, the phase reflected the height of the surface. If the ground was covered with vegetation, the return was influenced by the vegetation height, structure, and density. In the case of our study area, the absence of vegetation ensures the highest quality of SRTM-derived DEMs.

There are several methods to extract drainage network from Digital Elevation Models (DEM). In this study I used the methodology proposed by O’Callaghan and Mark (1984). This method used the four-direction algorithm (D8) to determine the flow direction from a cell to one of its 8 neighbors. This method is the faster to derive drainage channels from DEMs but does not produce reliable drainage density values, since the flow is always forced downstream. However, since most of the geomorphic indexes work only in the main or trunk channels, this method is the most widely used to calculate geomorphic indexes. The ArcGIS workflow includes 8 steps to extract a drainage network from a raw DEM. These processes are included in the geoprocessing toolbox of hydrology within ArcMap or ArcCatalog programs (**Fig. 3.2**). They are described in the next lines:

A) Fill sinks: This function fills sinks in a DEM raster grid. Sinks are cells with errors or undefined drainage directions cells surrounded by higher elevation cells and where the water becomes trapped within. Fill can also be used to remove peaks. The peaks are cells where no adjacent cells are higher and to remove these peaks, the input surface raster must be inverted. By applying this function the flow is ensured and the channels will be continuous.

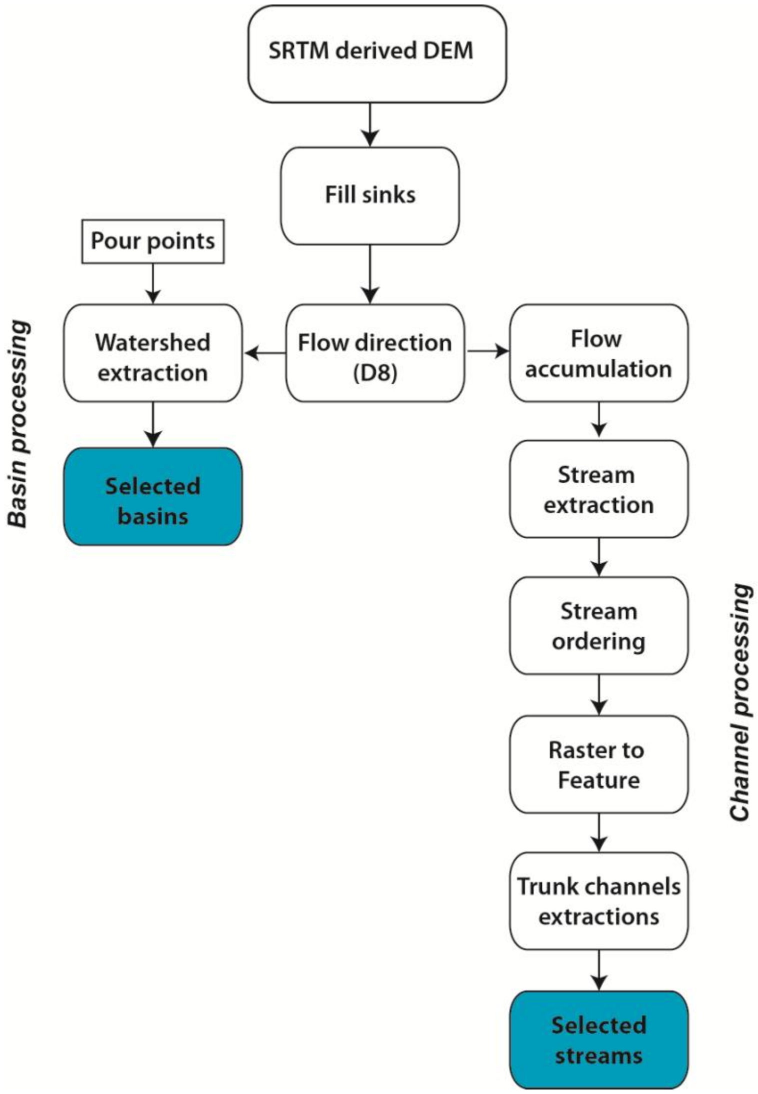

Figure 3.2. ArcGIS hydrology workflow for extracting selected basins and selected channels.

B) **Flow direction:** This function creates a raster of flow paths for the corrected and pit-filled DEM grid. This means that the processed cell is lower than the eight surrounded cells then the value of this cell will be adjusted to the value of the lowest neighbor cell and a flow direction is defined toward this cell. Computation of the flow direction uses 8 directions of possible flow paths "pour point" model that operates on the hypothesis that runoff from upstream cell flows through adjacent downstream cells with the lowest elevations or basically down to the highest elevation drop in relation to eight neighboring cells.

C) **Flow accumulation:** This function creates a raster of accumulated flow into each cell. It used as input the flow direction grid calculated in the last step. The result of flow accumulation is a raster of accumulated flow to each cell, as determined by accumulating the flow of all the upstream cells that flow in that determined cell.

D) **Delimitation of streams by reclassifying flow accumulation:** This function is a simple reclassification function that works over the flow accumulation raster. It used a threshold to differentiate cells that represent channels from those that not. Once a cell reaches this threshold, all the downstream cells will also classified as channels cells as the flow accumulation increase downstream. The threshold value will therefore depend on cell size and DEM dimensions. Generally, an initial threshold of the 1% of the total number of the cells in the model is used, and afterwards modified to obtain better or less resolution in the drainage network.

E) **Stream Order**: This step implies classifying the resulting network following a Strahler or Shrevee ordering. All the pixels are classified by their ordering hierarchy to improve a subsequent feature extraction. For better visualization of these orders/grades it is recommended to change the visualization of the raster from the properties of the raster in the table of contents.

F) **Stream to feature:** In this step, the stream raster is vectorized to represent the stream networks. This vectorization converts the raster into vector polylines. These vector features will serve as the basics for all the stream-based indexes as longitudinal normalized profiles, ksn, etc.

G) **Trunk channels processing:** The drainage network obtained in the previous step is made of multiple vector polylines**.** The majority of the geomorphic analyses used in this Thesis use the main or trunk channels. From the drainage network all secondary channels were deleted and the different reaches of the main channel merged in a single line. These channels (or they river heads) will be the input data for all the geomorphic analyses based in river profiles or river gradients.

H) **Watershed delineation:** The delineation of watersheds follows a parallel and independent processing than the one used to extract drainage channels. This function uses a previously defined point feature class with the outlet locations (pour points) and the flow direction raster calculated in the previous second step. The result is a raster watershed raster where cells are coded with the values of the pour points. This raster has to be consequently converted into multi drainage basin polygon features. These drainage basin polygon features will be used as input parameters for all basin-related geomorphic indexes.

2.1.2. Spatial analysis of the landscape pattern

In order to evaluate the general landscape configuration we used some spatial-based indexes that inform about the landscape configuration and distribution. The selected indexes are; surface or topographic roughness, swath profiles and the spatial estimation of the hipsometric integral (HI).

Topographic roughness.

Characterization and evaluation of surface or topographic roughness is essential in Earth Sciences. Each process operating at the Earth's surface both encounters and creates rough surfaces (Smith, 2014). However, there are numerous methods to estimate topographic roughness and even the concept of roughness have different genetic meanings. The term "surface roughness" is used to describe the complexity or variability of the surface, i.e. the variability of it.

Surface roughness can be examined by considering elevation probability distribution statistics as mean, standard deviation, skewness, kurtosis, or even hypsometry. In this PhD Thesis I used the approach proposed by Sanchez-Serrano (2000) of considering topographic roughness as a combination of the combine variability of the first altitude derivatives, slope and aspect (**Fig. 3.3**). This approximation does not take into account total altitude differences that can be examined in a better way by evaluating hypsometry.

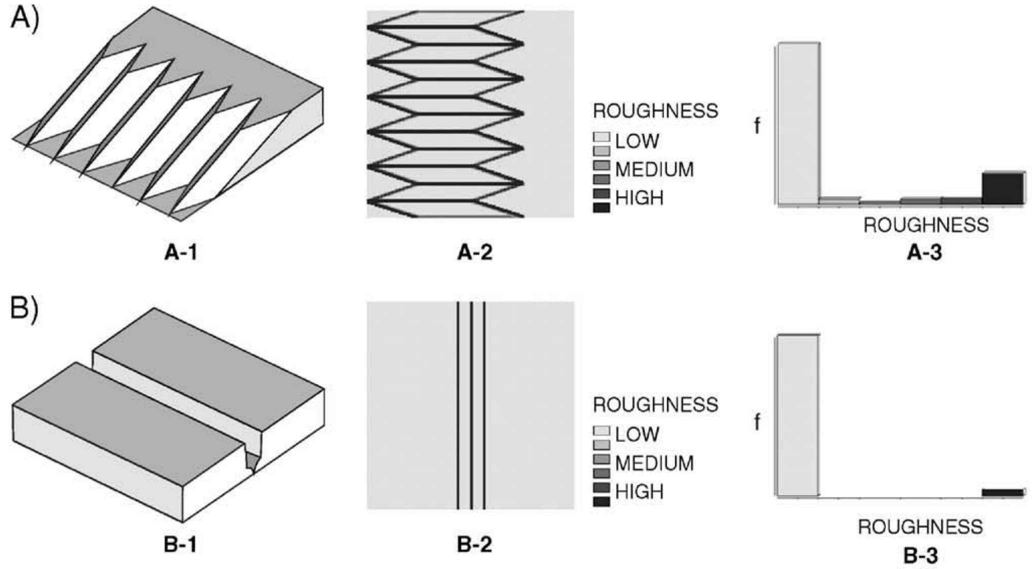

Figure 3.3. Theoretical roughness analysis of two simple theoretical forms. Theoretical simple surfaces (A-1; B-1), roughness map (A-2; B-2) and histogram of roughness classes (A-3; B-3) are shown in each case. High roughness values describe slope ruptures located in valleys and crests (Modified from Sanchez-Serrano, 2000).

In order to assess the variability of both parameters (slope and aspect) we considered the standard deviation for each cell respect to their 8 neighboring cells. This approach can be very easily computed for the slope gradient in GIS software, but the aspect maps needs a previous transformation to estimate the variability. This is due to the north slopes, in which aspect values change from 360º to º0 without representing variability in aspect. First, original orientations are measured from 0º to 180º and then from 180º to 0º (instead of 180º to 360º). Second, original orientations (measured from 0º to 360º) are rotated 90º in a clockwise direction (90ºE=360º) and then the first transformation is applied (**Fig. 3.4**). Thus, two superimposed maps are obtained. Each cell value is the maximum value for both maps. The assumption made is that only the difference in slope orientation between neighboring cells is relevant to roughness estimations. To produce the final roughness map, each cell of the slope and slope orientation maps were multiplied by each other. The final result is a map of roughness values that range between 0 and a maximum value, which depends on the maximum slope gradient and slope orientation variation.

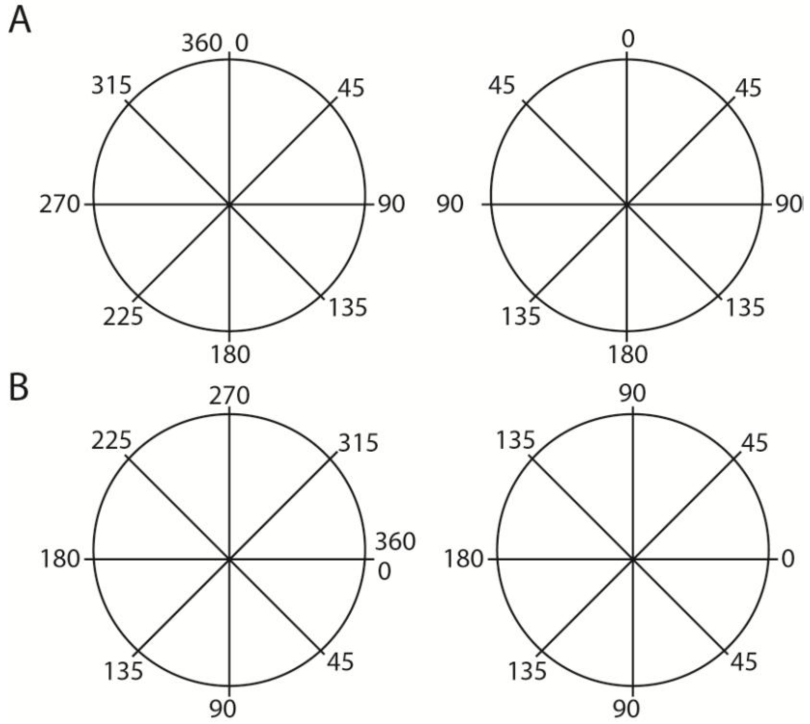

Figure 3.4. Transformation of aspect data for roughness calculation. A) Possible values of an aspect map and their correspondence to force the continuous variation between contiguous values. B) Aspect data rotated 90 º and transformed again to force contiguity between values.

Topographic swath profiles

Swath profiles are topographic profiles that condense elevation data into bands of profiles. These band-profiles are extracted from a rectangular swath rather than a simple line, as in conventional single profiles. Conventional swath profiles show elevation data projected onto a vertical plane parallel to the long axis of the swath rectangle, and statistical parameters (usually the maximum, minimum and mean elevations) are calculated. The curve for maximum elevations corresponds to the ridgelines and helps to identify topographic features, such as palaeo-surfaces. The curve for minimum elevations corresponds to the valley floors; the lowest topographic point in the profile. A quick estimate of the incision is given by the arithmetic difference between the maximum and minimum elevations, i.e. the local relief. Other parameters that can be extracted from these profiles are the mean elevation, or even first and third quartiles, which reflects the degree of maturity of the landscape in means of long-term uplifting versus erosion.

In the next chapter of this Thesis I present a new ArcGIS Add-in tool for extracting these profiles from vector line features and elevation raster models. The methodological discussion about swath profiles can be found in that chapter. This tool was used for the analyses of the DSTF region.

Hypsometry

Hypsometry describes area distribution at different elevations (Strahler, 1952; Schumm, 1956) and can be estimated using the hypsometric curve or the hypsometric integral (HI). The hypsometric curve represents the relative proportion of area below (or above) a given height (**Fig. 3.5a**). The hypsometric integral corresponds to the area below the hypsometric curve and therefore is correlated with the shape of this curve. The hypsometric integral can be approximated by means of the following equation (Pike and Wilson, 1971):

$$HI = \frac{Mean\ elevation - Minimum\ elevation}{Maximum\ elevation - Minimum\ elevation}$$

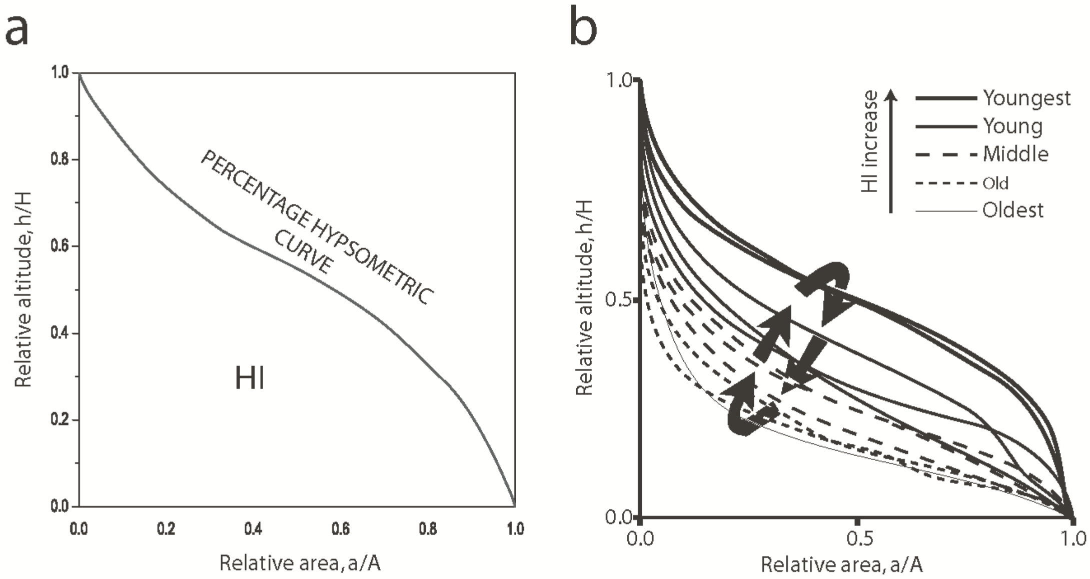

Figure 3.5. a) Hypsometric curves after Strahler (1952). Area of the region under the curve is known as the hypsometric integral (HI). b) Changes in hypsometric curves. Convex curves and high HI values are typical for youthful stages of maturity and s-shaped curves and concave curves together with HI values are typical for mature and old stages. Arrows indicate a direction of change in the curves according to change in mountain altitude during the geomorphic cycle (Taken from Pérez-Peña et al., 2009)

The hypsometric curve and the hypsometric integral are valuable tools in characterizing topography because they are correlated with the stage of geomorphic development of the landscape. Strahler (1952) correlated convex hypsometric curves with a youthful stage, S-shaped curves with a mature stage, and concave curves with a peneplain stage (**Fig. 3.5b**). This evolution is based on the assumption that a mountain is rapidly uplifted without serious denudation and then increases in dissection with a lowering in mean elevation (Davisian scheme). However, subsequent works have proposed different alternatives to this hypsometric curve evolution. Willgoose and Hancock (1998) modeled the evolution of simulated basins and found that in the case of declining equilibrium, hypsometric curves converged to a constant S-shaped form and not to the concave form proposed by Strahler (1952) for the peneplain stage. Ohmori (1993) analyzed several large-scale natural drainage basins in Japan (up to 10,000 km2) and made a study of simulated basins of empirical laws deduced from Japanese mountains. The resulting hypsometric curves were concave or S-shaped but never convex. In this case, the assumption of the Davisian scheme (an initial rapid uplift without erosion) is not valid; the Japanese mountains, although young, have been strongly eroded during uplift (Ohmori, 1993).

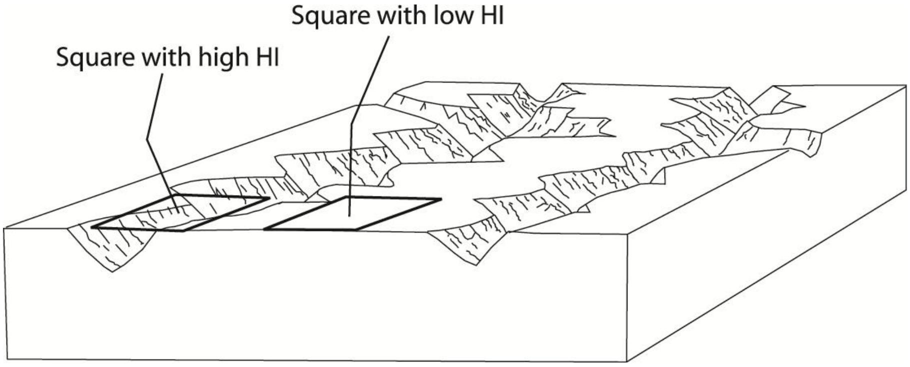

Figure 3.6. Schematic illustration showing how HI values estimated for regular squares can present high variation depending only on the square location (taken from Pérez-Peña et al., 2010)

The HI is thought to be influenced by basin parameters such as basin geometry, drainage area, and basin elevation drop (Lifton and Chase, 1992; Masek et al., 1994; Hurtrez et al., 1999; Chen et al., 2003). However, some recent works have demonstrated that demonstrated that HI values obtained for several basins and sub-basins do not correlate with basin area or basin shape (Walcott and Summerfield, 2008; Pérez-Peña et al., 2010).

In this PhD Thesis I will analyze hypsometry following different approaches. First I will spatially analyze hypsometry by calculating HI for regular squares instead of drainage basins (Pérez-Peña et al., 2010). This approach spatially analyzes hypsometry and presents a valid method to evaluate landscape dissection in a region (Pérez-Peña et al., 2010; Mahmoodand Gloaguen 2012; Siddiqui and Soldati, 2014). HI values obtained for regular squares can present a high inherent variability only depending or their position (**Fig. 3.6**). However this variability can be obviated by applying local indexes of spatial autocorrelation as Moran I or Getis-Ord (Pérez-Peña et al., 2010).

$$I = \left(\frac{N}{\sum_i \sum_j w_{ij}}\right)\left[\frac{\sum_i \sum_j w_{ij}(x_i-\mu)(x_j-\mu)}{\sum_i (x_i-\mu)^2}\right] \qquad G_i^* = \frac{\sum_j w_{ij}\,(d)x_j}{\sum_j x_j}$$

Moran Index (I) and Getis-Ord (Gi) indexes used to analyze HI values.*

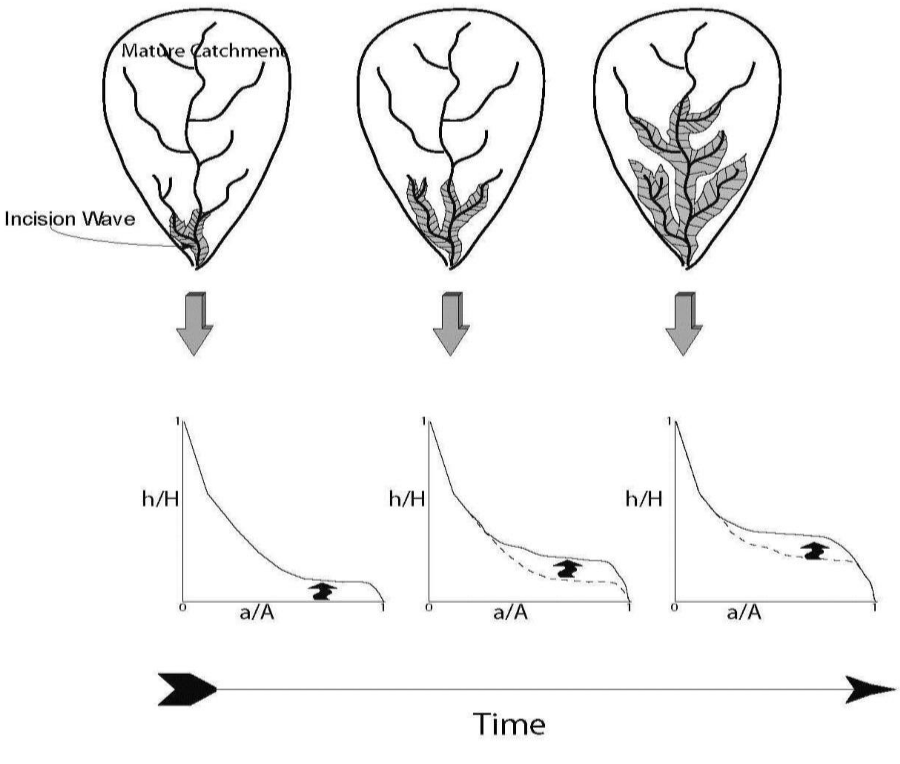

Figure 3.7. Evolution of a mature drainage basin after a capture process and its evolution through time (After Pérez-Peña, 2009).

Second, in order to evaluate the mass balance at basin-level I extracted the hypsometric curves and their HI values. I used the CalHypso ArcGIS Extension developed by Pérez-Peña et al. (2009). Through the evaluation of hypsometric curves at basin scale it is possible to analyze not only the stage of development of the basin, but also the response to base level lowering through time (Pérez-Peña et al., 2009; **Fig. 3.7**).

2.1.3. Analysis of the drainage network through geomorphic indexes

Normalized profiles

The erosion versus uplift rates can be interpreted through the analysis of longitudinal river profiles (Hovius 2000; Menedez et al., 2007; Pérez-Peña, 2009). The longitudinal stream profiles evolve over the time and their channels incise into the bedrock by chemical or physical processes (Whipple, 2004). The analysis of river longitudinal profiles has been used intensively to detect changes in river controlling factors; namely lithology, climate and tectonic uplift and hillslope processes (Seeber and Gornitz, 1983; Brookfield 1998; Pérez-Peña et al., 2009a; Kirby and Whipple, 2012; Giaconia et al., 2012; Anton et al., 2014; Troiani et al., 2014). However, the comparison of longitudinal profiles from rivers with different lengths and gradients can be intricate.

Demoulin (1998) proposed the representation of river longitudinal profiles in a normalized form. This form is known as the normalized longitudinal profile and it is constructed by normalizing elevations with respect to the relative elevation or amplitude and distances respect to the total channel length. This representation allow comparing rivers with different lengths and gradients (Demoulin, 1998; Ruszkiczay-Rüdiger et al., 2009; Matos et al., 2014). Moreover, this normalized representation highlights gradient variations as clear as semi-logarithmic profiles (Hack, 1957; Demoulin, 1998).

In the next chapter of this Thesis I present a new ArcGIS Add-in tool for extracting river longitudinal normalized profiles from vector line features and elevation raster models. The methodological discussion about these profiles can be found in that chapter. This tool was used for the analyses of the DSTF region.

Ridgeline profiles and bulk erosion estimation

Ridge line profiles are drawn by projecting rivers thalwegs onto a theoretical pre-incision layer constructed from the present-day lateral divides of the watersheds (Menendez et al., 2008; Pérez-Peña et al., 2010; **Fig. 3.8**). The advantage of these profiles is that they provide equivalent lengths as for the river profiles. However, these profiles cannot be considered as the pre-incision surface. Furthermore, it can generate a view of the structure of the relief for each basin allowing a relative comparison of bulk erosion between the different basins.

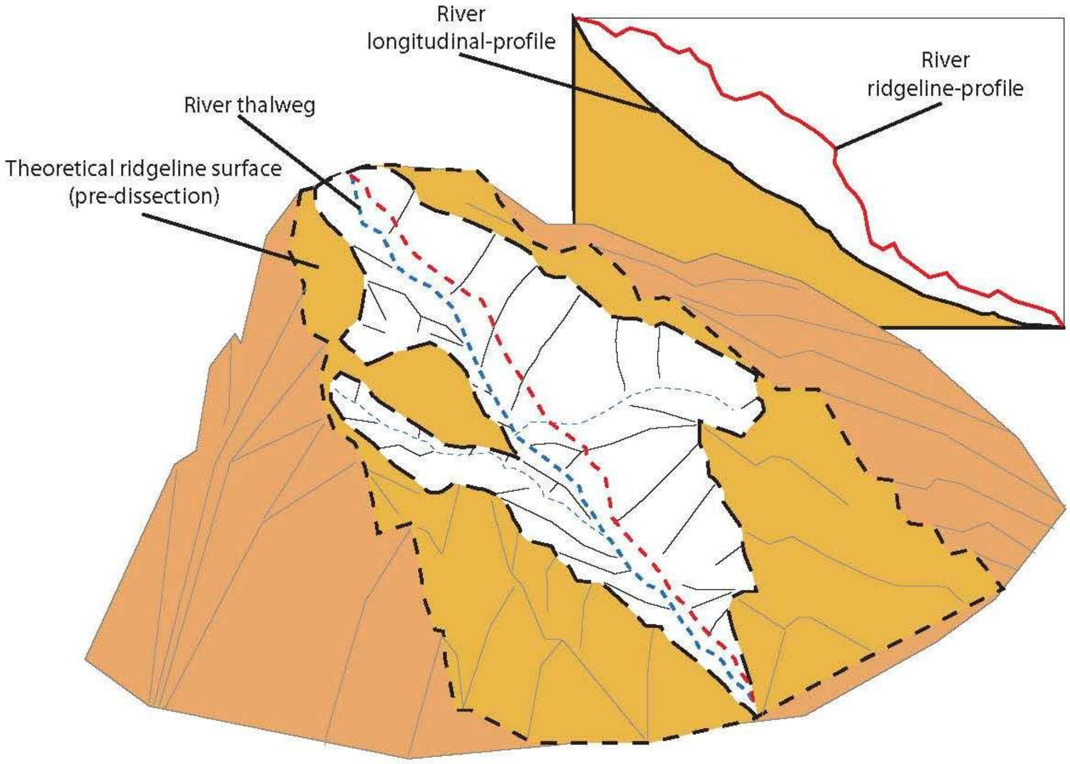

Figure 3.8. Evolution of the drainage basins with time and the correpondant hypsometric curve. (After Pérez-Peña, 2009).

Most of the time is more interesting to evaluate the differences between the present-day surface and the pre-incised surface that its built with the ridgeline surface than observing individual ridgeline profiles. Ridgeline profiles can only offer information of the maximum vertical incision related to the main trunk channels. However, by subtracting pre-incision surfaces from present-day topography it is possible to analyze the erosional pattern and its spatial distribution. This kind of analysis is thought to estimate the "bulk erosion" within the basin (Bellin et al., 2014) since it evaluates the differences between the theoretical pre-incised surface with the present-day elevations. It is noteworthy that this analysis assumes that erosion has to be negligible in basin's ridgelines, and thus the value has to be analyze with care since it can only represent a minimum erosion. Moreover, this value will be biased by basin size, making difficult comparisons between different basins of different sizes. However, despite all the assumptions, the most interesting feature of this analysis is to know the spatial distribution of the erosion within the basin.

Area-slope plots and Ksn index

Graded rivers in detachment-limit systems (bedrock channels) show an exponential relationship between channel slope (S) and up-stream area (A) (Hack, 1957). This well-known relation is described by the power-law:

$$S = k_s A^{-\Theta}$$

where ks is the channel steepness-index and Θ the concavity index (Flint, 1974). This power relation is depicted by most rivers when they reach a critical threshold drainage area in the range of 0.1-5km (Kirby and Whipple, 2001; Wobus et al., 2006). This power-law relation has been used in several tectonic studies, since rivers that are affected by active tectonics, changes in river bed lithology, and/or climate, present different area-slope relations and thus dissimilar ks and Θ (Wobus et al., 2006; Kirby and Whipple, 2012).

One way to determine ks and Θ for a river is to perform regressions in logarithmic slope-area plots (**Fig. 3.9**). Channels under the same factors will yield a linear relation in slope-area logarithmic plot. Moreover, changes within the same river profile will depict different linear relations. These plots constitute very useful tools when analyzing river knickpoints and can be used to differentiate migrating or vertical-steep knickpoints from slope-break knickpoints that separate areas with differential uplift (Whipple et al., 2013; Wobus et al., 2006; Burbank and Anderson, 2013; Kirby and Whipple, 2012). A topographic knickpoint is generated when a stream reach is steepened with respect to adjacent reaches, thus increasing stream power and erosion in it (Gardner, 1983). In logarithmic slope-area plots a vertical-steep knickpoint will appear as an anomalous steepened reach separating reaches with similar trends, i.e. ks (Fig. 4a), whereas slope-breaks knickpoints will be represented by transitional zones separating reaches with different ks (**Fig. 3.9**).Mobile vertical-step knickpoints in transient landscapes form in response to discrete drops in relative base level caused by stream capture, sea-level fall, or a pulse of rock uplift (Snyder et al., 2002; Crosby and Whipple, 2006; Reinhardt et al., 2007; Whipple et al., 2013), whereas anchored vertical-step knickpoints can respond to local changes of riverbed lithology (Whittaker et al., 2007, Whipple et al., 2013). In contrast, slope-breaks knickpoints develop in response to permanent changes in boundary conditions such as an increase or decrease in the rate of relative base-level fall (driven by differences in rock uplift rate) or a change in climate conditions (Bishop et al., 2005; Kirby and Whipple, 2013; Snyder et al, 2003).

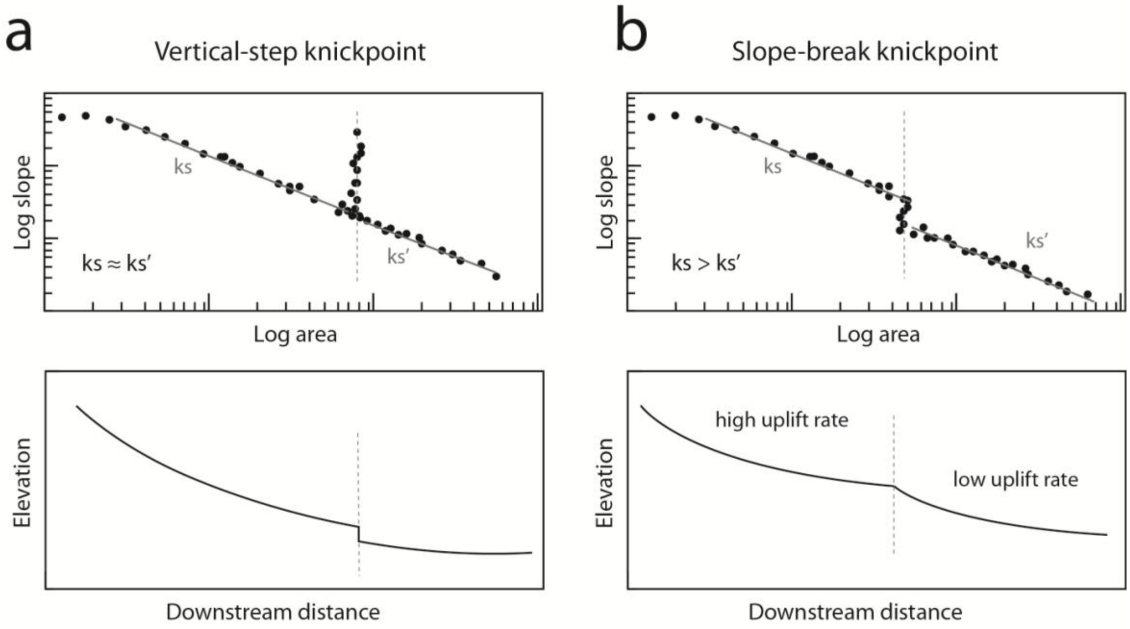

Figure 3.9. Logarithmic area-slope plots and differences between vertical-step and slope-break knickpoints.

Some studies have proposed that concavity index (Θ) varies in most natural channels in a narrow range between 0.4 and 0.6, and it is relatively insensitive to differences in uplift rate, lithology and/or climate at steady-state (Kirby and Whipple, 2012; Whipple et al., 2013). By contrary, steepness index (ks) is highly sensitive to all the mentioned factors.

However, there is a problem when comparing ks values extracted from slope-area logarithmic plots. Small deviations in concavity index cause large deviations in ks, being very difficult to compare river reaches with different concavities. Wobus et al. (2006) proposed the use of a "normalized" steepness index (ksn) that can be calculated for a river reach by using a fixed "reference" concavity. This method allows the comparison of profiles with different parameters and it has been widely used in tectonic geomorphology studies (Wobus et al., 2006; Whipple et al., 2013; Kirby and Whipple, 2012; Bellin et al., 2014; Matos et al., 2014; Scotti et al., 2014).

2.2 Field geology and structural interpretation

One of the main objectives of this Thesis is to attest the Quaternary tectonic activity of the AHS, the SHS and the northern WAF in the Dead Sea area. Prior to the field work, aerial photographs of the study area were analyzed for the initial identification interesting outcrops of faults potentially active. These aerial photos also assisted to pre-validate the 1:50,000 geological sheet maps published by the Natural Resources Authority in Jordan (**Fig. 3.10**). The latter maps are five sheets that cover the study area and they are: Maain (Shawabkeh 1993), Al-Karama (Shawabkeh, 2001), Alsalt (Munaizel and Khalil, 1993), Swaileh (Sawariah and Barjous, 1993) and Amman (Diabat and Abdelghafoor, 2004). Following the compilation of these maps, I made detailed digitization for every single element in order to facilitate the followed modifications on their units in concordant to the field works.

Three field campaigns were conducted in the study area in order to collect structural data and field observations. There were several outcrops with exposed structures and evidences of recent tectonic activity; I surveyed the area collecting structural data and carrying out sketches, photographs and detailed descriptions. The structural data measured in the field were mainly fault-slip information (faults, slickensides, sense of movement and types of lithology). Additionally, I measured more than six hundreds of joints and fractures that presume potential lineaments in the aerial photos and entered in the structural interpretation. The qualitative field data represent the field documentation of active tectonic outcrops where the first clear evidences are presented in this thesis. These outcrops show colluvial wedges with a possible coseismic origin, active slipping along major faults and remarkable landscape changes.

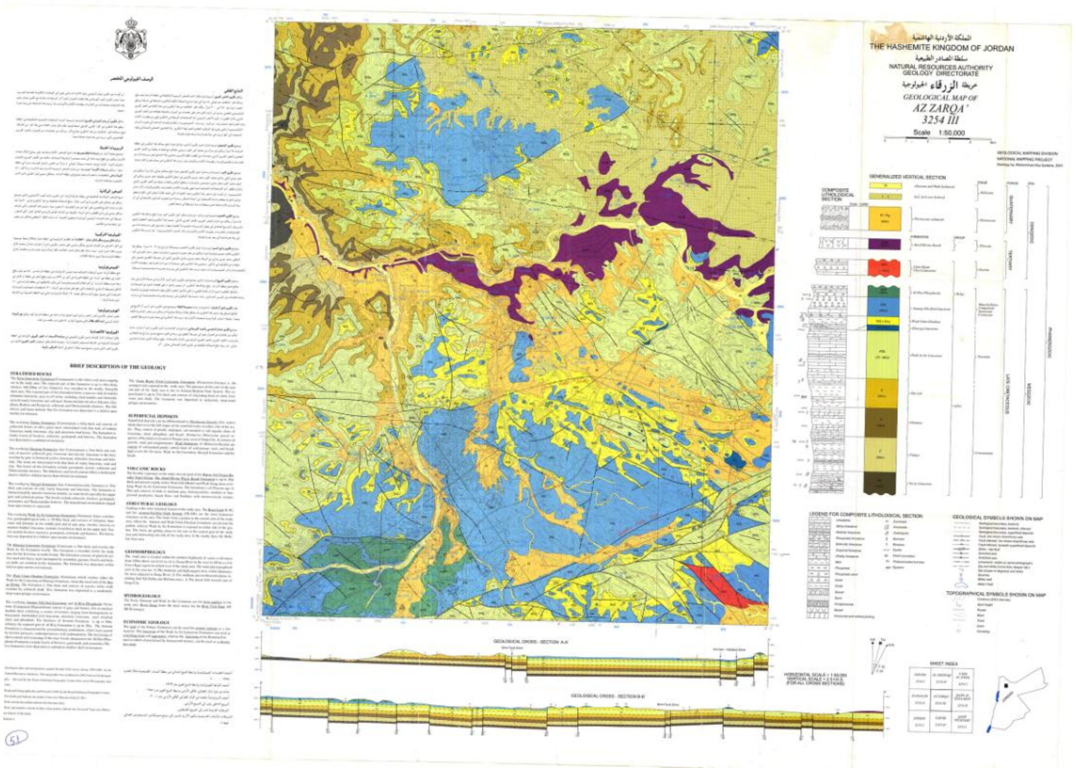

Figure 3.10. Geological map sheet of Zarqua published by the Natural Resources Authority in Jordan. These maps were used as base cartography in this Thesis. These maps were validated in field and the cartography was improved with my field data.

Structural interpretations of these data followed the classical structural geology principles and the surface-shallow active tectonics. I used different models of the fault propagation and stress distribution like Reidel shear models and Anderson models. I used different Digital Elevation Models (DEMs) of 20 and 30 m of resolution to derive hillshade maps for the support mapping work. These DEMs were downloaded from the Advanced Spaceborne Thermal Emission and Reflection Radiometer (ASTER DEM) and Shuttle Radar Topography Mission (SRTM Dem).

2.3 Paleostress analysis

Paleostress analysis uses measurements of micro and meso faults and slickensides collected in measure field station. I used a Frieburg equivalent compass (Krant Geological Structural 360º) which facilitates measuring the dip and strike in one operation by a vertical circle at the lid hinge. To locate the field stations I used a Garmin eTrex Vista HCx GPS with an accuracy of less than 10 m. I focused the field work on the outcrops of the major fault zones where these structures experienced different phases of deformation.

I focused on meso-scale faults because in multi-phased deformations, like in my study, large scale faults often underwent several displacements (Angelier 1994, Hardy et al., 2010). The early slip can be difficult to identify, especially if the fault reactivates under a different stress field and records large offsets, as this new slip overprints the old slickensides of the Cretaceous tectonic frame. Conversely, in small-scale faults, common in the study area, multiple slickensides can be preserved.

There are different methods for stress analysis inversion (Angelier, 1994; Zalohar and Verbac, 2007; Zalohar, 2009; 2012). I performed the analysis by using the "T-TECTO 3.0 Professional" software (Zalohar, 2009) and used the Gauss Method associated with the visualization of P and T dihedra (Zalohar and verbac, 2007).

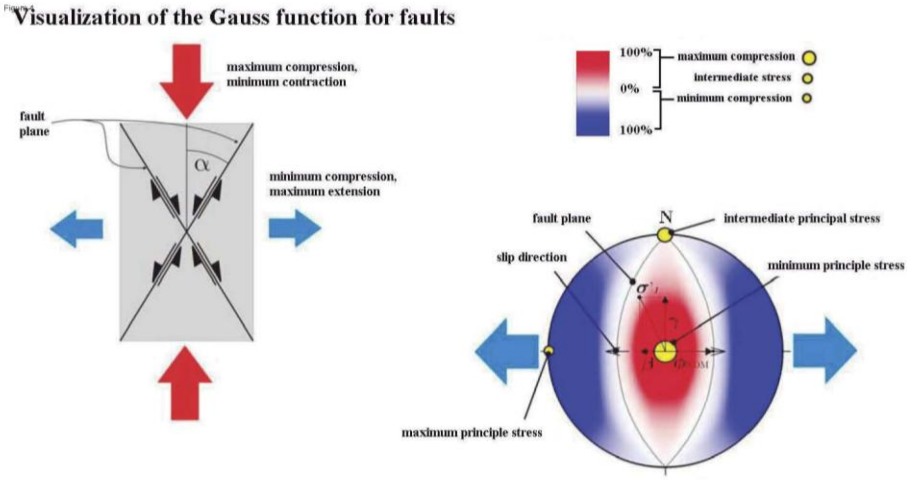

Figure 3.11. Symbology of the stress tensor obtained by the program T-TECTO 3.0.

This method allows analyzing a mixture of various field data (fault plane measurement, joints, open fractures, veins, disjunctive foliation and cleavage). The resulting stress tensor obtained from this method shows the compressive and extension fields of the ellipsoid in red and blue colors respectively. The virtual stress axes of the tensor are shown in red and blue arrows over a lower-hemisphere projection (Fig. 4). The stress-inversion results estimate the orientation of the three principle stresses (σ1, σ2 and σ3); where σ1 is the maximum compressive stress, σ2 is the intermediate compressive stress, and σ3 is the minimum compressive stress. The stress ratio is defined as D = (σ2- σ3) / (σ1- σ3).

Chapter 4

New ArcGIS Add-Ins to extract Normalized and Swath profiles

Preface

This chapter introduces the new ArcGIS add-ins developed through the elaboration of this thesis. The two new ArcGIS Add-ins are developed to automatically extraction of swath and normalized river profiles. Both Add-Ins are easy-windows interface tools and do not need complicated installation.

The test-example of these tools was the rivers and the landscape of the eastern margin of the Dead Sea and the results are included in chapter 4 along with the rest of the landscape analysis.

This chapter is subdivides into six subtitles listed as following:

- **4.1 Evolution of landscape analysis with GIS software and DEMs**
- **4.2 Theoretical background**
  - **4.2.1 Topographic swath profiles**
  - **4.2.2 River normalized profiles**
- **4.3 ArcGIS Add-Ins**
  - **4.3.1 SwathProfiler Add-In**
  - **4.3.2 NProfiler Add-In**
- **4.3 Technical considerations**

4.1 Evolution of landscape analysis with GIS software and DEMs

The present-day great availability of high-resolution Digital Elevation Models (DEMs) has improved tectonic geomorphology analyses in their methodological aspects and geological meaning. Parallel to the evolution of the high-resolution DEMs, advances of software and hardware have increased the demands of using these DEMs as base maps for tectonic geomorphology in the last decades. The tectonic geomorphology has played an important role in the active tectonic studies being a pre-evaluation tool for remote areas to identify potential tectonic activity (Keller and Pinter, 2002).

Most of the pioneering morphometric techniques proposed in the earliest 80s were hard to compute for larger areas and analyses only included small data sets (Mackin, 1948; Hack, 1957; Seeber and Gornitz, 1983; Merrits and Vincent, 1989). However, in the last times there have been significant advances in the scientific discussion over the suitability and meaning of some of these topographic parameters (Keller and Pinter, 2012; Wobus et al., 2006a; Goldrick and Bishop, 2007; Pérez-Peña et al., 2009a; Kirby and Whipple, 2012; Perron y Royden, 2013). This great advance has been supported by two main factors; i) robust and compact GIS software with increasing spatial analysis capabilities, and ii) the great availability of high-resolution Digital Elevation Models. Global DEMs as SRTM and/or ASTER permits analyzing remote areas with a very high geological and tectonic interest that, in turn, allow a better understanding of the active processes operating in such areas (Kirby and Whipple, 2001; Grohmann et al., 2007; Zang et al., 2011).

The applicability of some of the new morphometric techniques depends on available tools and specific software knowledge (Grohmann, 2004). In most cases researchers need to have both; a deep understanding of the geologic and tectonic meaning of the processes they are analyzing and a precise technical knowledge for applying morphometric techniques successfully. The evolution of techniques for landscape analysis has been related to the development of GIS software in both, hardware and software requirements, and to the availability of digital source data. Popular easy-to-use software packages like ArcGIS, QGIS, GvSIG, GRASS, etc., bridge the gap between the technical knowledge requirements and the application of well-known morphometric parameters (Grohmann, 2004; Guth, 2006; Coblentz y Karlstrom, 2011; Queiroz et al., 2015; Daxberger et al., 2014; Pérez-Peña et al., 2009b). These software packages also allow developing specific reusable scripts written with popular programming languages in science as Python, R, Matlab, Visual Basic, Java, etc. These capabilities definitively extent GIS capabilities in Earth Science and specifically in landscape analysis. They allow designing reusable tools that make morphometry a very powerful tool to evaluate how topography is shaped by active tectonics.

Among the different approaches in tectonic geomorphology, topographic patterns and drainage network analyses are the most widely and successfully used (Pérez-Peña et al., 2009a, b, 2010; Kirby and Whipple, 2012; Giaconia et al., 2012; Royden and Perron, 2013; Willet et al., 2014). To analyze the topographic patterns, earth scientists commonly elaborate topographic swath profiles to recognize general elements on the landscape that may be associated with the tectonic activity (e.g. Molin et al., 2004; 2012; Andreani et al. 2014; Scotti et al., 2014; Azañon et al., 2015). On the other hand, rivers are continuously adapting their profiles to climatic, lithological and tectonic conditions. Therefore, changes in these profiles will reflect variations in these controlling factors (Rigon et al., 1996; Jackson et al., 1996; Brookfield, 1998; Pérez-Peña et al., 2009a, 2010; Kirby and Whipple, 2012; Giaconia et al., 2012). In this regard, the comparison of normalized longitudinal profiles of rivers can highlights gradient differences related to the mentioned external conditions. Analyses based on topographic profiles have revealed being valuables to explore the short and long-term landscape response to tectonic activity and climate changes. The swath and the river longitudinal profiles are two of the most used analysis to explore the long and short term landscape responses.

4.2 Theoretical background

One of the best approximations to analyze the landscape is through longitudinal profiles. Topographic longitudinal profiles and river longitudinal profiles are two ways of analyzing the landscape response to driving internal and external forces and they have been widely used in tectonic geomorphology studies (Molin et al., 2004; Kirby and Whipple, 2012; Scotti et al., 2014; Azañon et al., 2015). Topographic profiles depict long-term landscape equilibrium, whereas river longitudinal profiles represent the short-term response of the landscape to the tectonic, lithologic and climatic changes. In other words, the river longitudinal profiles are an approximation for the recent to present-day response to the geological and active process and climatological variations, whilst swath profiles examine the long-term landscape state in response to these processes.

4.2.1 Topographic swath profiles

Topographic swath profiles are constructed by projecting equally spaced topographic profiles within a strip or swath (Baulig, 1926; Tricart and Cailleux, 1958; d’Agostino et al., 2001; Fielding, 1996). This kind of profiles provide a general view of the topographic pattern of a region and have been used widely to characterize regional-scale topography (d’Agostino et al., 2001; Riquelme et al., 2003; Grohmann, 2005; Molin et al., 2004; 2012; Scotti et al., 2014; Azañon et al., 2015).

Linear swath profiles can be constructed straightforward, but when the concept is expanded to non-linear profiles as mountain fronts or river valleys they can be subjected to systematic bias (Telbisz et al., 2013; Hergarten et al., 2014). There are several ways to sample elevation points for curvilinear profiles. Telbisz et al. (2013) proposed the stack of elevation values along non-parallel lines normal to the curved baseline. This method present some problems as indicated by Hergarten et al. (2014); i) the baseline has to be smoothed since the orientation of normal lines will be very sensitive to small-scale roughness of this baseline and ii) a single cell could contribute to more than one normal lines. On the other hand, Hergarten et al. (2014) proposed a different way to construct curved swath profiles by stacking elevations using all the cells of the DEM and calculating signed (or oriented) distances to the baseline. This method needs an intensive computational effort, since all the cells of the DEM have to be iterated in varying directions. In this work we used a different approach that maximize the performance and calculation time by using the capabilities of ESRI's built-in ArcObjects methods and classes. Our implementation calculates lines parallel to the base line and sample them with different step sizes depending of their lengths and considering as a reference the selected step size of the base line. In this way, all the parallel lines are sampled by the same number of points, and profile transverse metrics as quartile or mean are calculated with the same sample size throughout the swath profile (**Fig. 4.1**).

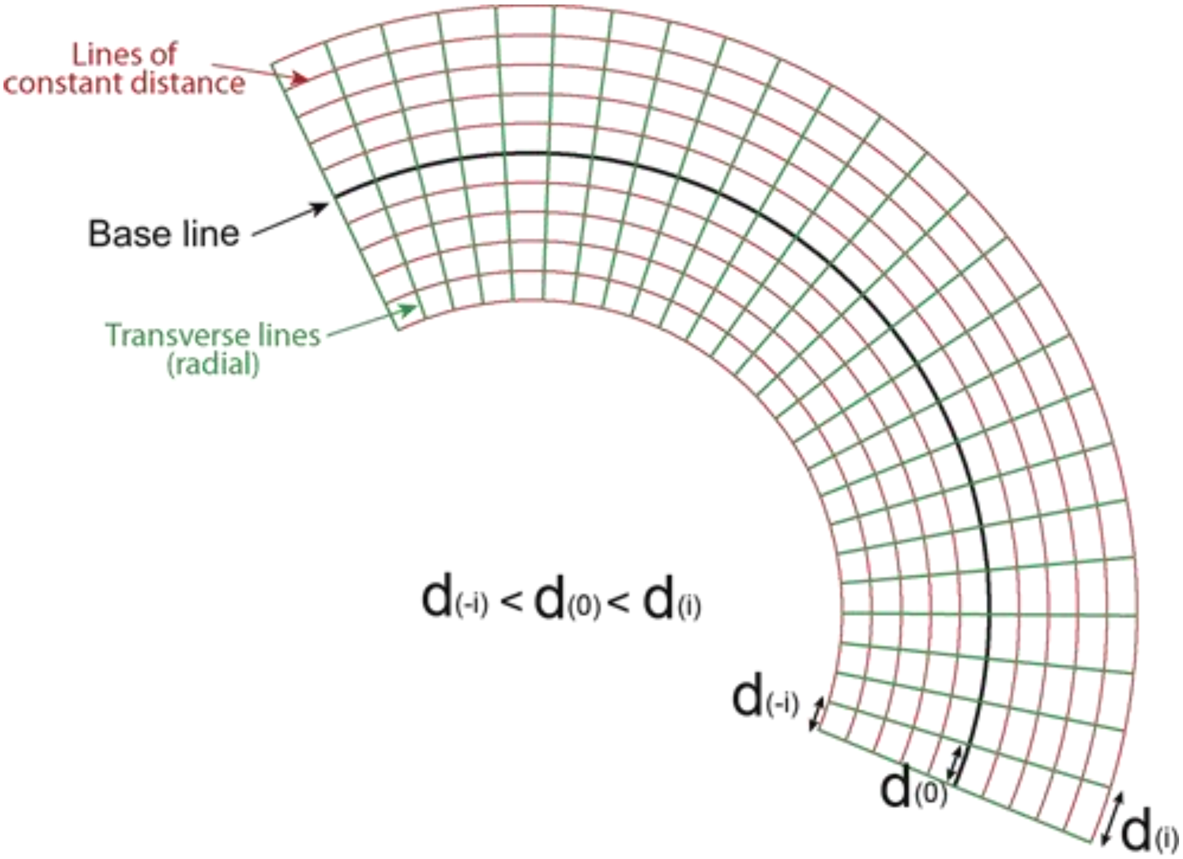

Figure 4.1. Construction of a curved swath profile. The default step-size (d0) is determined for the base line and re-calculated for all the parallel lines (red lines) to ensure that each line is sampled by the same number of points. Note that transverse lines (green lines) do not need to be perpendicular to the base line.

Swath profiles can be examined statistically to extract maximum, minimum and mean topographic elevation for each transect. Mean elevation is a good approximation to the general topographic trend of the landscape within the swath profile band, whereas maximum and minimum elevation can inform of landscape variations in the direction perpendicular to the swath profile. Moreover, other parameters as local relief (maximum elevation - minimum elevation) or quartile (Q1 - Q3) can also describe topographic variations along the swath. Generally, stable areas as basins or plateaus with low-to-moderate incision will yield low values of local relief and swath profiles where all lines will merge together. Conversely, high local relief and wider variations of swath profiles will be characteristics of mountain ranges or highly dissected landscapes exposed to high incision and/or uplifting.

Additionally to local relief, the relations between mean elevation respect to maximum and minimum elevation can reveal important information about the landscape state (Keller and Pinter, 2012; Wobus et al., 2006b). For a typical swath profile in most landscapes the mean elevation will lie closer to the minimum than to the maximum If the mean elevation approaches the maximum, this upward deflection could indicate a transient state of adjustment to higher uplift rates (Keller and Pinter, 2012; Wobus et al., 2006b). These deviations can be studied by examining the hypsometric integral (HI) for all the transects (Pike and Wilson, 1971).

$$HI = \frac{Hmean\ - Hmin}{Hmax - Hmin}$$

Values of HI near to 1 indicate that mean elevations are close to maximum elevations, thus depicting a young transient landscape; on the contrary, HI values near to 0 would indicate a mature landscape with mean elevations close to the minimum. However, the direct calculation of HI in swath transects can present some problems. In transects with low relief, i.e. plain areas, max, min and mean elevation will be very close and small variations in mean elevation can produce large differences in HI values (see P1 and P2 in **Fig. 4.2**). To avoid these artifacts we propose the use of a transverse hypsometric integral (THi), in which HI values will be weighted by the relative local relief (RRL).

$$THi = (HI - 0.5)w_i + 0.5$$

Since the use of a direct linear normalization will produce big differences in swath transects with different local relief, we used a logarithmic normalization (**Fig. 4.2**). In this normalization the weight for transects with very low relief is larger, whereas the weights for transects with middle-low to high local relief yield lower differences (see P3 and P4 in **Fig. 4.2**).

$$w_i = 0.2\ ln(\text{RLR}) + 0.1$$

$$Relative\ local\ relief\ (RLR) = \frac{LR_i}{LR_{max}}$$

In most natural landscape, hypsometric integral values under 0.2 or over 0.8 are extremely rare (Pérez-Peña et al., 2009c). Therefore, we can improve the description and comparison of hypsometry along a swath profile by re-scaling HI values between

0.2 and 0.8. We have called this latter index as enhanced transverse hypsometry index (THi*) and is defined as:

$$HI^* = \frac{(HI - 0.2)}{0.8 - 0.2}$$

$$THi^* = (HI^* - 0.5)w_i + 0.5$$

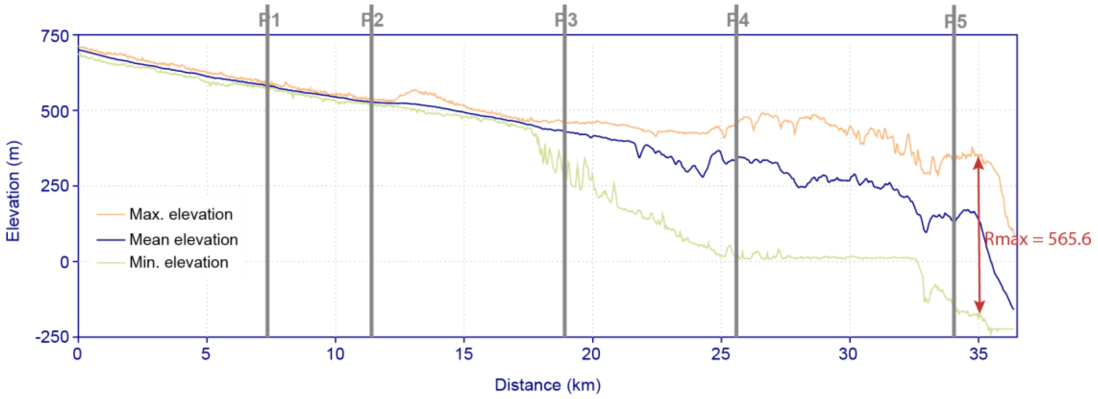

	P1	P2	P3	P4	P5
Max. elev	589	550	475	450	350
Mean elev	587	543	445	330	120
Min elev	580	543	325	10	-160
Relief	9	9	150	440	510
HI	0.78	0.22	0.80	0.73	0.55
THi	0.55	0.45	0.72	0.72	0.55
THi*	0.58	0.42	0.87	0.86	0.58

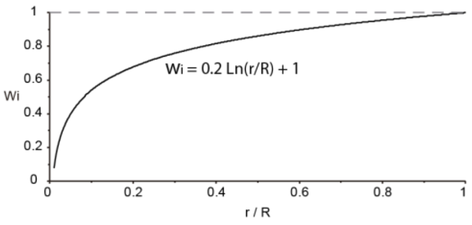

Figure 4.2. Relationships between relief (max. - min. elevation) and hypsometry in swath profiles. The points P1 and P2 present very different hypsometric integral (HI) values due to small variation in mean elevation in transect with very low relief. The proposed Transverse Hypsometric Integral (THi) uses a weight factor (w_i) that takes the logarithmic curve of the relative relief (r/R) to correct anomalous hypsometric variations. This normalization makes the swath sectors with very low relief approach to 0.5 (points P1 and P2), whereas barely modify transects with moderate to low relative relief (points P3, P4 and P5). The enhanced transverse Hypsometric Integral (THi) highlights hypsometric variations by re-scaling HI between 0.2 and 0.8 (see text for further explanation).*

4.2.2 River normalized profiles

Rivers in equilibrium condition flowing over homogeneous lithology develop a typical concave-shaped profile, with higher gradients in source areas and smoother gradients near their mouths. This concave-shape profile is the consequence of the inverse relation between discharge (that can be approximated by upstream area) and gradient (that can be approximate by channel slope). In graded rivers slope is progressively adjusted to provide, with available discharge and the prevailing channel characteristics, just the velocity required for transportation of all the load (Mackin, 1948). Deviation of this equilibrium or graded-profile will develop inflection point in the profile known as knickpoints (Whipple and Tucker, 1999; Burbank and Anderson, 2013) and will produce changes in the concavity of the longitudinal profile up and down-stream. The analysis of river longitudinal profiles has been used intensively to detect changes in river controlling factors; namely lithology, climate and tectonic uplift and hillslope processes (Seeber and Gornitz, 1983; Brookfield 1998; Pérez-Peña et al., 2009a; Kirby and Whipple, 2012; Giaconia et al., 2012; Anton et al., 2014; Troiani et al., 2014). However, the comparison of longitudinal profiles from rivers with different lengths and gradients can be intricate.

Demoulin (1998) proposed the representation of river longitudinal profiles in a normalized form. This form is known as the normalized longitudinal profile and it is constructed by normalizing elevations with respect to the relative elevation or amplitude and distances respect to the total channel length. This representation allow comparing rivers with different lengths and gradients (Demoulin, 1998; Ruszkiczay-Rüdiger et al., 2009; Matos et al., 2014). Moreover, this normalized representation highlights gradient variations as clear as semi-logarithmic profiles (Hack, 1957; Demoulin, 1998).

In this kind of profiles concavity (C_T) is defined as the percent area of the OAB triangle (Fig. 4) between the river profile and the straight line connecting source to mouth. Negative values of C_T will represent concave-up profiles where the river profile stands over the straight line AB whereas whereas positive values will indicate river convexity. Rectilinear river profiles will be characterized by C_T ~0 (Fig. 4). As river concavity is calculated as an integral, in each point of the profile we can define a local concavity (Ci) as the distance from the profile to the straight-line AB. Following this assumption we can define for each river a point of maximum concavity (C_{max}). This value will be redundant with river concavity (C_T), but its position respect to river source (L_{max}) can add very interesting information (**Fig. 4.3**). Theoretically the lower the L_{max}, the better graded the profile (Demoulin, 1998).

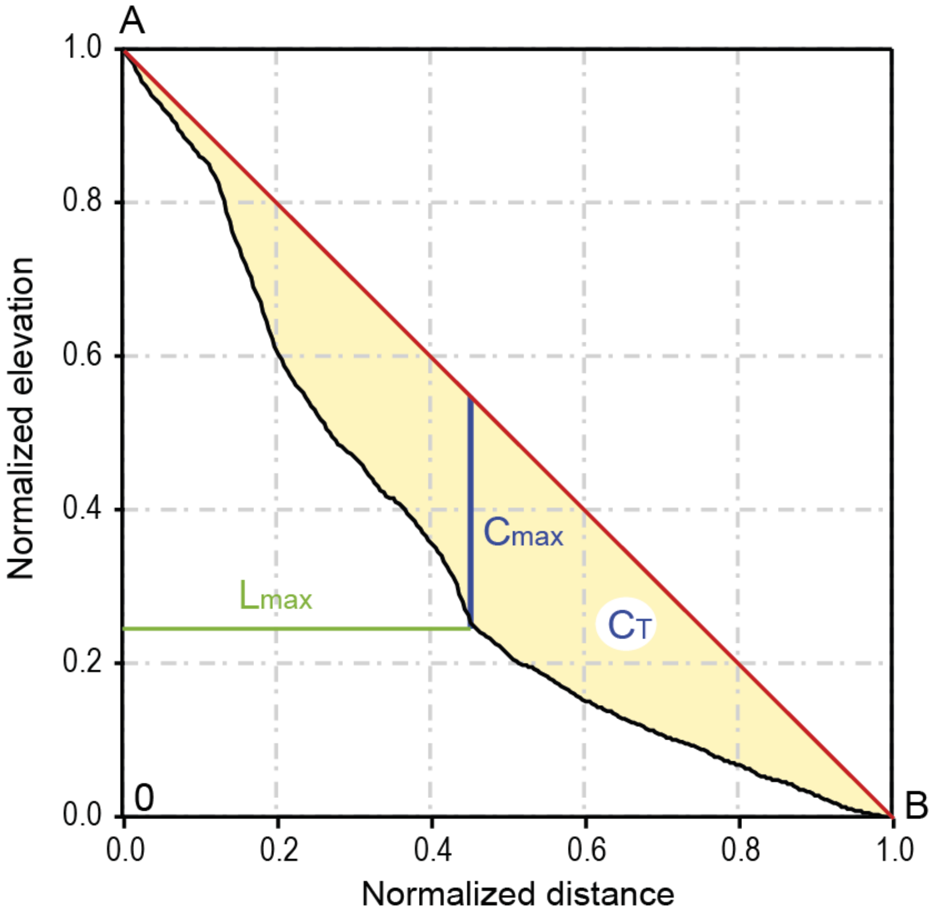

Figure 4.3. Normalized profile and associated parameters. A: Headwater, B: mouth, C_T *Concavity (expressed as a percentage respect to the AOB triangle),* C_{max}*: maximum concavity,* L_{max}*: position of the maximum concavity respect to river headwater. See text for further explanation.*

Castillo et al. (2013) suggested that this type of representation is more adequate for rivers in a transient-state with irregular profiles, in which traditional area-slope relations would be not valid. In their study, they demonstrated that the concavity index (ϴ) provided a useful measure of the morphology of transient reaches.

4.3 ArcGIS Add-Ins

The two Add-Ins have been desgined to automatically generate swath and normalized river profiles as complements for the ArcGIS v.10.x software package from ESRI. The two complements are programmed in Visual Basic.NET and they have been integrated as two separate Add-Ins for the ArcMap sofware (**Figs. 4.4 and 4.5**). Visual Basic.NET uses Microsoft .NET Framework that includes not only a complete object collection and powerful libraries, but also a rich graphic user interface (GUI) as windows, control boxes, menus, graphics charts, etc. This makes possible to design full software suites that can extend their functionalities beyond scripting tools designed with Model builder or Python. These applications can use ArcObjects COM libraries that are considered as the elemental software “building blocks” of ArcGIS. Accessing to the ArcObjects imply a higher complexity in the code than other scripting languages as Python or Model Builder. However, it allows more liberty to design and write analysis algorithms because; i) it is not limited to the use of built-in analysis tools (Toolboxes) and ii) it grants a direct access to geometries (vector and raster) by using ArcObjects methods and functions from the internal architecture of ArcGIS.

4.3.1 SwathProfiler Add-In

The SwathProfiler Add-In (**Fig. 4.4**) generate swath profiles and related metrics for vectorial features using a DEM as source for the topographic elevation. The input-box (**Fig. 4.4a**) allow selecting the input data and the width of the swath profile, considering input polyline features (linear or curved) as base lines. For each polyline a swath profile with 50 parallel lines (25 on each side of the baseline) is calculated by taking a sampling step-size of 1.5 times the cell size of the DEM in the baseline. This step-size is re-calculated for each parallel line ensuring that all parallel lines are sampled with the same number of points. The user can modify these values in the input box (**Fig. 4.4a**).

The display window (**Fig. 4.4b**) draws the swath profiles for the input polylines that can be selected by using the selection box. This window shows the profiles for all the parallel lines, as well as the maximum, minimum and mean profiles. It also calculates the first and third quartile and the local relief (max. elev. - min. elev.).

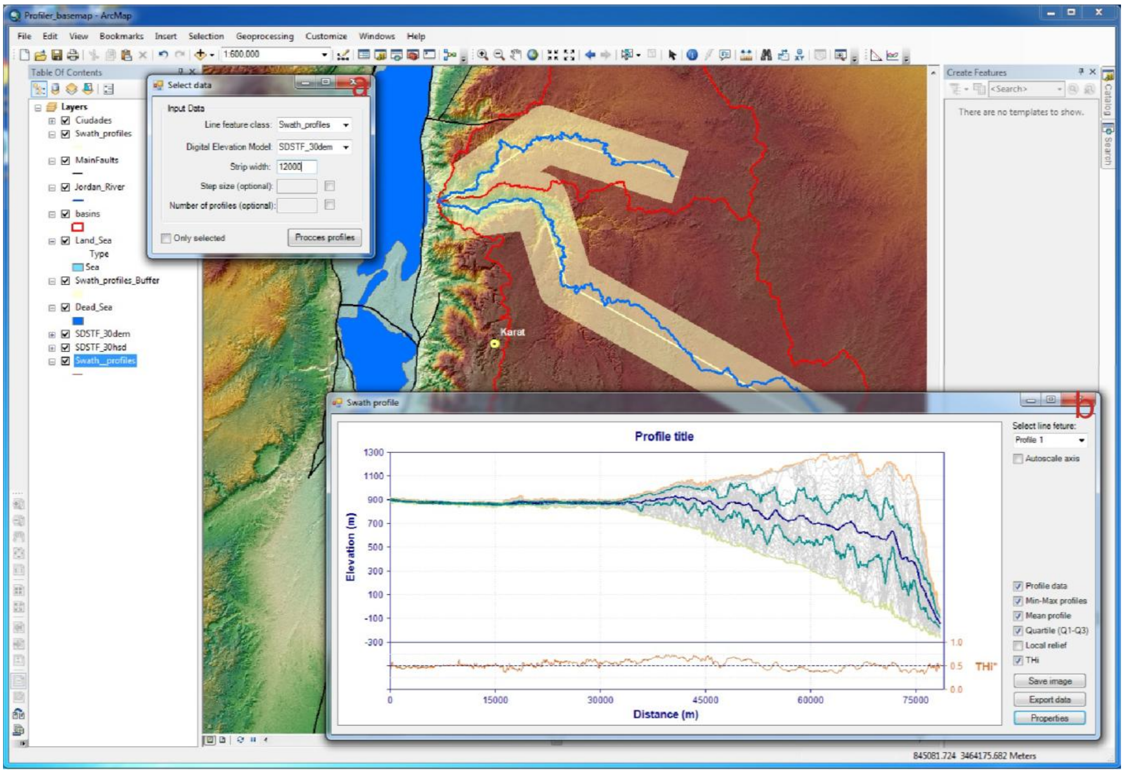

Select data

Input Data

Line feature class: Swath_profiles

Digital Elevation Model: SDSTF_30dem

Strip width: 12000

Step size (optional): ☐

Number of profiles (optional): ☐

☐ Only selected

Swath profile

Select line feture: Profile 1

☐ Autoscale axis

☑ Profile data

☑ Min-Max profiles

☑ Mean profile

☑ Quartile (Q1-Q3)

☐ Local relief

☑ THi

Figure 4.4. SwathProfiler Add-In within the ArcMap environment. The input window (a) allows the user to select the profile feature class (polyline), the elevation source (digital elevation model) and the swath parameters. The output window (b) draws all the swaths and allow selecting different kinds of visualizations as well as export data and save image files.

The transverse hypsometric integral (THi) is calculated following the methodological approach described in the previous section and can be added to the bottom part of the display window. In the properties form, the user can modify the colors and widths of the lines, modify chart properties and select to display the enhanced transverse hypsometric integral (THi*) instead of the THi. The program also allows exporting the chart to image files (raster and vector formats) and export individual values to text.

4.3.2 NProfiler Add-In

The NProfiler Add-In (**Fig. 4.5**) has been generated as an independent ArcMap Add-In to extract normalized profiles and related indexes. It takes as input data linear feature classes and a DEM for elevation source. Profile elevations are calculated by bilinear interpolation of the 4 nearest cells of the DEM, smoothing possible errors in individual cells. The river longitudinal profile is normalized to show The tool also allows removing "peaks" (points with higher elevation that the upstream points due to DEM errors) and smoothing the profile. The smoothing method uses a moving-window average that takes the percentage of the profile points specified as a smoothing factor. This smoothing can be especially useful for lower-resolution data sources.

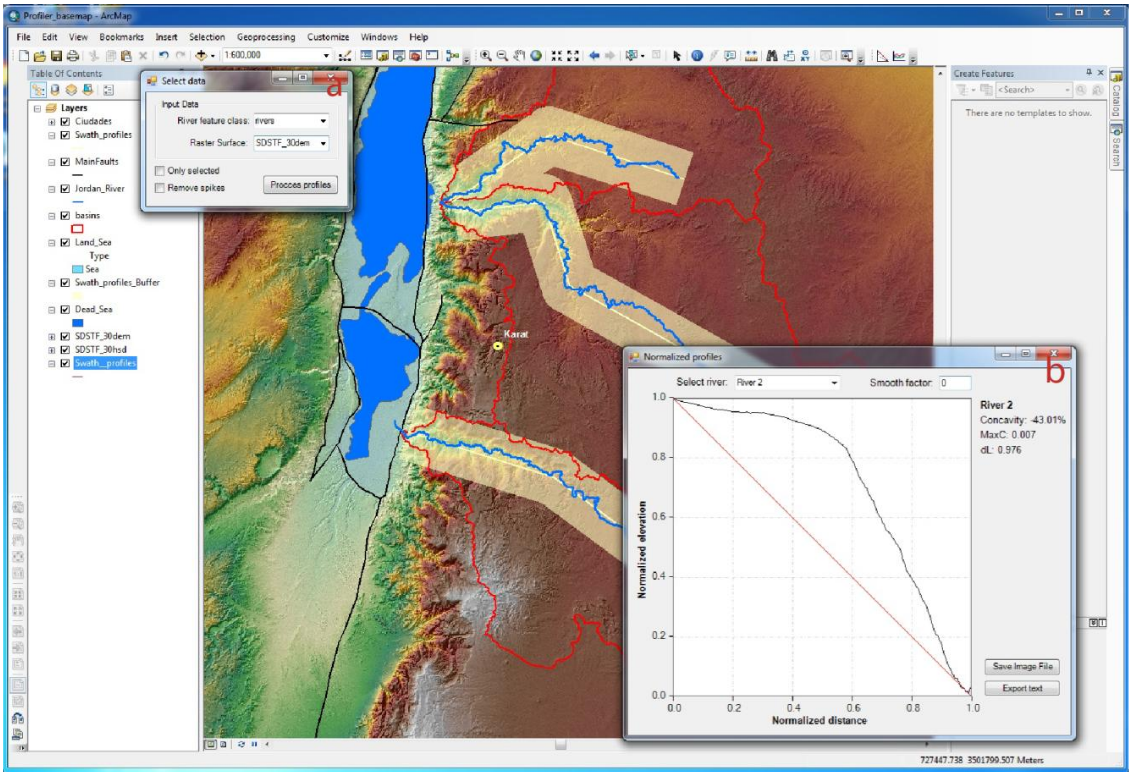

Select data

Input Data

River feature class: rivers

Raster Surface: SDSTF_30dem

☐ Only selected

☐ Remove spikes

Normalized profiles

Select river: River 2

Smooth factor: 0

River 2

Concavity: -43.01%

MaxC: 0.007

dL: 0.976

Figure 4.5. NProfiler Add-In within the ArcMap environment. The input window (a) allows the user to select the river feature class (polyline) and the elevation source (digital elevation model). The output window (b) draws all the normalized profiles and associated parameters (C_T, L_{max} and C_{max}) and allow saving image files.

The NProfiler Add-In also extracts C_T, C_{max} and L_{max} (see theoretical background section for further explanation). The graphic window visualizes the profile of the selected river and its related morphometric parameters (Fig. 5) and allow saving as image or vector format.

4.3 Technical considerations

The SwathProfiler and NProfiler Add-Ins are useful complements for the software package ArcGIS 10 to carry out advanced landscape analyses. These tools produce topographic swath profiles and normalized longitudinal river profiles in a simple, efficient and quick way. Swath profiles help in the interpretation of the regional topographic patterns and normalized river profiles allow comparing gradient variations of different rivers that may be controlled by climatic, lithological and/or tectonic factors. Therefore, the presented tools can streamline the DEM analysis workflow and allow focusing the efforts of the researchers on the geologic and tectonic interpretation of the results.

Chapter 5

Landscape analysis

Preface

In this chapter I present the landscape analysis of the study area through the application of several geomorphic indexes. I focused the study in the eastern margin of the Dead Sea, with the intention of analyzing the effects that the Quaternary activity of the Dead Sea Transform Fault (DSTF) produces in the landscape and in the drainage network.

The landscape analysis made in this PhD Thesis has two differentiated parts. First I analyzed the general landscape pattern through the application of spatial-based geomorphic indices as the slope, surface roughness, hypsometry and topographic swath profiles. With this analysis I aimed to describe and evaluate the general stage of landscape evolution in the study area, and examine the links between the tectonic structures and the general topographic patterns. In the second part of the analysis, I examined thoughtfully the drainage network of the eastern margin of the Dead Sea by applying several well-known geomorphic indexes in order to detect different pattern and highlight differences that could be due to dissimilar tectonic activity along the study area.

This chapter includes the following subtitles:

5.1 Analysis of the general landscape pattern

5.1.1. Geographic and topographic description of the study area

5.1.2. Surface roughness

5.1.3. Topographic Swath profiles

5.1.4. Spatial analysis of hypsometric integral

5.2 Drainage network analysis through geomorphic indexes

5.2.1. Normalized profiles

5.2.2. Hypsometric curves

5.2.3. Bulk erosion

5.2.4. Area-Slope relationships (Ksn index)

5.1 Analysis of the general landscape pattern

5.1.1. Geographic and topographic description of the study area

The study area selected for the landscape analysis centers in the Dead Sea region and includes approximately 50 km north and south to the Dead Sea present-day lake. From a topographic point of view, the area is characterized by the Trans-Jordanian Plateau (TJP) in the eastern side (mean elevation of ~900 m), the Dead Sea valley in the central part (at 427 m below sea level), and the Jerusalem Mountains in the west (with a mean elevation of 800-900 m) (**Fig. 5.1a**). This topographic configuration produces a high topographic gradient of 1300 m that, in turn, yields steep slopes and incised valleys located preferably along the eastern flank of the Dead Sea.

The Trans-Jordanian plateau, also known as Jordanian Highlands, separates the Jordan Valley and Dead Sea from the plains of the eastern deserts (Syrian and north Arabian deserts). It has an average elevation of 900 meters, although occasional summits that can reach 1200 m in the northern part and up to 1700 in the southern part (**Fig. 5.1a**). This region extends the whole length of the western part of Jordan, and hosts most of Jordan’s main populated areas, including Amman, Zarqa, Irbid and Karak. It has been populated in ancient times, as it is proved by the ruins of Jerash, Karak, Madaba, Petra and other historical sites. This area receives Jordan’s highest rainfall, and is the most richly vegetated in the country. The western edge of this plateau forms an escarpment along the eastern side of the Jordan Valley-Dead Sea depression and its continuation south of the Dead Sea. Most of the streams that drain this plateau are of a torrential nature carrying water only during the short season of winter rains. This E-W drainage network is characterized by incised valleys with deep canyons and presents the highest slopes in the study area (**Fig. 5.1b**).

The Jordan Valley is formed by the lower course of the Jordan River, which extends from the Sea of Galiee (212 meters below sea level) to the Dead Sea, the lowest point in the world at 427 meters below sea level. It constitute the western politician border of Jordan. The Jordan river valley has a variable width; from 5-6 km in its upper part near the Sea of Galilee, up to 17km where it flows into the Dead Sea. The Dead Sea is a landlocked lake fed by the Jordan river and run-off from side wadis. The internal sea is saturated with salt and minerals due to the intense evaporation and its absence of a sea outlet (salt concentration in the Dead Sea is eight times higher than the sea water). South of the Dead Sea, the dry Wadi Araba valley continues southwards along 155 kilometers, from the Dead Sea to the Gulf of Aqaba. Its eastern boundary is defined by the Wadi Araba Fault (WAF).

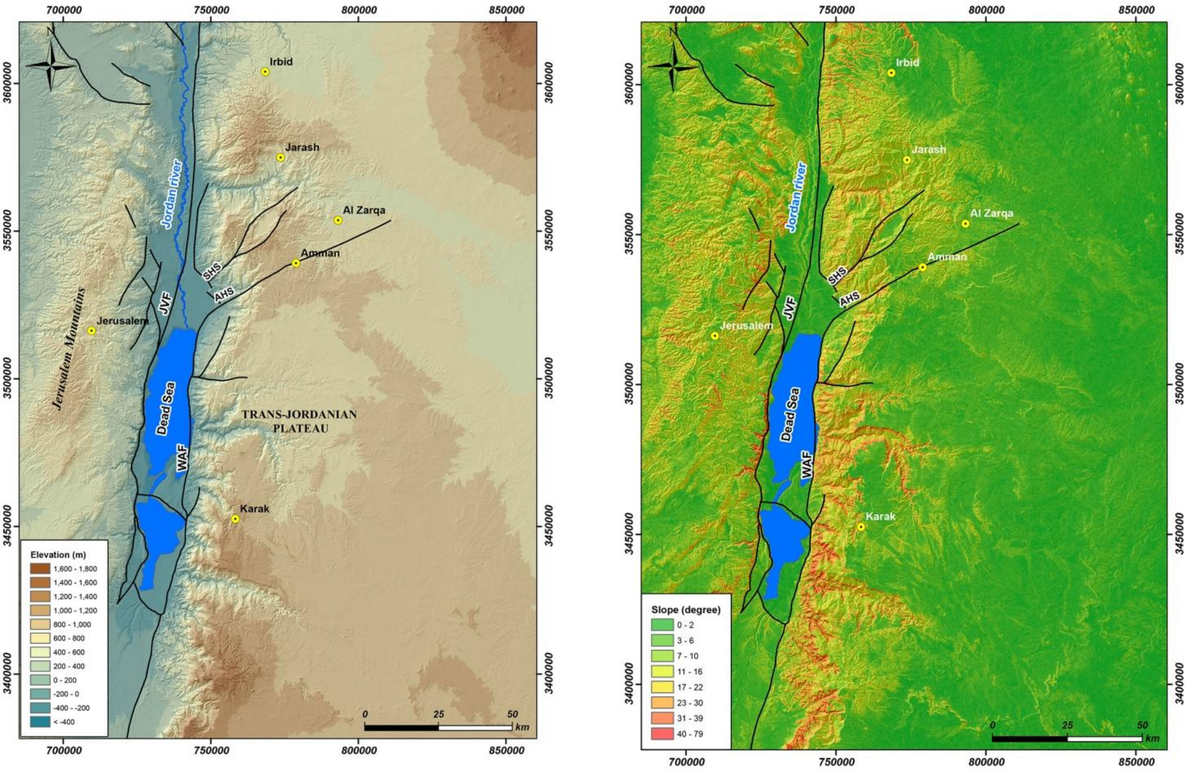

Figure 5.1. A) Digital Elevation Model of 30m showing the elevation distribution and the main topographic features of the study area. B) Slope map (degrees) obtained from the DEM. Note that high slopes concentrates between the Trans-Jordanian Plateau and the Dead Sea - Jordan Valley, being highest in the middle-to-south part of the eastern margin of the Dead Sea lake.

The eastern part of the area is defined by the Jerusalem Mountains (also known as Judaean Mountains). This mountain range runs north to south and includes Jerusalem, Hebron, Bethlehem and Ramallah, reaching elevations of 1000 meters. This area is out of the scope of this Thesis, and will not be discussed in this volume.

The Dead Sea has experienced a continuous subsidence in Pleistocene times, thus promoting the formation of an erosion wave that advanced eastwards from the Dead Sea depression into the TJP. This erosion wave is drawn in slope map as high values located preferably in the escarpment between the Dead Sea and the TJP. Noteworthy is that slope do not distribute homogeneous all along this escarpment, being higher in the south (**Fig. 5.1b**).

5.1.2. Surface roughness

Surface roughness measures the topographic fabric, i.e. the degree of variation of the landscape. This parameter is not a fully quantitative measure that can be defined in a unique and unequivocal way, and there are several methodologies to compute it (Smith, 2014). It is difficult to express surface roughness with absolute values, since it will depend on scale and local topographic pattern. However, it is possible to compare zones with high or low roughness in a qualitative or semi-quantitative way. Absolute values will not be as important as the overall distribution and group patterns.

The method selected in this Thesis to compute the surface roughness considers the combined variation of slope and aspect but not their absolute values. This means that surface roughness will not completely correlate to landscape dissection or erosion, but with drainage density and topographic fabric. Lower values of roughness will correspond to plain or homogeneous areas, whereas higher values will be characteristic of escarpments (independently of their total elevation) and areas with high drainage density, where variations in aspect and slope are expected.

Other important consideration when calculating surface roughness should be pay to the scale (Sanchez-Serrano, 2000). The variation of cell size and neighborhood will be a determinant factor in order to compare slope and aspect values. Since the selected method takes the variation of slope and aspect and not their absolute values, the nature of the DEM has to be taken into account. DEMs obtained by radargrammetry, as the one used in this Thesis, normally present a high frequency ‘noise’ that is characteristic of radar-derived elevation data. This noise can contribute to increase the roughness and introduce noise in the analysis. The DEM cell size it is also a critical variable that will affect the overall results. Since the objective of this analysis is the semi-quantitative comparison different regions, the original 30m resolution is too small. This cell-size will capture high-frequency noise from small-amplitude features, including the inherent DEM 'noise' discussed previously. In order to improve the results and obtain a more representative surface roughness for the whole study area, I first resample the input DEM in 120m resolution cells by averaging elevation values. Once the DEM was re-sampled I computed the surface roughness by using a rectangular neighborhood of 8 cells (i.e. 960 m). For the computation of the roughness I created an ArcGIS python script that made easier the subsequent rotations and neighborhood statistics computations required for this analysis (**Fig. 5.2**). Since the absolute values of roughness do not have a clear quantitative meaning, the resulting map was divided in 256 classes (8 bit). This final classification allows comparing in a clearer way different areas.

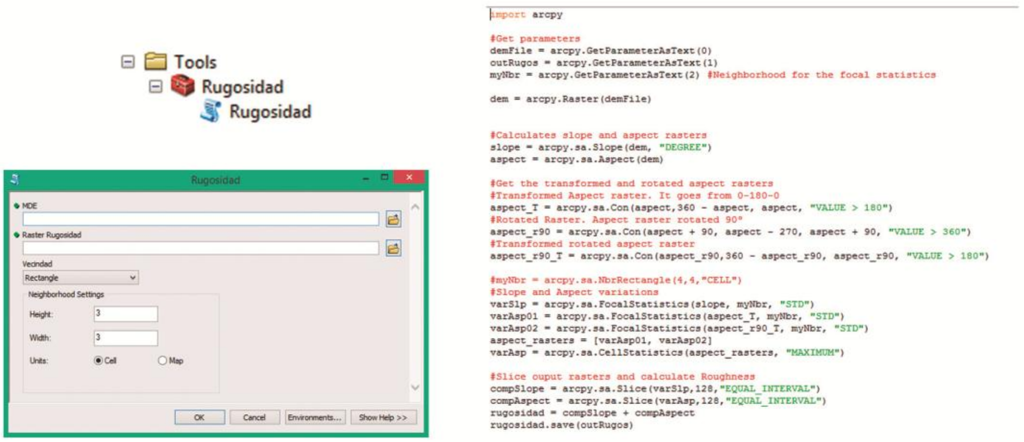

MDE

Raster Rugosidad

Vecindad: Rectangle

Neighborhood Settings

Height: 3

Width: 3

Units: ● Cell ○ Map

```
import arcpy

#Get parameters
demFile = arcpy.GetParameterAsText(0)
outRugos = arcpy.GetParameterAsText(1)
myNbr = arcpy.GetParameterAsText(2) #Neighborhood for the focal statistics

dem = arcpy.Raster(demFile)


#Calculates slope and aspect rasters
slope = arcpy.sa.Slope(dem, "DEGREE")
aspect = arcpy.sa.Aspect(dem)

#Get the transformed and rotated aspect rasters
#Transformed Aspect raster. It goes from 0-180-0
aspect_T = arcpy.sa.Con(aspect,360 - aspect, aspect, "VALUE > 180")
#Rotated Raster. Aspect raster rotated 90°
aspect_r90 = arcpy.sa.Con(aspect + 90, aspect - 270, aspect + 90, "VALUE > 360")
#Transformed rotated aspect raster
aspect_r90_T = arcpy.sa.Con(aspect_r90,360 - aspect_r90, aspect_r90, "VALUE > 180")

#myNbr = arcpy.sa.NbrRectangle(4,4,"CELL")
#Slope and Aspect variations
varSlp = arcpy.sa.FocalStatistics(slope, myNbr, "STD")
varAsp01 = arcpy.sa.FocalStatistics(aspect_T, myNbr, "STD")
varAsp02 = arcpy.sa.FocalStatistics(aspect_r90_T, myNbr, "STD")
aspect_rasters = [varAsp01, varAsp02]
varAsp = arcpy.sa.CellStatistics(aspect_rasters, "MAXIMUM")

#Slice ouput rasters and calculate Roughness
compSlope = arcpy.sa.Slice(varSlp,128,"EQUAL_INTERVAL")
compAspect = arcpy.sa.Slice(varAsp,128,"EQUAL_INTERVAL")
rugosidad = compSlope + compAspect
rugosidad.save(outRugos)
```

Figure 5.2. Python script created to compute surface roughness in ArcGIS. The script has been integrated in a toolbox and allow specifying the analysis neighborhood.

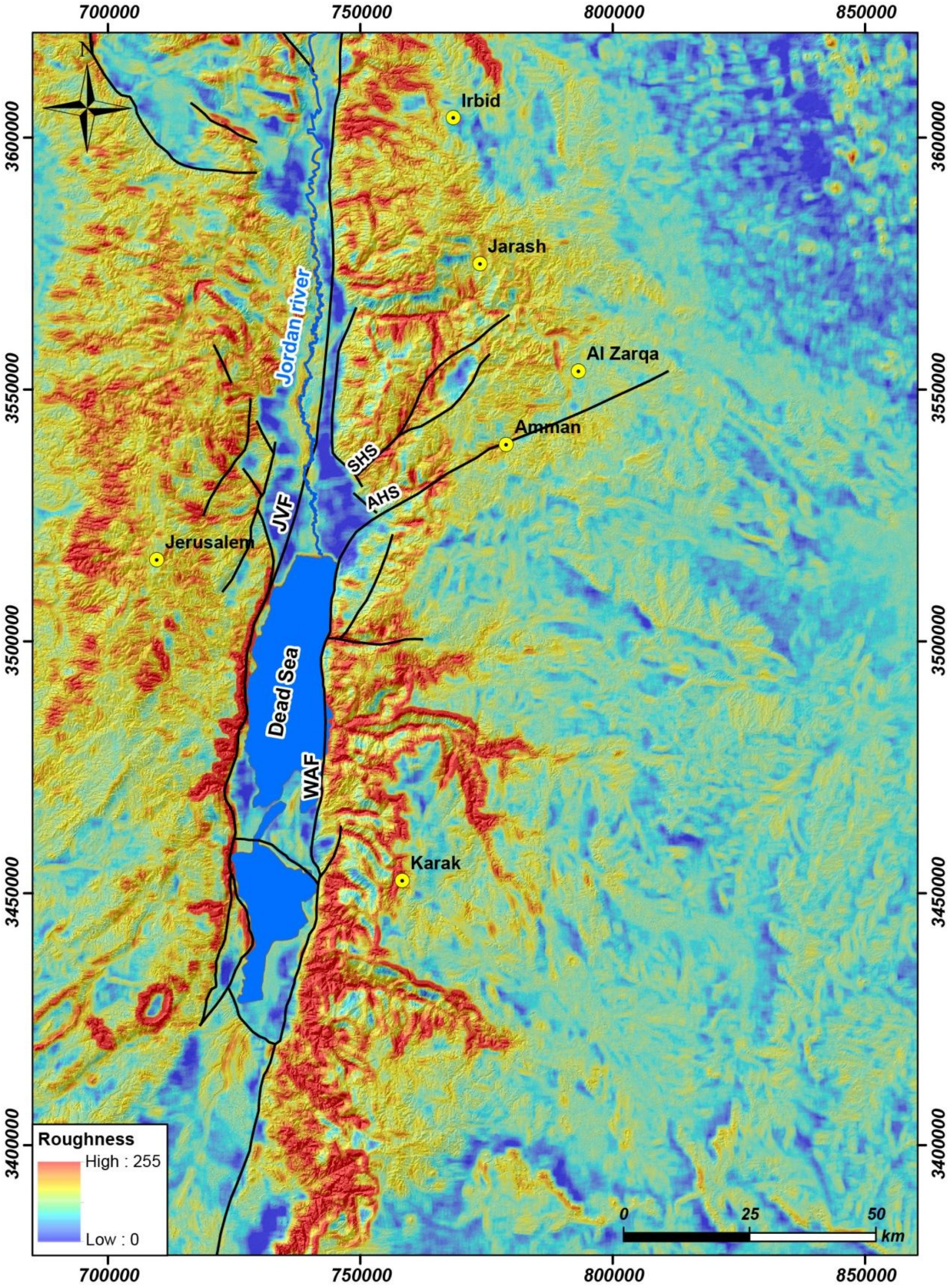

Fig. 5.3. Surface roughness of the study area calculated for a 8-cells neighborhood from a re-sampled 120m resolution DEM. Highest surface roughness correspond to the middle and southern parts of the eastern margin of the Dead Sea.

The resulting surface roughness map depicts interesting features (Fig. 5.3). High values correspond to the east and western margin of the Dead Sea, where drainage density is also higher, and low values are located over the TJP. Even thought the drainage density is high in both margins of the Dead Sea, the highest values concentrate in the middle-lower part of the eastern margin (Fig. 5.3). This topographic pattern can respond to the higher slopes and/or drainage density caused by the erosion wave that propagates from the Dead Sea into the TJP. It is also worth noting that the main tectonic structures in the area (WAF and JVF) act as clear boundaries between low and high values.

5.1.3. Topographic Swath profiles

In order to describe and analyze the topographic trend of the study area, we made several North-South and East-West swath profiles. We used the ArcGIS Add-In designed in this Thesis to extract 4 East-West profiles and 2 North-South profiles with a swath width of 12 km (**Fig. 5.4**). The elevation source was a Digital Elevation Model of 1 arc-second (~29m) obtained from the Shuttle Radar Topography Mission (SRTM). Each swath profile was 12 km width and included data from 51 parallel lines with a base step-size of 3/2 the cell-size (43 m).

The north-south profiles show very interesting features. While the eastern swath (NS02, **Fig. 5.5**) shows a plain plateau with almost no elevation variations (local-relief values lower than 200m all along the profile), the western one (NS01, **Fig. 5.5**) shows a highly dissected landscape with local-relief values up to 1000m. In this latter profile, the dissected valleys of the four main E-W rivers can be clearly identified. In the profile NS01, mean elevation, q3 and maximum elevation profiles are relatively close, thus indicating a young relief. This is also corroborated in the Transverse Hypsometry chart (THi), which shows differences between the north and the south part of the swath. The THi values of the center and southern part are slightly higher than those of the northern part (**Fig. 5.5**).

The most interesting feature of these north-south swath profiles is the difference in the maximum elevation and the topographic trend of the TJP. Despite the higher erosion in the NS02 profile, the TJP surface can be well identified with the maximum profile and q3 line (that lies very close to the maximum). In the NS02 profile the TJP is clearly characterized by a flat plateau with an average elevation of 700 m in the north, and 900 in the middle-southern sector. However, the same plateau in the NS01 profile shows prominent differences and clear high-amplitude topographic "undulations" that produce higher elevations up to 900 m in the northern part and 1300 to 1500 m in the southern one (**Fig. 5.5**).

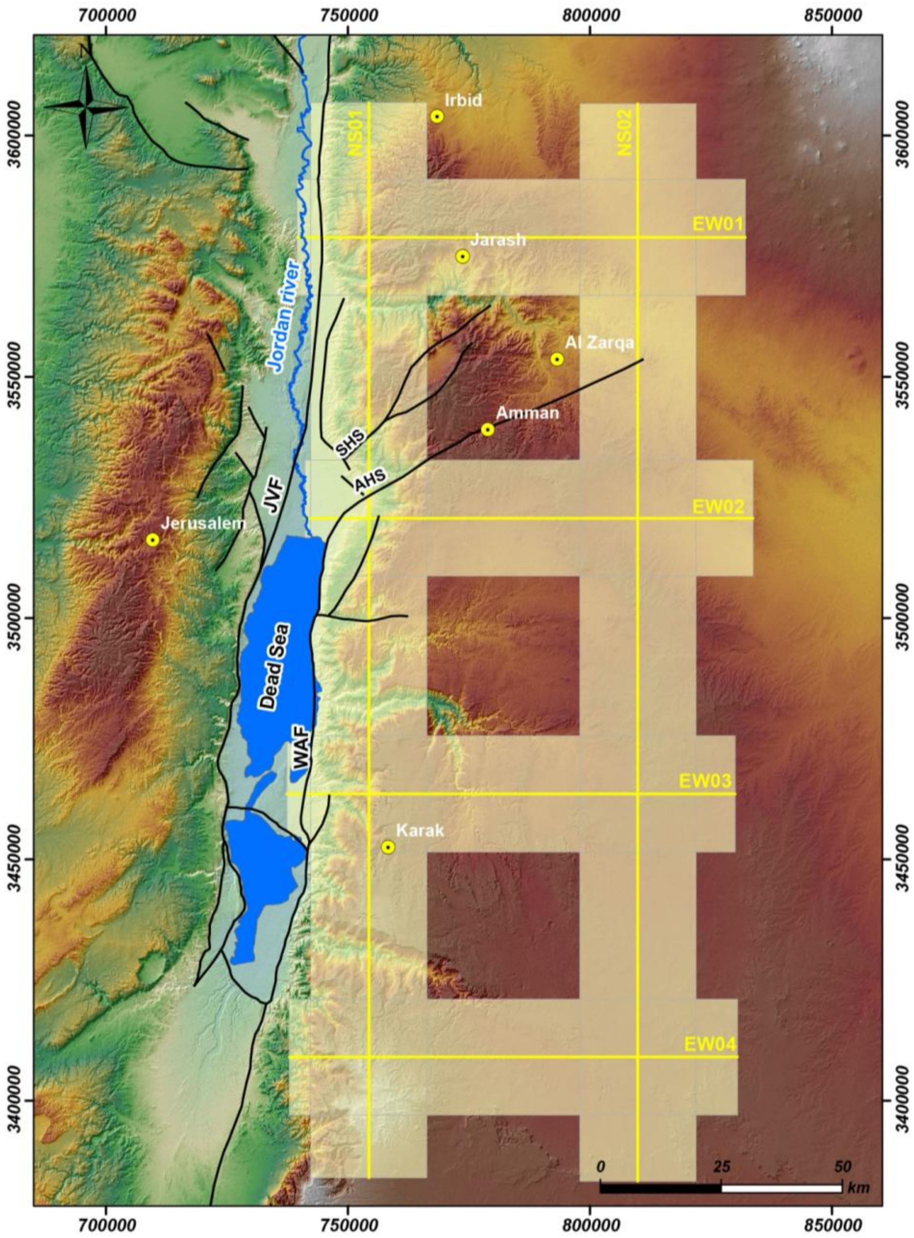

Figure 5.4. Location of the 6 swath profiles made in the eastern margin of the Dead Sea. All the profiles have a swath width of 12 km and data from 51 parallel lines with a base step-size of 43 m.

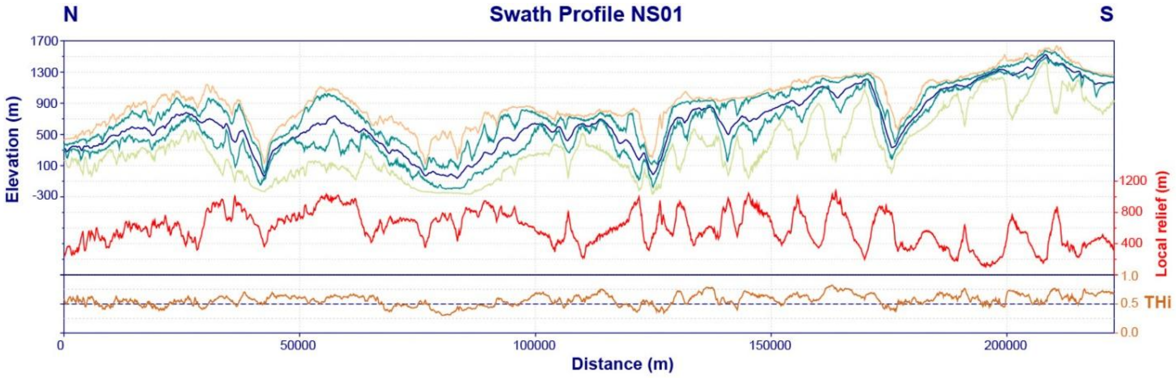

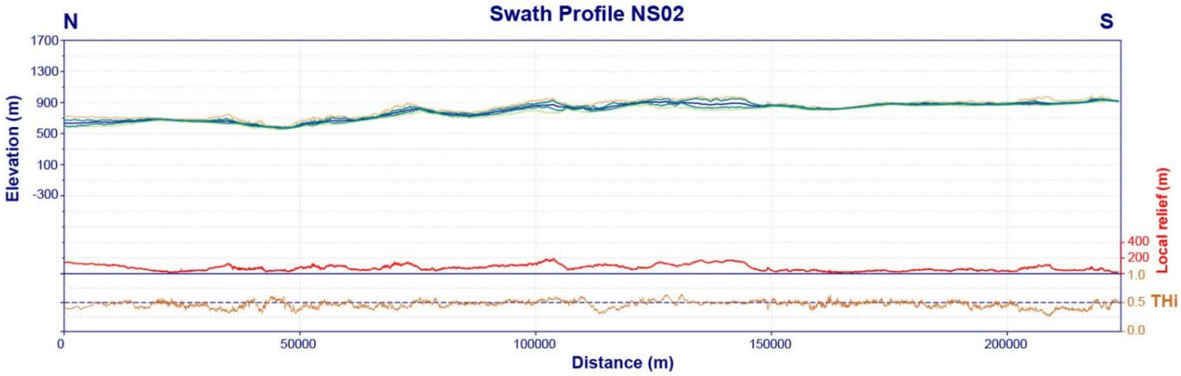

Figure 5.5. North-south swath profiles (see location in Figure 5.4). The easternmost swath profile, NS02, depicts the TJP as a flat surface with very low local relief, whereas the western swath, NS01, shows a highly dissected landscape with higher local-relief (up to 1000m). The q1 and maximum elevation lines define the TJP surface elevation. This TJP surface is quite different in both profiles; whereas in the NS02 is defined as a flat horizontal surface, in the NS01 profile present clear high amplitude undulations reaching higher elevations.

The four E-W profiles also show very interesting features (**Fig. 5.6**). In all the profiles the TJP is well defined as an elevated flat surface with low local-relief values (barely dissected by the fluvial network). Higher differences between maximum and minimum elevations are restricted to the western part, at the boundary between the Dead Sea-Jordan valley depression and the TJP. Western local-relief values are slightly higher in the southern profiles (800 m in NS03 and NS04) compared with the northern ones (600 m in NS01 and NS02). The topographic undulations drawn in the N-S profiles are also depicted in some of the east-west profiles. They are especially clear in the EW01 and EW04 profiles, where maximum elevations reach 1200 and 1500 meters in their western parts respectively (**Fig. 5.6**).

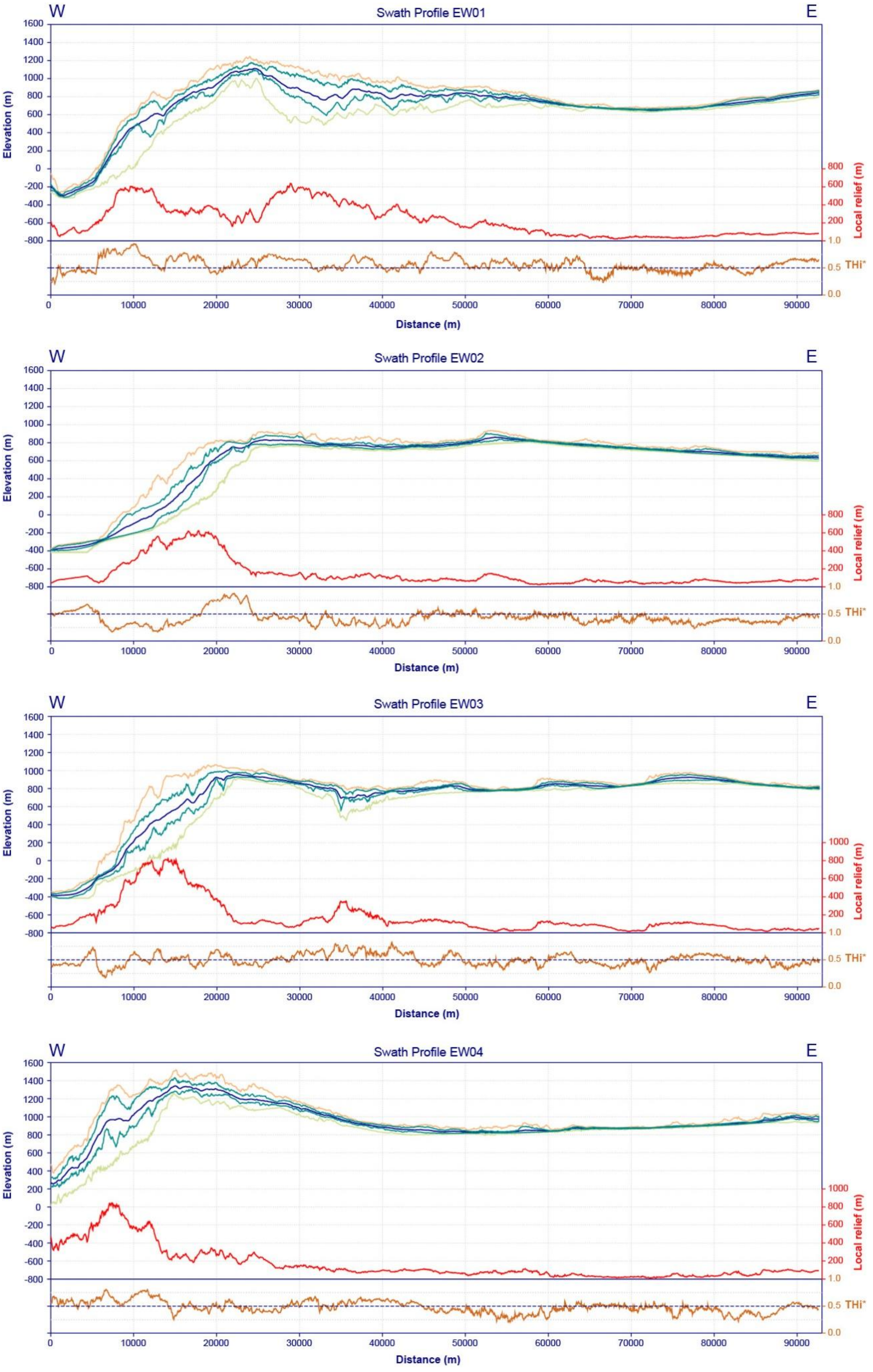

Figure 5.6. East-west swath profiles (see location in Figure 5.4). The four E-W profiles show clear topographic differences between the TJP and the Dead Sea-Jordan valley (see text for further explanation).

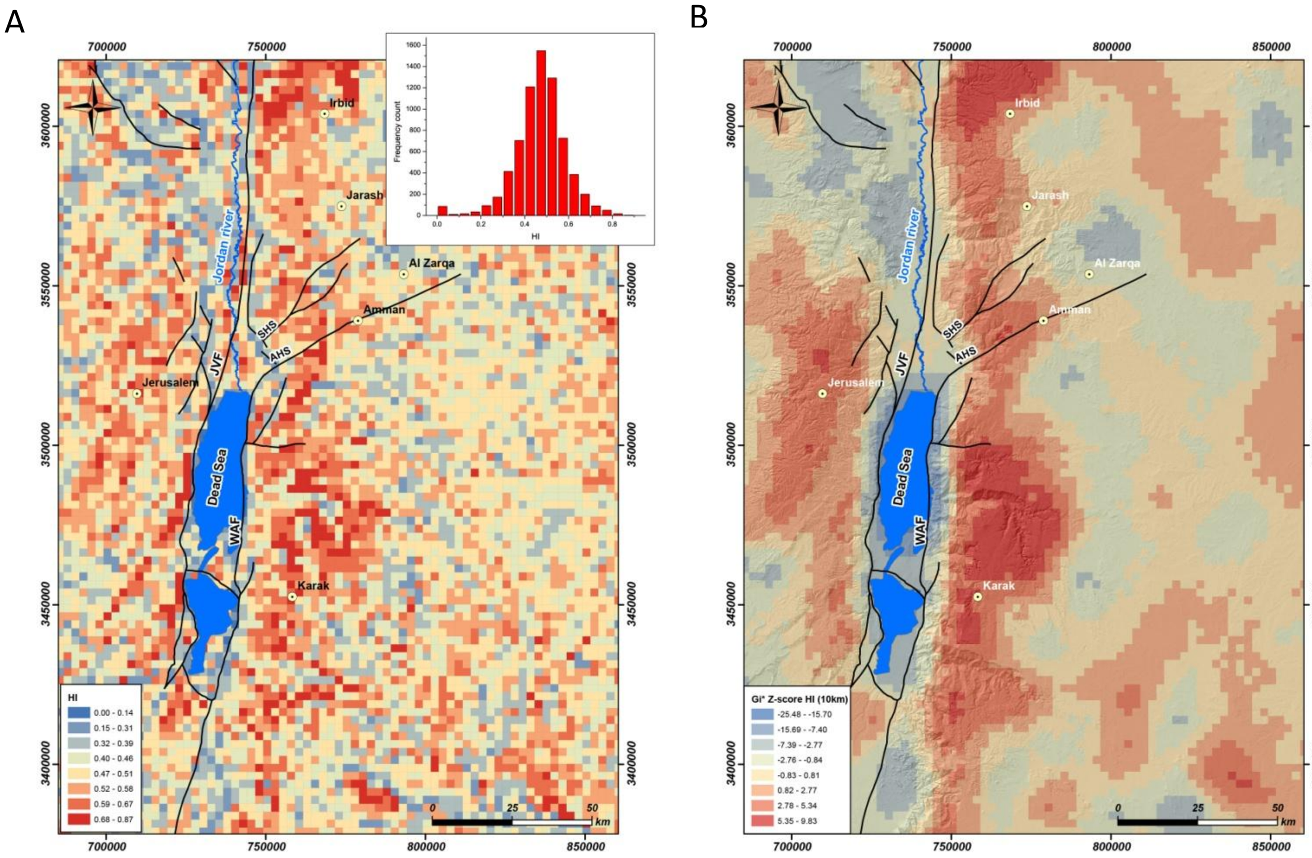

Figure 5.7. Spatial analysis of the hypsometry. A) Raw calculation of the Hypsometric Integral for 2.5 km squares using a 30m DEM. High values of HI seems to concentrate in the eastern side of the Dead Sea but clusters are not so clear. B) Spatial clustering of HI using the Getis-Ord (Gi) local index of spatial autocorrelation (LISA). The hot-spots of high and low values are very clear.*

5.1.4. Spatial analysis of hypsometric integral

In order to evaluate the landscape dissection we computed the HI for regular squares of 2.5 km using the 30m DEM from the SRTM. This size was selected because narrower E-W incised channels draining to the Dead Sea have widths of ~5km, and thus 2.5 km can efficiently record the topographic features of both margins of these channels. The raw estimation of HI values does not present clear patterns, but high values seem to concentrate in the eastern margin of the Dead Sea (**Fig. 5.7a**). The raw estimation of HI display a 'noisy' pattern that is the consequence of the use of regular squares instead of proper drainage basins (Pérez-Peña et al., 2009; Mahmood and Gloaguen, 2011; Siddiqui and Soldati, 2014).

Although the spatial clustering seems clear in the raw distribution of HI values (**Fig. 5.7a**), I calculated the Moran I index to test the spatial autocorrelation. This analysis yielded the following results:

- Moran's Index = 0.2498
- Expected Moran (for a random distribution) = 0.0001
- z-score = 131.24
- p-value = 0.000000

The calculated Moran's Index is considerably higher than the expected index for a random distrubution, with a significance p-value of 0 and a high z-score. These results indicate that HI values are grouped in clusters. In order to map these clusters, I computed the Getis-Ord (Gi*) statistic for the HI values using a distance threshold of 15 km. The resuling map shows well-defined high and low hot-spots (**Fig. 5.7b**). Higher values of HI distribute at both sides of the Dead Sea - Jordan Valley depression, being higher in the latter. The highest hot-spot is located in the eastern margin of the Dead Sea, agreeing with the previous analysis of slope and surface rougness. At this respect, these results do indicate landscape dissection and erosion and not topographic frabic, and suggests that the landscape in this area is in a younger stage of development (**Fig. 5.7b**). Interestling, the norhtern area located between Jarash, Al Zarqa and Amman, which corresponds to the drainage basin of Zarqa river (one of the main E-W channels), presents considerably lower values, thus indicating that erosion there could be older than in the southern part.

This highly dissected landscape responds to the advance of the erosion wave that propagates eastewards into the TJP. This erosion wave produces deep and narrower channels in the eastern side of the Dead Sea, thus indicating a higher vertical river incision typical of transient landscapes where the uplift rate (or subsidence rate in this particular case) is higher than the incision rate.

5.2 Drainage network analysis through geomorphic indexes

In order to analyze the drainge network evolution and its relationship with the tectonic activity of the DSTF I have analyzed several geomorphic indexes. The two primary feeder system of the Dead Sea are the Jordan river and the E-W channels of its eastern border. As the Jordan River its an alluvial channel that has been intensively anthropized, the drainage network analysis of this Thesis will center in the E-W channels of the eastern border of the Dead Sea. This E-W directed network has some particularities. Drainage basins are very diferent in shape and size. There are two main types of drainge basins; large drainage basins having sources in the TJP and localized erosion in their mouths, constrast to small basin that barely reach the TJP elevations.

I first extracted the drainage network from the 30m SRTM DEM by using the eight directions algorithm (D-8, O'Callaghan and Mark, 1984). As the Dead Sea region is an endorheic area, the "Fill" method produces an "overfilling" in the Dead Sea lake, which is seen as a very large sink. In order to avoid such errors, I first clipped the DEM in two parts taking the Jordan River and the Dead Sea center as a boundary. Once the sink and the peaks were corrected, I extracted the flow direction and flow accumulation rasters by using the D8 algorithm (included in ArcGIS hydrological tools). The drainage network was obtained by selecting a threshold of 5000 cells in the flow accumulation raster to define valid "stream cells". Once this drainage network was extracted, I selected basins with drainage areas bigger than 10 km^2. These selected basins include the four main basins of Zarqa, Walah, Mujeb and Hasa Rivers (basins nº 14, 25, 26, and 33 respectively) and 32 small-basins (**Fig. 5.8**).

5.2.1. Normalized profiles

I extracted the normalized profiles for the main channels of the 36 analyzed basins (**Fig. 5.9**). The majority of the analyzed profiles show rectilinear and convex profiles, and they can be roughly divided into four different general types; extremely convex profiles, linear profiles, convex-concave profiles and concave profiles.

The four largest basins (14, 25, 26 and 33) present extremely convex profiles. These rivers have two well-differentiated parts; an upper reach located over the TJP and a lower reach that corresponds to the scarpment between the Dead Sea-Jordan River depression and the TJP. Their normalized profiles are influenced by this configuration, showing an upper part with a convex profile with low gradient and an lower part with very high gradients. Despite the influence that the upper part of these rivers have in their normalize profiles, it is interesting that they do not show concavity even in their lower reaches, where erosion is higher. This fact would indicate that rivers are in a transient state, far away from their equilibrium profiles.

Rectilinear profiles include convex-rectilinear and slightly concave-rectilinear profiles. They are typical of small basins in the northern part of the study area. Most of these basin also show prominet knickpoints that separate well-differentiated part in normalized profiles (**Fig. 5.9**). A rectilinar profile suggests that there is not a well-defined slope-area power law. This can be indicative of a transient stage of development in these rivers.

Finally, convex-concave and concave profiles are present in some rivers in the northern and central parts of the study area and it is the most common in rivers from the southernmost part (excluding the Hasa river, nº 33) (**Fig. 5.9**). These profiles should be the characteristic one for short rivers draining a flat elevated plateau. If their upper part reach the elevated plateau will yield a rectilinear/convex profile, whereas their middle and lower part present concave profiles with higher gradients.

This analysis shows that most of the analyzed rivers are in a transient stage of development and lack well-defined power law relations. The transient-stage suggests that erosion-rates do not keep pace with subduction-rates, which have been accelarated in Pleistocene times.

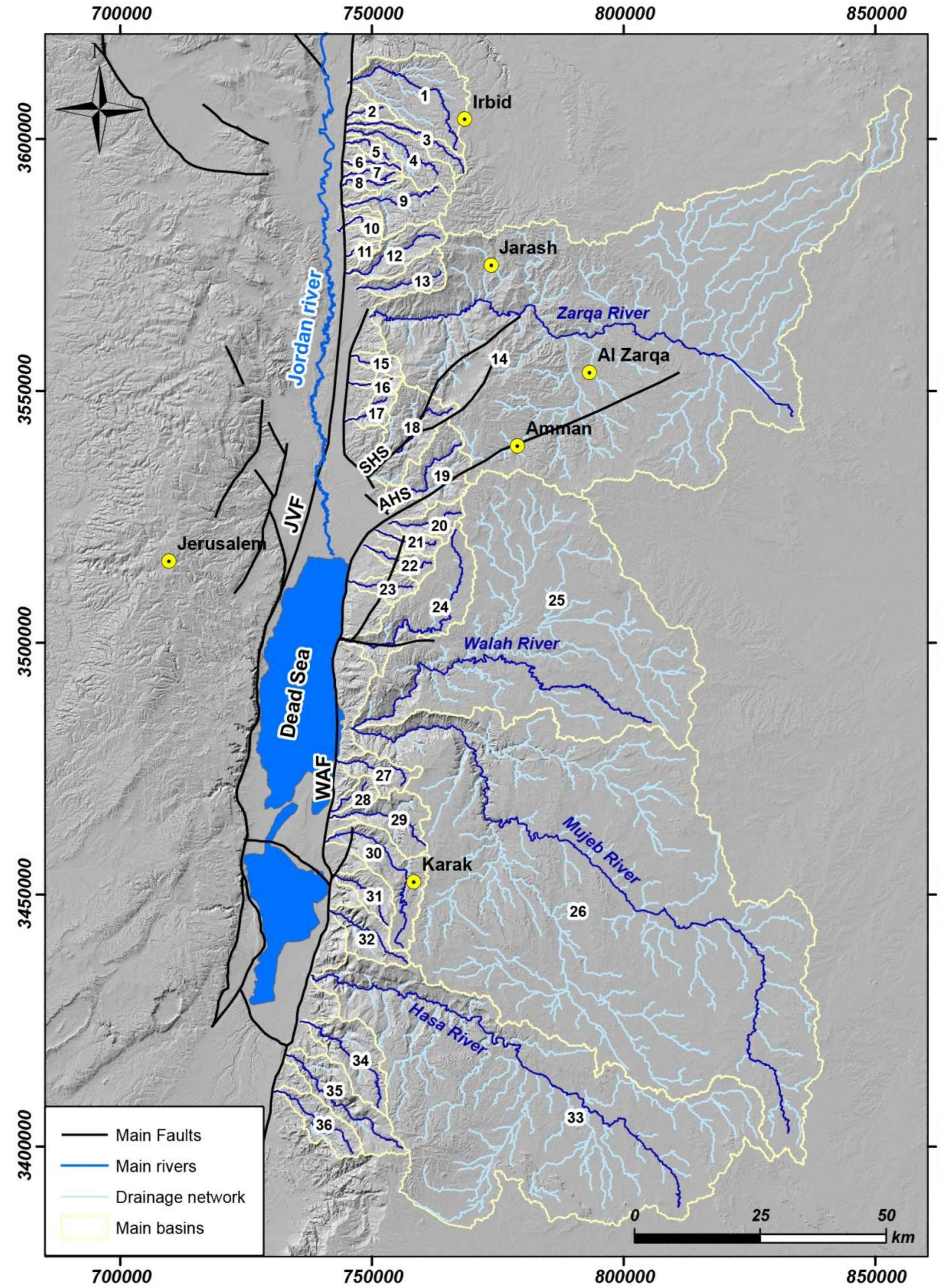

Figure 5.8. Drainage network extracted from the SRTM 30m DEM. It have been selected those basins with drainage areas bigger than 10 km^2 for the analysis. The 4 largest basins of Zarqa, Walah, Mujeb and Hasa rivers correspons to basin numbers 14, 25, 26 and 33 respectively.

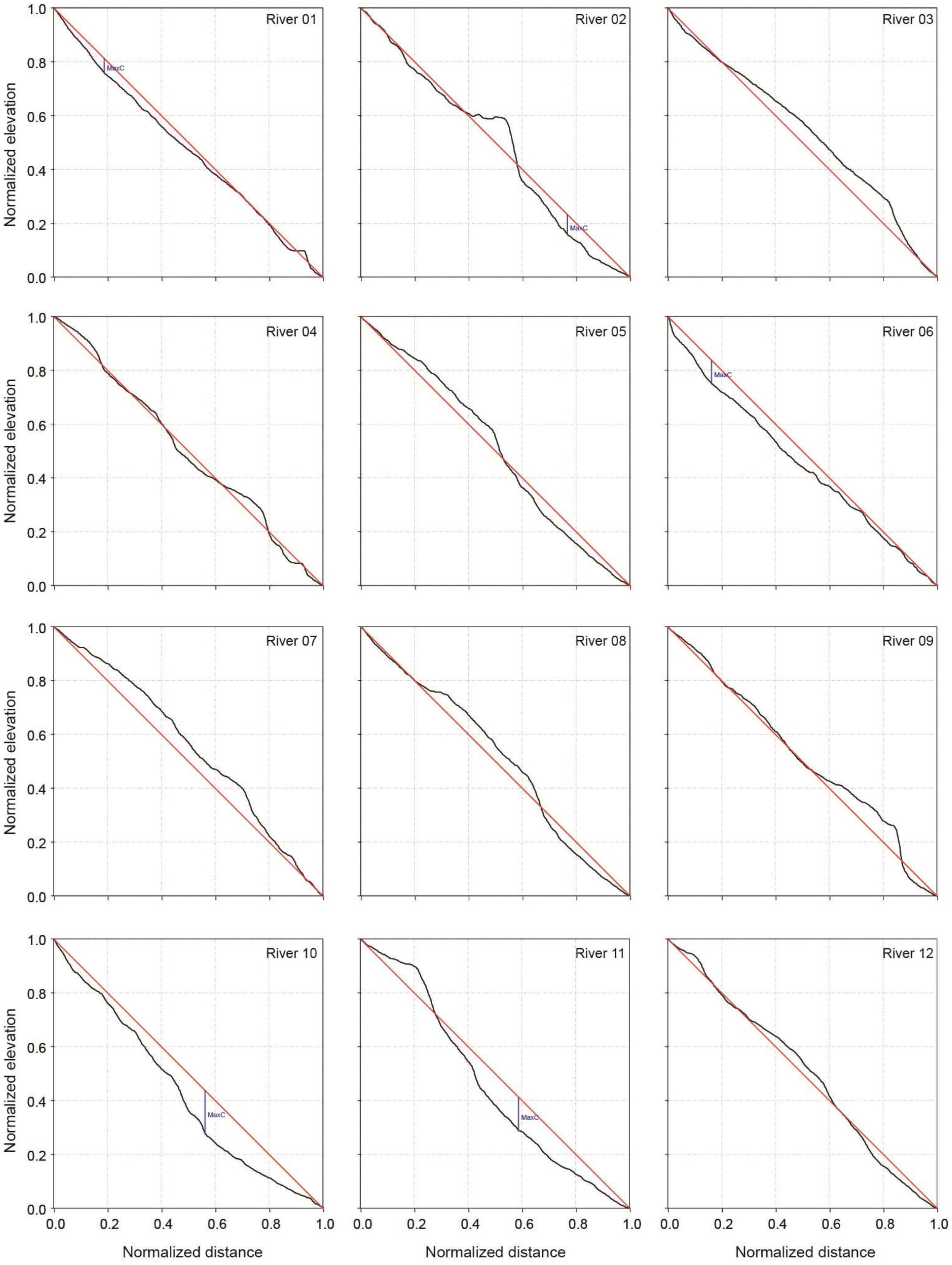

Figure 5.9. Normalized profiles for selected rivers (see Fig. 5.8 for location)

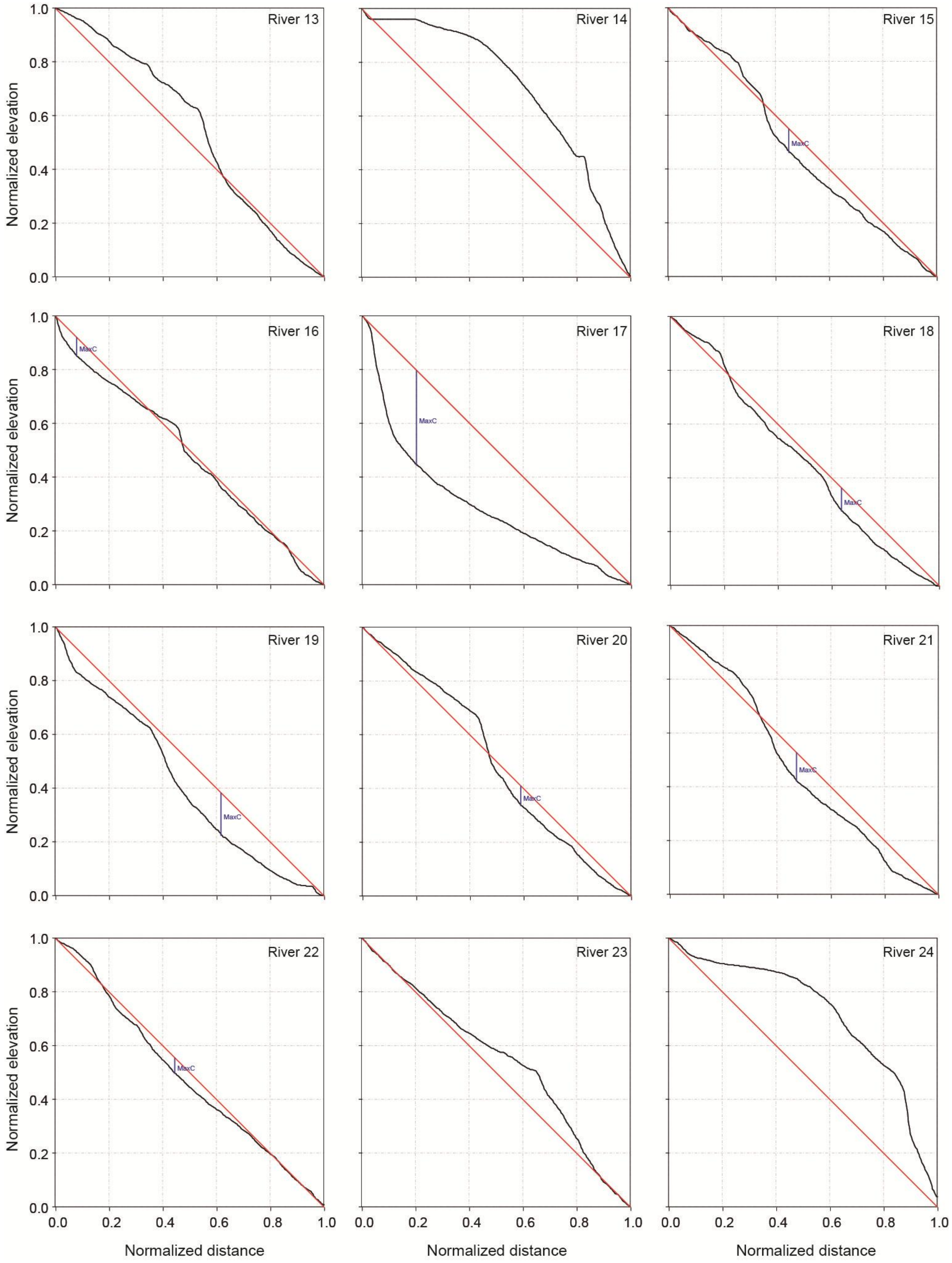

Figure 5.9. (Continuation). Normalized profiles for selected rivers (see Fig. 5.8 for location)

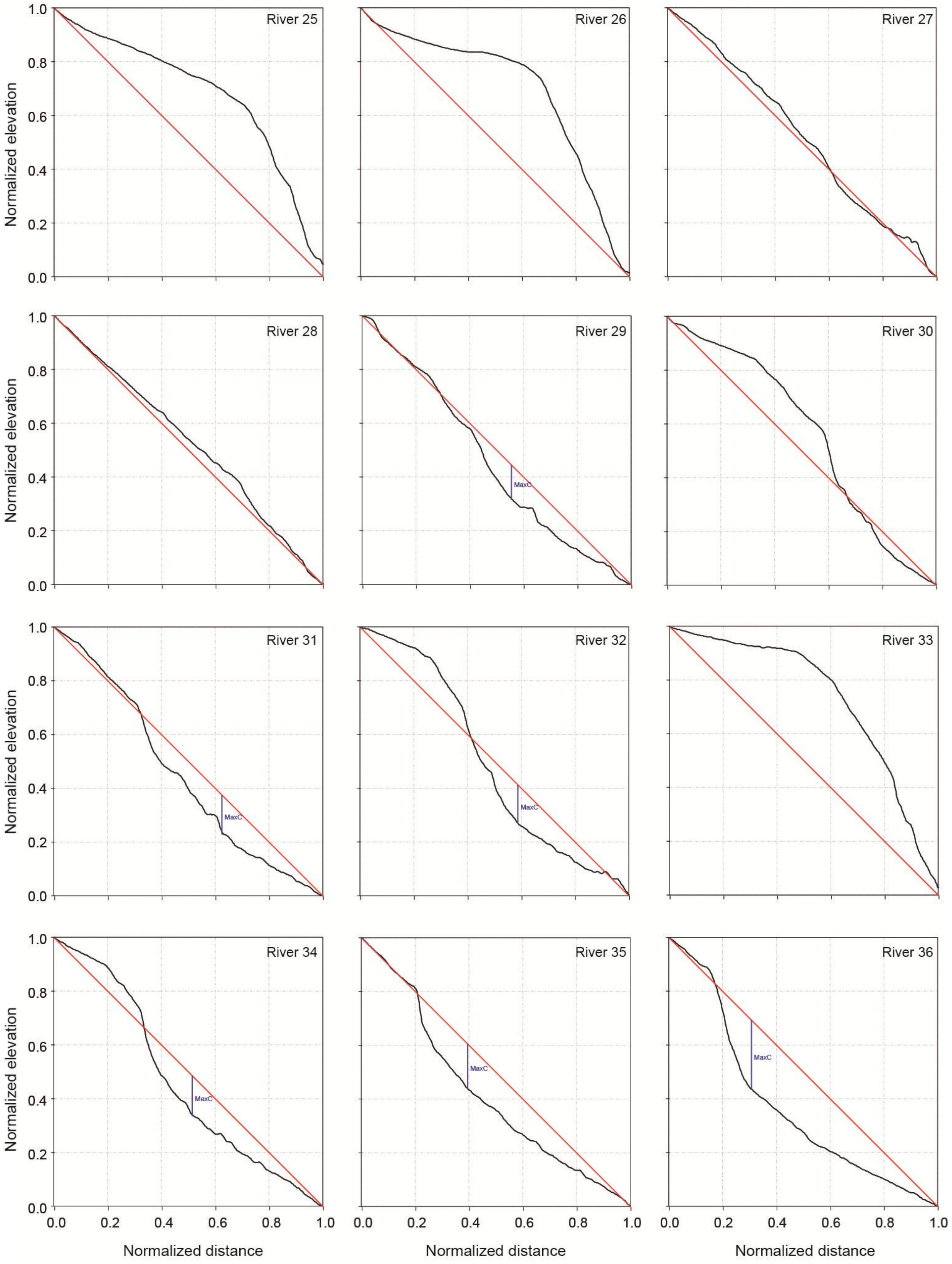

Figure 5.9. (Continuation). Normalized profiles for selected rivers (see Fig. 5.8 for location)

5.2.2. Hypsometric curves

To study the stage of development of the drainage basins we extracted their hypsometric curves. This analysis is similar to the spatial analysis of the hypsometric integral in regular squares already made before, but it differ in crucial points. First, each basin is characterized by a unique hypsometric curve and hypsometric parameters, independently of its size. Second, the unit of measure is the drainage basin, avoiding dispersion and 'noise'.

The hypsometric curves were extracted with the tool CalHypso (Pérez-Peña et al., 2009) for ArcGIS 10.1, and divided in tree main groups (**Fig. 5.10**). The first group contains the curves for the basins 1 to 13. All the curves present clear convex profiles, being the convexity higher in the curves 2 to 4 and 10 to 13. The second group is formed by the basins 14 to 24 with hypsometric curves concave for basins 14 to 17 and convex for the rest of them. The hypsometric curve of the Zarqa river present some particularities, in spite of having a low hypsometric integral presents a convex shape. This is due to the highest elevation up to 1400 m in its uppermost NE part (**Fig. 5.8**). The remainder basins (18 to 24) show convex profiles with high hypsometric integral values. The third group comprises the basins 25 to 36 and it is the more heterogeneous group of the three. The basins of the main rivers (Walah, Mujeb and Hasa, basin numbers 25, 26 and 33) present similar convex profiles, with a flat middle part and sharp gradient in their mouths. This is explained by their morphology; in the three cases most of the basin is located over the TJP and erosion is concentrated in its mouth. Basins number 27 to 32 depict clear convex profiles, with high hypsometric integral values, whereas concavity fall in the southernmost basins (34, 35 and 36).

The distribution of hypsometric integral (HI) values is also very interesting (**Fig. 5.11**). HI values are relatively high, only some small basin yield values lower than 0.5. The highest values concentrate in the eastern margin of the Dead Sea, indicating that landscape dissection and erosion is higher in those basins. These high values agree with the other analyses presented before.

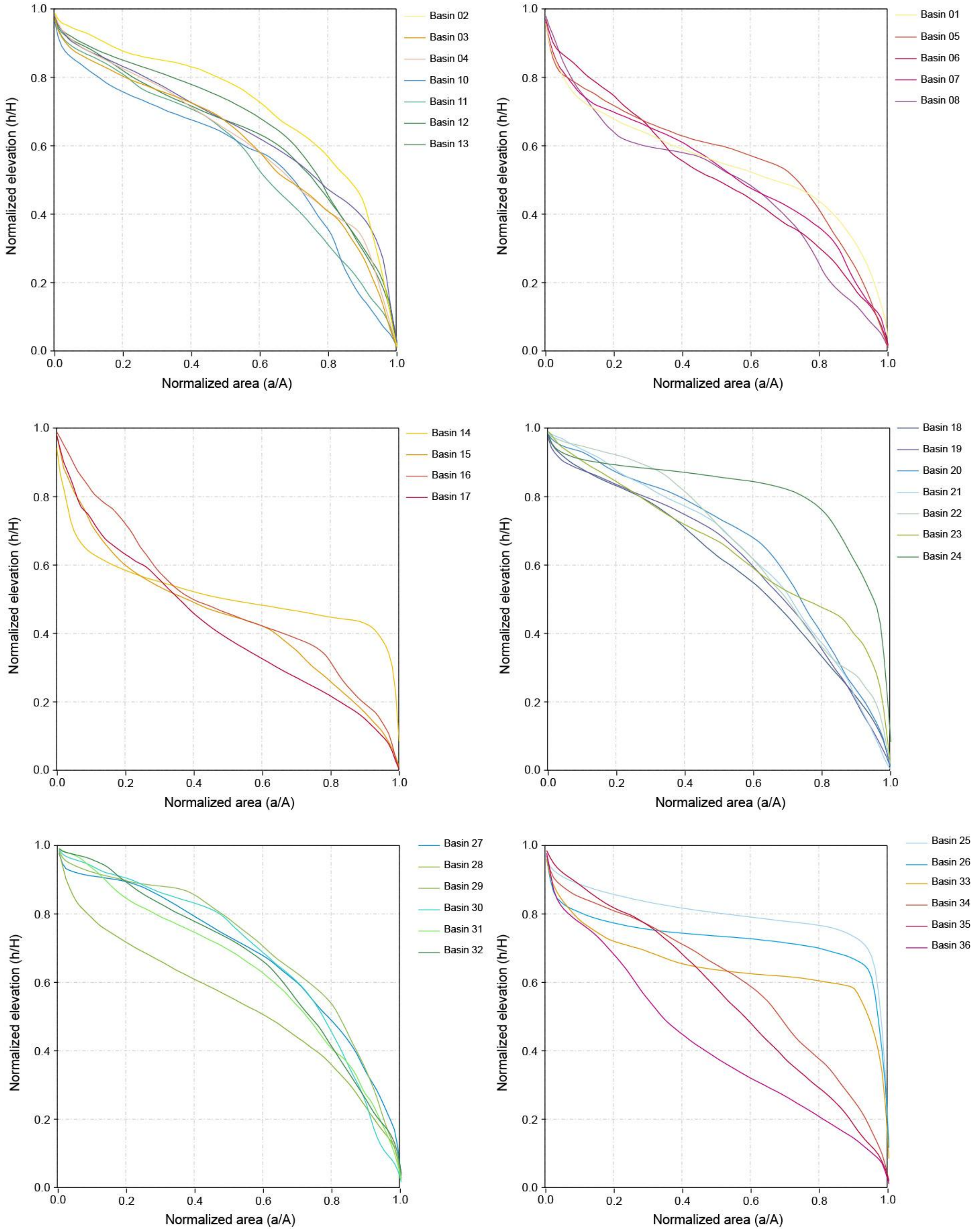

Figure 5.10. Hypsometric curves for the selected basins. The three groups correspond to northern, middle and southern basins. See Fig. 8.8 for location and text for description.

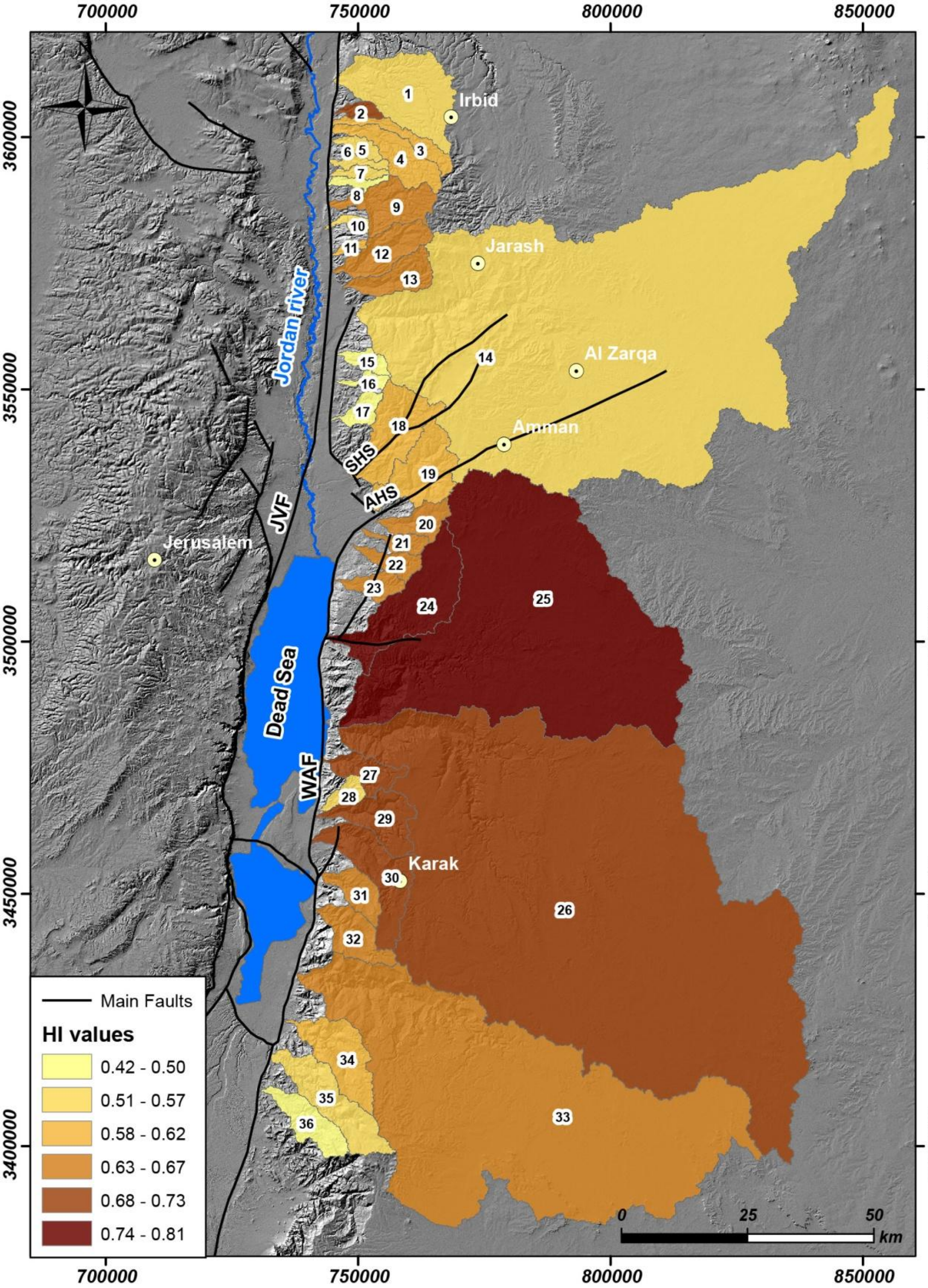

Figure 5.11. Distribution of hypsometric integral (HI) within the analyzed basins. Highest values concentrate in the eastern margin of the Dead Sea.

5.2.3. Bulk erosion

To calculate the bulk erosion for the analyzed basins I used the SRTM 30 m DEM. I interpolated elevations for the lines that represent basin boundaries. These elevation were obtained not only for line vertexes but for each cell of the DEM, thus densifiying original polylines. Taking these 3D lines as input, I constructed a triangular irregular network model (TIN) that was considered the reference or "un-eroded" surface. The bulk erosion map is the result of subtract the present-day surface (original 30m DEM) and this reference surface (**Fig. 5.12**).

The bulk erosion map (**Fig. 5.12**) shows the highest values in the eastern margin of the Dead Sea and in the Zarqa river. All the big basins (Zarqa, Walah, Mujeb and Hasa) depict higher values in their mouths, concentrated in narrow gorges in the three last rivers. In the case of the smaller basins, high values are restricted to basins from the eastern margin of the Dead Sea (from the basin number 24 on, **Fig. 5.12**). The obtained bulk erosion map agrees with the other results from the different landscape analysis. Erosion is higher in the eastern margin of the Dead Sea lake, coinciding with high hypsometric integral values and surface roughness.

5.2.4. Area-Slope relationships (Ksn index)

Area-slope relationships have been used intensively in the last years to analyze river responses to active tectonic and uplift. These relationships are based on the power law that relates slope and up-stream area in a particular catchment. As discharge will increase downstream, the river will have more stream power and thus slopes will be lower. This power relation is the responsible for the logarithmic shape that most river draw. By using this power relation it is possible to extract some geomorphic gradient-related indexes as the steepness (Ks) and Hack's stream gradient (SL). As SL index can be viewed as a particular case of the steepness index, we will consider only the latter for the analysis. The Ksn index offers reliable results for rivers in steady-state, where area and slope are related by the already mentioned power law. However, for rivers in a transient state, area and slope cannot depict a well-defined relation.

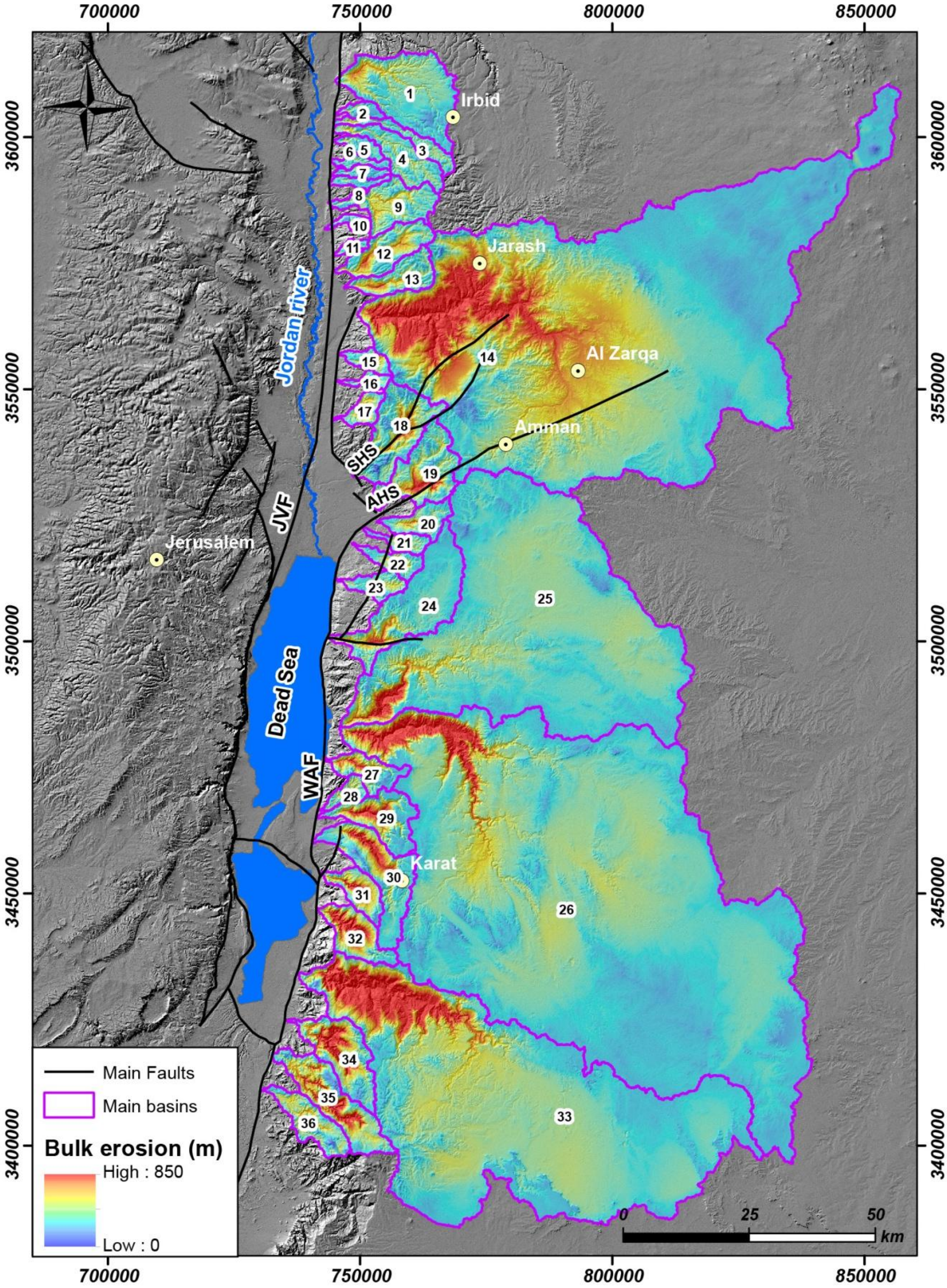

Figure 5.12. Bulk erosion map for the selected basins. This map show the elevation differences between a reference surface ("un-eroded" surface proxy) and the present-day topography. See text for explanation.

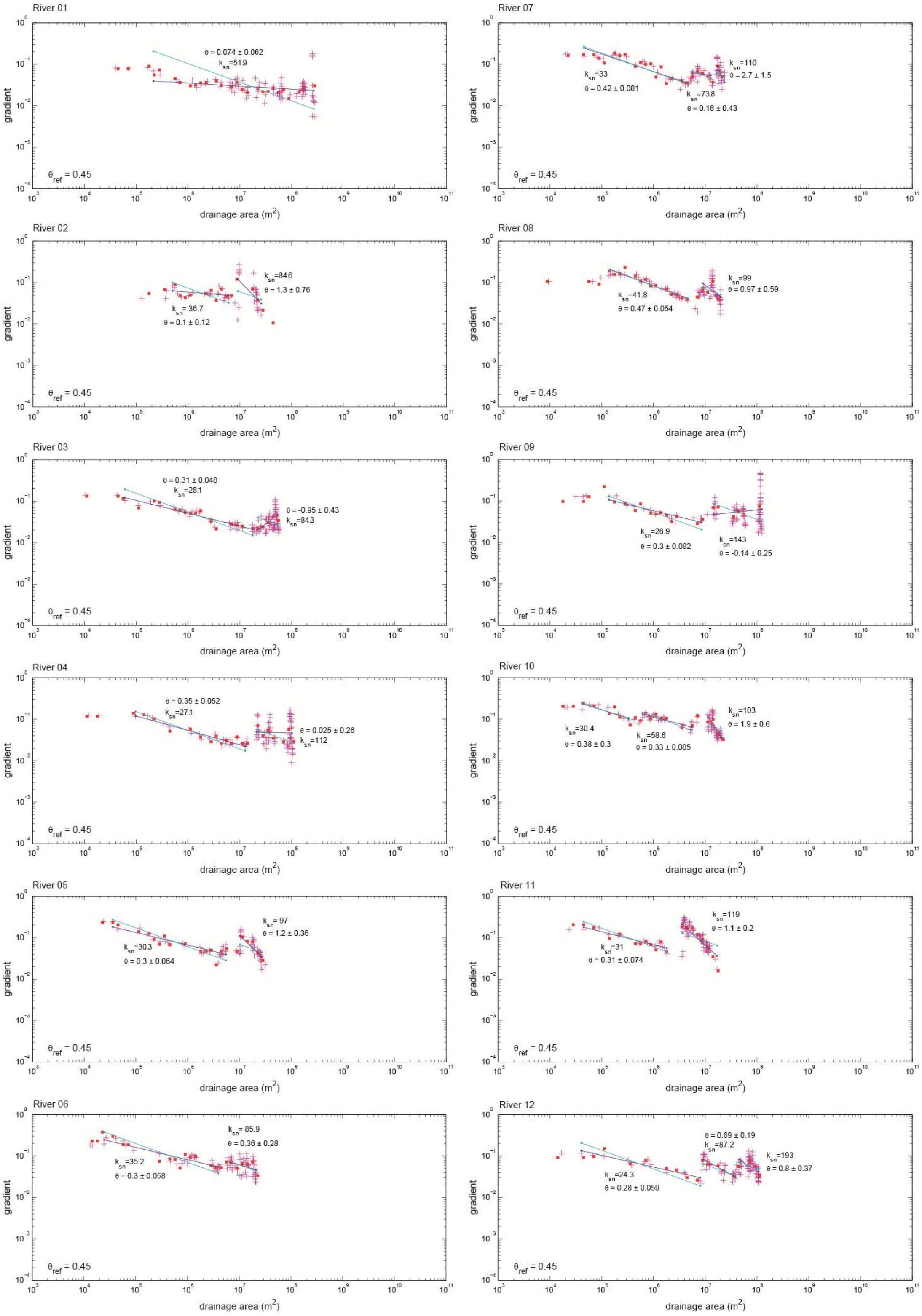

Figure 5.13. Area-slope plots for the analyzed rivers. In most river are clear two segments; a first segment with a low Ksn and a second segment with high Ksn values. The latter segments often lacks of a well-defined area-slope relationship, indicating a transient state.

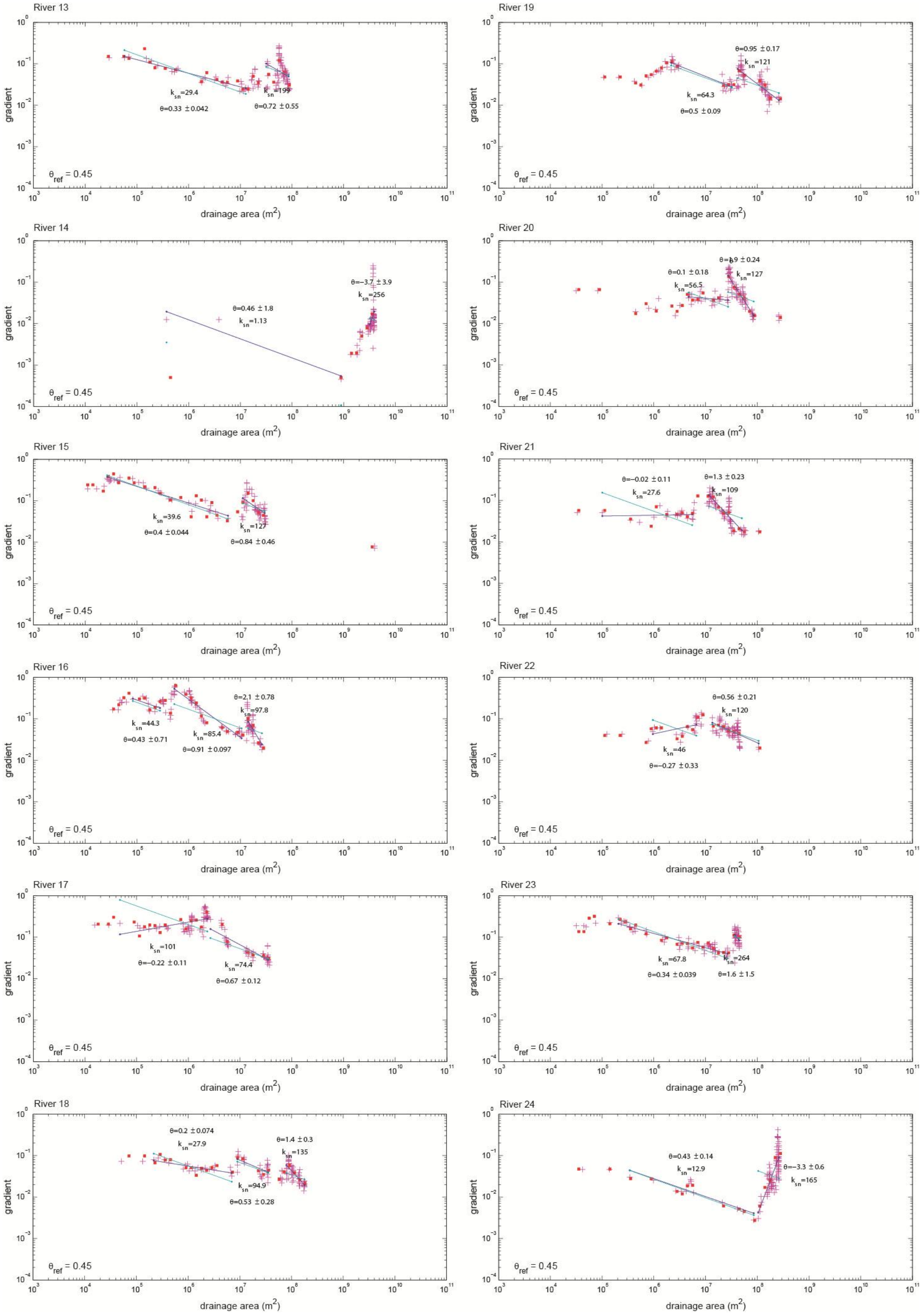

Figure 5.13. (continuation)

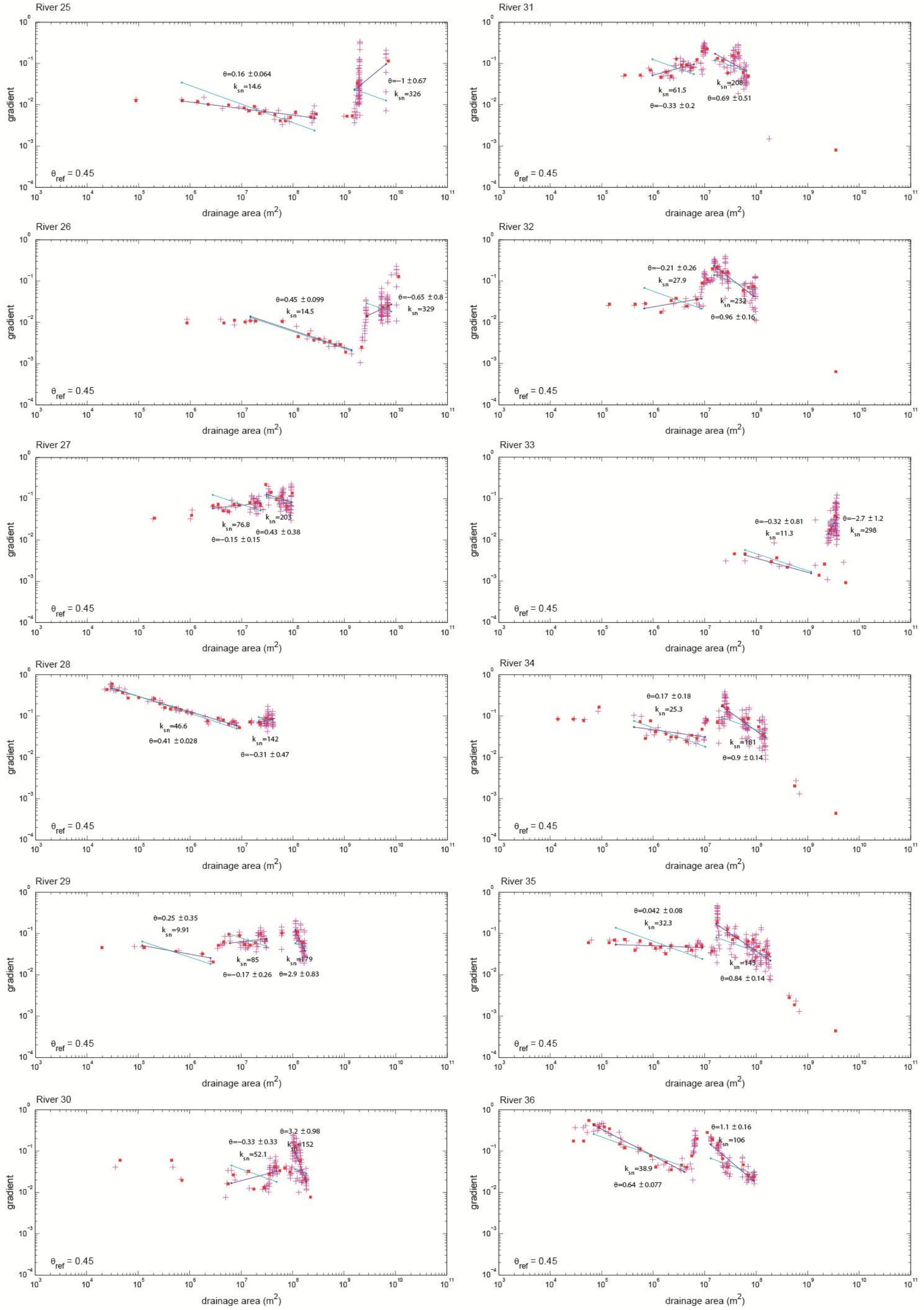

Figure 5.13. (continuation)

Most of the analyzed rivers lacks a well-defined area-slope relation, i.e., there are not clear segments in the area-slope charts (**Fig. 5.13**). This causes that Ksn values differ from Ksn values in steep reaches with high gradients. A common characteristic of many of the analyzed rivers is the presence of high-gradient segments near river mouths. Ksn index in these mouth segments yields very high values and profiles lack of well-defined slope-area relations (**Fig. 5.13**). The highest gradients and Ksn values are found in the rivers 14, 24, 25, 26 and 33, which also presented the maximum convexity in their normalized profiles. This fact indicates that convexity in normalized profiles is a clear sign of transient-state profiles due to high incision rates.

The Ksn index is thought to be related to the uplift rate (Kirby and Whypple, 2012; Azañón et al., 2015). This relation relays in the power relation of upstream area and gradient. In Rivers far away of their equilibrium profiles lacks well-defined area-slope relations, and thus Ksn values cannot be unequivocal calculated, not related to uplift rates. In this case, as rivers show transient profiles, we cannot use the derived Ksn values to infer uplift rates or to analyze the quantitative values of Ksn index. However, we can analyze obtained Ksn values in a semiquantitative or qualitative way. In this sense, the highest values of Ksn index locate in the eastern margin of the Dead Sea, thus agreeing with all the other indexes derived in this Thesis. This corroborate the higher subsidence rates in this area (as we consider that the Trans-Jordanian Plateau has not suffer important changes in elevation).

Chapter 6

Field evidences of Quaternary tectonic activity

Preface

This chapter presents the field work performed in the area to the NE of the Dead Sea to identify the Quaternary tectonic activity of the northern WAF, the AHS and the SHS. The evidences included in this chapter are new and point to the first field findings of the Quaternary tectonic activity of the aforementioned structures.

The deformation accommodated by these two structures and similar ones, could partly explain the slip-rates differences between the southern and northern DSFT segments. Moreover, the kinematic of these structures could respond to some questions that remain unsolved; as the northern closure of the Dead Sea.

The field work I made in this PhD Thesis was the validation and cartography of the geological map of the study area and the observation of Quaternary activity evidences in the main structures treated in this Thesis; WAF, AHS and SHS.

This chapter contains the following subtitles:

6.1 Geological map of the study area

6.2. Field evidences of Quaternary activity

6.2.1 Quaternary activity of the WAF

6.2.2 Quaternary activity of the AHS.

6.2.3 Quaternary activity of the SHS

6.1 Geological map of the study area

Two field campaigns were conducted in the study area in order to collect structural data and to document active tectonic features. These two field campaigns focused mainly in the WAF and the JVF in the NE corner of the Dead Sea as the promotors of the tectonic activity and directly activates the AHS in the area from the Dead Sea to Al-Bahath Valley. The field work of this thesis has validated the geological maps of the Natural Resources Authority of Jordan that correspond to the study area and produced a new geological map with the main geological formations and map units (**Fig. 6.1**). Two general schematic cross sections (A-B and C-D) were drawn to show the geological and structural setting of the studied area (**Fig. 6.2**).

The WAF in the study area is changing its nature of pure N-S strike-slip fault to oblique reverse sinistral fault in NE direction. The exact fault plane of this fault is undeterminable but the tracing it in the aerial photography is possible. The AHS traces are visible in the NE corner of the Dead Sea (**Fig. 6.3**). Formed by repetitive NE anticlines and synclines with major NE sinistral reverse faults, the AHS outcrops in the Al-Rama village, east AlKafrain village, AlBahath Valley, Western Amman, South Amman and continue to the Alhallabat palace in AlZarqa. Major tectonic activity of the AHS is observed in the southern parts of this structure with clear Quaternary and Holocene evidences. General trends of the main faults associated to this structure are concurrent to the original stresses (Cretaceous stresses) that dominated in the area. The new phase of deformation shows coherency with the present-day stress field of the DSTF favoring a NNW-SSE maximum compressive stress and NE-SW extensional forces. The SHS is another reactivated structures belonging to the SAS in Jordan. Spatially parallel to the AHS, the strike and nature of this fold-thrust structure. The southern west exposure of the SHS is in the Kafrain Village and then it passes through the Hidaidoun Valley, Wadi Shuaib, AlSalt, Swaileh and finally merged to an E-W dextral fault in the Zarqa River.

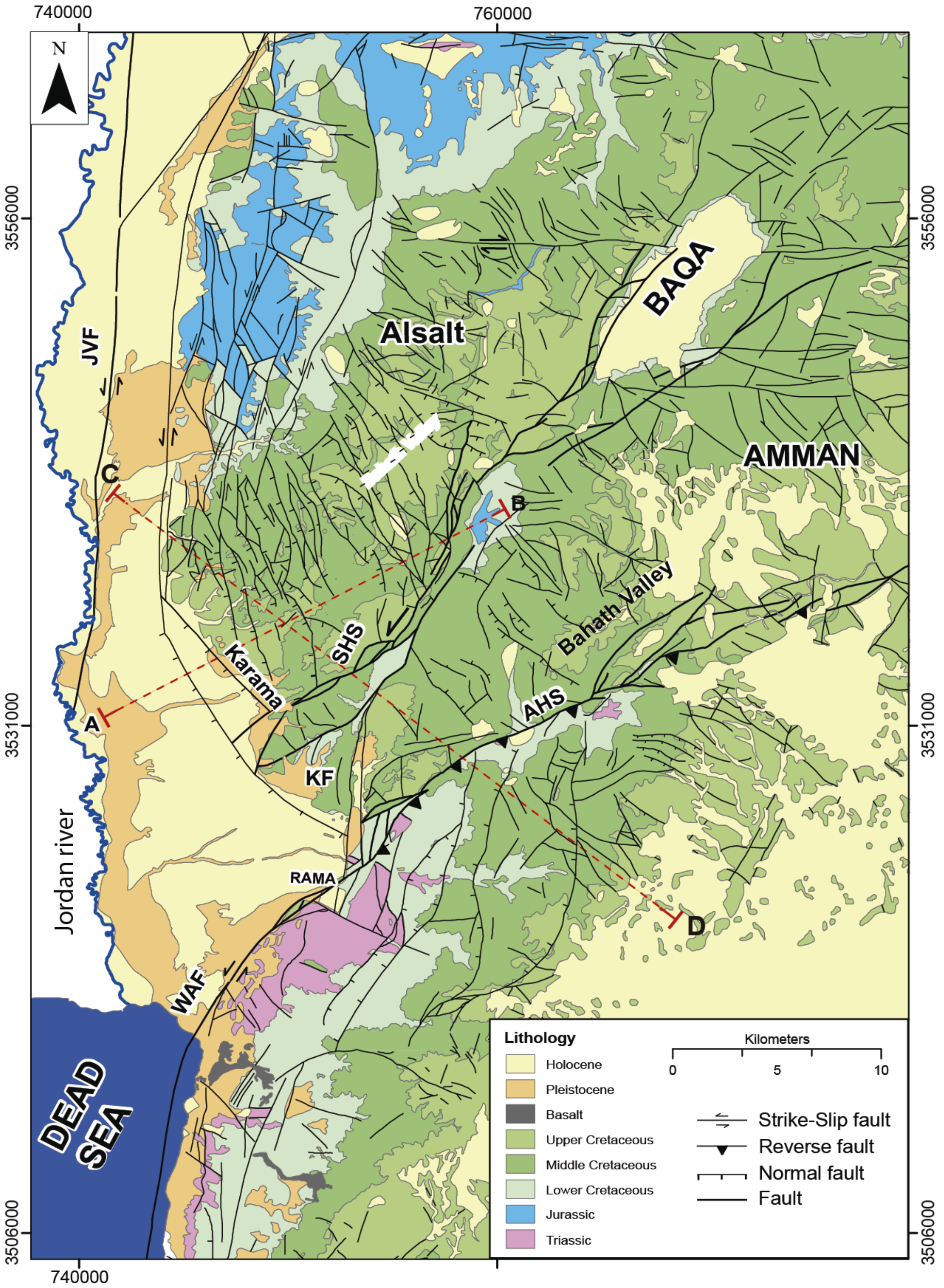

Figure 6.1. Geological map of the study area.

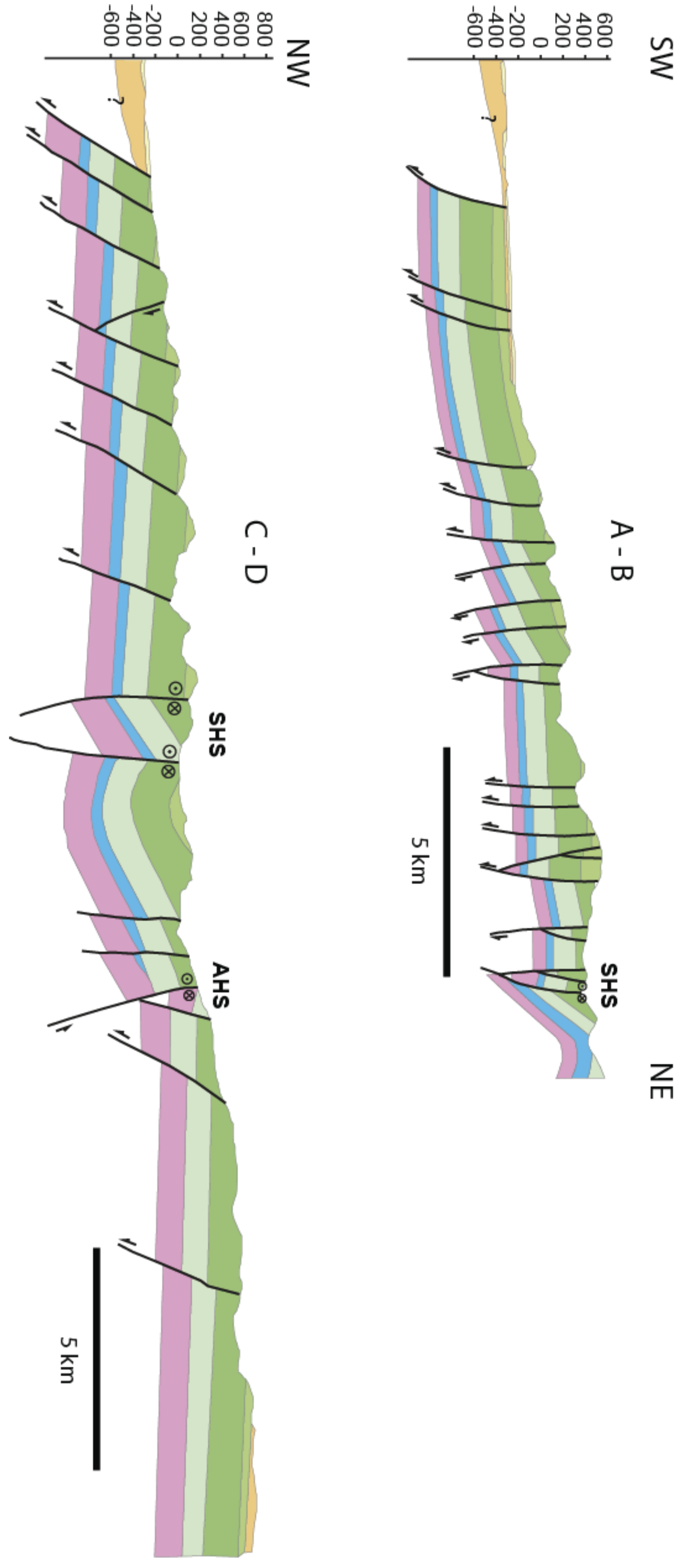

Figure 6.2. Cross sections (A-B) and (C-D).

6.2. Field evidences of Quaternary activity

6.2.1 Quaternary activity of the northern WAF

Traditionally has been considered that the northern WAF dies in the NE corner of the Dead Sea and the deformation is transferred to the western fault segment of the southern DSTF sector (Al-Zoubi et al., 2006, 2007). In this area, field outcrops are scarce since the WAF runs into Quaternary and Holocene sediments and does not present clear topographic morphologies, being very hard to identify on the field. This fact has motivated that WAF was never mapped further of the Al-Hijar Al-Twal site (8 km to the northeast of the Dead Sea). However, we examined several natural Wadis, new military trenches and quarries, where we found previously-unknown outcrops of the WAF cutting the Lisan formation and the Holocene sediments (**Fig. 6.3**).

The deformed Quaternary sediments outcrops present NE-SW sinistral strike-slip faults with significant reverse component and NW-SE normal faults. The location of these outcrops were never documented. Therefore the evidences reported in this thesis present a better explanation of the nature of the northern WAF and its relation with other important structures. It is noteworthy that this part of the fault was mapped with a normal component (Alzoubi et al., 2007) instead of reverse one that will fit better with the regional stress of the DSTF (Marco and Klinger, 2014).

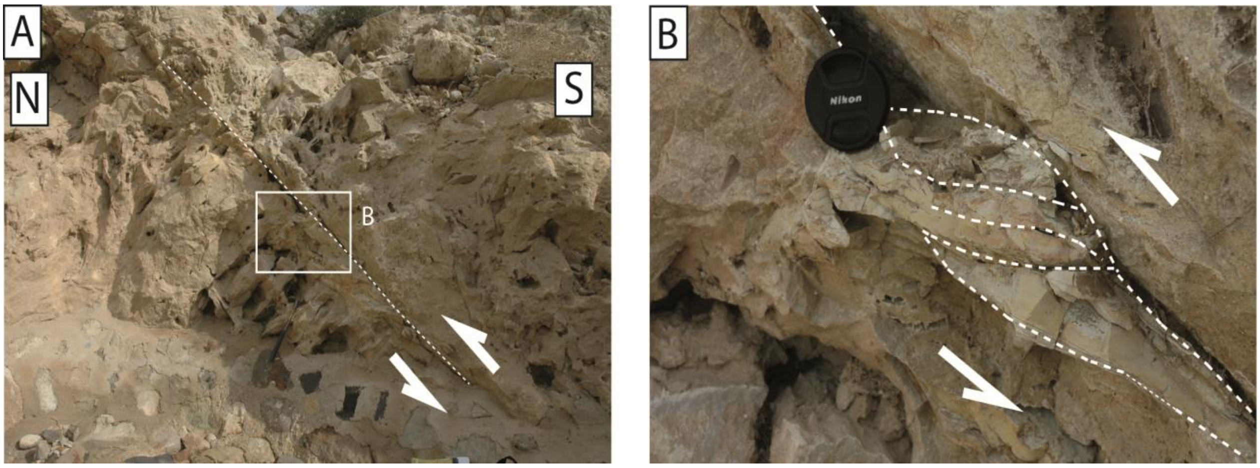

Figure 6.3. Deformed Quaternary travertines by the WAF on the NE corner of the Dead Sea. B) Closer view of almond structures on the fault plane.

The most indicative evidence of the Quaternary tectonic activity of the northern WAF is the deformation of Lisan and Damya lacustrine sediments (**Fig. 6.4**). The latter formation appears in small areas that mostly overlies the Lisan formation while the Lisan formation crops out in greater area of the Jordan Valley. The Lisan formation shows different types of deformation including syn-depositional seismites, recent reverse faulting, cracks and joints. Reverse sinistral faults affecting the Lisan formation were found in two kilometers to the northeastern corner of the Dead Sea and six kilometers northeastwards. In this area no field evidences had been reported before.

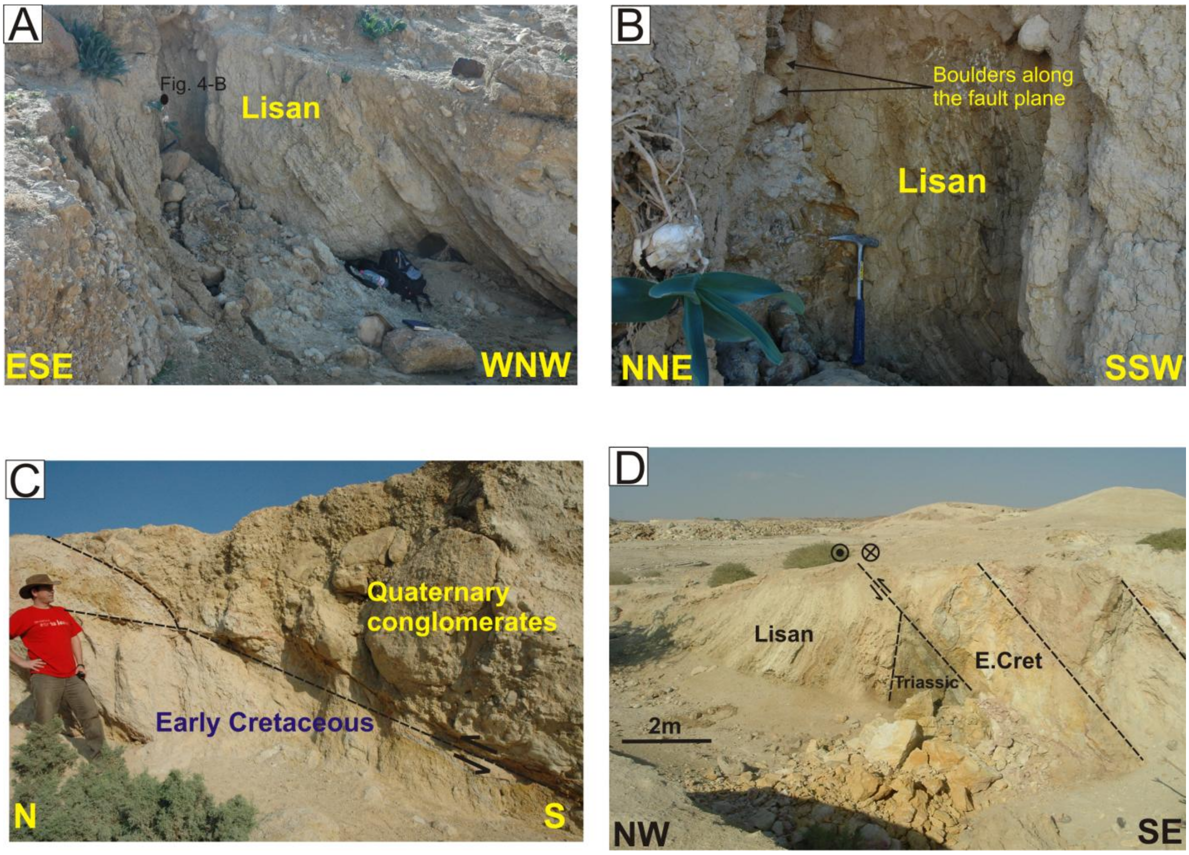

Figure 6.4. (A) WAF deforming the Lisan formation and Holocene deposits near Al-Rama village. (B) Detail of the fault plane of figure 3a where can be identified lacustrine deposits affected by the fault plane. (C) Holocene conglomerates over-thrusting early Cretaceous rocks and the Lisan formation. (D) Reverse-sinistral faults affecting the Lisan formation.

The Lisam formation also shows syn-sedimentary deformation in form of seismites (**Fig. 6.5**). Seismites are very common in the Lisan sedimentary sequence and range from few to tens centimeters in width. Cracks and Joints were also found in the Lisan formation and in the overlaying Damya formation, to the northeast of Al-Hijar Al-Twal site (**Fig. 6.6**).

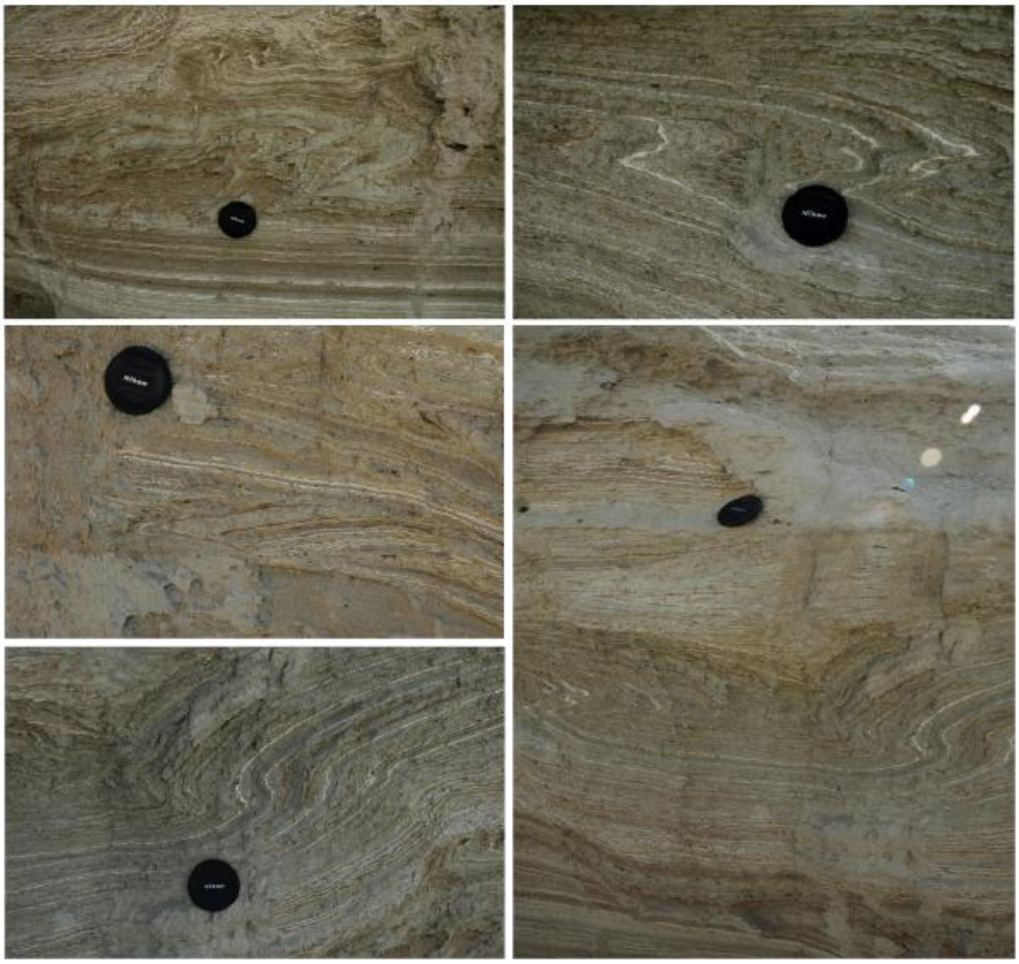

Figure 6.5. Lisan syn-depositional deformation (seismites) near the WAF.

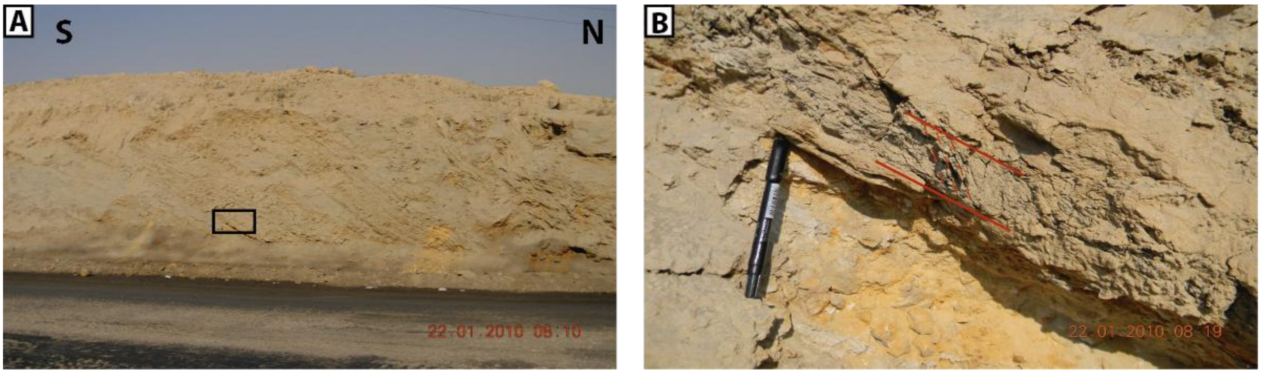

Figure 6.6. Lisan formation dipping to the NW with C-bands indicating a reverse movement.

In active faults systems, the colluvial wedges are common and form by the sedimentation of colluvial deposits in the wrench space caused by the fault movements (Porat et al., 2009; **Fig.6.7**).

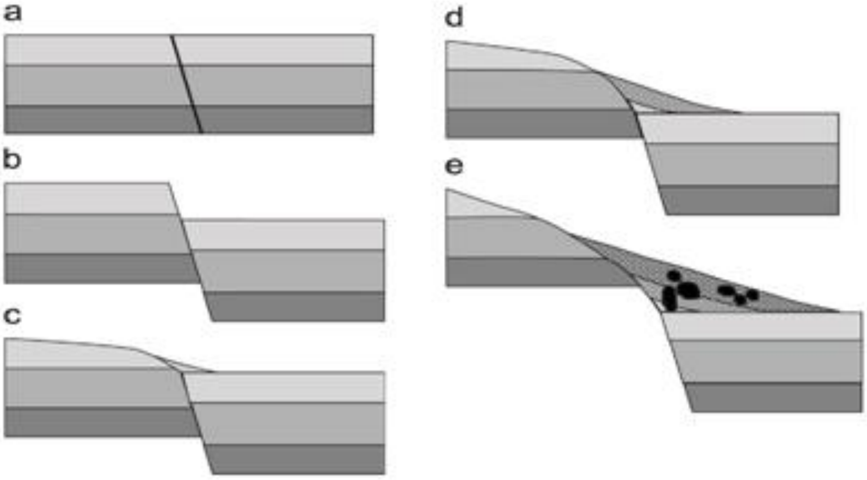

Figure 6.7. Colluvial wedges formation and evolution in active fault slipping (After Porat et al., 2009)

The conjugated faults to the WAF are normal dextral faults striking NW-SE and also found to be active in the area. Some of the colluvial wedges formed by these fault were documented at (3 and 11 km) to the northeast of the Dead Sea (**Fig. 6.8**). In figure **6.8a** one colluvial wedge is formed by displacing the Early Cretaceous rocks. In other outcrops (**Fig. 6.8b**) presents two colluvial wedges formed by two normal faults by displacing Early Cretaceous Marly Limestone downward over a hanging wall of Triassic dolomitic Limestone.

To the north of Al-Rama village (30 km southwest Amman) the WAF splits in two main branches; a pure sinistral strike-slip segment with a NNS-SSW direction that connects with the SHS in the area to the east of the Kafrain Dam (28 Km southwest of Amman), and another segment with reverse component that reactivates the AHS main fault planes.

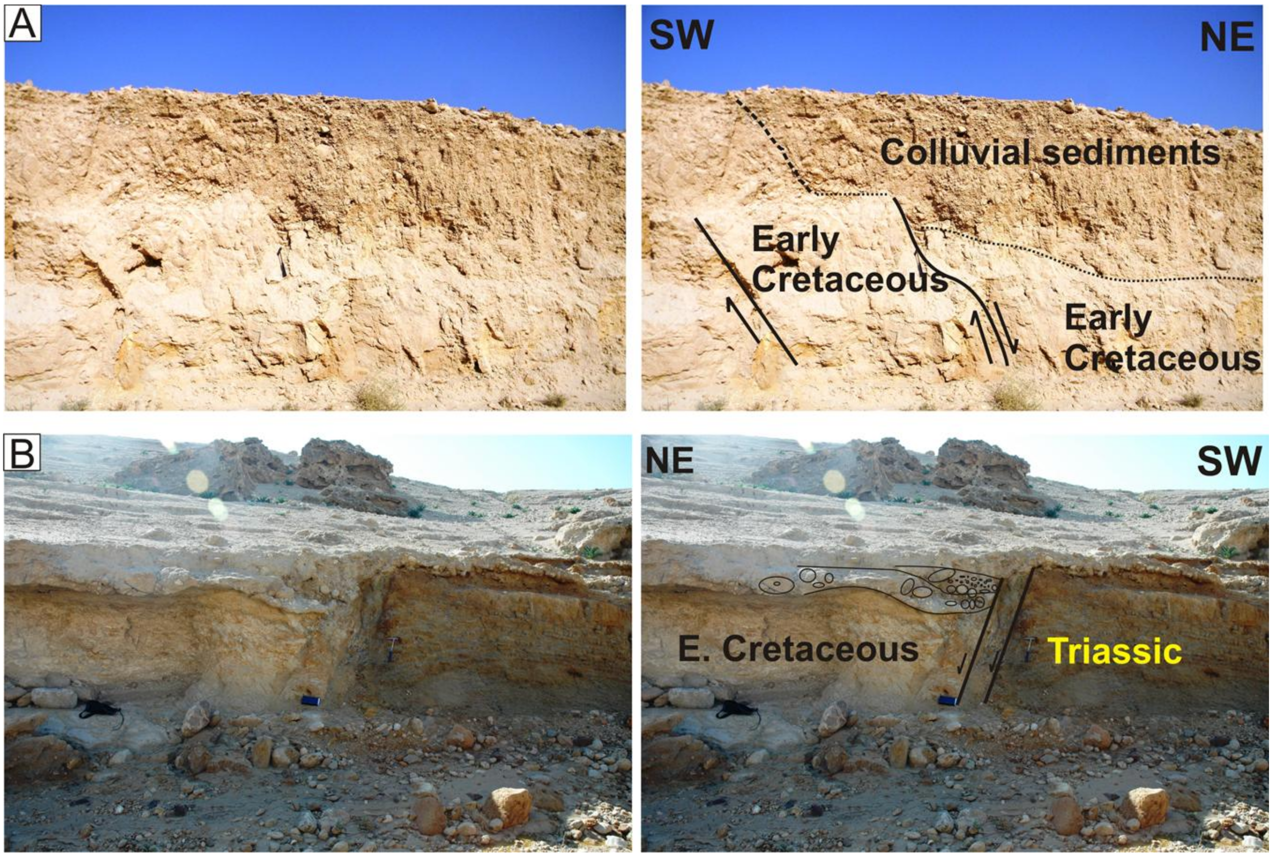

Figure 6.8. Examples of the Colluvial wedges in the WAF area produced by conjugated NW-SE normal faults near Rama village.

6.2.2 Quaternary activity of the AHS.

Most of the published works agree to assign a NNW-SSE horizontal maximum compressive stress (σ1) and an ENE-WSW horizontal minimum compressive stress (σ3) in the Dead Sea area (Hofstetter et al., 2007; Diabat, 2009; Hardy et al., 2010). By contrary, there are few studies about the AHS and the SHS structures (Quennell 1959; Miqble and Zacher, 1986; Diabat, 2009).

Although there is scattered outcrops of the AHS in the NE corner of the Dead Sea, the southwestern termination of the AHS was not well known and, therefore, not clearly mapped. However, the excavation for hotels construction in the eastern coast of the Dead Sea has revealed excellent outcrops of the AHS (**Fig. 6.9**). In this point we can find the southernmost exposure of the AHS, which is sealed by the Lisan formation and soil sediments (**Fig. 6.9**).

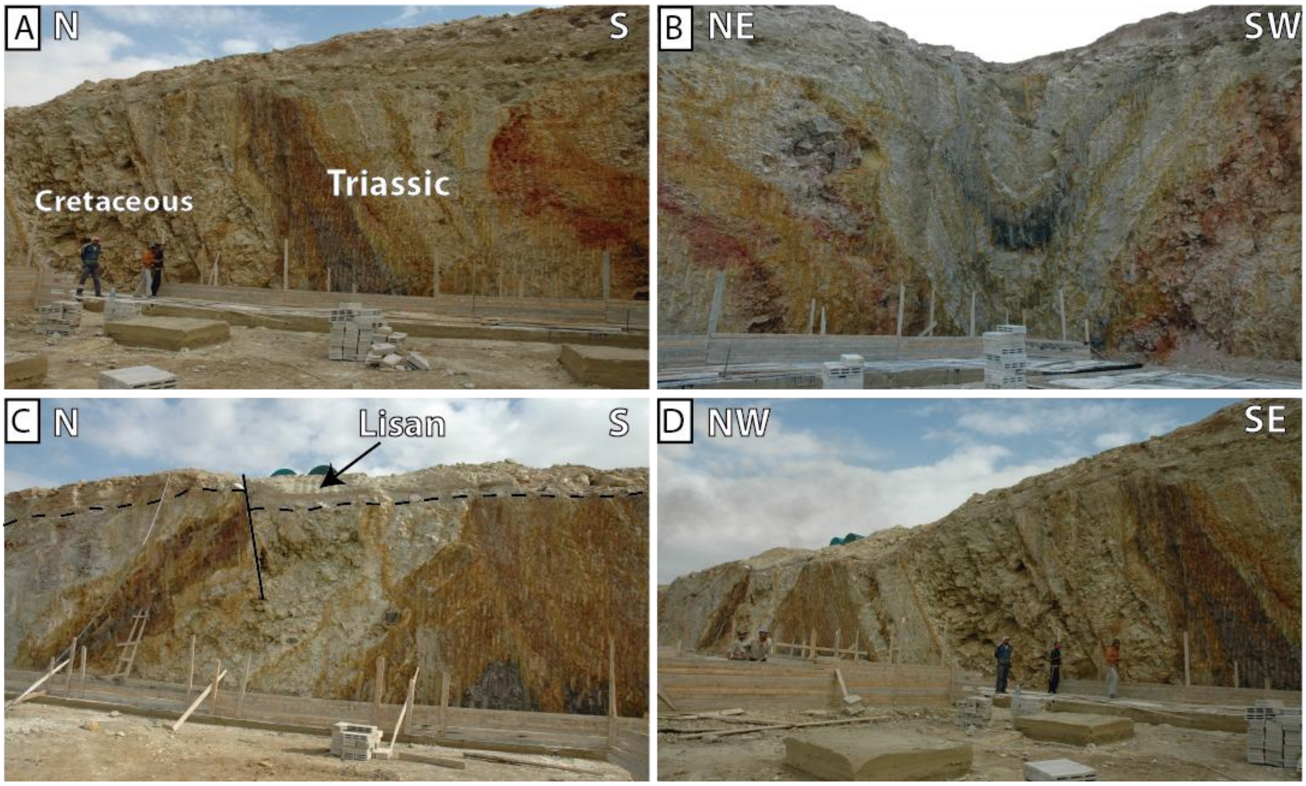

Figure 6.9. The AHS outcrops in the NE corner of the Dead Se.

The AHS, as well as the SHS, preserves the shape and the orientation of the old structure formed in the Late Cretaceous, but the new phase of deformation accompanied to the DSTF is overprinting the older one. The field works conducted through this thesis doctoral for the southern parts of the AHS point to tectonic reactivation applied to this sector of the AHS with several field evidenced.

In the NE of Al-Rama village, the main fault planes of the AHS present a new sinistral movement as the consequence of the reactivation of this structure by the WAF (**Fig. 6.10**). The new striations are overprinting the old ones (**Fig. 6.11**). Multiple slickensides indicate different stages of deformation. Old striations correspond to the old tectonic activity of these structures, whereas new ones record the last deformation and agree with the present-day stress field of the DSTF. This reactivation is not visible beyond the Bahath valley, where only old and inactive structures can be found.

In the NE of Al-Rama village, the main fault planes of the AHS present a new sinistral movement as the consequence of the reactivation of this structure by the WAF. The new striations are overprinting the old ones (**Fig. 6.11**). Multiple slickensides indicate different stages of deformation. Old striations correspond to the old tectonic activity of these structures, whereas new ones record the last deformation and agree with the present-day stress field of the DSTF. This reactivation is not visible beyond the Bahath valley, where only old and inactive structures can be found.

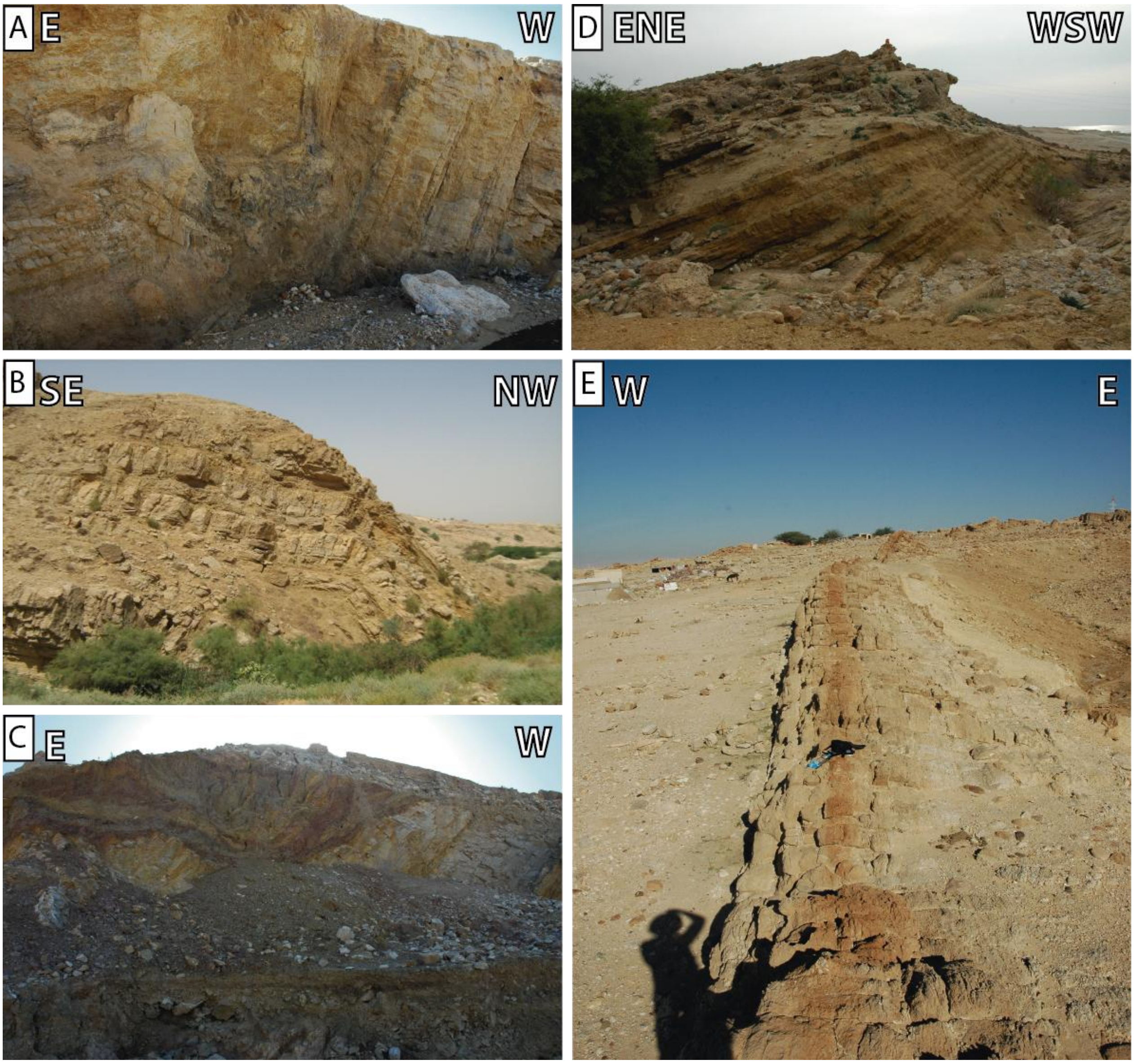

Figure 6.10. Traces of AHS in the area from the Dead Sea to AlRama village.

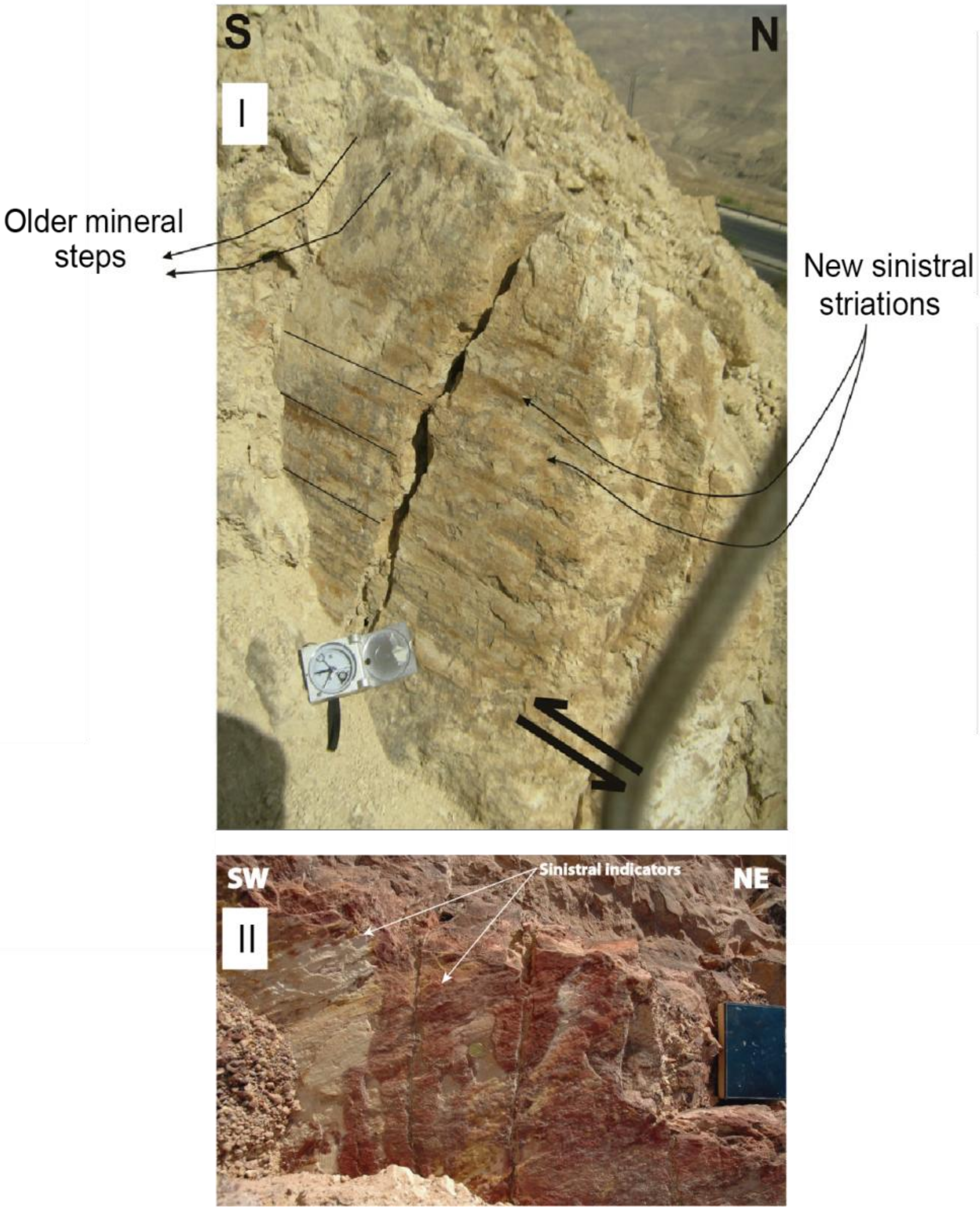

Figure 6.11. I)Newer left-lateral striations overprinting dip-slip mineral steps in the AHS. II) Sinistral reverse striation in Early Cretaceous sandstone in the Baqa´a.

I have documented these changes in the sense of movements along the major faults of the AHS at 8 and 9 km to the northeast of Al-Rama Village. In the Rama village, the transpressional forces along the WAF deform the Late Cretaceous Limestone rocks favoring sub-vertical dipping of these rock (**Fig. 6.12**).

Apart of these sinistral striations, the active tectonics of the AHS cause related landslides along the Na´ur-Dead Sea highway where it used to refer those landslides for road-cut sliding and clays swelling (Emad et al., 2013). In recent work, Palano et al.

(2013) presented a detailed GPS velocities research for the tectonic structures in the DSTF. Among these GPS-points, three points in the area of the AHS indicate sinistral movement within the fixed Arabia Plate. The three points show marginal slip along the AHS with velocity of < 0.1 mm/yr.

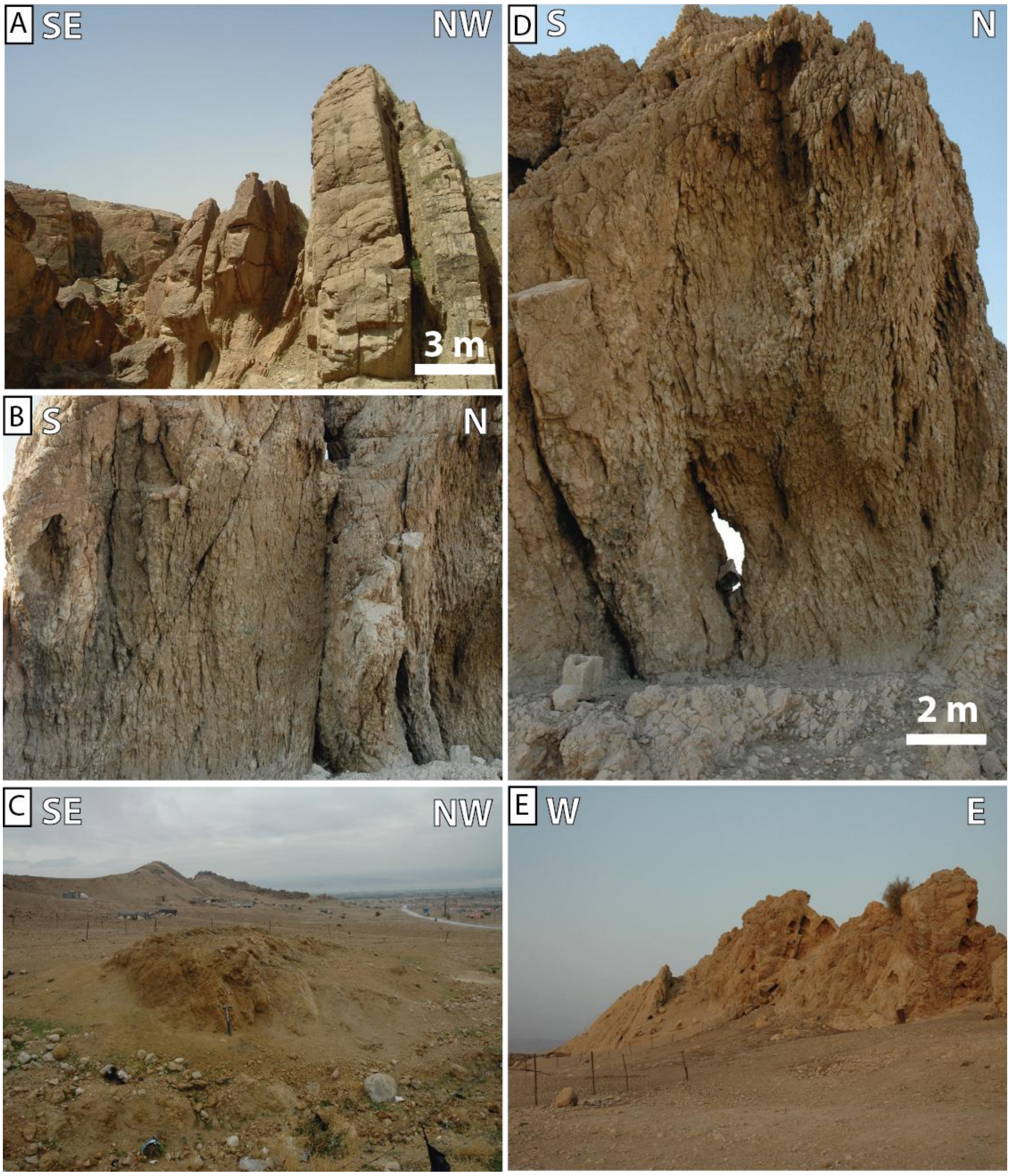

Figure 6.12. Vertical Late Cretaceous rocks in the Rama village.

6.2.3 Quaternary activity of the SHS

The SHS extends from the Kafrain Village to the Baqa basin and shows excellent outcrops of fold-bend faults. This structure forms gentle to steep slopes with well-developed fault planes. Active fault segments of the SHS present sinistral striations, indicating a reverse sinistral component. To the east of the Kafrain village, the Lisan formation is ductile deformed and small-scale folds are documented in this area (**Fig. 6.14**).

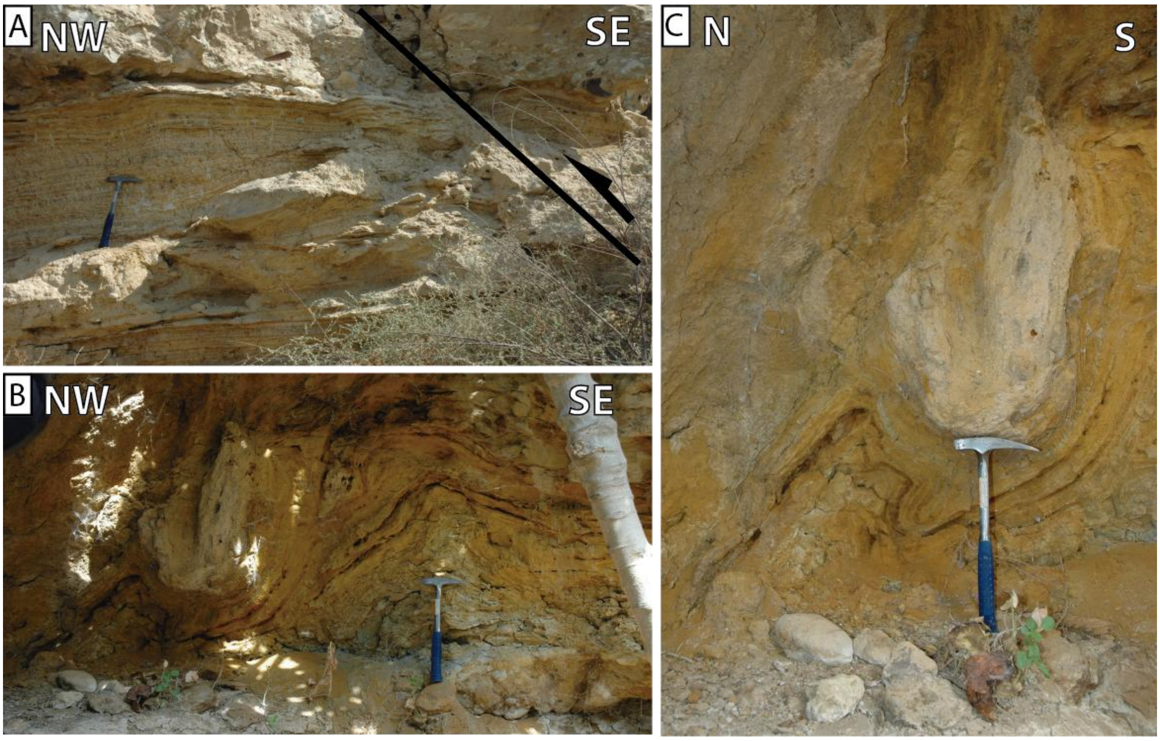

Figure 6.14. Deformation of the Lisan formation 2 km east of the Kafrain Village.

Northwestward and west of the SHS a high density of NW-SE active normal faults can be identified. These normal faults present low to moderate throws to the SW and do not cross over the main NE-SW active segment of the SHS. The tectonic activity of these normal faults is revealed by the presence of colluvial wedges of Holocene and soil sediments to the north of the Kafrain dam (**Fig. 6.15**). These colluvial wedges also indicate a very recent tectonic activity with related seismicity.

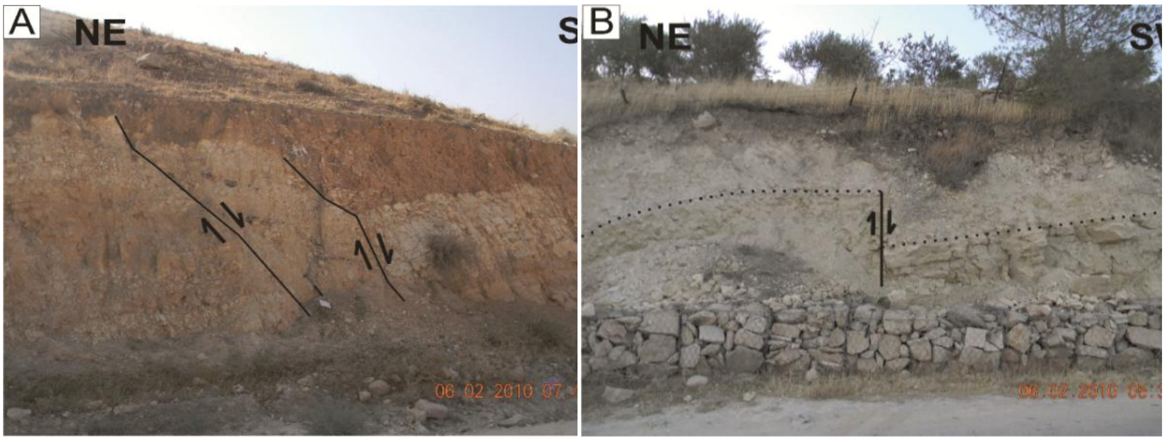

Figure 6.15. Colluvial wedges formed by NW-SE normal faults associated with the SHS.

In the NE termination of the SHS lies the Baqa´a basin, an erosional-tectonic landform (Fig. 6.1). The NE double-folded plunging Late Cretaceous rocks exhibit on of the SAS in NW Jordan. The associated faults of the SHS in the Baqa basin strike, mainly, NE–SW and NW-SE. The NE-SW faults are, generally, oblique reverse, with sinistral and dextral components, and pure reverse faults with some pure sinistral strike slip faults, while the NW-SE faults are dextral oblique normal and pure normal faults. The NE faults dip either to the northwest or to the southeast, with a high angle of 80º-60º (**Fig. 6.16**). There are also evidences of the recent tectonic activity within the Baqa'a Basin as colluvial wedges (**Fig. 6. 17**).

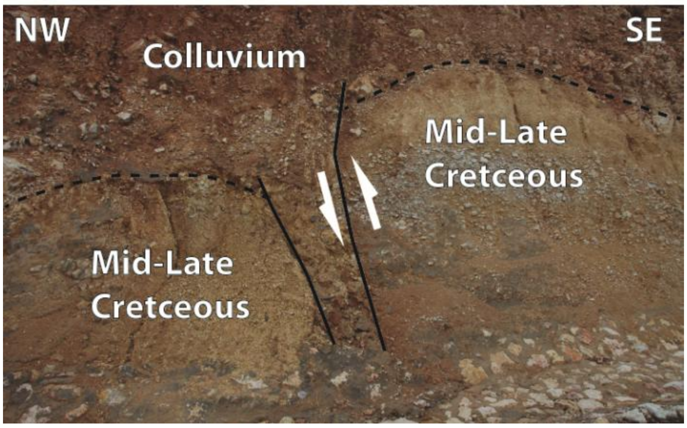

Figure 6.17. Colluvial wedge in the northern border of the basin by NE-SW sinistral reverse fault.

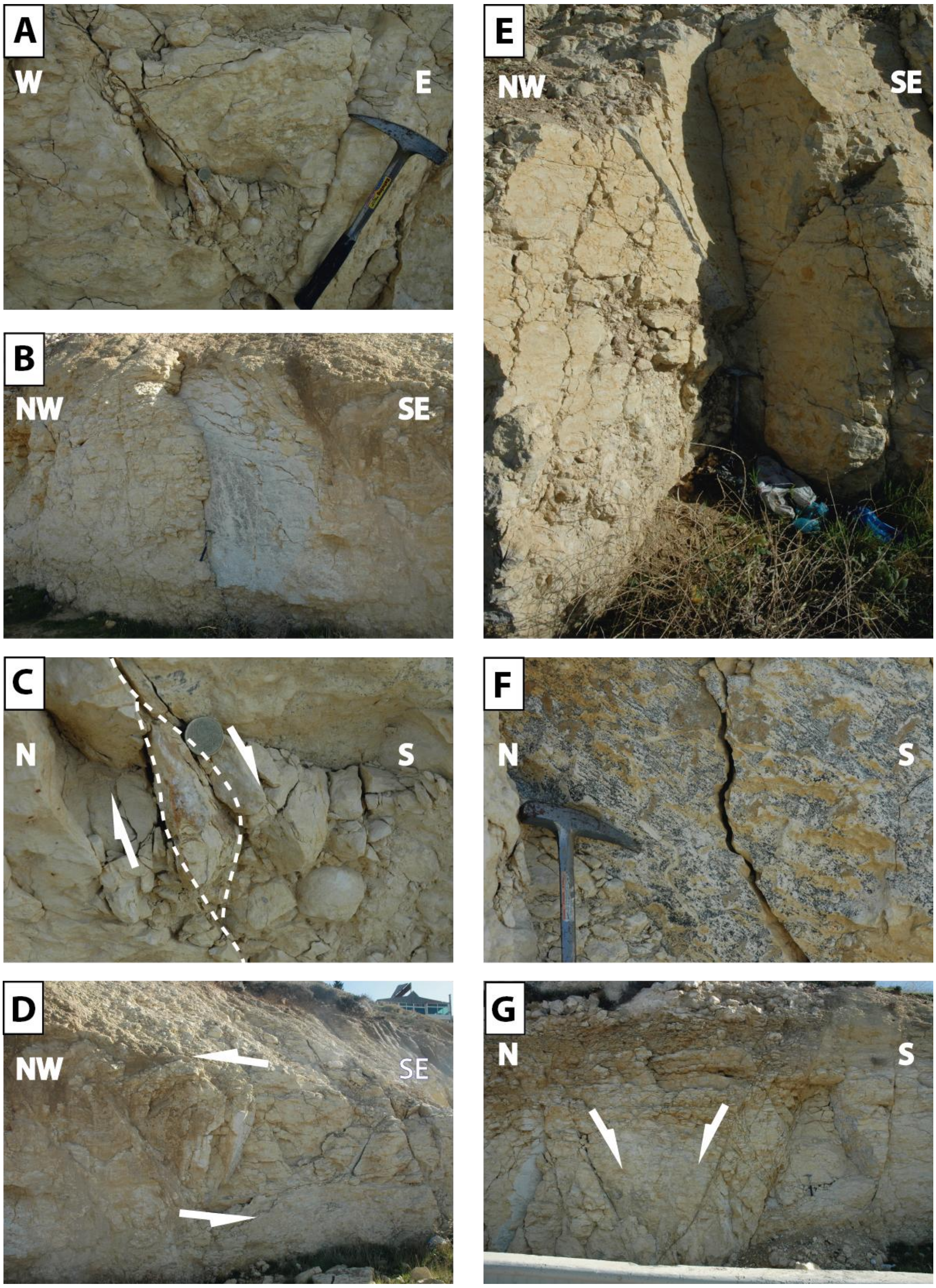

Figure 6.16. Field outcrops of a field station example in the northern border of Baqa´a. A) Congugated normal fault forming small-scale graben. B) Vertical pure sinistral strike-slip fault. C) Inferred normal fault by almond-structure of calcite vein. D) Sinistrally faulted block. E) NE-SW sinistral fault. F) Mineral steps and striations of sinistral reverse fault. G) Small graben formed by NW-SE normal faults.

Chapter 7

Stress-strain analysis

Preface

This chapter presents the stress-strain analysis obtained from the fault-slip data measured in the field. We performed a stress analysis based on fault-slip data for the Amman Hallabat (AHS) and Shueib (SHS) structures. Both structures formed in Cretaceous times under E-W to ESE-WNW maximum compressive stress and have been considered inactive in Neogene times. We have collected about 306 fault slip-data from 14 field stations in the area between the Dead Sea and the cities of Amman and Al Salt. With the aid of the software T-TECTO 3.0 we have obtained the main stress axes for each station. Our results suggest that most of the structures are coherent with the present-day stress pattern associated to the Dead Sea fault system, thus pointing to a possible reactivation of these structures under the DSTF stress tensor.

This chapter includes the following subtitles:

7.1 Stress fields of the DSTF, the AHS and the SHS

7.2 Analysis of field structural data

7.1 Stress fields of the DSTF, the AHS and the SHS

Several studies have analyzed the stress fields in the region under the light of the deformation accommodated by the DSTF (e.g. Eyal et al., 2001; Zain Eldeen et al., 2002; Diabat et al., 2004 and 2009; Hardy et al., 2010; Homberg and Bachmann, 2010). Likewise, the studies presented by Hoffstetter et al. (2007) and Palano et al. (2013) highlighted the current stress regime through seismicity and GPS data analysis. Most of the published works assign a NNW-SSE horizontal maximum compressive stress ($\sigma1$) and an ENE-WSW horizontal minimum compressive stress ($\sigma3$) in the Dead Sea area (Hofstetter et al., 2007; Diabat, 2009; Hardy et al., 2010). However, the studies about the AHS and the SHS are scarce, since these structures have been thought inactive since Cretaceous (Quennell 1959; Miqble and Zacher, 1981; Miqble, 1986; Diabat, 2009).

7.2 Analysis of field structural data

The bulk data of the field stations comprise two main trends of faults planes and fault traces traceble in the geological map at a larger scale. The faults mesurements used in our study area are meso-scaled faults (**Figs. 7.1 and 7.2**). Since the stress field implies a variety of fractures/faults scales, these faults reflect the same mechanisms as the large-scale faulting. The fault types were mainly NE-SW oblique reverse and NW-SE normal faults (**Fig. 7.1**). Less abundant, left and right strike-slip faults were measured striking N-S and NNW-SEE, respectively. The slip direction of the faults was determined using slickensides and calcite and/or gypsum fibers on fault planes (**Fig. 7.2**). Sense of slip indicators include tails and scratches as well as crescent marks formed by the intersection of the main fault plane with secondary fractures such as: R1, R2, X and T (**Figs. 7.1 and 7.2**).

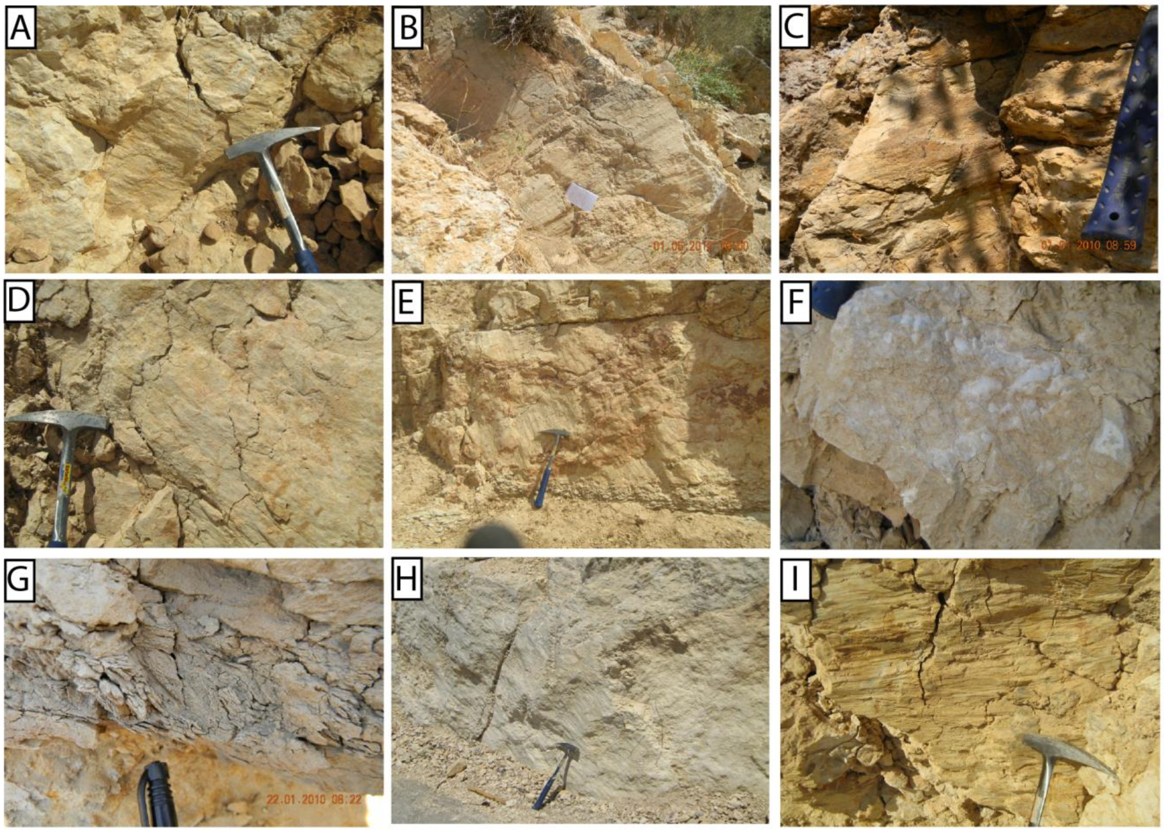

Figure 7.1. Three types of movement indicators along fault planes in the study area; slickensides (A, B, D, E, H, I), slicken-fibers and mineral steps (C, F), "C-S" structures in faulted sandstone layers (G).

Field observations in the southern parts of the study area and near to the Dead Sea show 30–40° trending left-lateral strike-slip faults cutting Quaternary deposits. The sense of movement of these faults is oblique-sinistral with a NE reverse component. Different phases of faulting are attested in some fault planes by the presence of multiple slickensides. Dip-slip striations are overprinted by strike-slip slickensides and calcite fibers suggesting the reactivation of these faults (**Fig. 7.2**). The normal faults found in most stations strike in the range of N110ºE to N170ºE (clockwise sense). Their dips generally exceed 55º, the majority of them dipping between 65º and 90º. The location and details of the 14 stations with the calculated paleostress ellipsoids are shown in **Figure 7.3** and **Table 7.1**. We have classified the obtained stress tensors into three categories: strike-slip, normal and thrust tensors.

Strike-slip stress tensors have the maximum (σ1) and minimum (σ3) stress axes sub-horizontal and the intermediate axis (σ2) sub-vertical. Normal stress tensors present σ1 sub-vertical and sub-horizontal σ3 and σ2. Thrust stress tensors have σ1 and σ2 sub-horizontal and σ3 sub-vertical.

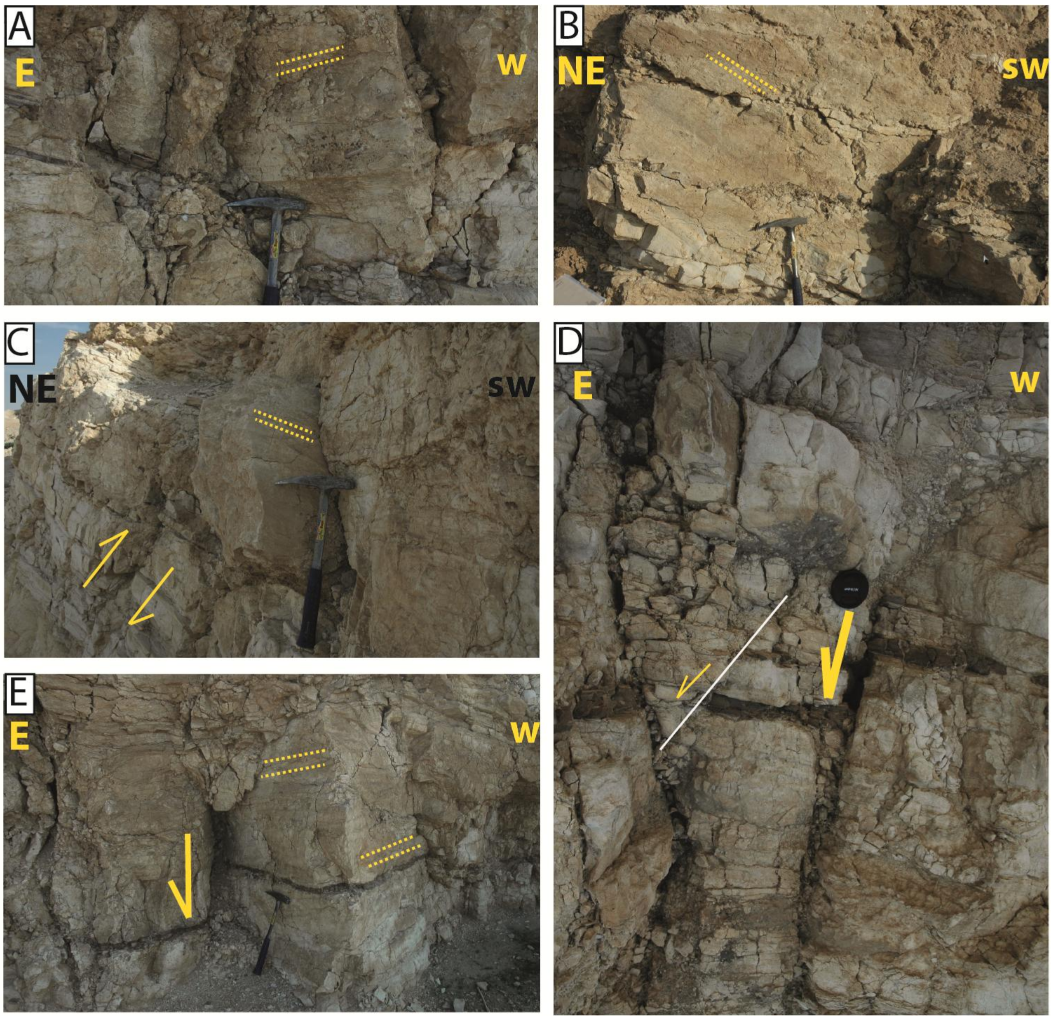

Figure 7.2. Field outcrops of the station number 2. Yellow dotted lines indicate the direction of the slickensides. (A) Sinistral strike-slip fault in NW-SE direction. (B) Vertical fault of oblique sinistral-thrust in NE-SW direction. (C) Sinistral strike-slip fault adjacent to reverse-sinistral fault. (D) Highly fractured block, two small normal faults (displacement of the brown thin Chert layer). (E) Double movements of normal and strike slip faults perpendicular to NE-SW sinistral strike-slip fault.

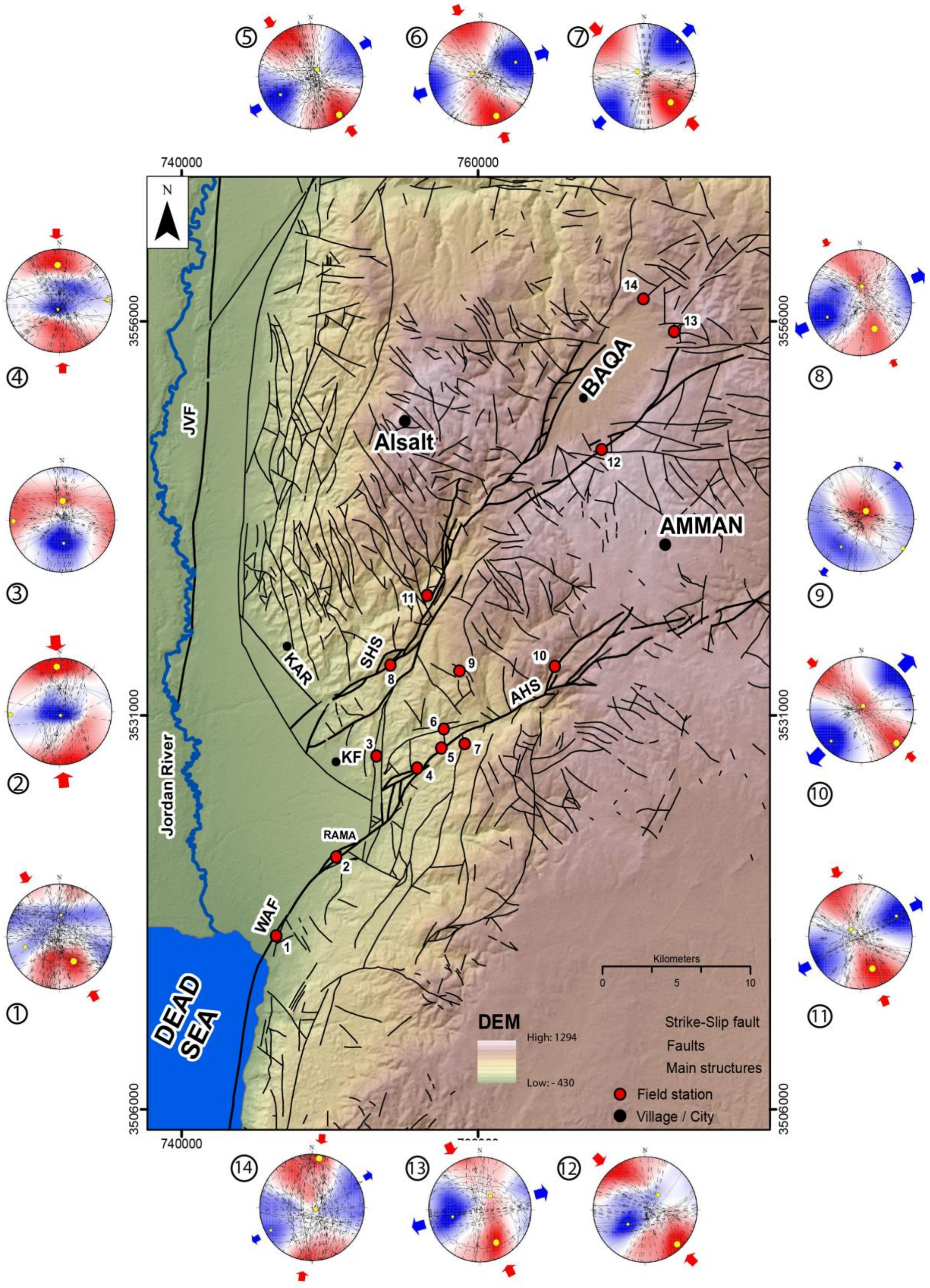

Figure 7.3. Stress tensors obtained for the 14 field stations. Locations of the field stations are marked by red circles and numbered from 1 to 14. The hill-shade base map is derived from 30m resolution digital elevation model from ASTER GDEM database.

The strike slip tensors were found in two forms; pure strike-slip and reverse strike-slip. Pure strike-slip tensors were found in 6 field stations (5, 6, 7, 10, 12, and 14) whilst the inverse component was identified in 4 stations (1, 8, 11 and 13). Generally, most of these stations spread over the main faults of the AHS and the SHS and only one is located in the WAF area (**Fig. 7.3**). Left lateral strike-slip faults strike N-S being parallel to the DSTF. Thrust tensors were found in field stations 2 and 4 (**Fig. 7.3 and Table 7.1**), and normal tensors in stations 3 and 9. Normal tensor was obtained in areas where intense meso-scale normal faulting was identified in the field.

Station No.	δ1		δ2		δ3		Type of Tensor
	Direction	Magnitude	Direction	Magnitude	Direction	Magnitude	
1	150/32	52%	253/20	N/A	5/45	28%	Strike-slip / Reverse component
2	356/9	68%	266/2	N/A	165/81	62%	Pure reverse
3	0/50	36%	268/3	N/A	176/41	72%	Oblique normal
4	357/19	52%	89/4	N/A	189/70	51%	Pure reverse
5	143/4	51%	43/69	N/A	239/21	56%	Pure strike-slip
6	160/7	51%	271/71	N/A	72/18	64%	Pure strike-slip
7	134/17	58%	305/72	N/A	45/3	62%	Pure strike-slip
8	150/29	36%	7/55	N/A	247/20	66%	Strike-slip / Reverse component
9	34/70	54%	125/1	N/A	215/23	41%	Pure Normal
10	133/3	45%	25/80	N/A	225/9	78%	Pure strike-slip
11	159/22	50%	306/64	N/A	61/12	58%	Pure strike-slip
12	137/5	55%	42/48	N/A	230/42	58%	Pure strike-slip
13	153/18	54%	38/53	N/A	256/31	63%	Strike-slip / Reverse component
14	8/3	43%	117/81	N/A	241/5	38%	Pure strike-slip

Table 7.1. Max, Min and Intermediate compressive stress details and type of tensor.

The rose diagram in illustrates the azimuthal distribution of the maximum stress axis (σ1) in the obtained stress tensors (**Fig. 7.4**). The azimuth of σ1 lies between N34º and N188º. Although this range is rather large, the 64% of the stress tensors have a σ1 direction between N140º and N180º. This data are quite consistent and indicate a maximun compression in a NNW–SSE direction.

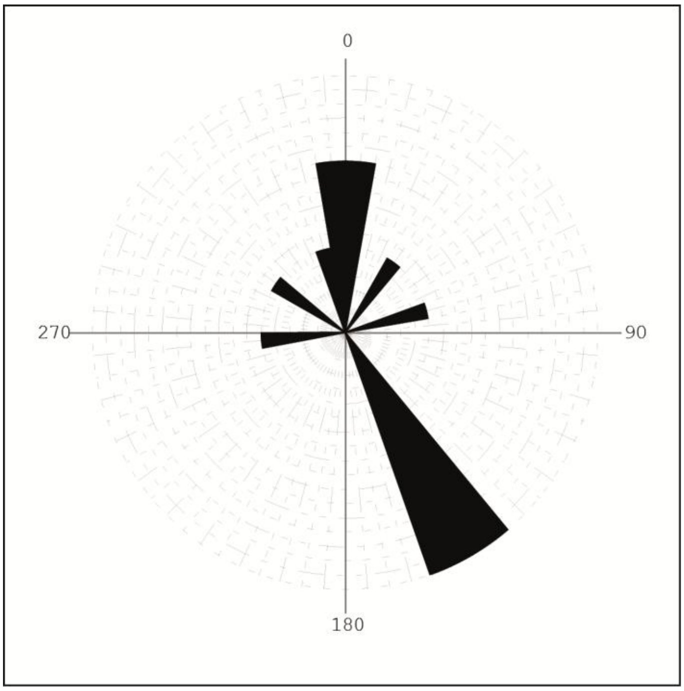

Figure 7.4. Rose diagram of the azimuthal distribution of the maximum compressive stress axis (σ1) in the 14 stations.

Chapter 8

Archaeological evidences of tectonic deformation

Preface

This chapter introduces the archaeological evidences of recent tectonic deformation found in the Tall al-Hammam archaeological site. This site lies between the AHS and SHS structure, and its deformation could be a strong evidence of the historical activity of these faults. This ruin was discovered by Dr. Steven Collins team from Trinity Southwest University/ College of archaeological / Albuquerque-New Mexico USA and it has been excavated since 2005. The evidences presented in this chapter were documented through the first field work I conducted on May 2012 that coincided with the seventh season of the archeological excavation.

Dr. Collins has proposed that this archaeological site corresponds to the ancient realm of Sodom, reported in biblical and koranic texts. The seismic damages reported in this Thesis could be used to reinforce the idea of that this old kingdom was destroyed by an earthquake. If this theory proves to be right, a good candidate to have trigger such event will be the AHS.

This chapter includes the following subtitles:

8.1 Archaeoseismological background of the study area

8.2 The Tall al-Hammam Archaeological site

8.3 Observed deformation

8.4 The theory of Sodom and Gomorrah

8.1 Archaeoseismological background of the study area

Ancient man-made structures are generally weak against earthquake and active tectonic deformation, providing good age-control for the timing of destructive earthquake events. Damage in archaeological sites has been used as valuable indicator of active tectonics, filling the gap between the instrumental seismic catalogs and paleo-seismological studies based on surface trenching (Klinger et al., 2000b; Neimi et al., 2001; Haynes et al., 2006; Marco, 2008; Marco and Klinger, 2014)

The Jordan valley, especially in its lower part, presents a very rich cultural heritage reflecting its continuous historical occupation by human communities (Marco, 2008; Ferry et al., 2011). This region, especially near the Dead Sea, hosts several archaeological sites (e.g. Telleilat Ghassul; Deir Alla; Tell Nimrein; Tell Alsa΄aideh). Most of these sites were dated using pottery and absolute ages using C^{14} aging method (Galli and Galadini 1999; Haynes et al., 2006; Marco, 2008; Ferry et al., 2011; Collins, 2013). Some of these archaeological relicts present clear tectonic deformations and have been used to infer slip rates, earthquake magnitude, or simply record active tectonic or historical earthquakes of this tectonically active region (Hayenes et al., 2006; Ferry et al., 2011). These kind of severe damage has been attributed to the active deformation of the southern part of the Dead Sea Transform Fault (DSTF) and used to estimate earthquake returns periods (Ferry et al. 2007 and 2011, Marco and Klinger, 2014 and references therein).

8.2 The Tall al-Hammam archaeological site

The Tall al-Hammam archaeological site is situated between the main two tectonic structures in the study area, the Amman Hallabat structure (AHS) and the Shueib structure (SHS) (**Fig. 8.1**). The recent activity of these two structures implies the possibility of occurrences of large historical earthquakes in the region and might shed light on the destruction of ancient cities and the disappearance of their cultures.

The Tall al-Hammam archaeological site is the largest MBA sites in the Jordan valley plain (Collins et al., 2010). The Tall al-Hammam archaeological site is located 27 km southwest of Amman and 14 km NNE-SSW the Dead Sea (Collins et al., 2009 and 2010) (**Fig. 8.1**). This ruin consists of two main parts, the upper and lower Tall (Tall is the Arabic name of hill), together with related dolmens and a tombs site to the east of the Tall. Collins et al., (2010) dated different man-made structures in this site for which they used it in the chronological classification of the communities occupied the area.

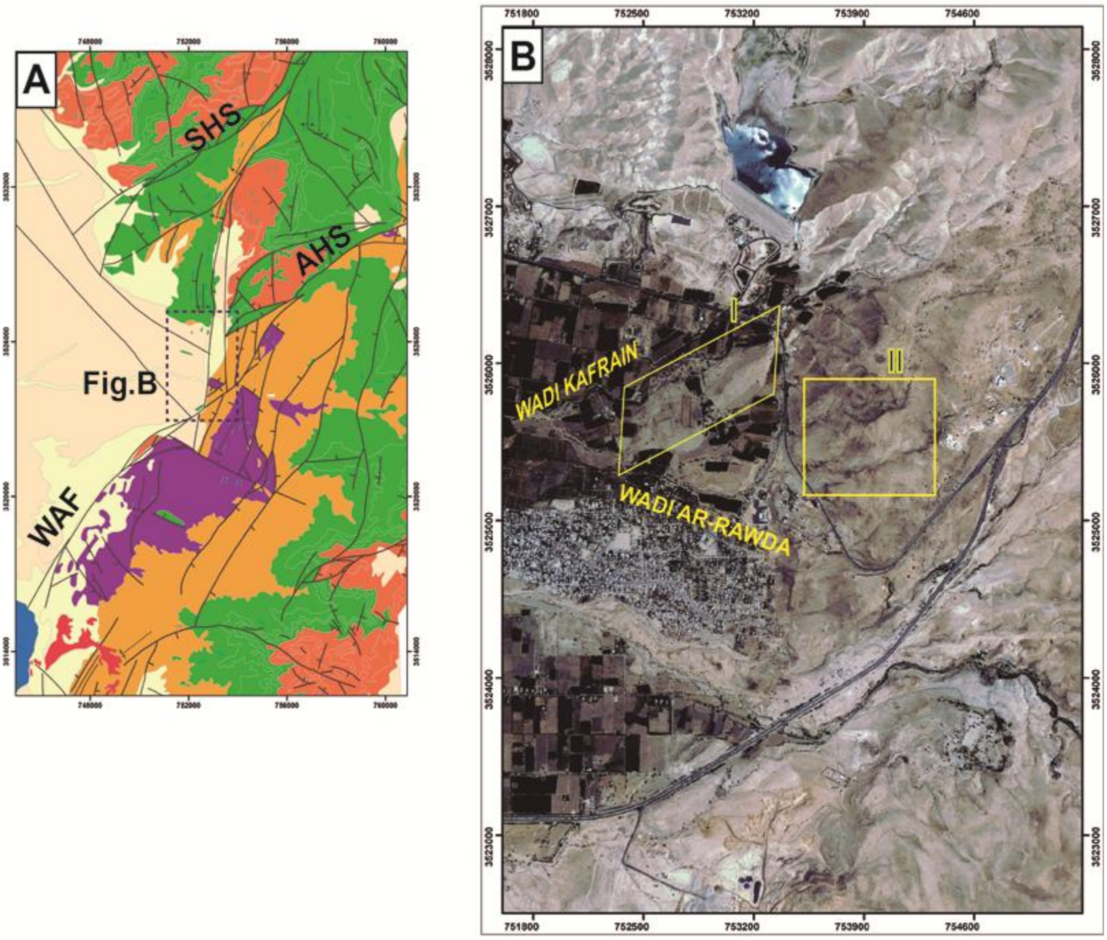

Figure 8.1. A) Location of the Tall al-Hammam archaeological site in respect to the main structures. B) Ortho-photograph showing the geographical setting of the ruin where (I) is the main tall site and (II) is the dolmen and caves site associated to the ruin.

Up to now, ten seasons of excavation revealed that occupation began at least during the Chalcolithic Period (CP, 4500-3500 BCE) and extended continuously through the Early Bronze Age (EBA, 3500-2350 BCE), the Intermediate Bronze Age (IBA, 2350-2000 BCE), and into the Middle Bronze Age (MBA, 2000-1550 BCE). Late Bronze Age (LBA) relicts are rare, and there is no discernable LBA architecture thus far. City walls, ancient streets, and different man-made structures in this archaeological site have been dated with the aid of the discovered pottery and antiquities (Collins et al. 2010).

According to the last discoveries, this site seems to be an urban hub of a significant city-state that controlled the trade routes coursing through the Middle Jordan Valley at least during the EB2 to MB2 (2500 to 1550 BC). This evolutionary and economic trade activity of these city forced the travel routes between the ancient northern and southern important kingdoms to pass through this city and in certain eras (i.g. Iron Age 2) it became a store city and distribution center of significant import (Collins et al., 2015).

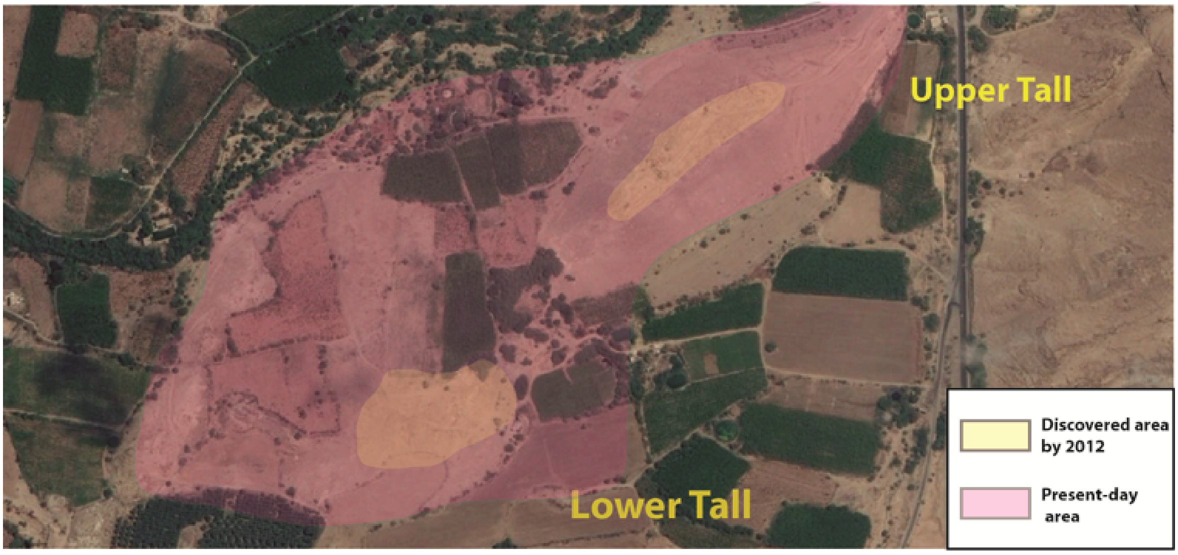

Figure 8.2. Aerial photo (from Google Earth) showing the excavated area at the time of my field work in the area and the total up to present-day excavated area.

I conducted an inspection to this archaeological site in order to find evidences of deformations that may evidence the occurrence of ancient earthquakes. The inspected area corresponds to the area unburied before of 2012 (yellow area in **Fig. 8.2**), since the rest of the excavation was discovered after my field campaing.

8.3 Observed deformation

The Tall al-Hammam in its lower Tall manifests dextral fault deformation evidenced by offset and tilts of some walls. These offsets are present in two Middle Bronze Age walls, which are displaced 26 and 20 cm respectively according with a dextral sense of movement (**Figs. 8.3a,b**).

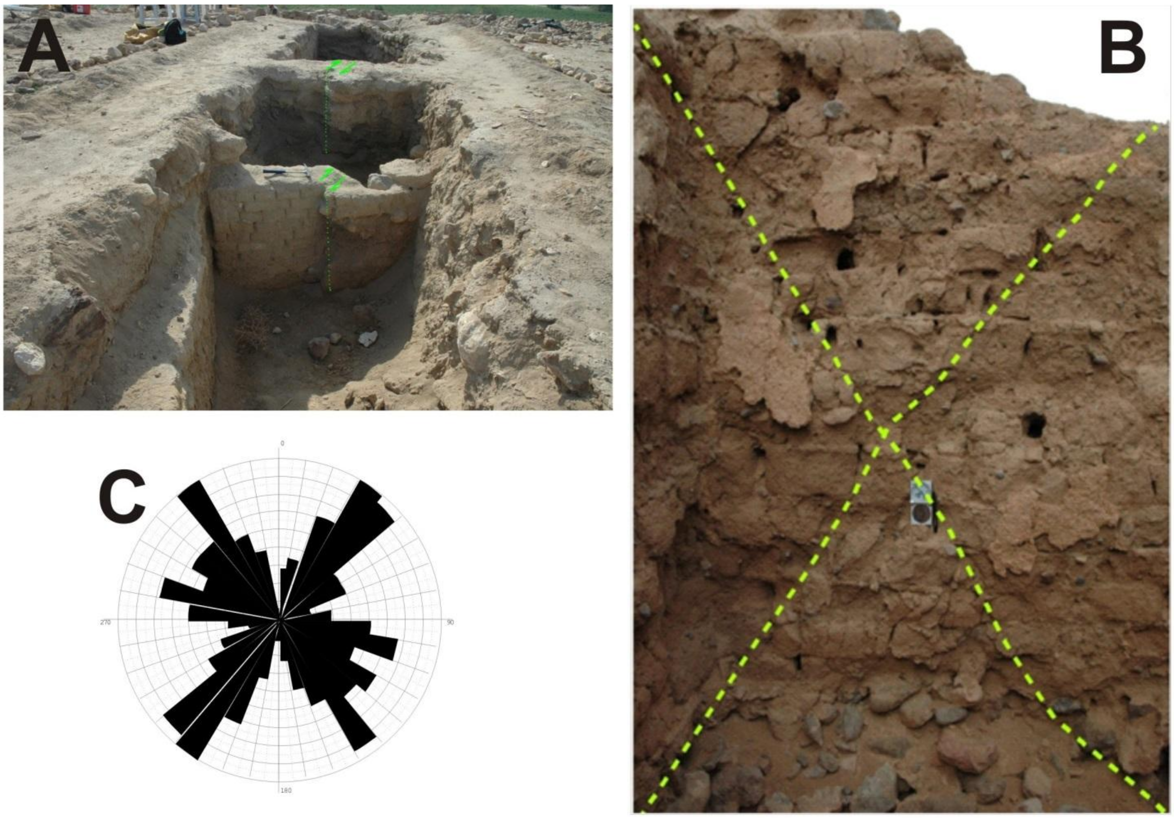

Figure 8.3 A) Faulted walls in the lower Tall, 26 and 18 cm offsets. B) Tilted wall in the upper Tall. C) Rose diagram of the crack and joints orientations.

Apart of these offsets, there are several joints and fractures in boulders within walls. We have measured 212 boulder fractures in the Upper Tall These fracture are either open, generally, 0.5-2 cm spaced fractures and non-spaced joints (**Fig. 8.4**). Fracture orientations strike mainly NW-SW and NE-SW (**Fig. 8.3c**).

Figure 8.4. Examples of the cracks measured in the upper Tall. The photo to the upper right corner shows general view of the upper Tall.

8.4 The theory of Sodom and Gomorrah

The excavation carried out by Dr. Collins in its successive field campaigns have unburied a much large area that the one analyzed in 2012. These new excavations suggest that the Tall el Hamman site could be the ruins of the ancient city of Sodom (**Fig. 8.5**). Despite some other authors have proposed other locations for the city of Sodom, Collins (2007, 2013) states that the present-day location of the Tall el-Hamman remains a better candidate that the previously proposed ones. The new excavation seasons have unburied the biggest Middle Bronce Age (MBA) ruin in the region, and presents the proper potential sites of the ancient cities of Gomorrah and Sodom mentioned in the Bible and in the Qurán (**Fig. 8.6**).

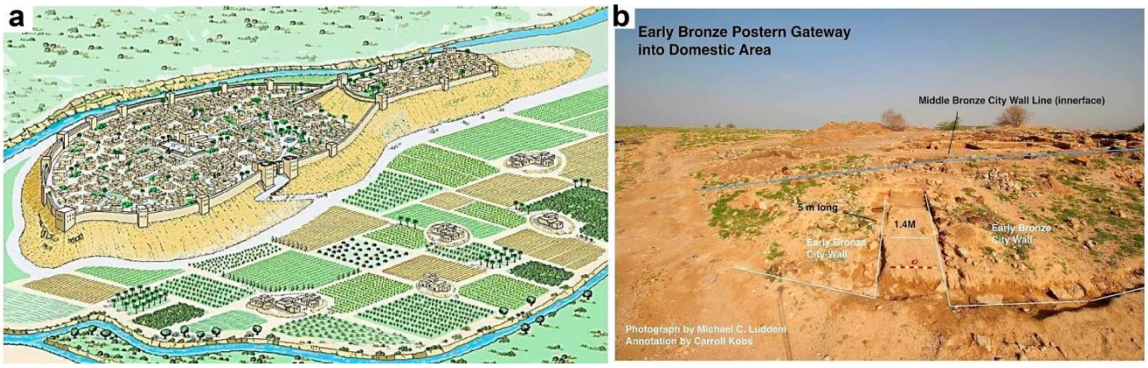

Figure 8.5. a) Representation of Tall el-Hamman during the Middle Bronze Age (drawing by L. Ritmeyer) and b) Early Bronze Postern Gateway into the Domestic Area of the Tall el-Hamman archaeological site (Modified from Collins et al., 2015).

According to Collins (2007; 2012; 2013) the Tall al-Hammam present clear evidences to be a very strong candidate for the location of the two cities of Sodom and Gomorrah based in the following reasons:

- Sodom and Gomorrah were the biggest cities in the southern Levant in the period 3600-1700 BC. This is coherent with the fact that the Tall al-Hammam is the biggest discovered MBA (*same time span*) ruin in the region.

- The City mentioned in the Bible and referred to the place were *Lot* relocated is about 20 miles east of the Jerusalem hills. This is exactly the location of Tall al-Hammam.

- The discovered ruins in the area to the NE of the Dead Sea “Kikkar” (Kikkar: the mentioned name of the Jordan valley in the Bible) did not present good candidature of the Sodom and Gomorrah before the discovery of the Tall al-Hammam.

Some authors have proposed that Sodom and Gomorrah were destroyed by a terrible natural apocalypse matching the description in the Book of Genesis, probably due to a big earthquake (Harris and Beardow, 1995; Neev and Emery, 1995; Chester and Ducan, 2009). The theory of the new location of the city of Sodom, together with the archaeological damages found in the field campaign will present a strong evidence of the seismic potential of the AHS.

Figure 8.6. Gommorrah and Sodom location according to the excavation results in the Tall al-Hammam site (After Collins 2013). Red dashed rectangular point to the borders of the PhD study area in respect to the ancient cities.

Chapter 9

Discussion

Preface

In this chapter I will discuss the main results of this Thesis. From the analyses presented in the previous chapters I will expose how the AHS and SHS have a clear Quaternary activity and play an important role in the northern closure of the Dead Sea. They have been reactivated by the present-day stress field of the DSTF as can been deducted by the field evidences of Quaternary activity and the stress-strain analysis discussed in chapter 7.

I will divide this discussion into 4 main points, where I will expose my conclusions over the i) Quaternary landscape evolution of the study area and how this analysis suggests that AHS and SHS are important structures, ii) the evidences of the Quaternary activity of the AHS and SHS structures and their evolution, iii) the kinematics of these structures respect to the present-day stress field of the DSTF and iv) finally I will propose a new model for the northern closure of the Dead Sea basin.

This chapter includes the following subtitles:

9.1 Quaternary landscape evolution of the northern WAF

9.2. Quaternary tectonic activity of the AHS and SHS structures

9.3. Kinematics of the AHS and SHS respect to the DSTF

9.4. A new model for the northern closure of the Dead Sea basin

9.1 Quaternary landscape evolution of the northern WAF

The northern part of the Wadi Araba Fault (WAF) constitutes the eastern boundary of the Dead Sea pull-apart basin. The landscape analysis done in this Thesis suggest interesting landscape features of this structure. All the morphometric analyses that evaluate the general landscape pattern depict similar features, with high values of erosion-incision associated with the drainage network of the eastern side of the Dead Sea and delimiting in a good way all the tectonic structures in the area.

The roughness map (**Fig. 5.3**) shows high values of surface roughness in the southern and central Dead Sea, whereas they are lower in the northeastern termination of it. The analyzed map shows a very good relation between the main faults with high values of roughness, that can be explained by a higher topographic variability related to these structures. The area north to the Dead Sea is characterized by low values of roughness and high values only can be found related to the AHS and SHS. This characteristic is also clear in the HI-LISA map (**Fig. 5.7**), where AHS and SHS represent the only clear boundary between low values north of the Dead Sea and high values related to the aforementioned structures. As the HI-LISA maps represent landscape dissection and not variability, it is more sensitive to river incision. In this map higher values concentrates in the central Dead Sea basin, and are probably related to a higher subsidence rates in that part.

The extracted swath profiles also depict interesting features that can be attributed to the tectonic activity of the structures studied in this Thesis. The TransJordanian Plateau is clear in all the profiles, as a quasi-flat surface where mean, maximum and minimum elevation merge together. The easternmost North-South swath (NS02, **Figs. 5.4 and 5.5**) depict the TJP as a flat surface with a regular elevation ranging 800-900 m. However, in the western N-S profile this same surface shows bends and draw local highs and lows. These "bends" could respond to a "topographic rebound" due to the high erosion conditioned by the subsidence of the WAF and related structures. In the East-West profiles this feature is clear as an upward bend of the TJP at its union with the Dead Sea (**Fig. 5.6**). It is noteworthy that this upward bend is less pronounced in the profile EW02 that crosses over the northern termination of the WAF. This feature agrees with the roughness and HI-LISA findings, whose values in that area where lower.

The most striking features of this topographic analysis can be summarized in:

- Roughness and HI-LISA maps show a good correlation with the active structures of the study area.
- There are not any evidence of a northern structure closing the Dead Sea apart of the NW-SE normal faults related to the AHS and SHS
- The northern termination of the WAF depict lower values of roughness and LISA-HI and no upward deflection of the TJP.

All of these findings suggests interesting conclusions: i) The AHS and SHS, if active in the Quaternary, could play an important role in the northern closure of the Dead Sea. ii) The nature of the northern termination of the WAF, which has been traditionaly interpreted as a normal fault with NW extension, probably has an inverse character as can be deducted by the lower relief and less erosion. This inverse character would better fit with the present-day stress field and the kinematics of the DSTF.

The geomorphic indexes calculated for the selected basins of the eastern margin of the Dead Sea also shows very interesting characteristics. The four largest basin of the study area (nº 14, 25, 26 and 33, see **Fig. 5.8**) depict highly convex normalized profiles, thus suggesting a transient-state of the drainage network. These awkward shapes are conditioned by river configuration, with an upper part located in the TJP and a middle and lower part flowing over the transition zone that merge the TJP with the Dead Sea. Smaller basins do show such convex shapes, but depict in most cases linear or smoothly convex profiles. This feature are due to a intense base-level lowering of the Dead Sea reaching elevation below present-day sea level. These rates should be lower in the southernmost part of the study area, where rivers 34 to 36 show "normal" profiles according with the topography (**Fig. 5.9**). They present an upper part (over the TJP) with linear to convex shape and a middle to lower parts with a well-defined concave profile, thus indicating a process of headward erosion that is not fueled by a so intense base-level lowering.

The hypsometric curves depict the same characteristics, suggesting a very young relief with basins that are being intensively eroded in their mouths and cannot reach equilibrium profiles (i.e. S-shaped curves). Again, the most convex hypsometric curves concentrate in the middle part of the Dead Sea basin (**Fig. 5.10**) with also higher values of hypsometric integral (HI) (Fig. 5.11). The four largest basins show characteristics profiles with a flat upper part that includes most of the area of the basin (**Fig. 5.10**). These curves also indicate extremely young landscape agreeing with normalized profiles.

The bulk erosion map calculated by subtracting the "pre-incision" surface (interpolated with basin ridgelines) from the present-say topography depict similar features than the other morphometric parameters. They are higher in the middle part of the Dead Sea, especially in the largest basins. At this respect, It has to be considered that lower values in small basin do not necessarily indicate lower erosion rates. In such small basin the lowering of watershed divides could play an important role. If watershed divides (or basin ridgelines) lower to a high rate, this could underestimate the "pre-incision" surface and yields not reliable values.

Finally the area-slope profiles and the Ksn values indicate a clear transient state of the landscape. Some of these profiles show a more or less defined linear trend in their upper parts but no relation in their lower parts (near river mouth). There is a clear break in slope-area profiles almost in all river, being the lower parts chaotic and without a clear trend. This is characteristic of transient-state profiles, where incision rates cannot counteract uplift rates (down-lift or subsidence in this case).

All the geomorphic indexes analyzed suggest a very young landscape in transient state. River in transient state do not depict well-defined trends and comparisons can be fruitless. They indicate a higher subsidence rate in the lower part of the Dead Sea basin, and probably a bit lower in the northern termination of the Dead Sea. These findings agree with the previous analysis, suggesting the different behavior of the WAF in their northern termination.

9.2. Quaternary tectonic activity of the AHS and SHS structures

There are only few active tectonic studies in the Jordanian side of the Dead Sea if compared with the western side. Active tectonic studies in this region have mainly focused in analyzing the DSTF main fault planes, excluding those areas thought inactive in Quaternary times. However the DSTF is not the only active structure accommodating stress in this plate boundary (Chaimov et al., 1990). In this study we found evidence of the Quaternary activity of the AHS and the SHS, thought inactive since Late Cretaceous. Recent GPS-derived slip-rates for the southern DSTF suggest that there are not significate differences between the WAF and the JVF (LeBeon et al., 2008; Al-Tarazi et al., 2011), thus indicating that the stress accommodate by the AHS and SHS must be marginal and probably concentrates in the southwestern termination of both structures. This marginal activity probably dies to the NE, since the movement that is being transferring to the AHS is small and not enough to reactivate the whole structure (**Fig. 9.1**).

In contrast with the high number of scientific works describing in detail the southern and central WAF, the northern termination of this active fault is not well constrained (e.g. Atalla, 1992; Klinger, 2000; Neimi et al., 2001; Haynes et al., 2006; Hoffstetter et al., 2007; AlZoubi et al., 2007; le Beon et al., 2008 and 2012; Porat et al., 2009). Previous authors have suggested that the WAF ends 2-3 kilometers NE of the Dead Sea (Al-Zoubi et al., 2006; 2007; Smit et al., 2008). However, our new field data for this area suggest clear tectonic activity of the WAF between the northern edge of the Dead Sea and the Al-Rama village. In this work I have presented evidences of tectonic deformation of the Pleistocene-Holocene Lisan and Damya formations along the approximately 12 km that separate the NE corner of the Dead Sea and the Al-Rama village. These outcrops show fault planes striking mainly N 25-30º E and dipping 60-70º NW, which agree with a continuation of the WAF. Moreover, in some of these sites there are colluvial wedges associated with fault planes and deformed Holocene soils related to conjugate normal oblique faults to the WAF.

The archaeological site of Tall el-Hamman present clear evidences of tectonic deformation. This ruin has been recently interpreted as the old city of Sodom, that was destroyed by a terrible natural apocalypse matching the description in the Book of Genesis, probably due to a big earthquake (Harris and Beardow, 1995; Neev and Emery, 1995; Chester and Ducan, 2009). The position of this site respect to the AHS could suggest this structure a possible seismic source for this earthquake. The theory of the new location of the city of Sodom, together with the archaeological damages found in the field campaign will evidence the seismic potential of the AHS. At this respect the absence of instrumental seismicity in the area could respond to the lower rates that should have this structure.

Most of the seismic events in the region are related to the DSTF, but the AHS and the SHS do not show significant seismic activity. There are few low-to-moderate seismic events in the last 80 years (instrumental period) associated with the AHS and SHS. However, these two structures proved seismogenic behavior within several sites in the study area as shown in the colluvial wedges. As in other part of the world, instrumental earthquake catalogs are not enough to characterize seismic hazard for tectonic structures with low-to-moderate activity as occurred in the cases of Christchurch earthquake and aftershocks in New Zealand (Quigley et al. 2010) and the Tohoku-Oki earthquake in Japan 2011 (Koyama et al., 2012).

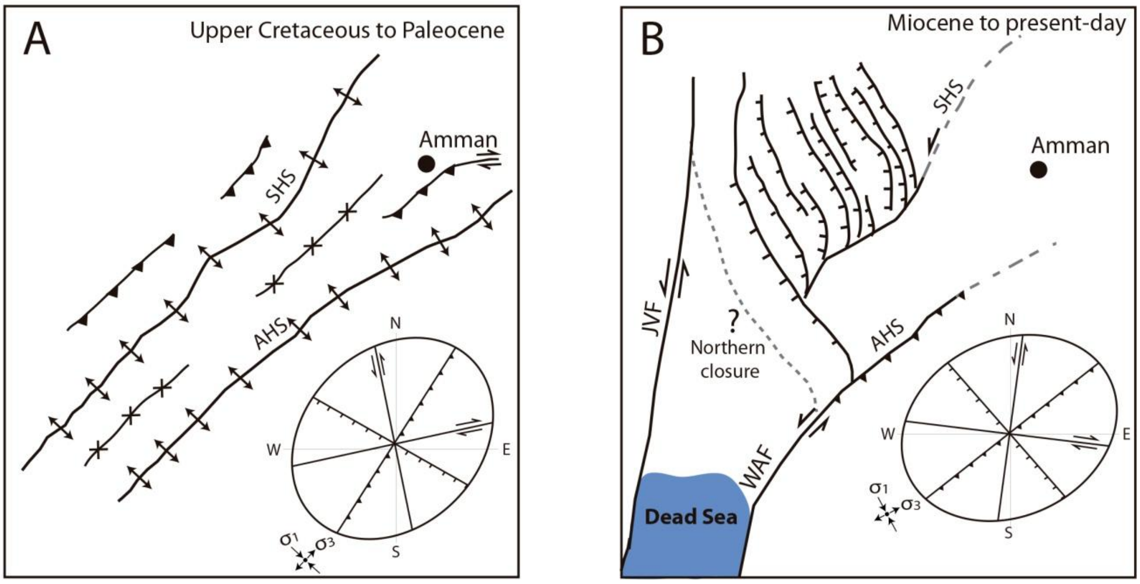

Figure 9.1. A) Tectonic sketch of the evolution of the AHS and the SHS in Upper Cretaceous to Paleocene B) Tectonic sketch showing the present-day configuration of the AHS and the SHS due to the Miocene reactivation by the stress field of the DSTF.

The AHS has been traditionally associated the fold-bend fault structure with dextral motion (Quennel 1959, Diabat 2009), but the field data presented in this work proves its sinistral component along some of the main fault planes that post-date the previous dextral striations. This tectonic activity is not present in the whole AHS, but is restricted to the area between the Al-Rama village and the Al-Bahath Valley. Although most of the stress of the WAF is transferred to the JVF as indicated by present-day GPS slip-rates, we suggest that a small part of this stress is being transferring to the AHS and reactivates some of its NE-SW striking main fault planes in the Quaternary times. These NE-SW planes would act as transpression structures with left-lateral component (**Fig. 9.1**). These new field evidences suggest that the northern termination of the WAF merge into the AHS, being hard to individualize both structures to the northeast of Al Rama village.

On the other hand, the tectonic activity of the SHS cannot be explained by the same mechanism. The SHS does not have a clear structural contact with the WAF and its reactivation might be related to the tectonic activity of the NW-SE normal faults between Alkarama and Alsalt villages. These normal faults present low-to-moderate throws, related colluvial wedges and show indicative SW directed extension with related topographic steps. The SHS presents some of the characteristics of transfer faults as defined by Gibbs (1984) and Martínez-Martínez et al. (2006); (i) the fault zone is roughly parallel to the extension direction, (ii) there is a lack of strike-slip offset along the fault and in some cases the offset is contrary to the slip, (iii) the detailed mapping proved that the normal faults do not cut through the SHS and in some areas coalesce with it. These normal faults are compatible with the present-day stress field of the DSTF and have the same orientation that the proposed northern closure of the Dead Sea (**Fig. 9.1**).

9.3. Kinematics of the AHS and SHS respect to the DSTF

Stress analyses of the tectonic structures in the entire DSTF region indicate two different phases of deformation (Zain Eldeen et al., 2002; Diabat et al., 2004; Lunina et al., 2005; Diabat, 2009: Hardy et al., 2010; Palano et al., 2013); NNW-SSE compression stress related to present-day stress field and WNW-SES compression stress of Cretaceous age. Diabat (2009) proposed a possible Quaternary activity in the northernmost part of AHS. This study obtained a σ1 and σ3 generally sub-horizontal and σ2 sub-vertical in most of the stress tensors. Thus, a major strike-slip system with σ1 swinging around N to NW direction was dominant in the studied structures. As it has been recognized in previous works (Chaimove et al., 1990; Eyal, 1996; Badawy and Horvath, 1999; Hofestetter et al., 2007; Eyal and Eyal, 2015), we consider that some of the structures at their junction with the DSTF still interact with it

In this study we obtained three types of stress tensors from the fault-slip inversion. Most of tensors (10 out of 14) are strike-slip type with a NNW-SSE maximum compressive stress axis with different orientation of σ1 and σ3. Only two tensors show normal deformation, with a sub-vertical σ1 and sub-horizontal σ3 and σ2. Both tensor types are compatible with the present-day tectonic frame of the Dead Sea stress field and the Reidel shear of the studied structures. Moreover, our field observations in the area suggest changes in the stress field of the AHS and the SHS from dextral thrust deformation during the Cretaceous to strike-slip and oblique reverse faulting in Quaternary.

Although reverse faulting characterizes the original movement along the AHS and the SHS, the sinistral component in NE orientation was never reported for these structures. During our field works, sinistral movement was documented in all the field stations (**Table 7.1**). The kinematics of the tectonic structures in our study area highlights oblique and left-lateral strike-slip movements along the old 30-40º oriented fault planes. Strike-slip and dip-slip kinematic indicators on the fault planes suggest that the faults were re-activated at a later stage.

During faulting, fractures spread in all directions being consistent with the Reidel shear model. This model suggests an NW-SE maximum compressive stress axes and NE-SW minimum compressive strength, similar to the regional stress field configuration. According to this model, structures like R2 (Normal faults) and X (Dextral faults) can occur in the tectonic context of the area. This kind of faults was found in the central study area between the AHS and the SHS (faults documented in field station no. 3). The X-fault type is abundant in the NW parts of the study area, whereas these fault-types are scarce in the region between the AHS and the SHS. The lack of these faults in this area can be explained by the control of NE sinistral-thrust faults of the AHS and the SHS. The youngest N-S to NNW-SSE compressional stress affected the area and produced the major oblique sinistral reverse fault and its related local structures.

The results of present-day stress analyses (e.g. Lunina et al., 2005; Hofstetter et al., 2007; Palano et al., 2013) and our study are consistent and support the hypothesis that stress axes follow the Anderson model in which two of the principal stresses are horizontal and the third one vertical. For the sites discussed in our work this criterion is attained. Because of 12 of 14 stress tensors show a NNW–SSE direction of compression compatible with the strike of the regional (σ1) stress (**Fig. 7.3**), we envisage that they also reflect the driving mechanism of Quaternary active tectonics.

9.4. A new model for the northern closure of the Dead Sea basin

The Dead Sea basin is an excellent example of pull-apart basin developed along strike-slip faults (Garfunkel and Ben-Avraham, 1996; Lazar et al. 2006; Ben-Avraham et al., 2010). However, some uncertainty remains in the identification of its eastern border fault (WAF) causing problems in determining the shape and the closure structure of this basin (Alzoubi et al. 2007; Ten Brink and Flores 2012). Several models had been suggested for this basin and most of them point that there is no clear transverse fault structures in the northern end of the basin (Lazar et al. 2006; ten Brink and Flores 2012). All these models assume that the eastern boundary fault (WAF) dies few kilometers NE from the Dead Sea Lake and geophysical data are scarce within the Jordanian side of the DSTF. The new data presented in this work point that the tectonic activity of AHS, SHS and normal faults between Alkarama and Alsalt villages is related to the DSFT stress field and may play a role in the northern closure of the Dead Sea basin. Normal faults between Alkarama and Alsalt villages probably merge into a low-angle detachment level that could be hard to identify in seismic reflection profiles. This system will not generate deep depocenters, thus being compatible with the models proposed by Al-Zoubi et al. (2007) and ten Brink and Flores (2012) of gradual thinning toward the northern end of the basin. Future geophysical research in the area should investigate the relation of these new active tectonic structures with the Dead Sea pull-apart basin.

Chapter 10

Conclusions

In this Thesis I presented a detailed geomorphic analysis of the eastern margin of the Dead Sea basin, focusing in the northern termination of the Wadi Araba Fault (southern segment of the DSTF). To perform this analysis I created two ArcGIS Add-Ins to extract normalized and swath profiles. These tools produce topographic swath profiles and normalized longitudinal river profiles in a simple, efficient and quick way. Swath profiles help in the interpretation of the regional topographic patterns and normalized river profiles allow to compare gradient variations of different rivers that may be controlled by climatic, lithological and/or tectonic factors. Therefore, the presented tools can streamline the DEM analysis workflow and allow focusing the efforts of the researchers on the geologic and tectonic interpretation of the results. I used these two complement in this Thesis to extract normalize and swath profiles within my study area.

The landscape analysis done I this Thesis suggest that the study area is very young and it is in a transient state of landscape development. Normalized profiles have characteristics convex or linear-convex shapes, as well as the hypsometric curves. Area-slope plots have high Ksn values and lacks clear linear correlation, especially in their middles and lower parts (near mouths), due to the transient state of the analyzed rivers. The roughness and HI-LISA analyses depicted a good correlation with the active structures of the study area that act as boundaries for erosion processes. There is a clear erosion wave advancing eastwards from the Dead Sea into the TransJordanian Plateau (TJP). These analysis lacks a clear evidence of a northern structure closing the Dead Sea apart of the NW-SE normal faults related to the AHS and SHS. In this sense, the northern termination of the WAF depict lower values of roughness and LISA-HI and no upward deflection of the TJP. Swath profiles show a upward "rebound" of the western corner of the TJP.

In this Thesis I have presented a new tectonic evaluation for the geological structures to the north and northeast of the Dead Sea in western Jordan. I have presented field evidences that prove the Quaternary tectonic activity of the Amman Hallabat Structure (AHS) and Shueib Structure (SHS) and re-defined the active northern termination of the Wadi Araba Fault (WAF) in Al-Rama village to merge northeastwards with the AHS.

The AHS and SHS structures have been reactivated as a response of two different mechanisms; the AHS receive a direct transference of a small part of the tectonic stress through the WAF, whereas the SHS acts as a sinistral transfer fault of a transtensional zone composed of numerous NE-SW normal faults active in the Quaternary .

The structural analysis of fault-slip data collected from the AHS, SHS and the northernmost WAF suggests a stress pattern with horizontal σ1 and σ3 axes striking NNW-SSE and NE-SW respectively. This stress pattern is similar to the one associated with the DSTF. These new findings were corroborated with field data of meso-scale faults in 12 out of 14 sites, thus supporting a Quaternary re-activation in the region. I presented field evidences of the different faulting mechanisms that affect the AHS and SHS. In both structures the old dextral-reverse striations were overprinted by newer ones of sinistral reverse and sinistral strike-slip kinematics. These conclusions are compatible with recent studies in the region and can explain the relationship between the WAF and the AHS and SHS in means of crustal stress distribution to the NE of the Dead Sea during the Miocene to Recent.

The seismogenic character of the AHS is clear from the damage found in the archaeological site of Tall el-Hamman, which has been recently interpreted as the ancient city of Sodom. The destruction of this city is attributed to bid earthquake, that may be also related with this structure. The NW-SE normal faults bounding the AHS and SHS could merge into a single fault plane that will act as the northern closure of the Dead Sea. Future geophysical research in the area should pay attention to these active structures as research in southern areas has prove fruitless.

Chapter 11

References

References

Abed , A.M. 2000. Geology of Jordan, Jordanian Geologists Association Publications, Amman. pp. 570. (In Arabic).

Abed, A.M. and Yaghan, R. 2000. On the paleoclimate of Jordan during the last glacial maximum. Palaeography, Palaeoclimateology, Palaeoecology, 160, 23-33. PII: S0031-0182(00)00042-0.

Abed, A.M., 1989. On the genesis of the phosphorite – chert association of the Amman formation in the Tel Es-Sur area, Ruseifa, Jordan, Science Geology Bulletin 42 (3), 141-153.

Abou Romieh, M., Westaway, R., Doud, M., Radwan, Y., Yassminh, R., Khalil, A., al-Ashkar, A., Loughlin, S., Arrell, K. and Bridgland, D. 2009. Active crustal shortening in NE Syria revealed by deformed terraces of the River Euphrates. Terra Nova, 21, 427-437.

Akyuz, H.S., Altunel, E., Karabacak, V., and Yalciner, C.C. 2006. Historical earthquake activity of the northern part of the Dead Sea Fault Zone, southern Turkey. Tectonophysics, 426, 281–293. doi:10.1016/j.tecto.2006.08.005.

Al Tarazi, E., Abu Rajab, J., Gomez, F., Cochran, W., Jaafar, R., and Ferry, M. 2011. GPS measurements of near-field deformation along the southern Dead Sea fault system. Geochem Geophys Geosyst 12:Q12021. doi: 10.1029/2011GC003736.

Alchalbi, A., Daoud, M., Gomez, F., McClusky, S., Reilinger, R., Abu Romeyeh, M., Alsouod, A., Yassminh, R., Ballani, B., Darawcheh, R., Sbeinati, R., Radwan, Y., Al Masri, R., Bayerly, M., Al Ghazzi, R. and Barazangi, M. 2010. Crustal deformation in northwestern Arabica from GPS mesurments in Syria: Slow slip rate along the northern Dead Sea Fault. Geophys. J. Int., 180, 125-135.

Almalki, K., Betts, P. G., andAilleres, L. 2015. The Red Sea – 50 years of geological and geophysical research. Earth-Science Reviews, 147, 109-140. Doi: 10.1016/j.earscirev.2015.05.002.

Al-Saad. D., Sawaf, T., Gebren, A., Barazangi, M., Best, J.A., and Chaimov, T. 1992. Crustal structure of central Syria: the intacontinental Palmyride mountain belt. Tectonophysics, 207, 345-358.

Al-Taj, M. 2000. Active faulting along the Jordan Valley segment of the Jordan-Dead Sea Transform. Ph.D Thesis, University of Jordan, Amman, 233 pp (unpublished).

Al-Tarawneh, M. 2011. Structural setting of the Jordan Northern Highlands: An Integrated Study using Surface and Sub-Surface Geological Data by Utilizing GIS Technology. PhD Thesis.University of Capetown.

Al-Tarazi, E., Sandvol, E., and Gomez, F. 2006. The February 11, 2004 Dead Sea earthquake ML=5.2 in Jordan and its tectonic implication. Tectonophysics, 422, 149–158.

Al-Tarazi, E.A. 1999. Regional seismic hazard study for the eastern Mediterranean (Trans-Jordan, Levant and Antaki) and Sinai region. Journal of African Earth Sciences, 28 (3), 743-750.

Al-Zoubi, A. S., Heinrichs, T., Qabbani, I. and Ten-Brink, U. S. 2007. The northern end of the Dead Sea basin: eometry from reflection seismic evidence, Tectonophysics, 434, 55–69, doi:10.1016/j.tecto.2007.02.007.

Al-Zoubi, A., Heinrichs, T., Sauter, M., and Qabani, I., 2006. Geological structure of the eastern side of the lower Jordan Valley/Dead Sea rift: reflection seismic evidence. Marine and Petroleum Geology, 23, 473–484.

Al-Zoubi, A.S. 2005. The 11th February, 2004 Earthquake of The Dead Sea, Jordan. American Journal of Environmental Sciences 1 (2): 142-148.

Ambraseys, N.N. 2006. Earthquakes and archaeology. Journal of Archaeological Sciences, 33, 1008-1016.

Ambraseys, N.N. and Jackson, J. A. 1998. Faulting associated with historical and recent earthquakes in the Eastern Mediterranean region. Geophys. J. Int., 133, 390-406.

Amireh, B. S., Jarrar, G., Henjes-Kunst, F., and Schneider, W. 1998. K-Ar dating, X-Ray diffractometry, optical and scanning electron microscopy of glauconies from the early Cretaceous Kurnub Group of Jordan. Geological Journal, 33(1), 49-65.

Andreani, L., Stanek, K., Gloaguen, R., Krentz, O., Domínguez-González, L., 2014. DEM-Based Analysis of Interactions between Tectonics and Landscapes in the Ore Mountains and Eger Rift (East Germany and NW Czech Republic). Remote Sens. 6, 7971–8001. doi:10.3390/rs6097971

Angelier, J. (1989): From orientation to magnitudes in paleostress determinations using fault slip data. Journal of Structural Geology, 11, p. 37-50.

Antón, L., de Vicente, G., Muñoz-Martín, A., Stokes, M., 2014. Using river long profiles and geomorphic indices to evaluate the geomorphological signature of continental scale drainage capture, Duero basin (NW Iberia). Geomorphology 206, 250–261. doi:10.1016/j.geomorph.2013.09.028

Atallah, M. 1992. Tectonic evolution of northern Wadi Araba, Jordan. Tectonophysics, 204, 17-26.

Atallah, M., Mustafa, H., El-Akhal, H., Al-Taj, M. 2005. Dhahal structure: an example of transpression associated with the Dead Sea transform in Wadi Araba, Jordan. Acta Geologica Polonica, 55 (4), 361-370.

Azañón, J.M., Galve, J.P., Pérez-Peña, J. V., Giaconia, F., Carvajal, R., Booth-Rea, G., Jabaloy, A., Vázquez, M., Azor, A., Roldán, F.J., 2015. Relief and drainage evolution during the exhumation of the Sierra Nevada (SE Spain): Is denudation keeping pace with uplift? Tectonophysics. doi:10.1016/j.tecto.2015.06.015

Badawy, A. and Horvath, F. 1999. The Sinai subplate and tectonic evolution of the northern Red Sea region. Journal of Geodynamics, 27, 433-450.

Bartov, Y., Arkin, Y., and Steinitz, G., 1976. The Zin fault. An example of Senonian faulting in the northern Negev of Israel. J. Earth Sci., 25, 40-44.

Bartov, Y., Steinitz, G., Eyal, M., and Eyal, Y. 1980. Sinistral movement along the Gulf of Aqaba – Its age and relation to the opening of the Red Sea. Nature, 285, 220–221.

Basha, S. H. 1978. On the occurrence of the genus Thomasinella (Lituolidae, Foraminiferida) in East Jordan. Rev. Espan. Micropaleont, 10, 67-73.

Baulig, H., 1926. Sur une méthode d'analyse altimétrique appliquée á la Bretagne. Bull. l'Association Geogr. Fr. 10, 7–9.

Bellin, N., Vanacker, V., Kubik, P.W., 2014. Denudation rates and tectonic geomorphology of the Spanish Betic Cordillera. Earth Planet. Sci. Lett. 390, 19–30. doi:10.1016/j.epsl.2013.12.045

Ben-Avraham, Z., Garfunkel, Z. and Lazar, M. 2008. Geology and Evolution of the Southern Dead Sea Fault with Emphasis on Subsurface Structure. Annu. Rev. Earth Planet. Sci., 36, 357-387.

Ben-Avraham, Z., Ginzburg, A., Makris, J., Eppelbaum, L., 2002. Crustal structure of the Levant Basin, eastern Mediterranean. Tectonophysics 346, 23–43.

Ben-Avraham, Z., Lyakhovsky, V., and Schubert, G. 2010. Drop-down formation of deep basins along the Dead Sea and other strike-slip fault systems. Geophys J Int 181:185–197. doi:10.1111/j.1365-246X.2010.04525.x

Bender, F. 1968. Geologie von Jordanien. Beitráge zur regionalen geologie der erde. Gebruder Borntraeger, Berlin, Stuttgart.

Bender, F. 1974, Geology of Jordan, 196 pp., Gebrüder Borntraeger, Berlin.

Bender, F. 1982. On the evolution of Wadi Araba – Jordan, Geol. Jord. Geol. Conference, p. 415 – 445. Amman, Jordan.

Bishop, P., Hoey, T.B., Jansen, J.D., Lexartza Artza, I., 2005. Knickpoint recession rate and catchment area: The case of uplifted rivers in Eastern Scotland. Earth Surf. Process. Landforms 30, 767–778. doi:10.1002/esp.1191

Brookfield, M.E., 1998. The evolution of the great river systems of southern Asia during the Cenozoic India-Asia collision: rivers draining southwards. Geomorphology 22, 285–312.

Bruner, I., 1990. Investigation of the subsurface in the northern Negev, Israel, using seismic reflection techniques. Ph.D. thesis, Tel-Aviv University

Burbank, D.W., Anderson, R.S., 2013. Tectonic Geomorphology, 2nd Edition, 2nd ed. Blackwell Science, Oxford.

Burden, D. J. 1959. Hand book of the geology of Jordan: to accompany and explain the three sheets of the 1: 250,000 geological map of Jordan east of the Rift, by A. M. Quennell, Government of the Hashemite Kingdom of Jordan, Benham, Colchester, 82.

Butler, R.W.H, Spencer, S. and Griffiths, H.M. 1998. The structural response to evolving plate kinematics during transperssion: evolution of the Lebanese retraining bend of the Dead Sea Transform. Geological Society, London, Special Publications, 135(1), 81-106.

Castillo, M., Bishop, P., Jansen, J.D., 2013. Knickpoint retreat and transient bedrock channel morphology triggered by base-level fall in small bedrock river catchments: The case of the Isle of Jura, Scotland. Geomorphology 180-181, 1–9. doi:10.1016/j.geomorph.2012.08.023

Chaimov, T.A., Barazangi, M., Al-Saad, D., Sawaf, T. and Gebran, A. 1990. Crustal shortening in the Palmyride fold belt, Syria, and implication for movement along the Dead Sea fault system. Tectonics, 9, 1369-1386.

Chen, Y.C., Sung, Q.C., and Cheng, K.Y., 2003. Along-strike variations of morphotectonic features in the Western Foothills of Taiwan: tectonic implications based on stream-gradient and hypsometric analysis. Geomorpholohy, 56 (1-2), 109-137.

Chester, D.K., Duncan, A.M., 2009. The Bible, theodicy and Christian responses to historic and contemporary earthquakes and volcanic eruptions. Environ. Hazards 8, 304–332. doi:10.3763/ehaz.2009.0025

Coblentz, D., Karlstrom, K.E., 2011. Tectonic geomorphometrics of the western United States: Speculations on the surface expression of upper mantle processes. Geochemistry Geophys. Geosystems 12. doi:10.1029/2011GC003579

Crosby, B.T., Whipple, K.X., 2006. Knickpoint initiation and distribution within fluvial networks: 236 waterfalls in the Waipaoa River, North Island, New Zealand. Geomorphology 82, 16–38. doi:10.1016/j.geomorph.2005.08.023

D'Agostino, N., Jackson, J. a., Dramis, F., Funiciello, R., 2001. Interactions between mantle upwelling, drainage evolution and active normal faulting: an example from the central Apennines (Italy). Geophys. J. Int. 147, 475–497.

Demoulin, A., 1998. Testing the tectonic significance of some parameters of longitudinal river profiles: the case of the Ardenne (Belgium, NW Europe). Geomorphology 24, 189–208. doi:10.1016/S0169-555X(98)00016-6

Diabat, A., Abdelghafoor, M., 2004. Geologic map of Amman. Geological mapping project. Natural Resources Authority, Jordan. Sheet 3153-I, Scale 1: 50,000.

Diabat, A.A. 2009. Structural and stress analysis based on fault-slip data in the Amman area, Jordan. Journal of African Earth Sciences, 54, 5,155-162.

Diabat, A.A., Atallah, M., and Salih, M. R. 2004. Paleostress analysis of the Cretaceous rocks in the eastern margin of the Dead Sea transform, Jordan, Journal of African Earth Sciences, 38, 449–460.

El-Isa, Z.H. and Mustafa, H. 1986. Earthquake deformations in the Lisan deposits and seismotectonic implications. Geophys J R Astron Soc, 86, 413–424.

Ellenblum, R., Marco, S., Agnon, A., Rockwell, T., and Boas, A. 1998. Crusader castle torn apart by earthquake at dawn, 20 May 1202. *Geology*, *26*(4), 303-306.

El-Motaal, E. A. and Kusky, Y.M. 2003. Tectonic evolution of the intraplate S-shaped Syrian arc fold-thrust belt of the Middle East region in the context of plate tectonics. The third international conference of the geology of Africa, 2, 139-157.

Eyal, Y. 1996. Stress field fluctuations along the Dead Sea rift since the middle Miocene. Tectonics, 15(1), 157–170.

Eyal, Y., Eyal, M., 2015. Nature of slip transfer between strike-slip faults: The Eastern Sinai (Egypt) shear zone, Dead Sea Transform. J. Struct. Geol. 76, 52–60. doi:10.1016/j.jsg.2015.03.014

Farr, T., Rosen, P.A., Caro, E., Crippen, R., Duren, R., Hensley, S., Kobrick, M., Paller, M., Rodriguez, E., Roth, L., Seal, D., Shaffer, S., Shimada, J., Umland, J., Wermer, M., Oskin, M., Burbank, D.W., Alsdorf, D., 2007. The shuttle radar topography mission. Rev. Geophys. 45, RG2004. doi:10.1029/2005RG000183

Ferry, M., Meghraoui, M., Karaki, N.A., Al-Taj, M., Khalil, L., 2011. Episodic behavior of the Jordan Valley section of the Dead Sea fault inferred from a 14-ka-long integrated catalog of large earthquakes. Bull. Seismol. Soc. Am. 101, 39–67. doi:10.1785/0120100097

Ferry., Meghraoui, M., Abou Karaki, N., Al-Taj, M., Amoush, H., Al-Dhaisat, S. and Barjous, M. 2007. A 48-Kyr-long slip rate history for the jordan valley segment of the Dead Sea Fault. Earth and Planetary Science Letters, 260, 394-406.

Fielding, E., Isacks, B., Barazangi, M. and Duncan, C., 1994. How flat is Tibet? Geology 22, 163. doi:10.1130/0091-7613

Flint, J.J., 1974. Stream gradient as a function of order, magnitude, and discharge. Water Resour. Res. 10, 969–973.

Freund R 1965. A model of the structural development of Israel and adjacent areas since Upper Cretaceous times. Geol Mag, 102, 189–205.

Freund, R, Zak, I., Garfunkel, Z. 1965. Age and rate of the sinistral movement along the Dead Sea reif. Nature 22, 253-255.

Fruend, R., Zak, I., Goldberg, M., Weissbord, T., and Derin, B. 1970. The shear along the Dead Sea Rift. Philosophical Transactions of the Royal Society. London, 267, 107-130.

Galli, P and Galadini, F. 2001. Surface faulting of archaeological relics. A review of case histories from the Dead Sea to the Alps. Tectonophysics, 335, 291-312.

Garfunkel, Z. 1981. Internal structure of the Dead Sea leaky transform (Rift) in relation to plate kinematics. Tectonophysics, 80, 80-108.

Garfunkel, Z. 2011. The long- and short-term lateral slip and seismicity along the Dead Sea transform: an interim reevaluation. Isr J Earth Sci, 58, 217–235. doi: 10.1560/IJES.58.3-4.217.

Garfunkel, Z. 2014. Lateral Motion and Deformation Along the Dead Sea Transform. In: Garfunkel Z et al (eds) Dead Sea transform fault system: reviews, Modern approaches in solid earth sciences 6. Springer, Dordrecht. 109-150.

Garfunkel, Z., Ben-Avraham, Z. 1996. The structure of the Dead Sea basin. Tectonophysics, 266, 155–176. doi:10.1016/s0040-1951(96)00188-6-

Ghazaleh, S.A. and Kempe, S. 2009. Geomorphology of Lake Lisan terraces along the eastern coast of the Dead Sea, Jordan. Geomorphology. doi:10.1016/j.geomorph.2009.02.015.

Ghazleh, S. A., Hartmann, J., Jansen, N., and Kempe, S. 2009. Water input requirements of the rapidly shrinking Dead Sea. Naturwissenschaften 96:637–643.

Giaconia, F., Booth-Rea, G., Martínez-Martínez, J.M., Azañón, J.M., Pérez-Peña, J. V., Pérez-Romero, J., Villegas, I., 2012. Geomorphic evidence of active tectonics in the Sierra Alhamilla (eastern Betics, SE Spain). Geomorphology 145-146, 90–106. doi:10.1016/j.geomorph.2011.12.043

Gibbs, A. D. (1984), Structural evolution of extensional basin margins, J. Geol. Soc. London, 141, 609–620.

Ginzburg A., Makris J., Fuchs K., Prodehl C., Kaminski W., Amitai, U. 1979. A seismic study of the crust and upper mantle of the Jordan-Dead Sea rift and their transition toward the Mediterranean Sea. J Geophys Res 84:1569–1582. doi:10.1029/JB084iB04p01569.Girdler, R.W. 1990. The Dead Sea transform fault system. Tectonophysics, 180, 1-13.

Goldrick, G., Bishop, P., 2007. Regional analysis of bedrock stream long profiles: evaluationof Hack’s SL form, and formulation and assessment of an alternative (the DS form). Earth Surface Processes and Landforms, 32, 649-671.

Gomez, F., Karam, G., Khawalie, M., McClusky, S., Vernant, P., Reilinger, R., Jaffar, R., Tabet, C., Khair, K. and Barazangi, M. 2007. Global Positioning System measurements of strain accumulation and slip transfer through the restraining bend aling the Dead Sea fault system in Lebanon. Gephys. J. Int., 168, 1021-1028.

Gomez, F., Khawlie, M. Tabet, C., Darkal, A.N., Khair, K. and Barazangi, M. 2006. Late Cenozoic uplift along the northern Dead Sea transform in Lebanon and Syria. Earth and Planetary Science Letters, 241, 913-931.

Gomez, F., Meghraoui, M., Darkal, A.N., Hijazi, F., Mouty, M., Sileiman, Y., Sbeinati, R., Darawcheh, R., Al-Ghazzi, R., and Barazangi, M. 2003. Holocene faulting and earthquake recurrence along the Serghaya branch of the Dead Sea fault system in Syrua and Lebanon. Geophys. J. Int., 1533, 658-674.

Grohmann, C.H., 2004. Morphometric analysis in geographic information systems: applications of free software GRASS and R. Comput. Geosci. 30, 1055–1067. doi:10.1016/j.cageo.2004.08.002

Grohmann, C.H., 2005. Trend-surface analysis of morphometric parameters: A case study in southeastern Brazil. Comput. Geosci. 31, 1007–1014. doi:10.1016/j.cageo.2005.02.011

Grohmann, C.H., Riccomini, C., Alves, F.M., 2007. SRTM-based morphotectonic analysis of the Pocos de Caldas Alkaline Massif, southeastern Brazil. Comput. Geosci. 33, 10–19. doi:10.1016/j.cageo.2006.05.002

Guth, P.L., 2006. Geomorphometry from SRTM: Comparison to NED. Photogramm. Eng. Remote Sensing 72, 269–277.

Hack, J.T., 1957. Studies of longitudinal profiles in Virginia and Maryland. U.S. Geol. Surv. Prof. Pap. 294-B.

Hall, J.K. 1996. Digital topography and bathymetry of the area of the Dead Sea depression. Tectonophysics, 266, 177–185. doi:10.1016/s0040-1951(96)00189-8.

Hardy, C., Homberg, C., Eyal, Y., Barrier, É., and Muller, C. 2010. Tectonic evolution of the southern Levant margin since Mesozoic. Tectonophysics, 494, 211-225. Doi: 10.1016/j.tecto.2010.09.007.

Harris, G.M., Beardow, A.P., 1995. The destruction of Sodom and Gomorrah: a geotechnical perspective. Quarterly Journal of Engineering Geology and Hydrogeology, 28(4), 349-362.

Hasse-Schramm, A., Goldstein, S. and Stein, M. 2004. U-Th dating of Lake Lisan (Late Pleistocene Dead Sea) aragonite and implications glacial East Mediterranean climate change. Geochimica et Cosmochimica Acta, 68(5), 985-1005. doi: 10.1016/j.gca.2003.07.016.

Haynes, J. M., Niemi, T. M. and Atallah, M. 2006. Evidence for ground-rupturing earthquakes on the Northern Wadi Araba fault at the archaeological site of Qasr Tilah, Dead Sea Transform fault system, Jordan. J. Seismol., 10, 415-430, doi: 10.1007/s10950-006-9028-9.

Hergarten, S., Robl, J., Stuwe, K. 2014. Extracting topographic swath profiles across curved geomorphic features. Earth Surface Dynamics, 2, 97-104. doi:10.5194/esurf-2-97-2014.

Hofstetter, R., Klinger, Y., Amrat, AQ., Rivera, L. and Dorbath, L. 2007. Stress tensor and focal mechanisms along the Dead Sea fault and related elements based on seismological data. Tectonophysics, 429, 165-181.

Hovius, N. 2000. Macroscale process systems of mountain belt erosion. En: Geomorphology and Global Tectonics (M.A. Summerfield, ed.). John Wiley & Sons, West Sussex, England, 77-105

Hurtrez, J., Lucazeau, F., 1999. Investigation of the relationships between basin morphology, tectonic uplift, and denudation from the study of an active fold belt in the Siwalik Hills, central Nepal. J. Geophys. … 104, 12779–12796.

Jackson, J., Norris, R., Youngson, J., 1996. The structural evolution of active fault and fold systems in central Otago, New Zealand: evidence revealed by drainage patterns. J. Struct. Geol. 18, 217–234. doi:10.1016/S0191-8141(96)80046-0

Keller, E.A., Pinter, N., 2002. Active Tectonics. Earthquakes, Uplift, and Landscape. Prentice Hall, New Jeresy, 362 pp.

Kirby, E., Whipple, K.X., 2001. Quantifying differential rock-uplift rates via stream profile analysis. Geology 29, 415. doi:10.1130/0091-7613

Kirby, E., Whipple, K.X., 2012. Expression of active tectonics in erosional landscapes. J. Struct. Geol. 44, 54–75. doi:10.1016/j.jsg.2012.07.009

Klinger, Y., Avouac, J.P., Dorbath, L. N. Abou Karaki and N. Tisnerat 2000. Seismic behaviour of the Dead Sea fault along Araba Valley , Jordan. Geophysical Journal International. 142, 769-782.

Koyama, J., Yoshizawa, K., Yomogida, K., and Tsuzuki, M. 2012. Variability of megathrust earthquakes in the world revealed by the 2011 Tohoku-oki Earthquake. Earth, planets and space, 64(12), 1189-1198.

Krienitz Stern, R. J. and Johnson, P. 2010. Continental lithosphere of the Arabian Plate: A geologic, petrologic, and geophysical síntesis. Earth-Science Reviews. 101, 29-67. doi: 10.1016/j.earscirev.2010.01.002.

Lazar, M., Ben-Avraham, Z., and Schattner, U. 2006. Formation of sequential basins along a strike-slip-fault-Geophysical observations from the Dead Sea basin. Tectonophyscis, 421, 53-69. doi:10.1016/j.tecto.2006.04.007.

Le Beon, M., Klinger, Y., Al-Qaryouti, M., Mériaux, A.S., Finkel, R.C., Elias, A., Mayyas, O., Ryerson, F.J. and Tapponnier, P. 2010. Early Holocene and Late Pleistocene slip rates of the southern Dead Sea Fault determined from 10Be cosmogenic dating of offset alluvial deposits. J. Geophys. Int., 115, B11414, doi:10.1029/2009JB007198.

Le Beon, M., Klinger, Y., Amrat, A.Q., Agnon, A., Dorbath, L., Baer, G., Ruegg, J.C., Charade, O. and Mayyas, O. 2008. Slip rate and locking depth from GPS profi les across the southern Dead Sea Transform. J Geophys Res (1978-2012), 113:B11403. doi: 10.1029/2007JB005280.

Le Beon, M., Klinger, Y., Meriaux, A.S., Al-Qaryouti, M., Finkel, R.C., Mayyas, O., and Tapponnier, P. 2012. Quaternary morphotectonic mapping of the Wadi Araba and implications for the tectonic activity of the southern Dead Sea fault. Tectonics 31:TC5003, 25.

Leroy, S.A.G., Marcos, S., Bookman, R. and Miller, C.S. 2010. Impact of earthquakes on agriculture during the Roman-Byzntine period from pollen records of the Dead Sea kaminated sediment. Quaternary Research, 73, 191-200.

Lifton, N.A., Chase, C.G., 1992. Tectonic, Climatic and lithologic influences on landscape fractal dimension and hypsomety: implications for landscape evolution in the San Gabriel Mountains, California. Geomorphology, 5, 77-114.

Lovelock, P.E.R. 1984. A Review of the Tectonics of the Northern Middle East Region. Geological Magazine, 121, 577-587.

Lunina, O.V., Mart, Y., Gladkov, A.S., 2005. Fracturing patterns, stress fields and earthquakes in the Southern Dead Sea rift. J. Geodyn. 40, 216–234. doi:10.1016/j.jog.2005.07.010

Mackin, J.H., 1948. Concept of the Graded River. GSA Bull. 59, 463–512.

Mahmood, S.A., Gloaguen, R., 2012. Appraisal of active tectonics in Hindu Kush: Insights from DEM derived geomorphic indices and drainage analysis. Geosci. Front. 3, 407–428. doi:10.1016/j.gsf.2011.12.002

Mahmoud, Y., Masson, F., Meghraoui, M., Cakir, Z., Alchalbi, A., Yavasoglu, H., Yonlu, O., Daoud, M., Ergintav, S., Inan, S. 2013. Kinematic study at the junction of the East Anatolian fault and the Dead Sea fault from GPS measurements. Journal of Geodynamics, 67, 30-39. Doi: 10.10.16/j.jog.2012.05.006.

Makhlouf, I.M., Turner, B.R. and Abed, A.M. 1990. Depositional Facies and Environments in the Lower Triassic Ma'in Formation, Dead Sea Area, Jordan. Dirasat B 17, 7-26. University Of Jordan, Amman.

Makris, J. and Rihm, R. 1991. Shear-controlled evolution of the Red Sea: pull apart model. Tectonophysics, 198, 441-466.

Malkawi, A. I. H., & Alawneh, A. S. 2000. Paleoearthquake features as indicators of potential earthquake activities in the Karameh Dam site. Natural Hazards, 22(1), 1-16.

Marco, S. 2008. Recognition of earthquake-related damage in archaeological sites: Examples from the Dead Sea fault zone. Tectonophysics, 453, 148-156.

Marco, S. and Klinger, Y. 2014. Review of on-fault Palaeo-seismic studies along the Dead Sea Fault. In: Garfunkel Z et al (eds) Dead Sea transform fault system: reviews, Modern approaches in solid earth sciences 6. Springer, Dordrecht. 183-205.

Marco, S., and Agnon, A. 2005. High-resolution stratigraphy reveals repeated earthquake faulting in the Masada Fault Zone, Dead Sea Transform. Tectonophysics, 408, 101-112.

Martínez-Martínez, J.M., Booth-Rea, G., Azañón, J.M., Torcal, F., 2006. Active transfer fault zone linking a segmented extensional system (Betics, southern Spain): Insight into heterogeneous extension driven by edge delamination. Tectonophysics 422, 159–173. doi:10.1016/j.tecto.2006.06.001

Masek, J.G., Isacks, B.L., Gubbels, T.L., and Fielding, E.J., 1994. Erosion and tectonics at the margins of Continental Plateaus. Journal of Geophysical Research, 99, 13941-13956.

Masson, F., Agnon, A., Klinger, Y. 2015. Variable behavior of the Dead Sea Fault along the southern Arava segment from GPS measurements. Comptes Rendus Geosciences. Doi: 10.1016/j.crte.2014.11.001.

Matos, B., 2014. Neotectonic and recently active faults in Bilogora Mountain area and assessment of their seismogenic potential. Doctoral thesis. pages. 256.

McClusky, S., Reilinger, R., Mahmoud, S., Ben Sari, D. and Tealeb, A. 2003. GPS constraints on Africa (Nubia) and Arabia plate motions. Geophys. J. Int., 155, 126-138.

Meghraoui, M., Gomez, F., Sbeinati, R., Van der Woerd, J., Mouty, M., Darkal, A.N., Radwan, Y., Layyous, I., Al Najjar, H., Darawcheh, R., Hijazi, F., Al-Ghazzi, R. and

Barazangi, M. 2003. Evidence for 830 years of seismic quiescence from palaeoseismology, archaeoseismology and historical seismicity along the Dead Sea fault in Syria. Earth and Planetary Science Letters, 210, 35-52.

Menendez, I., Silva, P.G., Martin-Betancor, M., Perez-Torrado, F.J., Guillou, H., Scaillet, S., 2008. Fluvial dissection, isostatic uplift, and geomorphological evolution of volcanic islands (Gran Canaria, Canary Islands, Spain). Geomorphology, 102(1), 189-203.

Merritts, D., Vincent, K.R., 1989. Geomorphic response of coastal streams to low, intermediate, and high rates of uplift, Medocino triple junction region, northern California. Geol. Soc. Am. … 101, 1373–1388.

Mikbel, Sh. and Zacher, W. 1981. The Wadi Shueib structure in Jordan. Neues Jaharbuch fuer Geologie und Paleontologie Monatshefte, 9, 215-225.

Mikbel, Sh., and Zacher, W., 1986. Fold Structures in Northern Jordan, N.JB. Geol. Palaont.Mh.H4, 248-256.

Molin, P., Fubelli, G., Nocentini, M., Sperini, S., Ignat, P., Grecu, F., Dramis, F., 2012. Interaction of mantle dynamics, crustal tectonics, and surface processes in the topography of the Romanian Carpathians: A geomorphological approach. Glob. Planet. Change 90-91, 58–72. doi:10.1016/j.gloplacha.2011.05.005

Molin, P., Pazzaglia, F.J., Dramis, F., 2004. Geomorphic expression of active tectonics in a rapidly-deforming forearc, Sila massif, Calabria, southern Italy. Am. J. Sci. 304, 559–589.

Muneizel, S. and Khalil, B. 1993. Geological Map Sheet 3154 III- As Salt, Scale 1:50000. Natural Resources Authority, Amman.

Neev, D., and Emery, K. O. 1995. The destruction of Sodom, Gomorrah, and Jericho: geological, climatological, and archaeological background. Oxford University Press.

Niemi, T. M., H. Zang, M. Atallah, and J.B.J. Harrison 2001. Late Pleistocene and Holocene slip rateo f the Northern Wadi Araba Fault, Dead Sea Transform, Jordan. J. Seismol., 5, 449-474. doi:10.1023/A:1011487912054.

Nusier, O. and Alawneh, A.S. 2006. Kafrein Earth Dam Probabilictic Seismic Hazard Assessment. Soil Mechanics and Foundation Engineering, 43(6), 18-21.

O'Callaghan, J.F., Mark, D.M., 1984. The extraction of drainage networks from digital elevation data. Computer Vision, Graphics, and Image Processing 28, 323–344.

Ohmori, H., 1993. Changes in the hypsometric curve through mountain building resulting from concurrent tectonics and denudation. Geomorphology 8, 263–277.

Palano, M., Imperscia, P., Gresta, S. 2013. Current stress and strain-rate fields across the Dead Sea Fault System: Constraints from seismological data and GPS observations. Earth and Planetary Sceince Letters, 369, 305-316. Doi: 10.1016/j.epsl.2013.03.043

Pérez-Peña, J. V., Azañón, J.M., Azor, A., 2009a. CalHypso: An ArcGIS extension to calculate hypsometric curves and their statistical moments. Applications to drainage basin analysis in SE Spain. Comput. Geosci. 35, 1214–1223. doi:10.1016/j.cageo.2008.06.006

Pérez-Peña, J. V., Azañón, J.M., Azor, A., Delgado, J., González-Lodeiro, F., 2009b. Spatial analysis of stream power using GIS: SLk anomaly maps. Earth Surf. Process. Landforms 34, 16–25. doi:10.1002/esp

Pérez-Peña, J. V., Azañón, J.M., Azor, A., Tuccimei, P., Della Seta, M., Soligo, M., 2009c. Quaternary landscape evolution and erosion rates for an intramontane Neogene basin (Guadix–Baza basin, SE Spain). Geomorphology 106, 206–218. doi:10.1016/j.geomorph.2008.10.018

Pérez-Peña, J. V., Azañón, J.M., Azor, A., Tuccimei, P., Della Seta, M., Soligo, M., 2009d. Quaternary landscape evolution and erosion rates for an intramontane Neogene basin (Guadix-Baza basin, SE Spain). Geomorphology 106, 206–218. doi:10.1016/j.geomorph.2008.10.018

Pérez-Peña, J. V., Azañón, J.M., Booth-Rea, G., Azor, a., Delgado, J., 2009e. Differentiating geology and tectonics using a spatial autocorrelation technique for the hypsometric integral. J. Geophys. Res. 114, F02018. doi:10.1029/2008JF001092

Pérez-Peña, J. V., Azañón, J.M., Booth-Rea, G., Azor, A., Delgado, J., 2009f. Differentiating geology and tectonics using a spatial autocorrelation technique for the hypsometric integral. J. Geophys. Res. F Earth Surf. 114. doi:10.1029/2008jf001092

Pérez-Peña, J.V., 2009. GIS-Based tools and methods for landscape analysis and active tectonic evaluation. Tesis doctoral. Universidad de Granada, Spain. pp. 139.

Pérez-Peña, J.V., Azor, A., Azañón, J.M., Keller, E.A. 2010. Active tectonics in the Sierra Nevada (Betics Cordillera, SE Spain): Insights from geomorphic indexes and drainage pattern analysis. Geomorphology, 119, 74-87.

Perron, J.T., Royden, L., 2013. An integral approach to bedrock river profile analysis. Earth Surf. Process. Landforms 38, 570–576. doi:10.1002/esp.3302

Picard, L. and Golani, 1965. Geological map of Israel. 1: 250,000. Survey of Israel, Tel Aviv.

Pike, R.J., Wilson, S.E., 1971. Elevation-Relief Ratio, Hypsometric Integral, and Geomorphic Area-Altitude Analysis. Geol. Soc. Am. Bull. 82, 1079 – 1084. doi:10.1130/0016-7606(1971)82[1079:ERHIAG]2.0.CO;2

Porat, N., Duller, G.A.T., Amit, R., Zilberman, E., and Enzel, Y. 2009. Recent faulting in the southern Arava, Dead Sea Transform: Evidence from single grain luminescence dating. Quaternary International, 199, 34-44. Doi:10.1016/j.quaint.2007.08.039

Queiroz, G.L., Salamuni, E., Nascimento, E.R., 2015. Knickpoint finder: A software tool that improves neotectonic analysis. Comput. Geosci. 76, 80–87. doi:10.1016/j.cageo.2014.11.004

Quennell, A.M. 1959. Tectonics of the Dead Sea Rift. 20th Internacional Congreso Geólogo. Asociación y Servicios Geólogos Africanos. 385 -403.

Quigley, M., Van Dissen, R., Villamor, P., Litchfield, N., Barrell, D., Furlong, K., Stahl, T., Duffy, B., Bilderback, E., Noble, D., Townsend, D., Begg, J., Jongens, R., Ries, W., Claridge, J., Klahn, A., Mackenzie, H., Smith, A., Hornblow, S., Nicol, R., Cox, S., Langridge, R., Pedley, K. 2010. Surface rupture of the Greendale Fault during the Mw 7.1 Darfield (Canterbury) earthquake, New Zealand: initial findings. Bulletin of the New Zealand Society for Earthquake Engineering 43(4): 236-242.

Reches, Z., Hoexter, D., 1981. Holocene seismic and tectonic activity in the Dead Sea area: the Dead Sea rift. Tectonophysics 80, 235–254.

Reinhardt, L.J., Dempster, T.J., Shroder, J.F., Persano, C., 2007. Tectonic denudation and topographic development in the Spanish Sierra Nevada. Tectonics 26, n/a–n/a. doi:10.1029/2006TC001954

Rigon, R., Rodriguez-Iturbe, I., Maritan, A., Giacometti, A., Tarboton, D.G., Rinaldo, A., 1996. On Hack’s Law. Water Resour. Res. 32, 3367.

Riquelme, R., Martinod, J., Hérail, G., Darrozes, J., Charrier, R., 2003. A geomorphological approach to determining the Neogene to Recent tectonic deformation in the Coastal Cordillera of northern Chile (Atacama). Tectonophysics 361, 255–275. doi:10.1016/S0040-1951(02)00649-2

Ruszkiczay-Rüdiger, Z., Fodor, L., Horváth, E., Telbisz, T., 2009. Discrimination of fluvial, eolian and neotectonic features in a low hilly landscape: A DEM-based morphotectonic analysis in the Central Pannonian Basin, Hungary. Geomorphology 104, 203–217. doi:10.1016/j.geomorph.2008.08.014

Rybakov, M., Goldshmidt, V., & Rotstein, Y. (1997). New regional gravity and magnetic maps of the Levant. Geophysical Research Letters, 24(1), 33-36.

Sahawneh, J. and Attallah, M. 2002, Tectonic Evolution of the North-Eastern Corner of the Dead Sea, ABHATH AL-YARMOUK: Basic Sci. & Eng., 11(2A), 581–598, Irbid, Jordan.

Salamon A. 2010. Patterns of seismic sequences in the Levant-interpretation of historical seismicity. Journal of Seismology, 14, 339-367.

Salamon, A., Hofstetter, A., Garfunkel, Z., and Ron, H. 2003. Seismotectonics of the Sinai Subplate – The Eastern Mediterranean Region. Geophys J Int., 155, 149–173.

Sanchez-Serrano, F. 2000. Análisis de la topografía y deformaciones recientes en el centro de la Peninsula Ibérica. PhD Thesis. Universidad Complutense de Madrid. p. 202

Sawariah, A., and Barjous, M. 1993. Geological Map Suwaylih Scale 1: 50,000, Sheet no. 3154-II. Natural Resources Authority, Amman, Jordan.

Sbeinati, M.R., Darawcheh, R., and Mouty, M. 2005. The historical earthquakes of Syria: an analysis of large and moderate earthquakes from 1365 B.C. to 1900 A.D. Ann Geophys, 48, 347–435.

Schumm, S.A., 1956. Evolution of drainage systems and slopes in badlands at Perth Amboy, New Jersey. Geological Society of America Bulletin 67, 597–646

Scotti, V.N., Molin, P., Faccenna, C., Soligo, M., Casas-Sainz, A., 2014. The influence of surface and tectonic processes on landscape evolution of the Iberian Chain (Spain): Quantitative geomorphological analysis and geochronology. Geomorphology 206, 37–57. doi:10.1016/j.geomorph.2013.09.017

Seeber, L., Gornitz, V., 1983. River profiles along the Himalayan arc as indicators of active tectonics. Tectonophysics 92, 335–367.

Shahar, J. 1994, The Syrian arc system: an overiew. Palaeography, Palaeoclimatology, Palaeoecology, 112, 125-142. SSDI 0031-0182(94)00035-7.

Shamir, G., Eyal, Y., and Bruner, I. 2006. Localized versus distributed shear in transform plate boundary zones: the case of the Dead Sea transform in the Jericho Valley. Geochem Geophys Geosyst, 6, 1–21.

Shawabkeh, K.F., 2001. Geological map of Al Karama — 3153-IV, 1:50.000, Internal Report of Natural Resources Authority, Amman, Jordan.

Siddiqui, S., Soldati, M., 2014. Appraisal of active tectonics using DEM-based hypsometric integral and trend surface analysis in Emilia-Romagna Apennines, northern Italy. Turkish J. Earth Sci. 23, 277–292. doi:10.3906/yer-1306-12

Smit, J., Brun, J.P., Fort, X., Cloetingh, S., and Ben-Avraham, Z. 2008. Salt tectonics in pull-apart basins with application to the Dead Sea Basin, Tectonophysics, 449, 1-16. doi:10.1016/j.tecto.2007.12.004.

Smith, M.W., 2014. Roughness in the Earth Sciences. Earth-Science Rev. 136, 202–225. doi:10.1016/j.earscirev.2014.05.016

Snyder, N.P., Whipple, K.X., Tucker, G.E., Merritts, D.J., 2003. Channel response to tectonic forcing: Field analysis of stream morphology and hydrology in the Mendocino triple junction region, northern California. Geomorphology 53, 97–127. doi:10.1016/S0169-555X(02)00349-5

Strahler, A.N., 1952. Hypsometric (area-altitude) analysis of erosional tophography. Geological Society of America Bulletin, 63, 1117-1142.

Telbisz, T., Kovács, G., Székely, B., Szabó, J. 2013. Topographic swath profile analysis: a generalization and sensitivity evaluation of a digital terrain analysis tool. Zeitschrift fur Geomophologie. DOI: 10.1127/0372-8854/2013/0110.

Ten Brink, U. S., Schoenberg, N., Kovachm R. L., Ben-Avraham, Z. 1990. Uplift and possible Moho offset across the Dead Sea transform. Tectonophysics, 180, 71-85.

Ten Brink, U.S., Flores, C.H. 2012. Geometry and subsidence history of the Dead Sea basin: a case for fl uid-induced mid-crustal shear zone? J Geophys Res 117:B01406. doi: 10.1029/2011JB008711.

Tricart, J., Cailleux, A., 1958. Cours de Geomorphologie I: Geomorphologie Structurale. C.D.U., Paris.

Troiani, F., Galve, J.P., Piacentini, D., Della Seta, M.,Guerrero, J., (2014). Spatial analysis of stream lengthgradient(SL) index for detecting hillslope processes: A case of the Gállego River headwaters (Central Pyrenees, Spain). Geomorphology 214, 183–197.

Walcott, R.C., Summerfield, M.A., 2008. Scale dependence of hypsometric integrals: An analysis of southeast African basin, Geomorphology, 96, 174-186.

Wdowinski, S., Bock,Y., Baer, G., Prawirodirdjo, L., Bechor, N., Naaman, S., Knafo, R., Forrai, Y. and Melzer, Y. 2004. GPS measurements of current cruastal movements along the Dead Sea Fault. J. Geophys. Res., 109, B05403, doi: 10. 1029/2003JB002640.

Weber, M., Abu-Ayyash, K., Abueladas, A., Agnon, A., Alasonati Tasárová, Z., Al-Zubi, H., Babeyko, A., Bartov, Y., Bauer, K., Becken, et al. 2009. Anatomy of the Dead Sea transform from lithospheric to microscopic scale. – Reviews of Geophysics, 47, RG2002, doi:10.1029/2008RG000264.

Weinstein, Y. and Garfunkel, Z. 2014. The Dead Sea Transform and the Volcanism in Northwestern Arabia. In: Garfunkel Z et al (eds) Dead Sea transform fault system: reviews, Modern approaches in solid earth sciences 6. Springer, Dordrecht. 91-108.

Westway, R. 1995. Deformation around stepovers in strike-slip fault zones. Journal of Structural Geology 17 (6), 831-846.

Wetzler, N., Sagy, A., and Marco, S., 2014. The association of micro-earthquake clusters with mapped faults in the Dead Sea basin, Journal of Geophysical Research: Solid Earth, 119, 8312-8330. Doi:10.1002/ 2013JB010877.

Whipple, K.X. 2004. Bedrock Rivers and the geomorphology of the active orogens. Annual Review of Earth and Planetary Sciences.. 151-185. Doi: 10.1146/annurex.eart.32.101802.120356.

Whipple, K.X., DiBiase, R.A., Crosby, B.T., 2013. Bedrocks Rivers, in: Shroder, J.F. (Ed.), Treatise on Geomorphology. Elsevier, Poland, 550–573. doi:10.1016/B978-0-12-374739-6.00254-2

Whipple, K.X., Tucker, G.E., 1999. Dynamics of the stream-power river incision model: Implications for height limits of mountain ranges, landscape response timescales, and research needs. J. Geophys. Res., 104, 661–674.

Whipple, K.X., Wobus, C., Crosby, B., Kirby, E., Sheehan, D. 2007. New tools for quantitative geomorphology Extraction and interpretation of stream profiles from digital topographic data: GSA Annual Meeting Short Course.

Willgoose, G., Hancock, G., 1998. Revisiting the hypsometric curve as an indicator of form and process in transport-limited catchment. Earth Surf. Process. Landforms 23, 611–623.